Université du Québec
Institut national de la recherche scientifique
Centre Énergie, Matériaux et Télécommunications

NOUVELLES ANTENNES MILLIMÉTRIQUES À LENTILLE UTILISANT DES STRUCTURES PÉRIODIQUES POREUSES EN PLASTIQUE

Par

Javad Pourahmadazar

Thèse présentée pour l'obtention du grade de
Doctorat en Télécommunication, Ph.D.
en Télécommunicatio

Jury d'évaluation

Examinateur externe	Michel Clénet, Ph.D. Defence Research and Development Canada (DRDC)
Examinateur externe	Khelifa Hettak, Ph.D. Communications Research Centre (CRC), Ottawa
Examinateur interne	Tarek Djerafi, Ph.D. INRS-EMT
Directeur de recherche	Tayeb A. Denidni, Ph.D. INRS-EMT

Dedicace

To my Parents Ebrahim and Pari

Acknowledgements

Abbreviations

ABS-M30	Acrylonitrile Butadiene Styrene
ADM/AM	Additive Manufacturing
Alumide	Polyamide Aluminum-Filled
CAD	Computer Aided Design
CST	Computer Simulation Technology
DDM	Direct Digital Manufacturing
DLP	Digital Light Processing
EBM	Electronic Beam Melting
EM	Electromagnetic
EOS	Electro-Optical Systems
FEM	Finite element method
FF	Free-Forming
FDM	Fused Deposition Modeling
FBR	Front-to-Back Ratio
FZP	Fresnel Zone Plate
FSS	Frequency Selective Surface
GRIN	Gradient refractive index
HFSS	High Frequency Structure Simulator
HMFE	Half Maxwell Fish-Eye
IST	iterative method
KK	Kramers Kronig
LM	Layered Manufacturing
mmWave	Millimeter-wave
MUT	Material Under Test
NRWM	Nicolson-Ross-Weir method
PA12	Polyamide 12, PA 12
PA-GF	Polyamide Glass-Filled
PA2241	Polyamide Flame-Retardant
PEC	Perfect Electrical Conductor
PLA	Poly or polylactic acid is a biodegradable aliphatic polyester
RP	Rapid Prototyping
UG-385/U	Round cover flange to 1.85mm Female Waveguide to Coax Adapter
SLS	Selective Laser Sintering
SLL	Side Lobe Level
SLA	Stereo-lithography
STL	Standard Tessellation Language
TPU 92A-1	Rubberlike Thermoplastic Polyurethane

T/R-L	Transmission/reflection line
TEM	Transverse Electromagnetic Modes
THz	Terahertz; 1 THz $= 10^{12}$ Hz
VNA	Vector Network Analyzer
WR15	Rectangular Waveguide Size 15
ZP	Zone Plate
P	Polarization
E	$E-$Field
H	$H-$Field
E'	Effective E-filed acting on porous cells
D	Aperture Diameter
F	Focal Distance
α	Polarizability of the porous cells
α_e	Electric Polarizability
θ	Polar angle in spherical coordinate system
ϕ	Azimuthal angle in spherical coordinate system
N	Number of spheres
V	Host medium volume
ϵ_0	Vacuum permittivity
ϵ_{Air}	Air permittivity
F	Fractional Volume
K	Effective Dielectric Constant
ϵ	Permittivity
ϵ_r	relative permittivity
μ	Permeability
λ_0	free-space wavelength
β	free space-wave phase constant
h	dielectric constant
ζ	Filling Ratio
$\tan \delta$	Loss tangent
FZP_2	Half-wave FZP
FZP_4	Quarter-wave FZP
EF_m	Exponential Fitting for material (m)
η	Cube cell vertex size
η^*	Optimum Efficiency
η_{taper}	Taper Efficiency
η_{SP}	Spill Over Efficiency
η_{total}/η_T	Spill Over Efficiency
n	is Cos^n-like/Axially symmetric radiation factor
Δ	is the normalized distance between the dipole antenna
$\parallel$	is parallel
$\perp$	is perpendicular

Abstract

Gradient refractive index (GRIN) structure is an optical result generated by a progressive variation of the refractive index of a host medium to improve the design of new microwave devices 1. So these host medium modifications can be used to produce lenses for all electromagnetic spectrums with flat surfaces, or 3D volumes that do not have the aberrations of traditional spherical lenses or may have a refraction gradient with a spherical, axial or radial variations [1, 2]. This refraction gradient can be realized in a homogeneous or inhomogeneous medium using subtractive or additive methods as a material porosity control technique. Porosity, or void fraction, is a technological method to permittivity control a measure of the void as a subtractive method by reducing the host medium or using a ratio of the material filling as an additive method, which can have a percentage between 0% and 100%, to realize the final platform [3].

Porous structures embedded in the homogeneous framework are of scientific and GRIN lens design interests because of their ability to achieve intended virtual permittivity throughout the bulk of the material. Not surprisingly, traditional virtual permittivity control with porous materials involving dielectrics by reducing a density (filling ratio) of spherical or cylindrical holes was already demonstrated in the 1950s along with all the techniques with the high freedom design order that could be produced with an additive manufacturing process [4]. Unfortunately, these results have not been given much attention today despite the very interesting and accurate analysis. In the 1950s, the first analysis to control virtual permittivity using an array of spherical and cylindrical cells in Teflon and polystyrene was investigated and proven with mathematical expressions [5, 4]. Based on cylindrical pore analyses, for high length-to-diameter ratio, the control of permittivity is related directly to the orientation of electric fields and cylindrical pore axes. By using these porosity methods, the permittivity control in the ranges between 1.1 up to host medium permittivity is obtainable. To expand this range, porous cells liquid materials such as acetonitrile/benzene mixture can be used to fill and increase relative permittivity of host medium up to $\epsilon = 37$.

In this thesis, we have introduced novel and optimized concepts in the frame of mmWave communications, namely nonmagnetic ($n = \sqrt{\epsilon\mu}, \mu = 1$) gradient refractive index (Δn) lens antennas. The two ideas are intended for improving current manufacturing technologies for GRIN devices in the mmWave spectrum: the Lüneburg lens and Fresnel zone plates (FZPs) in the homogeneous framework. On the one hand, material porosity can be useful to simplify virtual permittivity design, not only in the implementation and measurement steps but also to potentially enable new and broadband properties cells with simplified schemes for impairment compensation in the mmWave, and sub-mmWave spectrums. On the other hand, permittivity control techniques based on material porosity can also facilitate the development of new GRIN device design techniques for lens applications. In fact, the introduction of material theory based on material porosity processing is considered to be one of the most encouraging methods to control the intrinsic permittivity of the material.

As a collective conclusion, regarding the extensive range of applications of permittivity control with porous structures, we can foresee the vast amount of exciting uses for the graded medium design in planar or 3D objects. Due to the extensive collection of utilization, this proposed concept uses 3D printing devices that can be employed (some of them have been experimentally confirmed in this thesis), and the presented project may motivate the development of an innovative form of lens devices, more efficient lens devices as an antenna in the areas of mmWave communication. Advantages of these virtual permittivity design using full dielectric or full metal homogeneous approaches include (i) a notable simplification of the currently required graded setups based on material change approach to achieve the equivalent variety of functionalities; (ii) the possibility of realizing all-optical GRIN devices for lens antenna design applications, with development from mm to nm printing ranges to be achieved, so far, through additive manufacturing technology widely used nowadays; and (iii) the significant rest of previous GRIN medium design practical difficulties in the lens devices manufacturing processes is solved. All the suggested schemes appear as stable and dependable solutions for efficiently GRIN lens designs of practical applications, and they may also be entirely placed in the industry for short-term fabrication. Overall, we expect that the contributed investigation outcome of our porous design approach for the lens antenna design will have a markedly relevant scientific and economic effect in such diverse areas as mmWave communication and wave focus applications.

Keywords: Antenna, additive manufacturing process, Fresnel Zone Plate, gradient refractive index (GRIN), lens, Luneburg/Lüneburg, material porosity, mmWave, perforated, stereolithography, selective laser sintering, 3D printing.

Résumé

La structure de l'indice de réfraction de gradient (GRIN) est un résultat optique généré par une variation progressive de l'indice de réfraction d'un milieu hôte pour améliorer la conception de nouveaux dispositifs à micro-ondes 1. Ainsi, ces modifications du milieu hôte peuvent être utilisées pour produire des lentilles pour tous les spectres électromagnétiques à surfaces planes, ou volumes 3D ne présentant pas les aberrations des lentilles sphériques traditionnelles ou présentant un gradient de réfraction avec des variations sphériques, axiales ou radiales [1, 2]. Ce gradient de réfraction peut être réalisé dans un milieu homogène ou inhomogène en utilisant des méthodes soustractives ou additives comme technique de contrôle de la porosité du matériau. La porosité, ou fraction de vide, est une méthode technologique de contrôle de la permittivité permettant de mesurer le vide comme méthode soustractive en réduisant le milieu hôte ou en utilisant un ratio du remplissage de matériau comme méthode additive, qui peut avoir un pourcentage entre 0 % et 100 %, pour réaliser la plate-forme finale [3].

Les structures poreuses intégrées dans le cadre homogène ont des intérêts scientifiques et trouvent leur utilité dans la conception de lentilles GRIN en raison de leur capacité à atteindre la permittivité virtuelle voulue dans la masse du matériau. Sans surprise, le contrôle de la permittivité virtuelle traditionnelle avec des matériaux poreux impliquant des diélectriques en réduisant la densité (taux de remplissage) des trous sphériques ou cylindriques était déjà prouvée dans les années 1950 de même que toutes les techniques avec l'ordre de conception de haute liberté qui pourrait être produit avec un processus de fabrication additif [4]. Malheureusement, ces résultats n'ont pas reçu beaucoup d'attention aujourd'hui malgré l'analyse très intéressante et précise. Dans les années 1950, la première analyse visant à contrôler la permittivité virtuelle, en utilisant un tableau de cellules sphériques et cylindriques dans le Téflon et le polystyrène, a été étudiée et prouvée avec des expressions mathématiques [5, 4]. Sur la base des analyses de pores cylindriques, pour un rapport longueur-diamètre élevé, le contrôle de la permittivité est directement lié à l'orientation des champs électriques et des axes de pores cylindriques. En utilisant ces méthodes de porosité, le contrôle de la permittivité dans les plages comprises entre 1,1 et la permittivité du milieu hôte peut être obtenu. Pour élargir cette gamme, des matériaux liquides à cellules poreuses tels que le mélange acétonitrile/benzène peuvent être utilisés pour remplir et augmenter la permittivité relative du milieu hôte jusqu'à $\epsilon = 37$.

Dans cette thèse, nous avons introduit des concepts innovants et optimisés dans le cadre des communications mmWave, à savoir antennes optiques non magnétiques à gradient de réfraction. Les deux idées sont destinées à améliorer les technologies de fabrication actuelles pour les dispositifs GRIN dans le spectre mmWave: la lentille Lüneburg et les plaques zonales de Fresnel (FZP) dans le cadre homogène. D'une part, la porosité du matériau peut être utile pour simplifier la conception de permittivité virtuelle, non seulement dans les étapes de mise en œuvre et de mesure, mais aussi pour activer des cellules potentielles avec de nouvelles propriétés à large bande et des schémas simplifiés de

compensation de perte dans les spectres mmWave et sub-mmWave. D'un autre côté, les techniques de contrôle de la permittivité basées sur la porosité du matériau peuvent également faciliter le développement de nouvelles techniques de conception de dispositifs GRIN pour les applications de lentilles. En fait, l'introduction de la théorie des matériaux basée sur le traitement de la porosité est l'une des méthodes les plus encourageantes pour contrôler la permittivité intrinsèque du matériau.

En conclusion, en ce qui concerne la vaste gamme d'applications du contrôle de la permittivité avec des structures poreuses, nous pouvons prévoir plusieurs cas d'utilisations passionnantes pour le design gradué du support dans les objets planaires ou 3D. En raison de la vaste collection d'utilisation, ce concept proposé utilise des dispositifs d'impression 3D (certains d'entre eux ont été confirmés expérimentalement dans cette thèse), et le projet présenté peut motiver le développement d'une forme innovante de dispositif de lentilles plus efficaces sous forme d'antenne dans les domaines de la communication mmWave. Les avantages de cette conception de la permittivité virtuelle en utilisant des approches homogènes diélectriques ou métalliques complètes comprennent: (i) une simplification notable des configurations graduées actuellement requises et basées sur l'approche de changement de matériau pour obtenir la variété équivalente de fonctionnalités; (ii) la possibilité de réaliser des dispositifs GRIN tout optique pour des applications de conception d'antennes de lentilles, avec développement de plages d'impression de mm à nm à atteindre, jusqu'à présent, grâce à une technologie de fabrication additive largement utilisée de nos jours; et (iii) le reste significatif des difficultés pratiques antérieures de conception de milieu GRIN dans les procédés de fabrication des dispositifs de lentilles est résolu. Tous les schémas proposés apparaissent comme des solutions stables et fiables pour des conceptions de lentilles GRIN efficaces pour des applications pratiques, et ils peuvent également être entièrement intégrés dans l'industrie pour une fabrication à court terme. Dans l'ensemble, nous nous attendons à ce que le résultat de notre approche de conception poreuse pour la conception d'antennes à lentilles ait un effet scientifique et économique nettement pertinent dans des domaines aussi divers telque la communication mmWave et les applications de focalisation des ondes.

Mots-clés: Antenne, procédé de fabrication additif, plaque de Fresnel, indice de réfraction de gradient (GRIN), lentille, Luneburg, porosité du matériau, mmWave, perforation, stéréolithographie, frittage laser sélectif, impression en 3D.

Contents

Liste des figures

xxi

Chapter 1

Introduction

1.1 Motivation

Advances in additive manufacturing process and materials to the design of gradient refractive index (GRIN) lenses with perforation methods are enabling a host of new possibilities and perspectives for low-cost lens antenna architectures. This work review and analyses of allowing additive manufacturing technologies and graded topologies of lens designs with the material porosity methods. This work illustrates the basic perforated lens design approaches in homogenous medium and explores advanced abilities of this architecture, such as Fresnel zone plates, Lunenburg, a Half-fish eye, and Eaton lens towards electromagnetic spectrums. Design aspects are studied in the development of material porosity control techniques to provide intended permittivity with material deforming. Finally, the articles conclude by addressing future challenges and opportunities for these printed lenses.

1.2 Gradient refractive index (GRIN)

Gradient refractive index (GRIN) structure is an optical result generated by a progressive variation of the refractive index of a host medium to improve the design of new microwave devices 1. So these host medium modifications can be used to produce lenses for all electromagnetic spectrums with flat surfaces, or 3D volumes that do not have the aberrations of traditional spherical lenses or may

have a refraction gradient with a spherical, axial or radial variations [1, 2]. This refraction gradient can be realized in a homogeneous or inhomogeneous medium using subtractive or additive methods as a material porosity control technique. Porosity, or void fraction, is a technological method to permittivity control a measure of the void as a subtractive method by reducing the host medium or using a ratio of the material filling as an additive method, which can have a percentage between 0% and 100%, to realize the final platform [3].

Porous structures embedded in the homogeneous framework are of scientific and GRIN lens design interests because of their ability to achieve intended virtual permittivity throughout the bulk of the material using additive manufacturing processes. Advances in additive manufacturing process and materials to the design of gradient refractive index (GRIN) lenses with perforation methods are enabling a host of new possibilities and perspectives for low-cost lens antenna architectures. This work review and analyses of allowing additive manufacturing technologies and graded topologies of lens designs with the material porosity methods. Not surprisingly, traditional virtual permittivity control with porous materials involving dielectrics by reducing a density (filling ratio) of spherical or cylindrical holes was already demonstrated in the 1950s along with all the techniques with the high freedom design order that could be produced with an additive manufacturing process [4]. Unfortunately, these results have not been given much attention today despite the very interesting and accurate analysis. In the 1950s, the first analysis to control virtual permittivity using an array of spherical and cylindrical cells in Teflon and polystyrene was investigated and proven with mathematical expressions [5, 4]. Based on cylindrical pore analyses, for high length-to-diameter ratio, the control of permittivity is related directly to the orientation of electric fields and cylindrical pore axes. By using these porosity methods, the permittivity control in the ranges between 1.1 up to host medium permittivity is obtainable. To expand this range, porous cells liquid materials such as acetonitrile/benzene mixture can be used to fill and increase relative permittivity of host medium up to $\epsilon = 37$.

Moreover, plastic-based samples with different shape pores sizes were discussed, and the inclusion of dielectric characteristics analysis such as permittivity ϵ and permeability μ in porous host materials gave rise to new phenomena and design virtual permittivities. But despite this report for materials permittivity reduction and applications, none of these techniques led to practical successes in GRIN lens [1] design until 3D printing inventions because of manufacturing and implementations limitations 26, 27. The permittivity control via pores for graded index medium can be arranged

according to size, shapes, and volumes [5, 4]. Therefore, the wide range virtual permittivity control with using high dielectric host medium is achievable, and its applications are of interest in GRIN lens design for microwave, millimeter-wave, and optic electromagnetic spectrums.

For pore sizes classification, the range of pores classifies the material porosity type into micropores (less than 2 nm), mesopores (2 nm to 50 nm), and macrospores with voids size above 50 nm. In last decades, most of the reported literature for printed GRIN lens structures are macrospores type porosity control which is achieved with additive manufacturing methods for antenna engineering [28]. Conventionally, most optical lenses have been made by subtractive techniques, such as cutting grooves [29], cutting air-holes [6, 7, 30, 8], and machining lenses [31].

1.3   3D printing/additive manufacturing

3D printing is an additive manufacturing [32, 33] process that can realize 3D created objects by adding one layer at a time from the bottom up with a predefined material. The term additive manufacturing (ADM) is shown in such technologies like rapid prototyping (RP), layered manufacturing, direct digital manufacturing (DDM), and 3D printing [32]. Therefore, there is no difference between all of these processes, and they are synonyms for the same process. In recent years, this technology has attracted more attention for manufacturing because of its low fabrication cost, high scalability, ease of implementation, and combination of both metal and dielectric materials. Moreover, this technology can be considered as a green technology, which is an alternative to conventional laminating fabrication methods. This material jetting process can realize 3D-created objects by adding one layer of a predefined material at a time. Also, the materials' deformation in both flexible and rigid forms, which is needed with 3D printing technology, is another capability of this technology. Therefore, this design freedom can be used to realize material porosity-based devices, which is impossible or difficult with conventional methods, especially for GRIN lens design prototypes [10].

To realize printed structures with material jetting technology with either dielectric materials [32, 33] or metal [32, 21, 20], the first step is designing and slicing the prototypes in digital form. This 3D prototype model is patterned after it is designed with 3D software and is sliced in digital form and transformed to the printer for prototyping. This software using a manufacturing device can prepare a $100\mu m$ thickness accuracy layer for printing, and this accuracy is different from device

to device and from technology to technology. This dielectrically designed patterns can be achieved layer by layer with a 3D printer in a method called printing resolution. The prototyping resolution varies from technology to technology, but the standard layer thickness is 100 - 150μm, and the high-definition layer thickness is around 60μm. However, this printing accuracy with $\pm$ 0.3% (with a limit of $\pm$ 0.3 mm) tolerance varies.

1.4   Thesis organization

In this thesis, we have introduced novel and optimized concepts in the frame of mmWave communications, namely nonmagnetic ($n = \sqrt{\epsilon\mu}, \mu = 1$) gradient refractive index (Δn) lens antennas. The two ideas are intended for improving current manufacturing technologies for GRIN devices in the mmWave spectrum: the Lüneburg lens and Fresnel zone plates (FZPs) in the homogeneous framework. On the one hand, material porosity can be useful to simplify virtual permittivity design, not only in the implementation and measurement steps but also to potentially enable new and broadband properties cells with simplified schemes for impairment compensation in the mmWave, and sub-mmWave spectrums. On the other hand, permittivity control techniques based on material porosity can also facilitate the development of new GRIN device design techniques for lens applications. In fact, the introduction of material theory based on material porosity processing is considered to be one of the most encouraging methods to control the intrinsic permittivity of the material.

The remarkable applicability of classical permittivity control with a volume reduction in a homogeneous medium within a full dielectric or full metal platform is due to its capacity to simultaneously control the amplitude and phase of GRIN medium subzones with an arbitrary material by use of porous cells or deformed structures. The ordered GRIN compositions based on permeable cells and reconstruction steps of these techniques and classifications have been reviewed in Chapter 2. Corkum's [5] initial tries before 3D printing technologies have been introduced, highlighting the principal problems of its virtual permittivity configuration, namely the fact that the virtual output permittivity for foam-based plastic with cylindrical air-holes directly related to the type of material, cell heights, and E-field orientations. To overcome the problem, an alternative spherical configuration has been reported by Ward's, which was introduced by Corkum [5] a few years after his original proposal in Bell Laboratories. This spherical porous configuration was more independent

of the incident wave orientation because of the symmetrical structure of the object compared to permeable cylinder cells. Thus, in the spherical porous structures, the different incident wave's angles can be used to control virtual permittivity of the medium.

In Chapter 3, we also reviewed the concept of deformed material based on cube-shaped plastic cells with rods connectors to realize Fresnel zone plates by additive manufacturing (ADM) processes. The additive manufacturing process consists of a technology solution to enable the implementation of complex shape porosity cells using a volume reduction similar to previous porosity techniques, employing polymer based plastics. For this purpose, the new porous cell with 3D-printing manufacturing ability consists of cube-shaped plastics analyzed to provide intended permittivity in a homogeneous medium. The concepts for the design and analysis methods reviewed in Chapter 2 constitute the core of the original porous GRIN ideas presented in this thesis.

In particular, the free forming (FF) approach has been employed to generate deformed materials based on 3D printing technology to control the amplitude and phase profiles of the intended permittivity for required lens function subzones. Also, this free-forming and generation virtual permittivity method has been revised to implement simple planar half-wave and quarter-wave Fresnel zones, with a general multi-dielectric Fresnel zones technique for mmWave wavelength. The recommended design significantly simplifies previous multi-dielectric inhomogeneous approaches by (i) using single dielectric combined with material porosity and additive manufacturing processes, overcoming the manufacturing complexity with required permittivity implementation and the cost, and (ii) reducing multiple reflections of the plate because of the high permittivity zones by smaller effective permittivity zones to produce the intended phase shift with lower attenuation. Indeed, we present two transmission-mode dielectric Fresnel-Zone Plate Lens (FZPL) antennas for use within the V-band spectrum. The proposed FZPs are realized via pure plastic material using two different additive manufacturing processes. The proposed FZP lenses are designed with half ($\lambda/2$) and quarter ($\lambda/4$) phase correction rings at 60-GHz with $30\lambda_0$ diameter, where λ_0 is the free-space wavelength. The permittivity effect for lens sub-zones is controlled by material porosity in cube-shaped structures. The 3D printed zone plate lenses are built using additive manufacturing plastic materials with a thickness of λ_0 and constant relative permittivities equal to 2.76 and 3.6. Different types of antenna with $\cos^n$-like radiation patterns as lens illuminators are analyzed on the vertical plane of the flat lenses to have a high efficiency over the considered operating band. Simulations

and experimental measurements show a reasonably close match, therefore allowing for a reliable predictability.

In Chapter 4, the concept of a parallel-plate, porous, dielectric Lüneburg lens is introduced with the tubular cells of a classical permittivity control approach in the TEM waveguide. The strong potential of this approach is in its capacity for simultaneously controlling the material filling ratio through cell thickness and radius with two degrees of freedom. The cost for achieving GRIN lenses using inhomogeneous metamaterial forms lies in fabrication problems, the challenge of broad-range virtual permittivity control, and the narrow bandwidth properties which comprise at least half of the full dielectric structures' bandwidth. A possible configurations based on intended GRIN lens platforms and rules have been suggested, namely, an air hole approach. The proposed arrangement have been analytically confirmed by implementing interesting homogeneous GRIN lens designs with applications of mmWave communications. Indeed with using air-hole approach, a 3D printed cylindrical full dielectric Luneburg lens antenna with physical porosity control to achieve intended permittivity of subzones in homogenous framework is presented for millimeter-wave applications. The microstrip dipole antenna with Cos^{10}-like radiation patterns is used as lens illuminator inside a parallel-plate waveguide operating in V-band. The intended gradient refractive indices are achieved using material porosity control in air-hole-based approach through the homogeneous medium to satisfy the required lens focusing rules. The air-hole radius is used to control the predetermined permittivity according to the presented lens focusing rules. To achieve this goal, the numerical analyses and approximations are performed to define the intended air-hole radius concerning the wave launcher illumination between parallel plates in TEM mode. The proposed lenses are fabricated using an additive manufacturing polyimide plastic with the thickness of $\lambda_0/2$ and relative permittivities of $\epsilon_r = 3.4$. Selective laser sintering is the fabrication method utilized to manufacture this framework. The simulations and experiments verify the suggested designs method and results.

In chapter 5, we introduce a novel nonmagnetic porous lens for creating millimeter-wave Fresnel zone plate lens antennas with broadband and high gain responses. Such configuration is composed of various permeable cells in the homogeneous framework based on a permittivity reduction technique distributed across a lens aperture surface. Each permeable cell is a cubical cell with a controlled vertex size to realize intended virtual permittivity of sub-zones composed of nonmagnetic Alumide material. Each cell with the different rods and vertex size is analyzed based on quasi-static modeling by extracting a trusted area for the dispersion diagram, and the whole half-wave phase correction

FZP structure is designed with the desired dielectric cells within this area. A prototype of the suggested half-wave FZP with the focal length to aperture diameter ratio of (F/D) 0.87 operating at 30GHz is fabricated with the SLS additive manufacturing process and analytically identified both in simulations and measurements. It is confirmed that the fabricated FZP with porous techniques in the homogeneous medium operates without any significant irregularities compared to previous manufacturing techniques with further advantages. The intended FZPL antenna provides a realized gain of 35 dB and 67% efficiency for an optimized circular horn antenna with Cos^{41}-like illuminations and shows a gain variation of about 3.6 dB in the 28–38 GHz range. The FZPL antenna shows low side-lobe levels and constant radiation characteristics over its operating band.

In chapter 6, we briefly review various potential lines of future porous-base GRIN lens research considered to be of high relevance by the author.

In chapter 7, summarizes the porous lens presented in this Thesis and proposes potential prospects for future work in French.

As a collective conclusion, regarding the extensive range of applications of permittivity control with porous structures, we can foresee the vast amount of exciting uses for the graded medium design in planar or 3D objects. Due to the extensive collection of utilization, this proposed concept uses 3D printing devices that can be employed (some of them have been experimentally confirmed in this thesis), and the presented project may motivate the development of an innovative form of lens devices, more efficient lens devices as an antenna in the areas of mmWave communication. Advantages of these virtual permittivity design using full dielectric or full metal homogeneous approaches include (i) a notable simplification of the currently required graded setups based on material change approach to achieve the equivalent variety of functionalities; (ii) the possibility of realizing all-optical GRIN devices for lens antenna design applications, with development from mm to nm printing ranges to be achieved, so far, through additive manufacturing technology widely used nowadays; and (iii) the significant rest of previous GRIN medium design practical difficulties in the lens devices manufacturing processes is solved. All the suggested schemes appear as stable and dependable solutions for efficiently GRIN lens designs of practical applications, and they may also be entirely placed in the industry for short-term fabrication. Overall, we expect that the contributed investigation outcome of our porous design approach for the lens antenna design will have a markedly

relevant scientific and economic effect in such diverse areas as mmWave communication and wave focus applications.

Chapter 2

Ordered porous structures for emerging GRIN Lenses: A Review

This chapter has been taken partly from author submitted article with the similar title to IEEE TAP-CPMT.

2.1 Introduction to GRIN structures

Gradient refractive index (GRIN) structure is an optical result generated by a progressive variation of the refractive index of a host medium to improve the design of new microwave devices [1]. So these host medium modifications can be used to produce lenses for all electromagnetic spectrums with flat surfaces, or 3D volumes that do not have the aberrations of traditional spherical lenses or may have a refraction gradient with a spherical, axial or radial variations [1, 2]. This refraction gradient can be realized in a homogeneous or inhomogeneous medium using subtractive or additive methods as a material porosity control technique.

Porosity, or void fraction, is a technological method to permittivity control a measure of the void as a subtractive method by reducing the host medium or using a ratio of the material filling as an additive method, which can have a percentage between 0% and 100%, to realize the final platform [3]. Porous structures embedded in the homogeneous framework are of scientific and GRIN lens design interests because of their ability to achieve intended virtual permittivity throughout the

bulk of the material. Not surprisingly, traditional virtual permittivity control with porous materials involving dielectrics by reducing a density (filling ratio) of spherical or cylindrical holes was already demonstrated in the 1950s along with all the techniques with the high freedom design order that could be produced with an additive manufacturing process [4]. Unfortunately, these results have not been given much attention today despite the very interesting and accurate analysis.

In the 1950s, the first analysis to control virtual permittivity using an array of spherical and cylindrical cells in Teflon and polystyrene was investigated and proven with mathematical expressions [5, 4]. Based on cylindrical pore analyses, for high length-to-diameter (L/D) ratio, the control of permittivity is related directly to the orientation of $E-$fields and cylindrical pore axes. By using these porosity methods, the permittivity control in the ranges between $\epsilon = 1.1$ ($\sim \epsilon_{Air} = 1$) up to host medium permittivity is obtainable. To expand this range, porous cells liquid materials such as acetonitrile/benzene mixture can be used to fill and increase relative permittivity of host medium up to $\epsilon_r = 37$[19, 14]. Moreover, plastic-based samples with different shape pores sizes were discussed, and the inclusion of dielectric characteristics analysis such as permittivity ϵ and permeability μ in porous host materials gave rise to new phenomena and design virtual permittivities.

But despite this report for materials permittivity reduction and applications, none of these techniques led to practical successes in GRIN lens design until 3D printing inventions because of manufacturing and implementation limitations [1, 26, 27, 34]. The permittivity control via pores for graded index medium can be arranged according to size, shapes, and volumes [5, 4]. Therefore, the wide range virtual permittivity control with using high dielectric host medium [19, 14] is achievable, and its applications are of interest in GRIN lens design for microwave, millimeter-wave, and optic electromagnetic spectrums. For pore sizes classification, the range of pores classifies the material porosity type based on porosity cells width over diameters ($\frac{w_{pores}}{D_{pores}} = \zeta_p$) into micropores ($\zeta_p \leq 2nm$), mesopores ($\zeta_p \leq 50nm$), and macrospores with voids size above ($\zeta_p \geq 50nm$) [34]. In last decades, most of the reported literature for printed GRIN lens structures are macrospores type porosity control which is achieved with additive manufacturing methods for antenna engineering applications [28]. Conventionally, most optical lenses have been made by subtractive techniques, such as cutting grooves [29], cutting air-holes[6, 7], and machining lenses.

This review is prepared as follows to analysis the proposed method to provide lens schemes in the homogeneous frameworks [6, 7, 9, 11, 16, 30, 31, 32, 33, 35, 10, 21, 22, 20, 8, 17, 18, 12]. Section

II focuses on artificial dielectric utilizing porous deforming by effective medium design approaches and related examples. Section III categories the porosity techniques for virtual permittivity design. Finally, Section IV reviews future approaches, manufacturing difficulties, and potential clarifications particular to electromagnetic applications such as lens and antenna designs with conceivable additive manufacturing technologies.

2.2   3D Printing Process and Materials

3D printing is an additive manufacturing [32, 33, 35] process that can realize 3D created objects by adding one layer at a time from the bottom up with a predefined material. The term additive manufacturing (ADM) is shown in such technologies like rapid prototyping (RP), layered manufacturing, direct digital manufacturing (DDM), and 3D printing [32, 35]. Therefore, there is no difference between all of these processes, and they are synonyms for the same process. In recent years, this technology has attracted more attention for manufacturing because of its low fabrication cost, high scalability, ease of implementation, and combination of both metal and dielectric materials. Moreover, this technology can be considered as a green technology, which is an alternative to conventional laminating fabrication methods.

This material jetting process can realize 3D-created objects by adding one layer of a predefined material at a time. Also, the materials' deformation in both flexible and rigid forms, which is needed with 3D printing technology, is another capability of this technology. Therefore, this design freedom can be used to realize material porosity-based devices, which is impossible or difficult with conventional methods, especially for GRIN lens design prototypes [35, 10]. To realize printed structures with material jetting technology with either dielectric materials [32, 33] or metal [32, 21, 20], the first step is designing and slicing the prototypes in digital form. This 3D prototype model is patterned after it is designed with 3D software and is sliced in digital form and transformed to the printer for prototyping. This software using a manufacturing device can prepare a $100\mu m$ thickness accuracy layer for printing, and this accuracy is different from device to device and from technology to technology. This dielectrically designed patterns can be achieved layer by layer with a 3D printer in a method called printing resolution. The prototyping resolution varies from technology to technology, but the standard layer thickness is 100 - $150\mu m$, and the high-definition layer thickness is around $60\mu m$. However, this printing accuracy with $\pm$ 0.3% (with a limit of $\pm$ 0.3 mm) tolerance

varies. Digital light processing (DLP) [33, 35, 36], fused deposition modeling (FDM) [33, 35, 36], electronic beam melting (EBM)[33, 35, 36], stereolithography (SLA)[33] and selective laser sintering (SLS)[33, 35, 36] are some of the technologies with differences in used raw materials.

Therefore, the realization of structures with element sizes lower than λ size in operating frequency from microwave to submillimeter-wave is feasible. Also, because of the possibility of using different relative permittivity materials such as PLA, polyimide, and ABS-M30, a wide range of refractive indices to realize gradient index structures using material porosity techniques is feasible. FDM and SLS technologies are the most mature for microwave and millimeter-wave 3-D printed dielectric materials [32, 33].

In reported works, the SLS, SLA, and FDM manufacturing processes are used for the manufacturing of microwave and GRIN prototypes, and results are compared with conventional manufactured components [32, 21, 36]. During SLS, small particles of powder base materials such as plastic, glass, or ceramic are combined by laser heat to form a rigid 3-D structure [32, 33]. This process was invented in the 1980s by Deckard and Beaman at the University of Texas (UT) [32, 36]. Comparable to other 3-D-printing devices, an SLS device mechanism starts with a computer-aided design (CAD) file [33, 36]. CAD files are transformed to digital .STL format with interface software, which plays a crucial role in transformation of desired layers between hardware and computers [33, 35, 36]. Up to [36] reports, in this printing machine method, the printed objects are created with powder base materials such as PA12, which is coated on top of the thin printed layer on the SLS machine work plate. A laser controlled by a computer, in addition to printing the object, also performs the task of detecting corners of the realized object onto the powder particles[36]. Then, the sintering and melting process by laser beam continues over and over to print the whole object[36]. When the whole object printing layers are thoroughly developed, it should be left in SLS device for cooling of entire object[36]. Unlike other 3D printing methods, the SLS uses a tiny additional tool after the release of an object, which means that, regularly, when they exit the SLS device, objects should not be rinsed otherwise or adequately changed [36]. SLS does not need to use additional support to keep an object inside while it is still printing compare to SLA or FDM methods[33, 36]. This addittive manufacturing processing includes distinct materials such as nylon or polystyrene, metals such as steel, titanium, and composite mixtures, and green sand [36, 37]. The ability of SLS powder base printing to create highly sophisticated geometry quickly and directly contributes to digital CAD data compared to other techniques[33, 35, 36]. SLS is increasingly used in the industry

with low-quantity components requiring high-quality ones such as the aerospace industry, sports car engineering, and microwave engineering [33, 35, 36].

2.3 Additive manufacturing materials and measurements

2.3.1 3D printing Materials

3-D printings or additive manufacturing processes are a polymerization procedure that employs light-sensitive polymers to realize objects[35, 38, 39, 40, 41, 42, 43, 44]. These materials become harder due to the cross-flow process when they are exposed to ultraviolet (UV) light or light [41, 42, 43, 44]. Distinct types of commercial photopolymers available for ADM processes are as follow: polycarbonate (PC) from Stratasys [44], Stratasys ABS-M30[44], and Stratasys PC-ABS blend[44], which are useful for FDM-based technologies; DSM Somos 9120[44], DSM Somos-DMX-SL 100[44], DSM Somos-Prototherm UV-cured[44], and DSM NanoForm 15120 UV-cured[44], which are applicable to SL-based devices; and alumide, polyimide, PA 12 (polyamide)[44], alumide (polyamide aluminum-filled), PA-GF (polyamide glass-filled)[44], TPU 92A-1 (rubberlike thermo-plastic polyurethane), and PA 2241 FR (polyamide flame-retardant), which are more applicable materials for SLS-based printers [44]. As these materials are designed for the primary purpose of constructing mechanical components, the electrical property analysis data such as the permittivity (ϵ), permeability (μ), and loss tangents ($\tan\delta$) of these polymers are not widely available for the lens and antenna design applications [35]. Accordingly, particular intrinsic material properties analysis should be used to control this permittivity with porous structures or the deformed shape structures [35].

The experimental measurement results for the permittivity μ, and permeability ϵ of the desired electromagnetic spectrum are mandatory to the best realization of virtual permittivity using porous structures in the intended host medium [35, 45]. Since most of the introduced 3-D printing polymer plastics are magnetless materials, where the relative permeability is $\mu_r = 1$ [35], the porous technique to reduce, increase, and control intrinsic relative permittivity is an easy option to design GRIN homogenous medium components by analyzing only ϵ_r [35]. The majority of material characteristics for ADM materials demonstrated and analyzed in the low-frequency regime <18GHz. Therefore, the precise frequency characteristic of printing materials is essential for the successful design of

millimeter-wave and submillimeter-wave devices. The vital factors for the analysis of each plastic material for GRIN medium implementation with frequency attributes are ϵ_r, $\tan\delta$, and refractive index ($n_r = \sqrt{\epsilon_r \mu_r}$) [35, 46].

In this analysis, the loss tangent ($\tan\delta$) is the ratio of the lossy reaction to the $E-$field in the curl equation to the lossless response [45]. This factor authorizes antenna, and lens engineers to provide requirements for low-loss performance design applications [45]. The dielectric constant (ϵ_d) is another essential factor in design of porous structures because it controls the transmission line characteristic impedance of the proposed material that affects reflection loss and the bandwidth of the system [45]. On this basis [45], the broadband EM characteristic analysis should be done for each material samples and porous implemented designs individually to estimate the total percent of error for mentioned porosity. Broadband EM characterization of 3D printed material properties investigates the frequency dependent characteristic of permittivity and loss tangent parameters which authorize control virtual permittivity for the homogeneous frameworks [45]. The extraction of ϵ_r for the printed samples w/without porous cells on $E-$field illumination orientation and operating frequency especially for high-frequency applications is the principal goal of this process[45].

As we know, the permittivity is a complex parameter which is related to other factors such as frequency and temperature[45]. This complex parameter is regularly represented as relative value $\epsilon_r : \epsilon = \epsilon_r \epsilon_0 = \epsilon_0(\epsilon_r^{'} - j\epsilon_r^{''})$, where $\epsilon_0 = 8,85 \times 10^{-12} F/m$[45]. The real part of this equation is called the dielectric constant, and it is not constant in frequency, and the ratio of the Im/Re parts is termed the dissipation factor or $\tan\delta$[45, 47, 48].

2.3.2 Dielectric Measurement Methods

In previous decades, various methods have been developed to measure complex properties of dielectric materials, such as frequency domain or time domain methods with one port or two ports vector network analyzer setup [45, 47, 48, 14, 46]. All of the reported methods are restricted to particular frequencies, applications and material types such as a solid or liquid form by its specific constraint. These methods can be employed with a programmed software kit upon which to extract intended data to dielectric property parameters such as permittivity and permeability with the measured S-parameters using VNA.These conversion methods can be used to convert extracted S-parameter results to material characteristics data by Nicolson-Ross-Weir method (NRWM) [45, 47], NIST iter-

ative method [45, 47], new non-iterative method (NNIST) [45, 47], Kramers-Kronig relations (KK) [45, 47], and Short circuit line method [45, 47], which are applicable to most bulk printed materials. For this reason, different methods were developed for the measurement of dielectric properties including Transmission/reflection line (T/R-L) [45, 47], open-ended coaxial probes [45, 47], free space method [45, 47], dielectric-resonators [45, 47], near-field scanning probes [45, 47], and the resonant method [45, 47].

As a result of millimeter-wave and submillimeter-wave applications, dielectric material measurements especially for porous printed structures, unlike thin plastic samples, are very difficult to cover inclusively [45, 48, 14]. Based on porosity type which includes cylindrical and spherical shapes, the $E-$field orientation should be analyzed carefully for each sample especially for anisotropic materials[45, 47]. Because each structure has its own niche, it requires individual analysis[45, 47]. The measurement methods like TE_{01} cavities which are utilizing tangential field orientations to dielectric specimen are more accurate than normal fields' orientation setups because of the absence of effects of air-gap or interface depolarization. We can summarize these fabrication methods as follow [[45], Figs:2-4]:

1. Transmission/Reflection line method is the most popular and efficient broadband dielectric measurement method [45, 47, 46]. In this method, only the TE mode in waveguides and TEM mode in coaxial line are assumed to propagate, and results involve S_{11} and S_{21} measurements. This method is suitable for lossy to low loss material under test (MUTs) and printed solids which can be applied for measurements of species in the frequency range of 1MHz$\leq f \leq$100GHz [45].

2. The open-ended coaxial probe is a non-destructive measurement method, and it extracts permittivity results from S_{11}, which is best for liquid or semi-solid materials [45, 47]. This method assumes only the TEM or TE mode is used to propagate fields to measure reflection coefficients from specimens [45, 47]. This method can be applied for measurements of species in the frequency range of 1MHz$\leq f \leq$10GHz [45].

3. The free space method is a non-contacting method suitable for broadband applications. This method is best for high temperatures, gases, and flat samples, and it assumes only the TEM propagation mode for S_{11} and S_{21} measurements [45, 47].
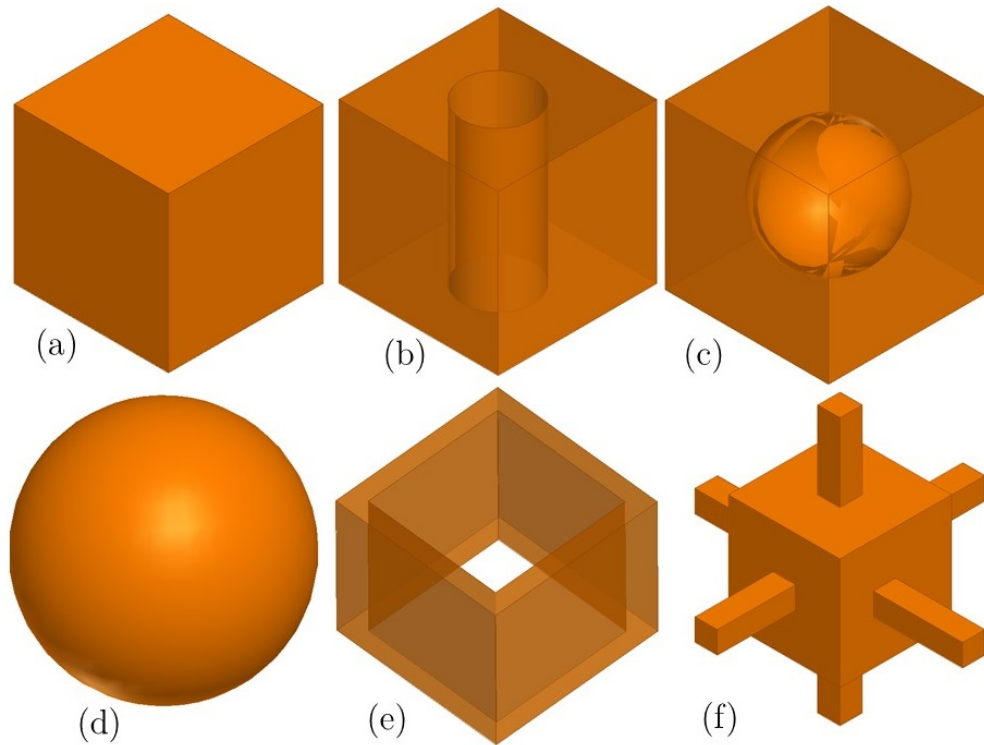
Figure 2.1 – **Dielectric or metal Single cell porous structures to functional control of dielectric permittivity (ϵ_{eff}), refractive index (n_r) and produce GRIN mediums peredetemined permittivty. (a) a typical cube structure to control dielectric permittivity by changing cube thickness; its proper for vertical E-field orientations. (b) A perforated structure with cylindrical shape porosity to control permittivity. It has two degrees of freedom as cylinder radius and hight. (c) a perforated cube with spherical porosity. (d) a Spherical cell. (e) a perforated cube. (f) a cube-shaped porosity cell with rod connections which is suitable to produce spherical GRIN mediums;**

4. The resonant method (Cavity) provides high accuracies for dielectric properties, and it is best for low-loss MUTs and small-sample measurements [45, 47]. This method assumes the TE or TM propagation mode for S_{11} and S_{21} measurements. This method can be applied for measurements of species in the frequency range of $100MHz \leq f \leq 10GHz$ [45].

Based on this basis, the RF engineers need to choose their suitable methods to extract the intended data from measurements to satisfy their requirements for analysis [45, 47]. To categorize these methods better, we can classify these measurement methods based on fixture type, material category, accuracy, and specimen preparation in detail [45]. The discrete frequency test fixtures provide report values at a few resonant EM modes, and broadband test fixtures provide a manner with which to sweep a stimulus frequency for users [45, 47]. Baker analysis show a generic classification system of measurement methods for dielectric materials based on four factors, including the matrix of dielectric measurement methods, the frequency ranges for different dielectric test fixture
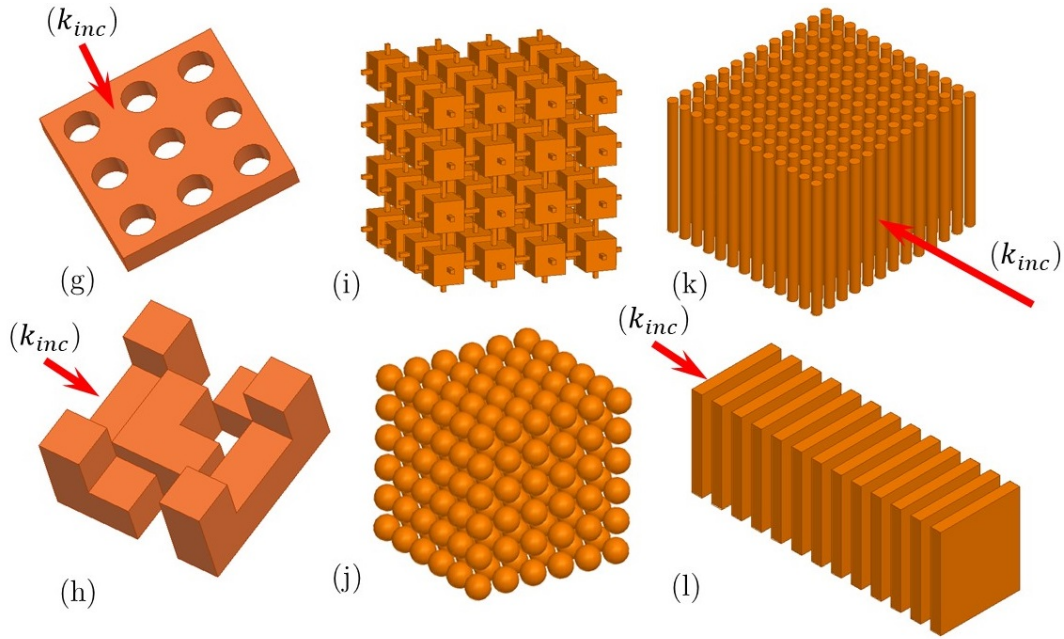
Figure 2.2 – Conventional array fashions to control permittivity virtual with the homogeneous frameworks. Spatially homogeneous medium to realize predetermined permittivity or can be used with distinct porous cells to achieve GRIN medium[6, 7, 8] (g), provide control permittivity by cube thickness and realize GRIN medium for beam shaping over the wavefront of $E-$ field ($\perp$incidence) [9] (h), In deformed dielectrics, the $E-$field has a propagating component along the direction of incidence wave, cube-shaped lattice [10, 11, 12] (i), spherical lattice [5, 4] (j), Typical proposed structure settings include 3D array for GRIN medium design [13] (k), or can be realized in a waveguide geometry[13], [14, 15] (l);

categories, and measurements of the responses to MUT fixtures, respectively [45]. This is wholly suited to a given material category by combining fixture type with the material category [45, 47]. Various additive manufacturing materials are analyzed by these techniques before the design are printed microwave devices or provided virtual permittivity based on material deforming schemes GRIN devices [44].

2.4   Artificial permittivity utilizing using porous deforming

The control of virtual permittivity to realize the desired function, such as radial in Lunenburg lens [49, 50, 51, 52, 53] structures or other particular applications, is directly related to size, shapes, and volumes of porosity, which are called cells, as shown in Fig. 2.1. Because of advances in additive manufacturing processes and materials, the need to create GRIN lens structures has steadily increased over the recent year, which can lead to the fabrication of superior and complicated structures cheaply and quickly. Fig.2.1 to Fig.2.2 shows conventional single porous cells structures to

fashion array porosities to functional control permittivity virtual and achieve graded mediums. In this process, a reduction of pore sizes or filling ratio would reduce the host medium permittivity and the ability of permittivity control with differing scales. The continuous growth of the additive manufacturing technologies, specifically in material types with different permittivities, makes the expansions and applications of GRIN lens structures reasonable.

In recent years, numerous lenses, based on porosity techniques, have been expanded to create GRIN lens devices, such as Half Maxwell Fish-Eye (HMFE) [53], Lunenburg [54, 55], Eaton lens [54, 55, 56], Flat lenses [42, 57], and coherent beam tilting [30] applications. Four of the most reported material porosities consist of spherical [5, 4], cylindrical [5], and cube shapes [49, 12] and rods [14, 15]. To provide the desired permittivity, the physical parameters of the ordered porous cells are analyzed to achieve the required phase gradient in each subzone for graded index mediums[5, 4]. Cylindrical cells, due to their easy implementations with drill holes [6] compared to spherical [5, 4] and cube-shaped [49, 50] cells, have been found to be good candidates for realizing graded index environments with control of hole density or the physical dimensions of holes in the fulfillment of proposed printable lens requirements [39, 58, 59, 60].

On the other hand, for wide-scanning angles, wide bandwidth, compact layouts, fan-beam radiation patterns, and types of feeding elements with a beam launcher such as an Omni antenna, horn, or waveguide fed, the porous technique and incident wave direction (k_{inc}) into the graded medium should be considered based on applications [61, 62]. Between these works, distinct printed lenses have already been developed for millimeter-wave applications. In 2003, Petosa carried out an initial investigation of perforated lenses based on cylindrical holes [6]. In [49, 50], Liang demonstrated further research on cube-shaped cells using polymer jetting rapid prototyping at 10GHz. The design methodology of the GRIN lenses such as planar or non-planar prototypes can be carried out to design perforated base architecture lenses utilizing additive manufacturing processes from microwave to visible light frequencies [63, 64, 13]. In mentioned perforated lenses, the transverse electromagnetic (TEM) propagation incorporates the device [6, 65]. The principle of GRIN lenses in parallel-plate propagation modes with waveguide or horn feed beam launchers is one of the possible solutions for feeding [49, 6]. In [65], and [66], distinct design GRIN lenses have been presented, but the difficulty in implementations for sub-zone permittivities and narrowbands were the significant drawbacks of these solutions. Virtually design permittivities are easy and cheap alternatives to solve the problems mentioned above [53, 56]. Since 2008, various theoretical and experimental studies

based on different materials have been done after the Cokrum report [5]. Ward's analysis relaxed the restriction that the incident rays for illuminators need to be parallel to the cylinder axis [4]. Petosa, et al.[6], designed zone plate lenses with the perforated air hole zones at 30GHz [6]. Sato et al. [7] investigated this using only a constant cylinder size with various concentrations of holes to provide the effect of required continuous varying dielectric constant in host medium. Hao, et al., presented a procedure for designing cube-shaped cells to find the refractive index variation function to design a spherical Lunenburg lens at 10GHz with ABS plastic, which could provide the desired pencil beam radiation over an operating band [49], [50] and this analysis was later generalized by Brakora, et al., at 30GHz using ceramic base additive manufacturing process [12].

Towards additive manufacturing process with some restrictions to provide continually changing radial permittivity, any desired cell-shapes to offer intended graded index is possible, whereas the solution of this kind of manufacturing was difficult or impossible with previous methods. This is despite the fact that distinct ϵ_{eff} based on ordered cells have also been reported [49], including changing dielectric sheets using Air-holes in TEM waveguides, utilizing effective permittivity using metamaterial unit cell sheets in $E-$ and $H-$planes, or adjusting the metallic unit-cells sizes on a printed substrates sheets; in addition, most of these solutions are for building 2D lenses. Also, the conventional manufacturing process of a 3-D spherical Luneburg lens, Fresnel zone plates, and 3-D half Maxwell fisheye lens with acceptable permittivity to satisfy lens equations are time-consuming and prone to shape accuracy, high manufacturing costs, narrow bandwidth, and high dissipation.

The fabrication of these lenses with RF companies such as Konkur, LuneTech, Mayurakshi Equipments, Matsing, and Rosendahl is possible, but because of a large number of layers, shape accuracy, and layers air gaps, the total fabrication costs are high. The advantages of using this technology are not limited to these lenses. It also allows the use of integrated manufacturing technology to design and construct more complex lenses [26, 10, 49, 12], including plate lenses [31], with impedance matching layers [31], by creating porosity in the longitudinal or transverse sections of the lens. This method makes it possible to design and construct $H-$plan homogeneous low loss millimeter-wave antennas including beam scanning capabilities, and stable frequency beams, with a fan-beam radiation patterns for communications and radar applications [31, 32]. However, planar high-dielectric homogeneous lenses suffer from high reflections because of impedance mismatching between host medium and free space [31]. To solve this drawback, material porosity techniques are used to design impedance matching regions in the homogeneous platform, to reduce reflection

of mismatching by single or multiple layer transformers[31]. The full FDTD analysis of this homogenous medium technique for non-planar lenses is summarized in [31, 32]. These benefits include improving the Front-to-Back ratio (FBR) and reducing beam distortions.

In [31], an $H-$plan lens with single quarter-wave matching region realizing with material porosity technique in silicon host medium was presented for W-band to reduce mismatching with Air-space in a homogeneous medium[31, 32]. This technology makes it possible to use distinct planar lenses design in the linear phased array. The architecture of the porosity technique makes it possible to create higher gain and narrower beam in $E-$plane compared to conventional open-ended waveguide $H-$plane arrays. Interestingly, the optimal results for the material porosity-based GRIN lenses found in the previous literatures were somewhat different and improved with cheaper manufacturing costs compared to conventional designs. The performance of GRIN lenses could therefore potentially be enhanced by using an alternative porous architecture method based on printed materials for satisfying predetermined lens-graded regions rules.

In recent decades, the virtual permittivity utilizing 3D arrays of spherical holes lattice, cylindrical holes lattice, or deformed plastic shapes in base materials of Teflon, Plexiglas, polystyrene, ABS plastics, and others have been reviewed [5, 12, 35, 11]. Based on these analyses, theoretical expressions and mathematical equations are extracted related to the host medium's permittivity, the sizes and shapes of holes, and filling ratio parameters to define trusted design area [12, 35, 11]. The virtual permittivity analysis is restricted to filling ratio vs. λ in desired frequency with theoretical expressions or extracted equations based on exponential fittings (EF) [10, 12, 11]. In this scheme, the mathematical analysis in terms of the filling ratio controlling parameters is applied to dielectric host media, and all variations are analyzed based on material reduction to reduce permittivity or the addition of another type of material to increase permittivity. However, for all kinds of porous methods, control of the permittivity with porous skeleton directly associated the $E-$field orientation [4]. Values of virtual permittivities based on porosity techniques in the range of 1.1 to 12 ($\Delta n = 11$) have been achieved with Al_2O_3 composed cubical lattice frame [12]; this could be increased by using high permittivity materials for host media.

The practical control of the permittivity of a host material by the free deformation of the host medium has been realized since adding manufacturing revolutions. The early reported host materials are usually made of a lightweight foam base plastic that has a dielectric constant slightly larger than
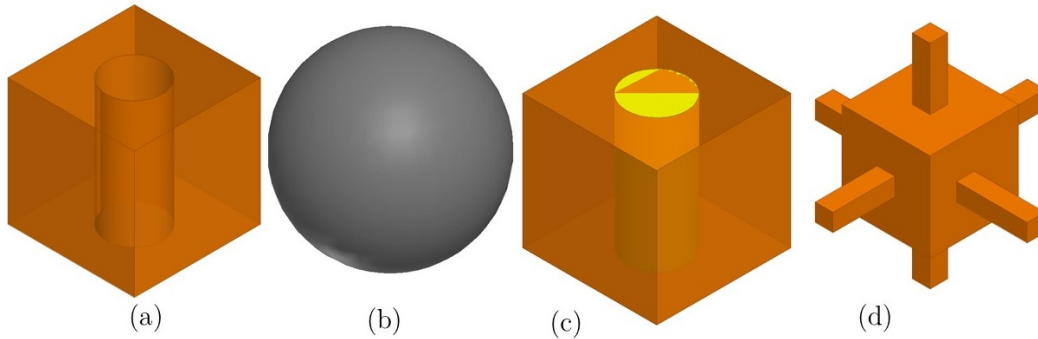
Figure 2.3 – **Categories of Porosity Techniques for Virtual Permittivity Design: (a) Air-hole base porosity. (b) full metal. (c) Permittivity-filled Material Porosities, and (d) free forming porous structures;**

unity ($\simeq 1.2$), and the virtual permittivity control range was limited [5]. The permittivity constant control was not limited to just dielectrics. The initial investigation of metallic disks, spheres, disks, and rods was carried out in 1946 by Winston Kock of Bell Laboratories [5]. Some further research by metallic and dielectric spheres was demonstrated in [4]. The design methodology for isotropic arrays of sphere void prototypes that are reviewed in [5] can be carried out to design perforated base architecture lenses utilizing additive manufacturing process. The perforated methodology for isotropic arrays is analyzed in [5] based on polyfoam or styrofoam and metal, and their applications are restricted because of low mechanical strength. In 1956, Ward presented a new class of virtual dielectrics based on hard polymer plastics and relaxed the restriction on high-vibration devices with better mechanical characteristics [4]. The improved virtual permittivity utilized isotropic arrays of spherical or cylindrical porous elements in high-permittivity and polymer base plastic material [4]. Polystyrene, Plexiglas, and Teflon have been used in this analysis with success. These results are of interest in gradient refractive index lens utilizations.

2.5   Categories of Porosity Techniques for Virtual Permittivity Design

There are four common porous cells applied in the design of virtual permittivity, which is summarized in Figs.2.3 (a-d). Here, we define porosity methods used to design intended permittivity based on the homogenous scheme; the majority of virtual permittivity designs in this category manipulate the material ratio by reducing or deforming the host medium that composes the cells. One of many

possible approaches is shown in Fig. 2.3(a), whereby an air-hole cavity in cylindrical forms embedded in the different host medium. The second approach is full metalic option, is shown in Fig. 2.3(b), whereby spherical metal cells with specific permittivity is embedded in the different host medium. Hence, if a graded refractive index is desired, a variant spherical volume can be united into the host medium to make this approach feasible [4]. It is also possible to increase intended permittivity with the use of higher dielectric constant materials from the host medium in liquid or powder form to increase desired graded medium range. This scheme is presented in Fig. 2.3(c) [19]. Hence, to control the virtual permittivity in dynamic form, this method can potentially be used in the different materials portion of the element to fabricate with additive manufacturing materials, resulting in the innovative design of GRIN lens, as shown in Fig. 2.3(d). Finally, for circularly polarized waves, the combination of dielectric and metal elements results with 3D printing technologies can be considered to produce the required phase shifts in GRIN lens subzones, as shown in Fig. 2.3(c) form cell because of ease of fabrication. Each of these four methods is elaborated in more detail in the following sections.

2.5.1 Virtual permittivity designed based on Air-hole porosity

While inhomogeneous gradient refractive index mediums modify the subzones dielectrics to change their refractive index, homogeneous medium achieves this using air-filled cells [5, 4, 6, 7]. Air-hole porosity that controls the refractive index of subzones virtual has been known for a long time. For example, through the use of drilled holes in the foam and Plexiglas [4], the first virtual permittivity controlled was based on homogeneous design [6]. However, it is critical to accurately control the choice of the intended permittivity to the size of spheres and cylinders in order to achieve the broad dielectric ranges achievable with air-filled elements and this early design based on foam plastics only achieved about 1.1 to 2.6 range ($\Delta n = 1.5$)[5]. More permittivity range was achieved from this concept by contemplating various loading geometrical schemes for the air-filled holes based on $E-$filed orientations [5, 4, 7] and embedding the holes to dielectric host medium in appropriate size [7, 30, 31].

It is also conceivable to use additive manufacturing systems materials and manufacturing processes for the same design [7, 30]. Fig.2.3 (a) shows an example of the air-filled base porosity into the plastic to achieve virtual permittivty. Mostly, this technique can be considered as changing the
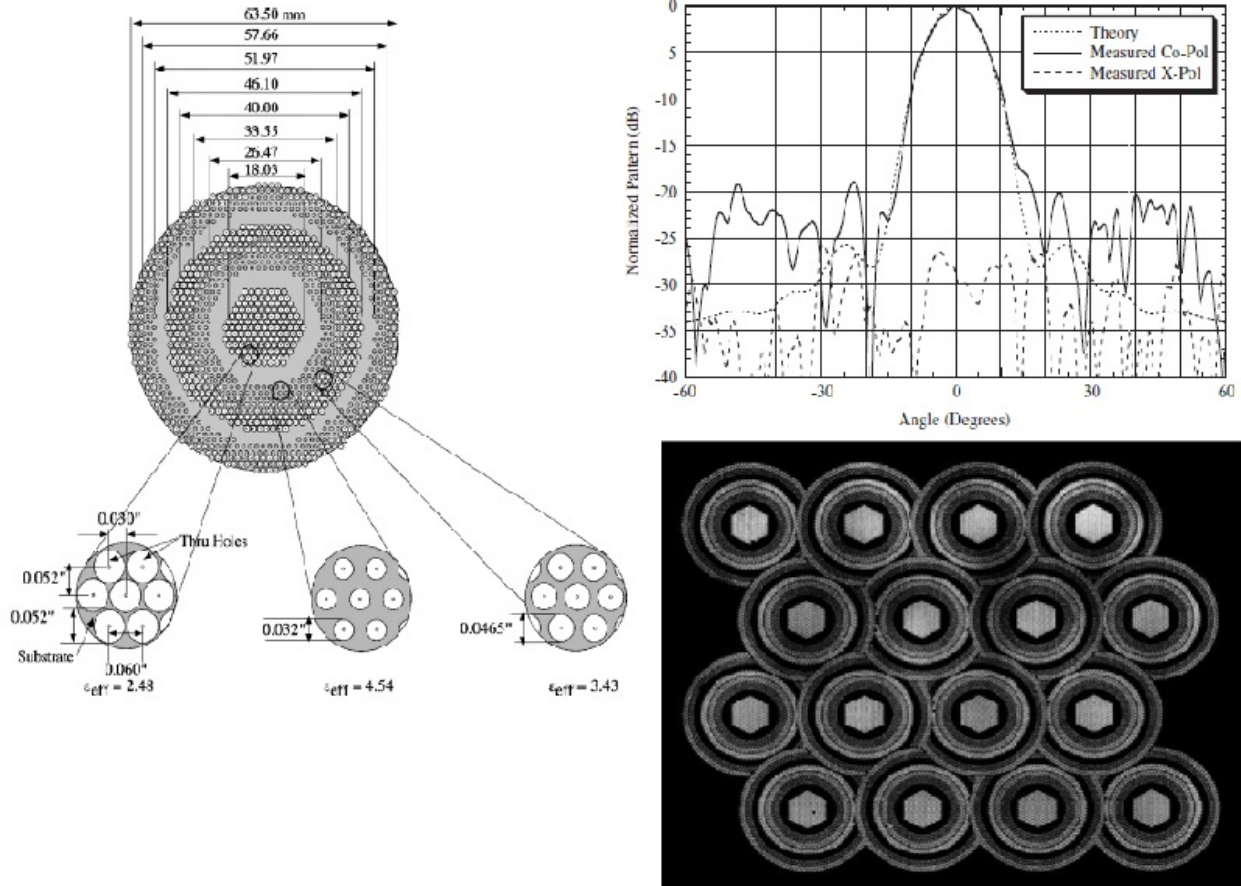
Figure 2.4 – Example of perforated Fresnel zone plate lens using the air-hole base porosity technique for virtual permittivity realization. This restriction is done based on the extracted mathematical equalization for dielectric zone plates. The obtained peak gain for the proposed lens is around 18.5 *dB* with at 28GHz[6].;

effective permittivity (ϵ_{eff}) of the GRIN medium zones. Hence, the distinct shape of air-filled holes has been contemplated to implement virtual permittivity, based on this idea, to design impedance matching layers and to improve mismatching between air and lens medium [31]. Holes in the form of rectangular air-filled porosity have been integrated with the homogeneous $H-$plane lens platform to control the mismatching of refractive index between the lens and air medium with corresponding wavelength width.

Such schemes depend on Clausius-Mossotti's relation analysis that allows for mathematical expressions of the effect of air-filled porosity on the large-scale material variations [67]. An example, using air-holes in polystyrene, Plexiglas, Teflon is presented in [5, 4]. In addition to using the cylindrical air-filled porosity to permittivity changes in dielectric, more exotic fabrication methods have also been observed, such as the micromachined high-loss silicon for reducing the side lobe levels
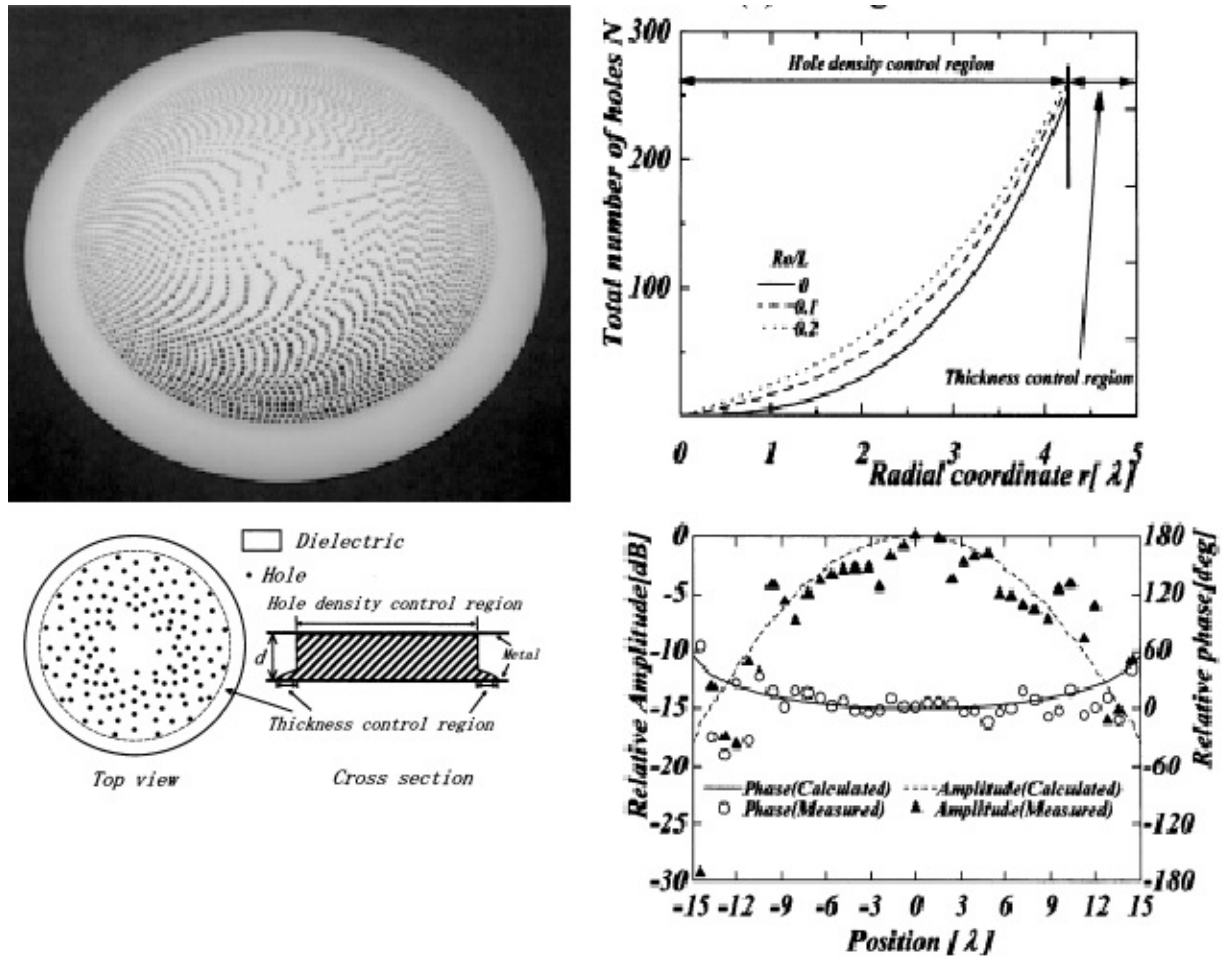
Figure 2.5 – **Example of Luneburg lens using the air-hole base porosity technique utilizing control of fixed air-hole density for virtual permittivity realization. This restriction is done based on the extracted mathematical equalization. The obtained maximum gain for the proposed lens is around 30.4dB with an efficiency lower than 30 % over the operating bandwidth with slot array antenna as an illuminator[7].;**

and increasing the gain for waveguide-fed $H-$plan lens [7, 30, 31]. In the homogeneous scheme, the resonant frequency of metamaterial-based GRIN lenses is manipulated by varying the permittivity of the host medium, which is the operating principle of Luneburg [7, 16], reflect-array [8], Fresnel zone plate [6], Maxwell's fisheye lens, and Eaton lens elements [54, 55] in using dielectrics.

Employing of air-hole approach to control zone plate intended permittivity in Fresnel type GRIN structure is provided as a first perforated design concept by Petosa in 2006 [6] after Sato's design concepts with air-holes density control in 2002[7]. Fig. 2.4 shows the example of the all-dielectric Fresnel lens array devices using the air-hole approach for broadband millimeter-wave applications.
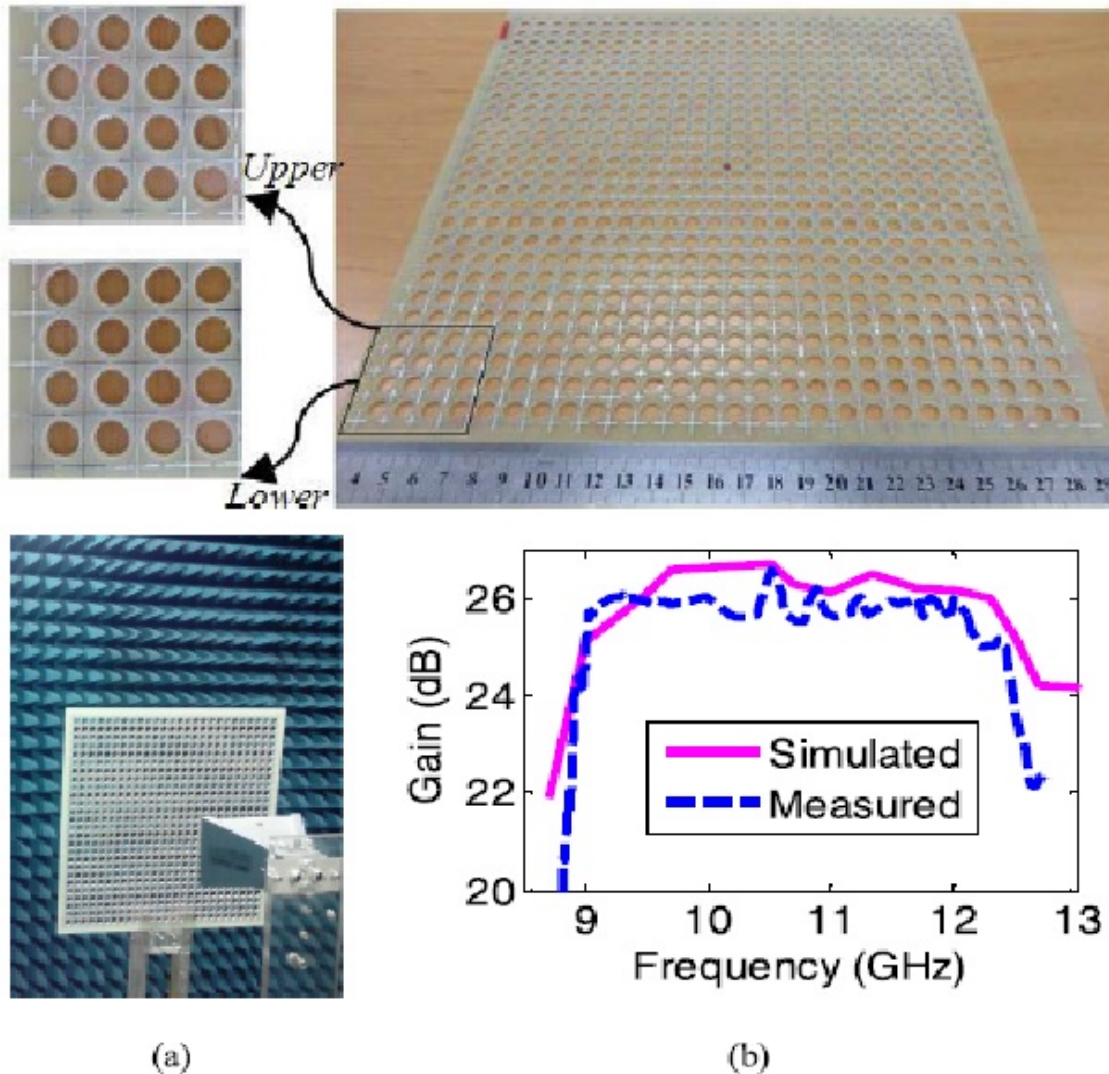
Figure 2.6 – A homogeneous reflectarray antenna using the air-hole perforation elements at 10GHz is presented with horn antenna feed. (a) Example of perforated reflectarray in an anechoic chamber with measurment setup, (b) simulated and measured antenna gain with 29.5% bandwidth;[8].;

This prototype is done based on air-hole approach with the perforated single module substrate. A manufactured Fresnel lens array configuration with multi-permittivity control range for millimeter-wave spectrum with air-holes dimensions is presented in Fig.2.4 (a). The photograph of the produced lens with the air-holes approach in sixteen elements is displayed in Fig.2.4 (b). The recommended Fresnel device affords air-hole array in the lossy substrate to provide lens subzones. Because of the microstrip antenna feed with low efficiency, the produced porous lens output illumination efficiency is similarly low.

In [7], the virtual permittivity control in Luneburg lens scheme is concentrated on air-holes density with the radius sizes smaller than operating frequency at 10GHz, and 45GHz. Holes are formed and formulated in the host medium which is parallel to the orientation of $E-$field. Air-hole cells employing with mathematical control of permittivity which would provide the permittivity distribution by hole density in the homogeneous framework have been experimentally illustrated in[7] for Luneburg lens design at 10GHz, as shown in Fig. 2.5. Because of not analyzed feed type for this prototype, the produced porous lens output illumination efficiency is similarly low. In other lens type scheme, the periodic perforation with the air-holes approach is introduced in the design of reflectarray substrate to reduces the antenna weight by FR4 substrate as a host medium, and radar cross-section (RCS) reduction outside antenna running bandwidth, as shown in Fig. 2.6 [8] with an efficiency of 40% in center of operating frequency which is still low compared to other conventional printed lenses.

Utilizing of air-hole approach to control intended permittivity in a dielectric slab is not restricted to microwave frequencies. Fig.2.7 shows the example of the all-dielectric subwavelength Si-GRIN lens device using the air-hole approach for broadband THz imaging [16].This prototype is done based on air-hole approach with the additive manufacturing process in silicon bed. A manufactured Si-GRIN lens for 0.4 to 1.6 THz beam focusing is shown in Fig.2.7 (a) [16]. The SEM image of the produced lens with air-holes approach to control of intended permittivity in silicon slab with $50\mu m$ resolution is presented in Fig.2.7(b). Transversal $\mid E \mid -$field output for the THz beam, which is crossing through the presented Si-GRIN lens for perpendicular illumination is proposed in Fig.2.7 (c) to show the execution of this approach in THz electromagnetic spectrum [16]. The recommended THz device affords air-hole array in low absorptive silicon material to develop expected GRIN medium for THz beam focusing, which is revealed possibility of this approach in the THz regime.

In electromagnetic field tapering based on dielectric gradient refractive index lenses, this approach is another reasonable method. Design of the all-dielectric 3D electromagnetic filed tapering lens using the air-hole porosity technique for broadband 10GHz applications is presented in Fig. 2.8(a) [17]. This prototype is prepared based on two distinct air-hole approaches with the additive manufacturing process, as shown in Fig.2.8(b). A manufactured 3D lens for 10GHz beam tapering is prepared with 3D printing material with $\epsilon_r = 2.8$ to provide the virtual refractive index in $\Delta n = 1.8$ contrasts. The effective virtual permittivity is produced with an air-holes approach to control of intended permittivity of predetermined zones in the homogeneous plastic slab. Transver-

sal $|E|$-field output for the 3D taper GRIN lens, which is crossing through the presented device for perpendicular ($\perp$) illumination is revealed in Fig.2.8(c)[17] to better presentation of this lens mechanism, and design validation.

As applications of the wave tilting, wave tapering and wave focusing, gradient index utilizing air-hole approach in the homogeneous framework is prsented. In these design schemes, porous lens devices for 45° wave tilting, a 16° beam-steering lens and beam-focusing at 10GHz are produced and manufactured [18]. Transversal $|E|$-field measurements for the proposed porous devices confirm the recommended GRIN schemes and the device configurations [18]. The quasi-static method is used to provide a trusted area for $\Delta n = 2.7$ refractive index deviation. Fig. 2.9(a-c) shows the photographs of the presented GRIN porous devices [18].
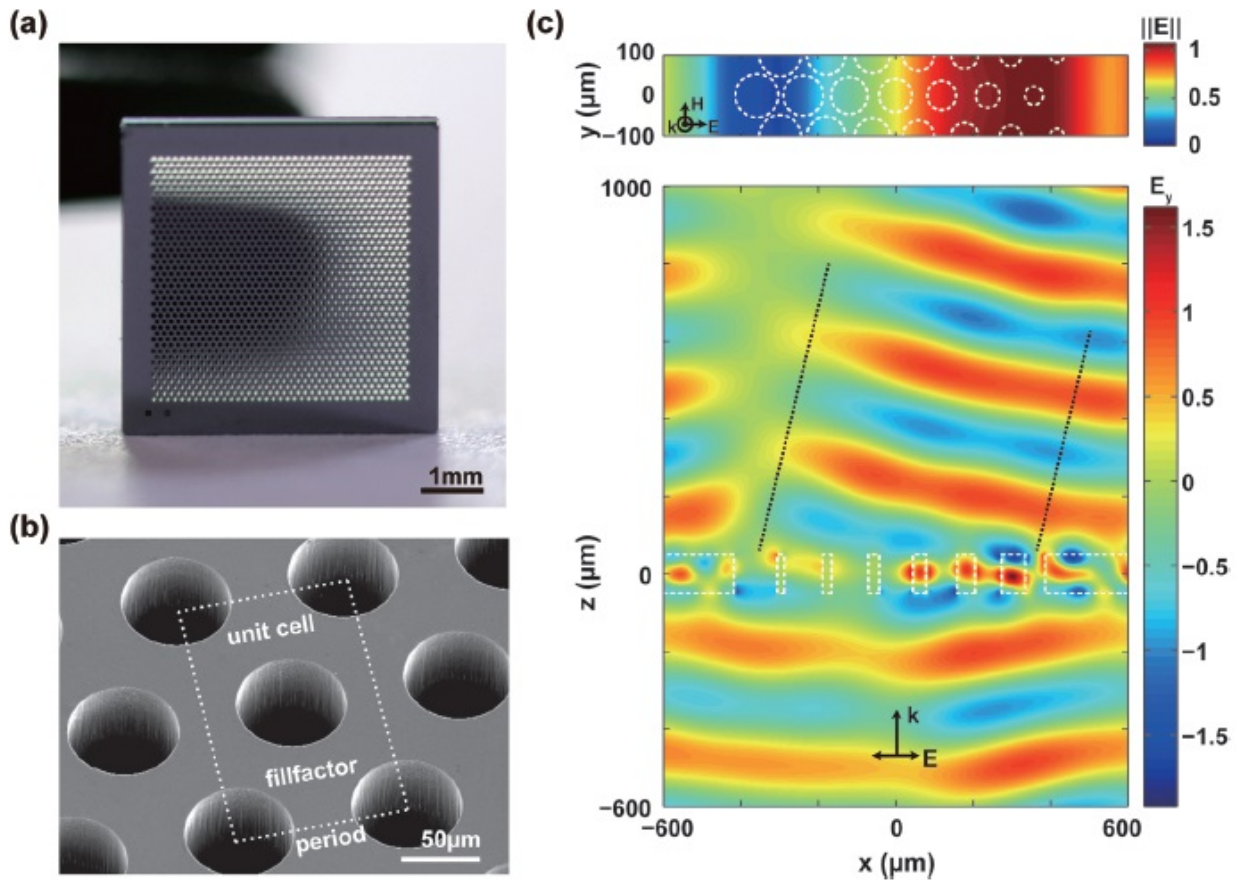
Figure 2.7 − **Example of the all-dielectric 3D electromagnetic filed tapering lens using the air-hole base porosity technique for broadband THz applications. This prototype is done based on two distinct air-hole approaches with the additive manufacturing process. (a) A manufactured 3D lens for THz beam tapering. (b) The effective virtual permittivity is produced with an air-holes approach to control of intended permittivity in the homogeneous plastic slab. (c) Transversal $|E|$ −field output for the 3D taper, which is crossing through the presented lens for perpendicular ($\perp$) illumination[16].;**
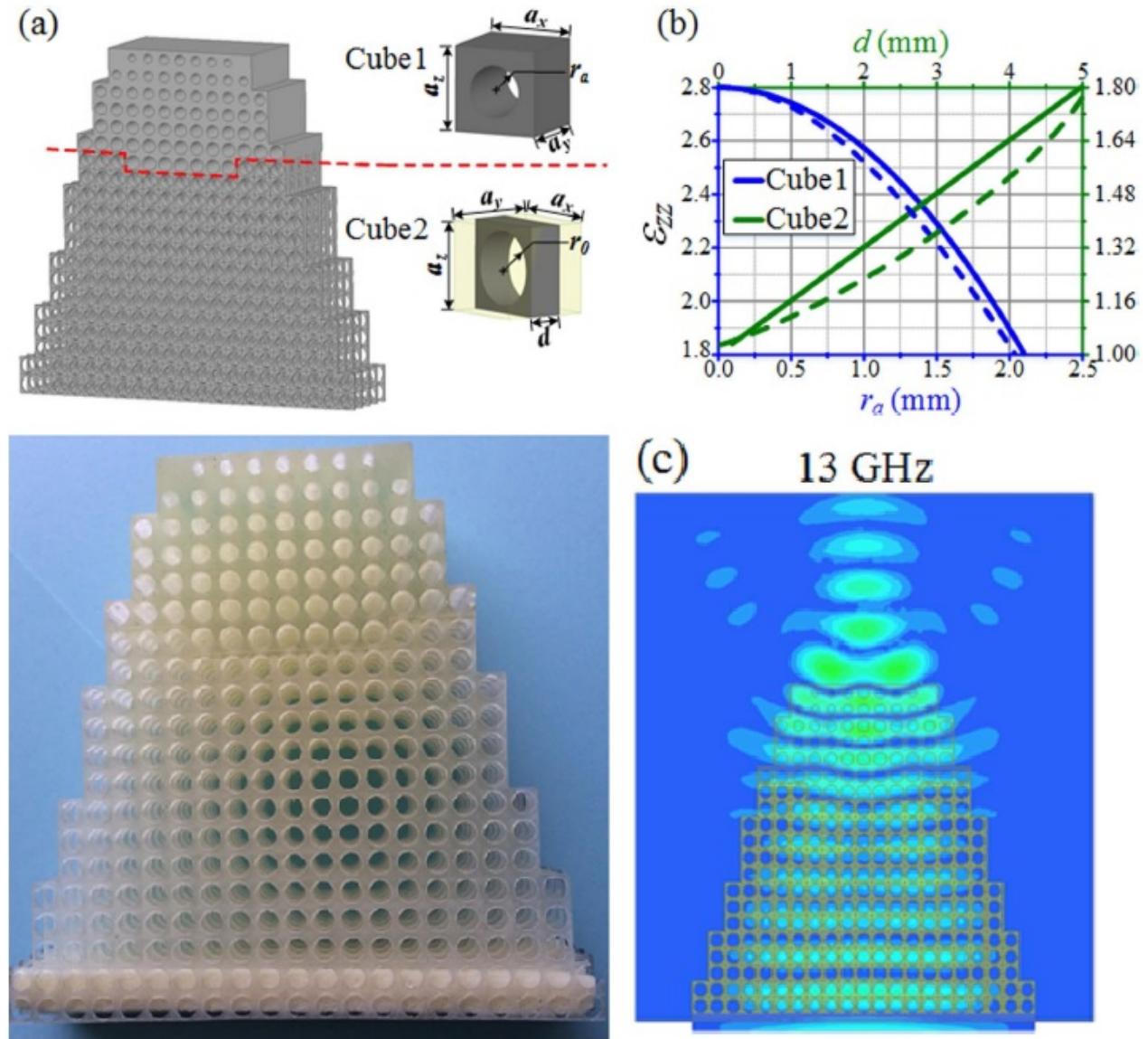
Figure 2.8 – **Example of the all-dielectric subwavelength full dielectric-GRIN lens using the air-hole base porosity technique at 13GHz. This prototype is done based on air-hole approach with the additive manufacturing process. (a) A manufactured GRIN lens 13GHz beam focusing. (b) The parametric analysis of the produced air-holes approach to control of intended permittivity in plastic slab. (c) Transversal | E |-field output for the incident beam, which is crossing through the presented GRIN lens for perpendicular ($\perp$) illumination[17].;**

Nanofibers of mesoporous range have also been used to control virtual permittivity with the nanotechnology fabrication method, which is suitable for sub-millimeter-wave and THz spectrum [68, 69]. An example of employing nanofiber as a composite porosity in a homogeneous medium is analyzed in [69], which is best for increasing intended permittivity to overcome host medium permittivity limits [69]. Composite material design based on nanofibers share many traits in common with gradient refractive index mediums [68, 69].

In fact, the principal differences between a gradient medium and composite materials are: i) the dispersion characteristics of composite materials do not regularly manage to direct electromagnetic waves for focusing; ii) the phase gradient medium sub-zones are modified in accordance with optic rules, while those in composite materials are distributed totally randomly or semi-randomly; and iii) the periodicity in the GRIN medium is sub-wavelength, while that in the nanofiber composite is not analysed. Furthermore, the equivalent virtual permittivity of nanofiber composites in the perpendicular $E-$field orientation is usually higher than in the parallel form. Each cell of air-filled virtual permittivity, which can be a sphere, cylinder, or a cube, can be observed as a scattered place within a periodic waveguide [3]. Therefore, the Floquent theory can be used to analyze each cell in HFSS or CST for a particular incidence angle before fabrication with high accuracy, and the reflection coefficients can be used to describe a range of permittivity control for the cell. Also, an equivalent circuit can be synthesized based on these results.

Upon theoretical analysis, a mathematical equation or trusted design area can be developed to provide intended virtual permittivity that yields, regarding the sphere size (filling ratio), the host medium permittivity and density of sphere type porosity (number/unit volume). One of the principal investigates in this area associates to Cockrum [5], and Ward [4] studies. In this scheme based on [4], the virtual permittivty implementation theory is limited to the lattice of a spherical cell array of air-filled porous objects. The polarization comparison for sphere-shaped cells with $\bar{P}$ is provided by $\alpha \bar{E}'t$ [4]. Where E' denotes effective E-filed acting on sphere cells, α is the polarizability of the proposed cells, t is $\frac{N}{V^3}$ and N is the sphere cells repetition number in the volume of intended host medium (V) [4]. For sphere cell, polarizability (α) is associated with the sphere material permittivty and the host medium dielectric constant [4]. This polarizability is provided by Eq. 2.1 [4]:

$$\alpha = 4\pi\epsilon_0\epsilon_1 R^3 \frac{(\epsilon_2 - \epsilon_1)}{\epsilon_2 + 2\epsilon_1}, \tag{2.1}$$

where ϵ_2 is the permittivty of the material for sphere cells, R is the sphere radius, $\epsilon_0 = 8.85 \times 10^{-12} \frac{F}{m}$ is the vacuum permittivity, and ϵ_1 is the host medium permittivty. In this equalization,

the effective electric field acting on spheres is used based on [4] assumptions, which is given by Eq.(2.2),

$$\bar{E}' = \frac{\bar{P}}{3\epsilon_0\epsilon_1} + \bar{E}, \tag{2.2}$$

In this Equation, $\bar{E}$ means the intended E-field that is illuminated on sphere cells and produces $\bar{P}$ [4]. The recommended equation by considering the sphere cells mutual interactions determined the equivalent representation of Clausius-Mossotti rule for this scheme [4]. Finally, by replacing equation (2.1) with (2.2), the final equation for polarization is obtained as follows by Eq.(2.3) [4],

$$\bar{P} = 3\Delta\epsilon_0\epsilon_1\left(\frac{\bar{P}}{3\epsilon_0\epsilon_1} + \bar{E}\right) = a\bar{E}'t, \tag{2.3}$$

In this equation, Δ is given by FC where C denotes $(\epsilon_2 - \epsilon_1)/(\epsilon_2 + 2\epsilon_1)$, and based on Corkum's [4] fractional volume assumptions, Eq. (2.3) has been simplified based on the fractional volume equation as $F = 4\pi R^3 t/3$ [4]. The fundamental relation $\bar{P} = (\epsilon_0\epsilon - \epsilon_0\epsilon_1)\bar{E}$ is used to introduce and simplify (2.3) into the effective dielectric constant ϵ_{eff} [4]. The resulting expression can be simplified to ϵ/ϵ_1, which is given by Eq.(2.4) [4],

$$\frac{\epsilon_{eff}}{\epsilon_1} = \frac{(1 + 2FC)}{(1 - FC)}, \tag{2.4}$$

where the C is $C = (1 - \epsilon_1)/(1 + 2\epsilon_1)$ and depends to the dielectric properties of used materials, and F associated to the number (N) and size of the spheres R [4]. In this approach with air-filled sphere porous structures, ϵ_1 is equal to 1 [5, 4], and C is equal to $(\epsilon_2 - 1)/(\epsilon_2 + 2)$ [5]. These are all possibilities for GRIN device implementations with this approach in the homogeneous model, which is still undergoing.
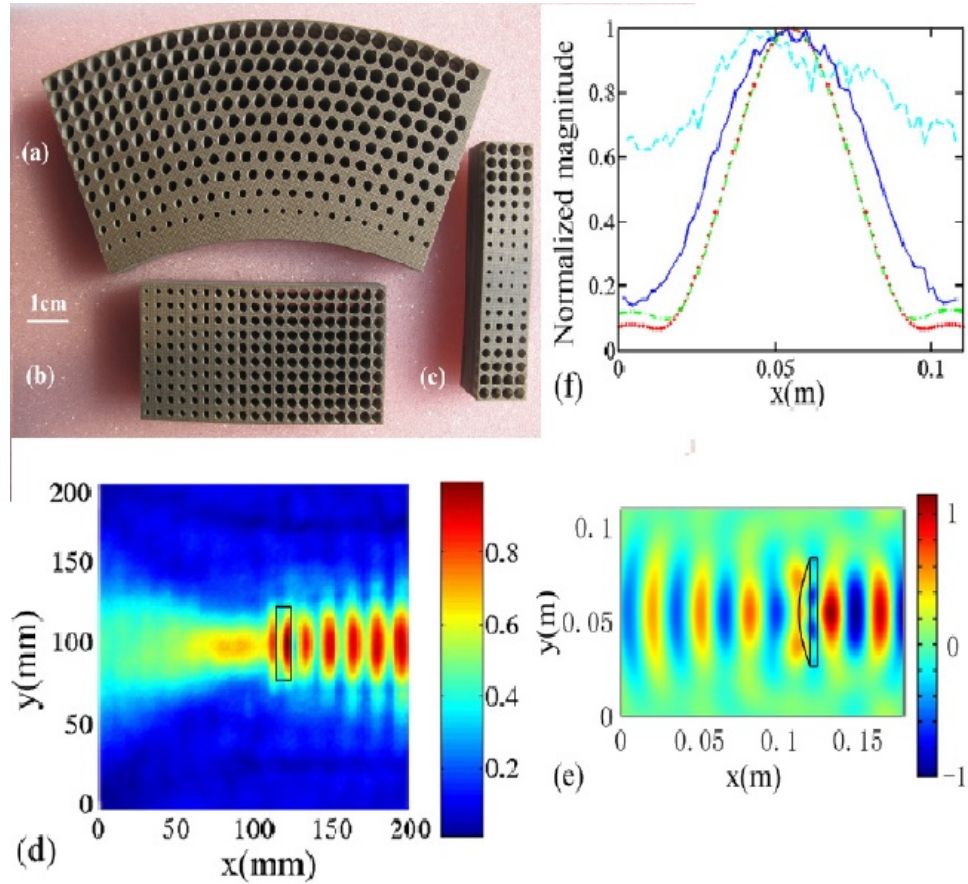
Figure 2.9 – **Example of the all-dielectric wave tilting, wave tapering, and wave focusing gradient index using the air-hole base porosity technique for 10GHz is performed. This prototype is done based on air-hole approach with the additive manufacturing process. (a) A manufactured GRIN bend lens for $45°$ beam tilting. (b) A built $16°$ beam steering GRIN lens. (c) A manufactured beam focusing lens. (d) Transversal measured $|E|-$field output for the focusing lens; (e) Transversal simulated $|E|-$field output for the hyperbolic lens structure with f/D dimension equal to (d) device; (f) simulated and measured normalized $|E|$-field magnitude for the GRIN lens device focal point at 10GHz;[18].;**

2.5.2 Virtual Permittivity Design Based on Different Permittivity-filled Material Porosities

Rather than controlling the virtual permittivity with air-filled porosity as presented so far [5, 4], it is also possible to enhance dielectric and ferroelectric properties by a dielectric-filled porous approach. In this case, the nanofibers with a large aspect ratio are used as dielectric fillers in polymers to enhance host medium permittivity. The percent of nanofibers is then controlled in low volume fraction, resulting in intended permittivity value. This method was first applied to polymer-based composites and then extended to conductive nanocarbon fillers by applying controllable phase tubes length and radius which can also be used to design integrated waveguides. The dielectric-filled

approach to designing a GRIN medium presents both benefits and drawbacks when compared to the air-filled porosity technique.

First, the air-filled porous cells in the former method are more accessible to development, optimization, and fabrication. Indeed, while modeling is quite similar for both approaches, the fact that the dielectric and ferroelectric properties can be optimized independently in the dielectric-filled approach results in high range control of permittivity [69]. For instance, in design sample simulations, it is quite straightforward to achieve a high range of virtual permittivity control and add ferroelectric properties, whereas doing so in the lab and adding filled fibers in polymers or an intended host medium can require complicated additive manufacturing processes or devices which are still under study [68, 69, 61].

Second improvement of this method is that higher dielectric constant behavior is achieved since a higher refractive index medium can be designed to produce a high refraction capability for reengineered GRIN lenses with impedance matching layers [31]. Several studies have been developed based on the second approach of virtual permittivity control, which is focused on the permittivity control of GRIN medium metasurfaces [70] and frequency selective surface (FSS) [71, 72] as periodic structures design. Lens design using the second approach in the homogeneous medium allowed permittivity tuning with nanoscale density in a specified coating shape, including a circular ring, a planar grid, or other forms over the desired host medium in the intended frequency [70].

Several dielectric-filled porous shapes such as the sphere and the cylinder have been analyzed based on the air-filled approach analysis [5, 4]. In this approach, similarly, an approximate dielectric constant based on a sphere-filled dielectric in a homogeneous medium can be obtained by substituting the sphere's dielectric constant (ϵ_2) in Eq.(2.4) [5]. Therefore, the new medium's permittivity will be associated to the filling substance of the porous sphere cell, the size of the sphere cells, and the space between them [5]. This approach research is notably done in material engineering departments to control permittivity virtually, but still, a GRIN medium realization with a predetermined shape and ranges demands more investigation by antenna engineers to actualize GRIN lens antennas in the microwave and millimeter-wave spectrum. Also, this approach has not been taken into account by other departments because of the many problems involved in combining of different materials and fabricating issues to control the dielectric permittivity for GRIN medium design, and all presented works have been limited to high frequencies (THz) and optical lenses [70].

In [19], the virtual permittivity control in 90° Eaton lens scheme is concentrated on different permittivity filled material porosity at 15GHz. In this scheme, woodpile dielectric metamaterial cells are formed and formulated as host medium and bed frame to fill with the liquid material to provide large refractive index up to 6.32. Provided cells employing with mathematical control of refractive index to satisfy Eaton lens rules which would provide the permittivity distribution by filled material have been experimentally illustrated in[19] for Eaton GRIN lens design at 15GHz, as shown in Fig. 2.10. Transversal | E |-field output for the incident wave, which is crossing through the originated Eaton lens with 90° tilting is revealed in Fig. 2.11 for validation [19]. Because of complexity and high costs of fabrication, this approach is not considered well enough for antenna engineering in the microwave and millimeter-wave regime.

$$n_i^2 = \frac{R_{eaton}}{nr_i} + \sqrt{(\frac{R_{eaton}}{nr_i})^2 - 1}. \tag{2.5}$$

where R_{eaton} is the Eaton lens total radius and n_i is the intended refractive index for each subzones. This equation is applicable to $r_i \leq R$ range where $i = 1, 2, ..., N$, and for $r_i > R$, the determined refractive index is equal to 1 [19].

2.5.3 Virtual permittivity design based on full metal porosities

A smart choice for above virtual permittivity control methods, although restricted to the conductive materials, is that of the metal-only homogeneous medium [21, 20, 67]. This principle design and analysis were initially applied to the metal delay lenses in 1948 by W. Kock [67], and the associated development system and equations based on metallic sphere array are well known [4]. Here, we review a primary formulation for the dielectric constant of metallic-sphere array-based medium [5, 4]. Let us consider a spherical metallic-cell such that the cell is embedded in metal or suspended in air as depicted in Fig. 2.3.

Based on mentioned theory above, by arranging perfect electric conductor (PEC) spheres in the cubic array and placing these arrays in a uniform static $E-$field or an alternating $E-$field, the metallic sphere's free charge will be removed by the applied field [5]. This movement will happen when the diameter of the spheres is much smaller than the wavelength within the resulting dielectric medium [5]. A smart choice for above virtual permittivity control methods [5], although restricted
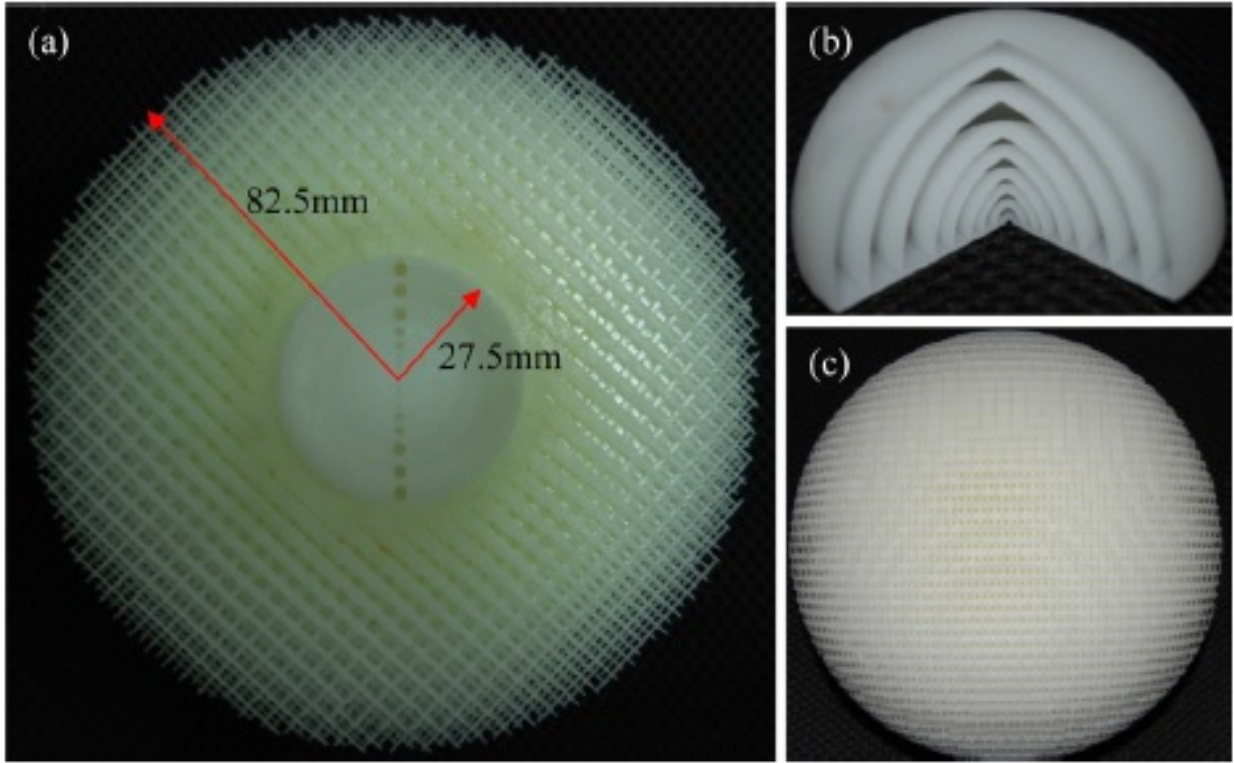
Figure 2.10 – Example of the all-dielectric Eaton lens using the different permittivity filled material porosity for 15GHz is presented. (a) A half manufactured Eaton lens for 90° beam tilting before liquid material injection to provide high refractive index framework. (b) An internal built container before filling with a liquid; (c) the final model for the created lens [19].;

to the conductive materials, such as Copper, Aluminum, Titanium, and CarbonMide, with increased electrical conductivity, is that of the metal-only homogeneous medium. This movement will happen when the diameter of the spheres is much smaller than the λ within the resulting host dielectric [5]. The sphere polarizability is provided based on the Clausius-Mossotti equation (See [5] appendix) given by Eq. (2.6) [5, 4]:

$$\frac{\epsilon_e - 1}{\epsilon_e + 2} = \frac{\alpha_e t}{3}, \tag{2.6}$$
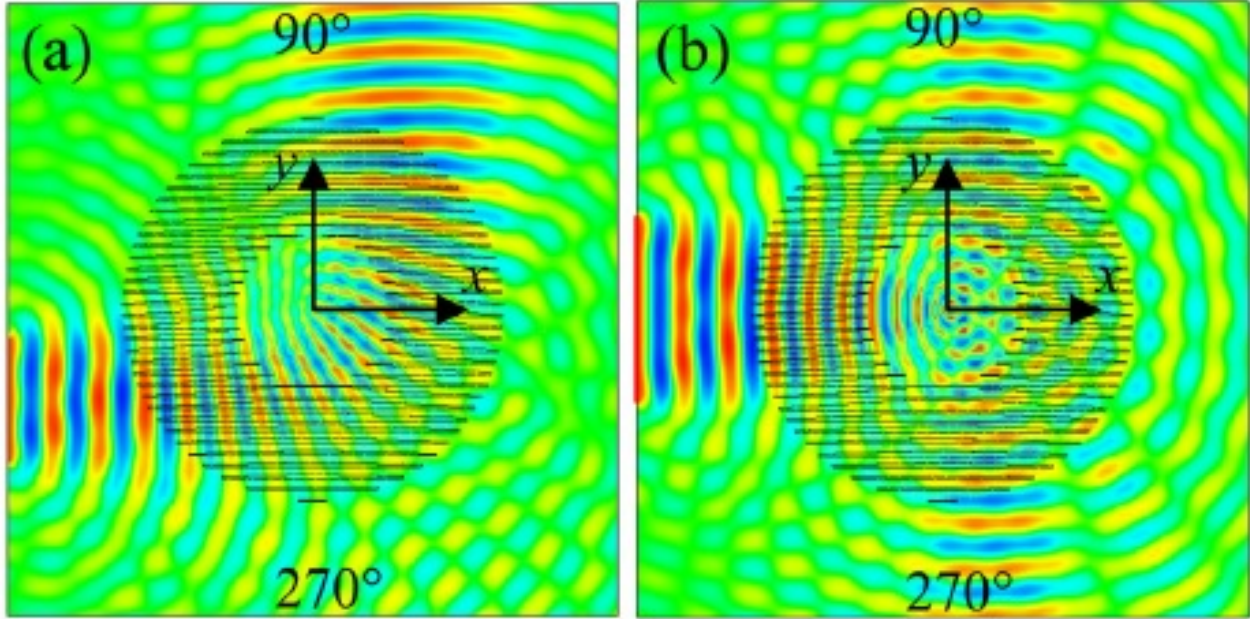
Figure 2.11 − **Transversal simulated** $|E|$−**field output for crossing of wave from entire the 3D-Eaton lens frame for both (a) off-centre, and (b) on-centre illuminations[19].;**

Where α_e is the sphere cells electric polarizability, $\frac{N}{V} = t$ is the number of repetition for spheres cells per unit volume, and ϵ_e is the relative dielectric constant of the sphere material. This equation can be simplified to (2.7) based on the $\alpha_e = 4\pi R^3$ substitution [5, 4].

$$\epsilon_e = \frac{1 + (2.7\pi a^3 t)}{1 - (1.3\pi a^3 t)}. \tag{2.7}$$

Note that this expression is analyzed for only a metal-sphere array cell by Winston Kock, and for other cell shapes, it requires a general analysis based on the Clausius-Mossotti equation Eq.(2.6)[5]. The principle of development and specifications for the spherical metal cells are simply assumed from Eq.(2.6) [5, 4].

Metal GRIN lenses for beam-shaping of electromagnetic waves are still at an early developmental stage. Fixed reflect-array, delay lenses, Luneburg lenses, and Fresnel zone plate lenses based on whole metal principles have been investigated. These incur the intended sub-zones phase shift when the zones' virtual permittivity is manipulated through free-forming style cells in Luneburg lenses employing the homogenous platform [20], metal thickness in Fresnel zone plates [73], or cylindrical holes in delay lenses [67]. However, to our knowledge, metal-only homogeneous lenses manipulated with this approach have yet to be realized in low-efficiency form. This scheme, while giving an
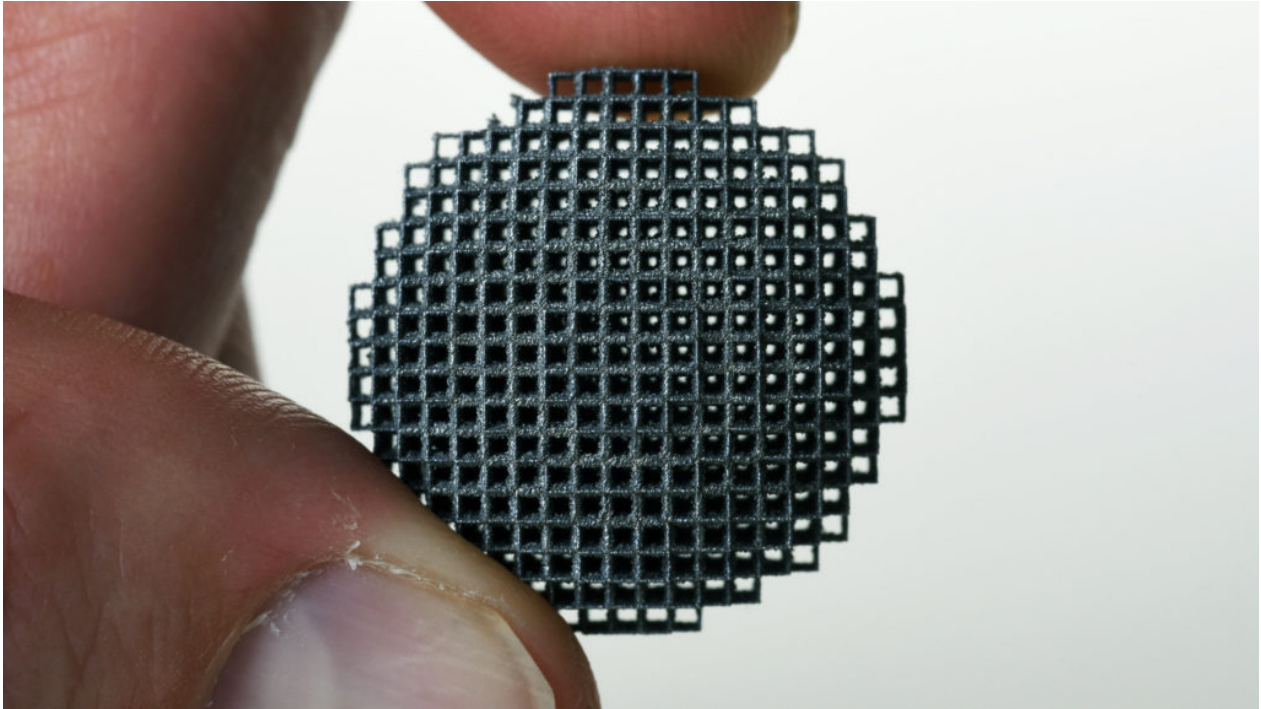
Figure 2.12 – **Example of the metal only Luneburgh lens using metal printing addittive manufacturing process is presented. [20].;**

unbeaten performance in the millimeter-wavelength concentration of waves, metallic perforated structures with free-forming shapes, or spherical and cylindrical porous cells, suffers from essential absorption losses which critically restricts their efficiency.

The proposed design in Fig. 2.12 is a particular free-forming geometry based on the whole metal platform used in directional antenna purposes and realized based on 3D printing [20]. In this scheme, the density of the inner sphere becomes higher and provides the intended Luneburg lens design commands to get $n = 1.4$ refractive index in the lens center. The metal cells, with complex forms, are used to realize the predetermined layers' permittivity [20]. If a beam launcher, such as a horn antenna or an open waveguide, is located on the perforated lens surface, the incident energy will be converted into planar waves on the reverse side of the lens skeleton. The total gain for the proposed design is determined by the size of the printed lens. Indeed, this structure is due to having the symmetrical geometry, and it can also be used in reverse form. In this running mode, the lens, as mentioned earlier, can act as a replacement for a parabolic reflector antenna. To approach this aim, the full dielectric material demands to serve as a lens platform and not as a metal. Nevertheless, the designed composition shows the accuracy of fine elements, which the SLS printer can achieve.
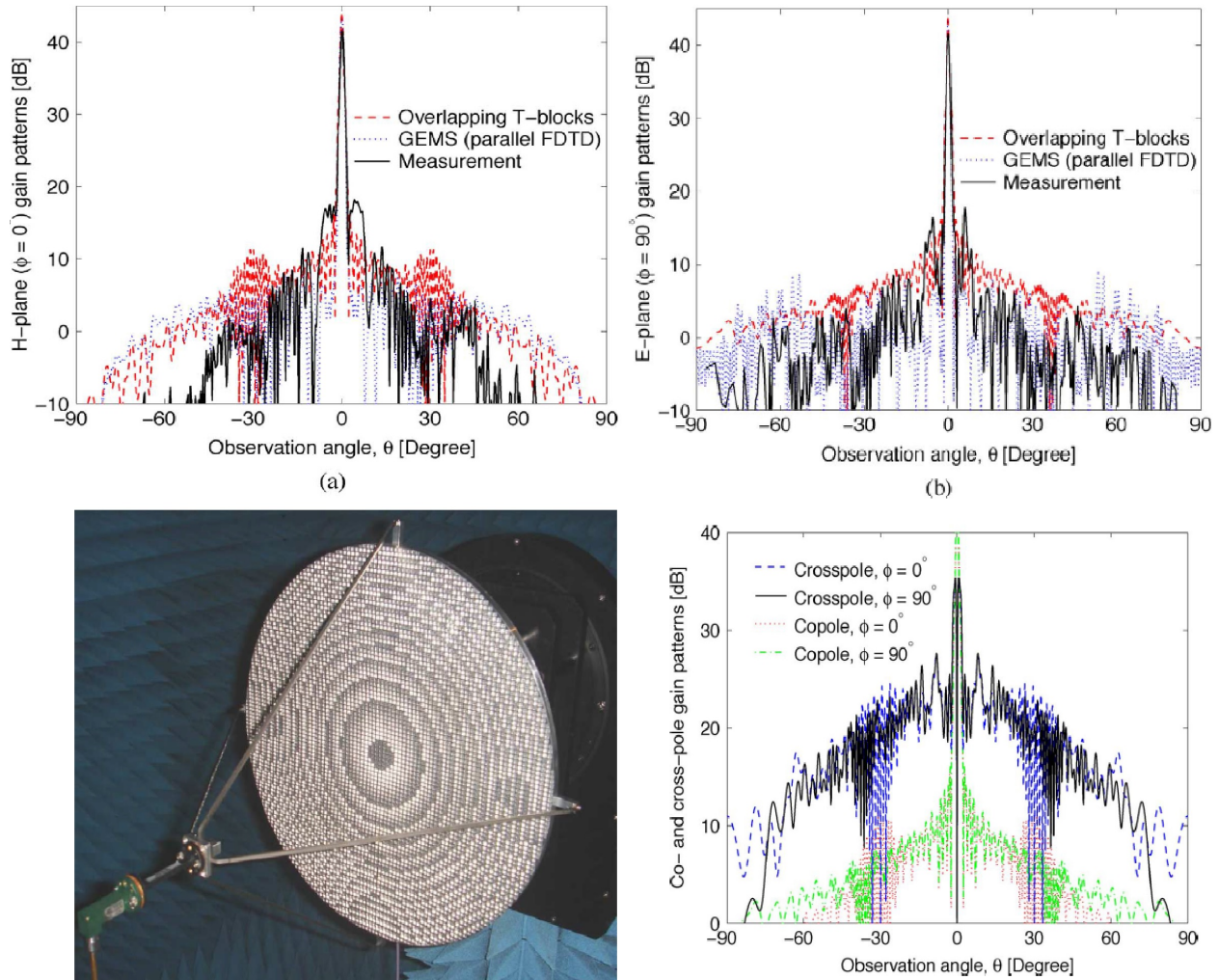
Figure 2.13 – **Example of the full metal perforated reflectarray antenna using rectangular grooves cells in metal framwork for 75GHz is performed. A measured radiation pattern for proposed porous metal-only structure at 75GHz: (a) $H-$Plane ($\phi = 0°$), (b) $E-$Plane ($\phi = 90°$);(c)The fabricated lens antenna in the anechoic chamber; (d) co- and cross-polarization of gain patterns versus θ angle.[21].;**

The analysis of the metal-only GRIN lens structures is not only limited to Luneburg lenses [20]. As shown in Fig.2.13, a full metal reflectarray to operate at 75GHz is introduced in this approach with multiple rectangular grooves. The homogeneous platform reflectarray is an alternative design method because of homogeneous schemes with numerous advantages, such as low manufacturing cost, high mechanical strength and easy fabrication with the additive manufacturing process. The advanced lens diameter is $30cm$. It has been designed and examined at 75GHz with a total gain of 42.23 dB, an aperture efficiency of the perforated metal lens is 30% and a cross polarization level for this scheme is lower than -40 dB, as shown in Fig.2.13 (a-d) [21].
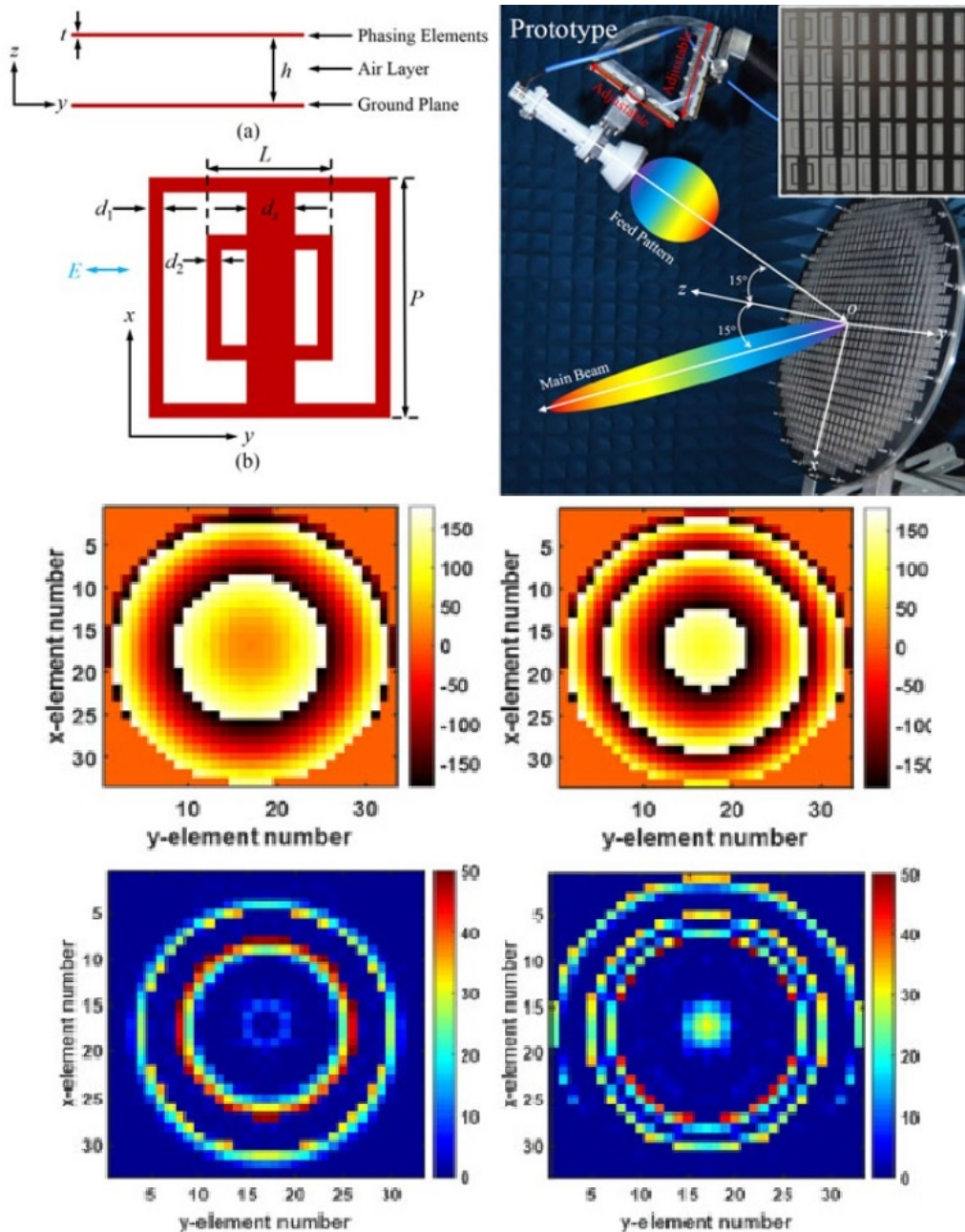
Figure 2.14 – Example of full metal lens antenna using slot type perforation in a metal framework for X- and Ku-band applications is performed. Slot type elements in the metal framework: (a) Side view, (b) Top view; (c) A pencil beam radiation pattern for proposed porous metal-only structure at 15GHz; Intended phase distribution entire the lens aperture for the proposed homogeneous framework reflectarray antenna is plotted: (a) 10GHz, (b) 15GHz; and weighted phase error distribution entire the lens aperture is plotted: (a) 10GHz, (b) 15GHz[22].;

In [22], the intended phase distribution control in the reflectarray scheme is concentrated on metal-only porosity technique at 15GHz. In this scheme, slot type elements are developed and formulated as host medium and bed frame provides sufficient phase shift entire lens aperture, as
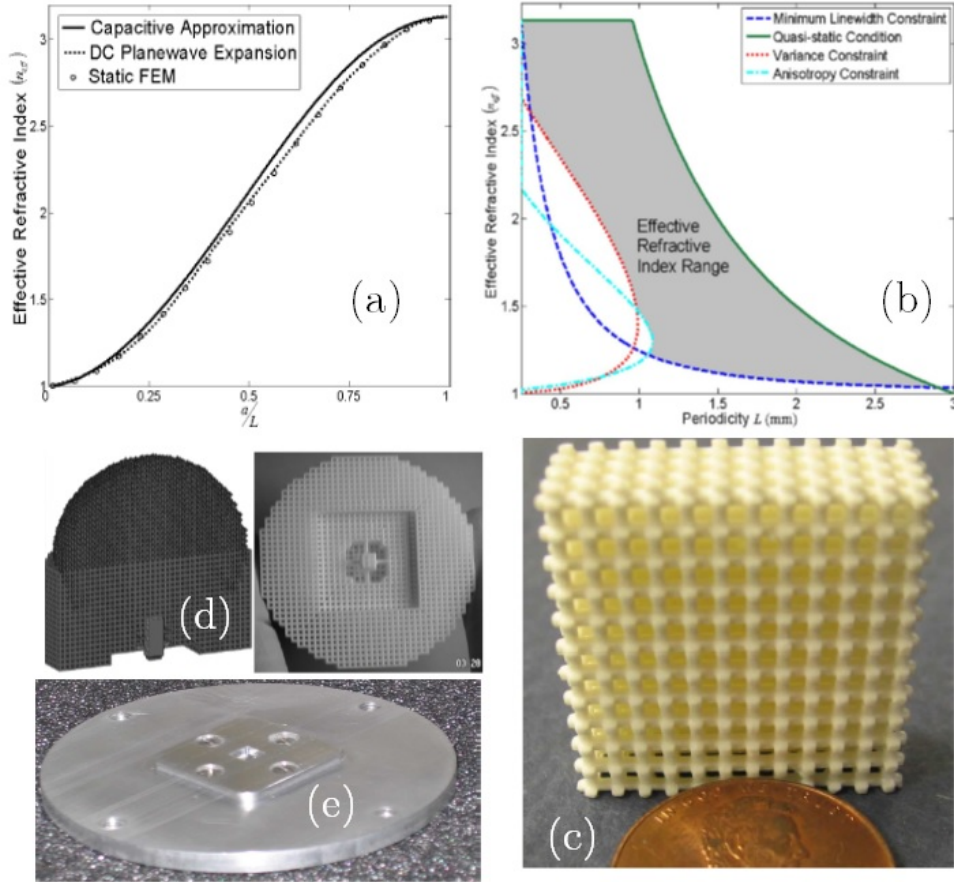
Figure 2.15 – Example of the cubical lattice Luneburg lens antenna in a ceramic Al_2O_3 framework is performed for 30GHz applications. (a) illustration of effective refractive index variations versus cube dimensions for capacitive, DC plane wave, and static FEM approximations; (b) Range of trusted area for cube-shaped cell dimension with four constraints for Alumide based cells; (c) The manufactured cubical lattice with constant refractive index; (d) The fabricated Luneburg lens; and (e) Fabricated open waveguide for lens feed;[12].

shown in Fig.2.14 (a-c). Provided cells employing with mathematical control of phase shift to satisfy Fig.2.14(d-e) required phase shift distribution on the lens aperture at 10GHz, and 15GHz, respectively. The advanced lens diameter is $380mm$. It has been designed and examined at X and Ku-bands with total gains of 29dB, and 32.6dB, aperture efficiency of 51.3% and 51.1%, respectively. [22].

2.5.4 Virtual permittivity design based on free forming porous structures that can only be built with a 3D printer

The study on virtual permittivity control cells with free forming dielectric materials logically first concentrated on the control of two parameters: the filling ratio and cells fabrication. On the above basis, this analysis verified that the gradient refractive index approach is a favorable solution in high gain with a focusing lens, and urges studying more advanced abilities regarding manufacturing with reasonable costs and operating frequency. Notably, the idea of free forming design dielectric cells based on additive manufacturing processes and materials is to support dynamic local refractive control for beam shaping based on GRIN mediums while simultaneously achieving two and three-dimensional devices in full dielectric platform. Such forward performance modes would even further the interest in full dielectric planoconcave, reflectarray, Lunenburg, Fresnel zones, polarizer, and THz sieve lens providing, for instance, a shared aperture for bi-functional applications as needed in millimeter-wave (MMwave) and submillimeter-wave applications is one of those approaches [74]. Additionally, the high range of refractive index with high permittivity dielectrics can be implemented to reduce lens sizes based on optic transformations toward MMwave and sub-MMwave focusing purposes.

It is significant to note that the free forming design concept includes two of the most common schemes, such as cube-shaped cells [10, 12, 11], the extended u-shape rods [15], the distinct height cubes [9], and the lattices with spatially variant self-collimation [75] are fundamentally beneficial to multi-reconfiguration when compared to the other three approaches. This benefit is because the implementation of complicated structures and shapes for the advanced control of beam shapes and virtual permittivity in the aperture surface can come with a combination or a single form of all approaches as mentioned above. For instance, the total fabrication costs of the three-dimensional lens, with conventional companies, are so high because of a large number of layers, shape accuracy, and layers of air gaps. Such issues do not exist in 3D-printed GRIN lenses from microwave to millimeter-wave spectrum. As a consequence, several advanced 3D prints with conventional desired fashion, such as the Lunenburg or the new fashion distribution of the gradient refractive indices, have been introduced recently. So far, these investigations mainly focused on describing the ability of the porous cells, and the porosity level is briefly mentioned in the rest of this section.

The 3D-printed cube-shaped cells employ two principal goal controls of virtual permittivity in a predetermined area with dependent control of the phase of each sub-zones for GRIN medium, and the mechanical strength keep the cells in a predetermined position without any effect for the zones' phases [10, 12, 11]. Some universal principle of such printed cells is illustrated in Fig.2.2, where the height of cells and cube size play a central role in reaching the proposed approach. Rods are loaded by analyzed thickness to connect pairs of cells as shown in Fig. 2.3 [26, 10, 12, 11]. In the case of the incident field component, the rods' thicknesses do not affect the phase based on the device requirements because they are designed with permittivity near to air in the presented electromagnetic spectrum. More recently, the implementation of cube-shaped allowing the control of virtual permittivity in 3D printed spherical Lunenburg lens [26, 10, 12, 76, 77, 78, 79], and a quarter and half-wave Fresnel zone plates have been explored [11, 80, 23, 81, 82, 83, 24].
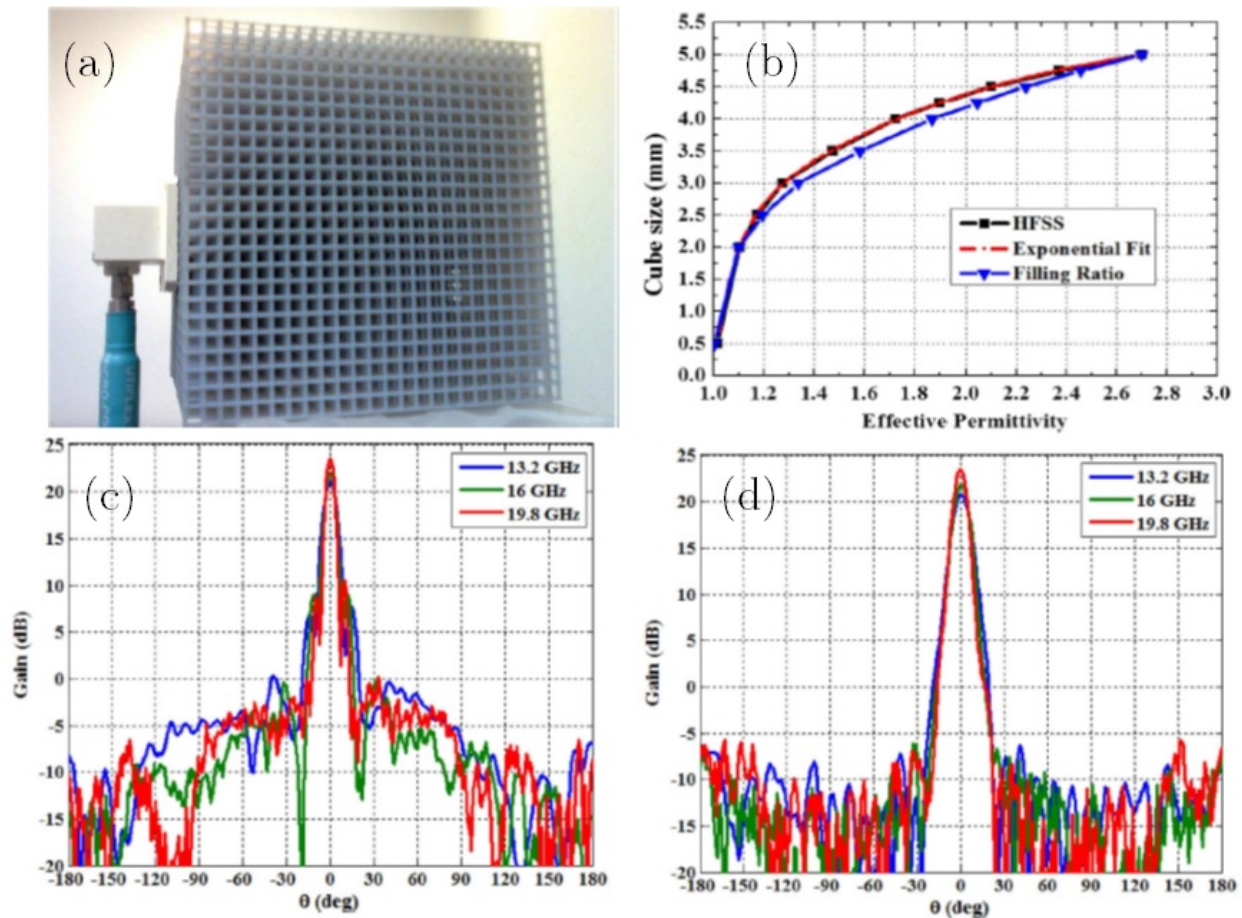
Figure 2.16 – **Example of the full dielectric Luneburg lens antenna using cube-shaped framework for Ku-band applications is achieved. (a) Side view of Lens framework, (b) permittivity distribution for cube sizes; A pencil beam radiation pattern for proposed porous lens over Ku-band: (a) E-plane, (b) H-plane; [10]**

In [12], the virtual permittivity control in 3D Luneburg lens scheme is focused on cube-shaped cell material porosity based on fragile ceramic with stereolithography method at 30GHz. In this scheme, cube-shaped cells are formed and formulated with quasi-static capacitive modeling as host medium and bed frame to realize extended Luneburg lens. Provided cells refractive index is employing with three analysis to access good accuracy without full-wave simulations, as shown in Fig. 2.15. These analyses are capacitive approximations, direct current plane wave expansion, and static FEM, as shown in Fig. 2.15(a).

Based on the proposed cell model analysis, four restrictions are determined with refractive index variations versus cell periodicity. The common areas for these restrictions are illustrated as a trusted design area with 5% error, as shown in Fig.2.15(b), with cubical lattice, as shown in Fig.2.15(c). The proposed lens s extended for inner waveguide feed method, as shown in Fig.2.15(c),(d). In this configuration, the proportion of rod size and cube filling ratio for control of effective refractive index is examined in the entire model, and improve lens mechanical strength.

Design of the all-dielectric Luneburg using the cube-shaped porosity technique for antenna applications is presented in Fig. 2.16(a) [10]. This prototype is prepared based on fixed rods size with permittivity near to air, as shown in Fig.2.16(b). A manufactured 3D lens for 10GHz is prepared with 3D printing material with $\epsilon_r = 2.7$ to provide the virtual refractive index in $\Delta n = 1.7$ contrasts.

The effective virtual permittivity is produced with control or filling ratio approach to control of intended permittivity of predetermined zones in the homogeneous plastic slab. The E-field radiation output for the 3D lens, which is crossing through the displayed design for perpendicular ($\perp$) illumination is revealed in Fig.2.16.

Based on FDM, cube-shaped cell analysis [26, 10], the rod size of cube-shaped cells was fixed near to $\epsilon_{Air} = 1$ to connect provided cubes to realize sphere form, and the cube vertex size. Cubes vertex size as a filling ratio parameter was used to achieve 1.1 up to 1.4 refractive indexes to satisfy lens rules. In this design scheme, the provided loss tangent ($\tan\delta$) deviations for layers were not close together, which cannot show the spherical lenses performance ideally, especially for millimeter wavelength applications. This issue shows itself as a 7dB gain drop over the operating band. However, the results and performance are very well at 10GHz, and it can apply to the microwave industry as a new method of manufacturing a large number of layers quickly and reduce total fabrication costs

noticeably. In the previously analyzed ceramic material for a similar structure at 30GHz [12], both rods' thickness and cube sizes are analyzed together to solve this issue. This analysis is done based on the ceramic stereolithography material with a dispersion diagram analysis for rod size vs. cube size variations. In this scheme, a logical area to find a cube size with intended host medium permittivity the logical cube cell is provided to control virtual permittivity based on intended material permittivity, which helped the designer to manufacture an extended 3D Lunenburg lens near the ideal lens performance with the 2dB gain drop.

Based on this information, two types of perforated quarter-wave ($\lambda/4$) and half-wave $\lambda/2$ zone plates' antennas is presented with the above techniques for 60GHz, as shown in Fig.2.17. In the Fresnel zone plate scheme, the rod thickness is fixed near air permittivity at 60GHz. Based on reported analyses for virtual permittivity, implementations have been done with HFSS and exponential fitting approximations, to find the intended permittivity. In [12], the design approach is done based on distinct rod thickness because the planar form of ZP plates was not possible as it can make the designed lens corrugated and result in a difficulty in fabrication with large phase difference outcomes. For this reason, based on full dielectric zone plate rules, an FZP_2 (half-wave) and FZP_4 (quarter-wave) have been designed, manufactured, and measured. They presented a full dielectric zone plate with the cube-shaped cell [11]. The ZP's permittivity deviations are not radial like those of the Lunenburg, half Maxwell fisheye (HMFE) and Eaton lens, and the lens performance is directly relative to zone permittivity and thickness. All of this information has been added to [11] design. Aside from designing porous lenses techniques and reducing the estimated error for virtual permittivity achievements, we can increase the total homogeneous lens efficiencies by optimizing the lenses feeds based on the Kildal [84] and Collins [85] analysis for symmetric illuminations, which is a necessity to examine for high-efficiency results [24]. These examinations are independent of homogeneous or inhomogeneous lenses feeds [86, 87, 88, 89, 25], and it can improve lens efficiency at least 5%.

2.6 Future Challenges

As mentioned above, it is unknown why sphere shapes porous cell to realize virtual permittivity do not analyze more for GRIN medium implementation even with the high possibility of execution with the additive manufacturing processes. Spherical porous structures containing a symmetrical
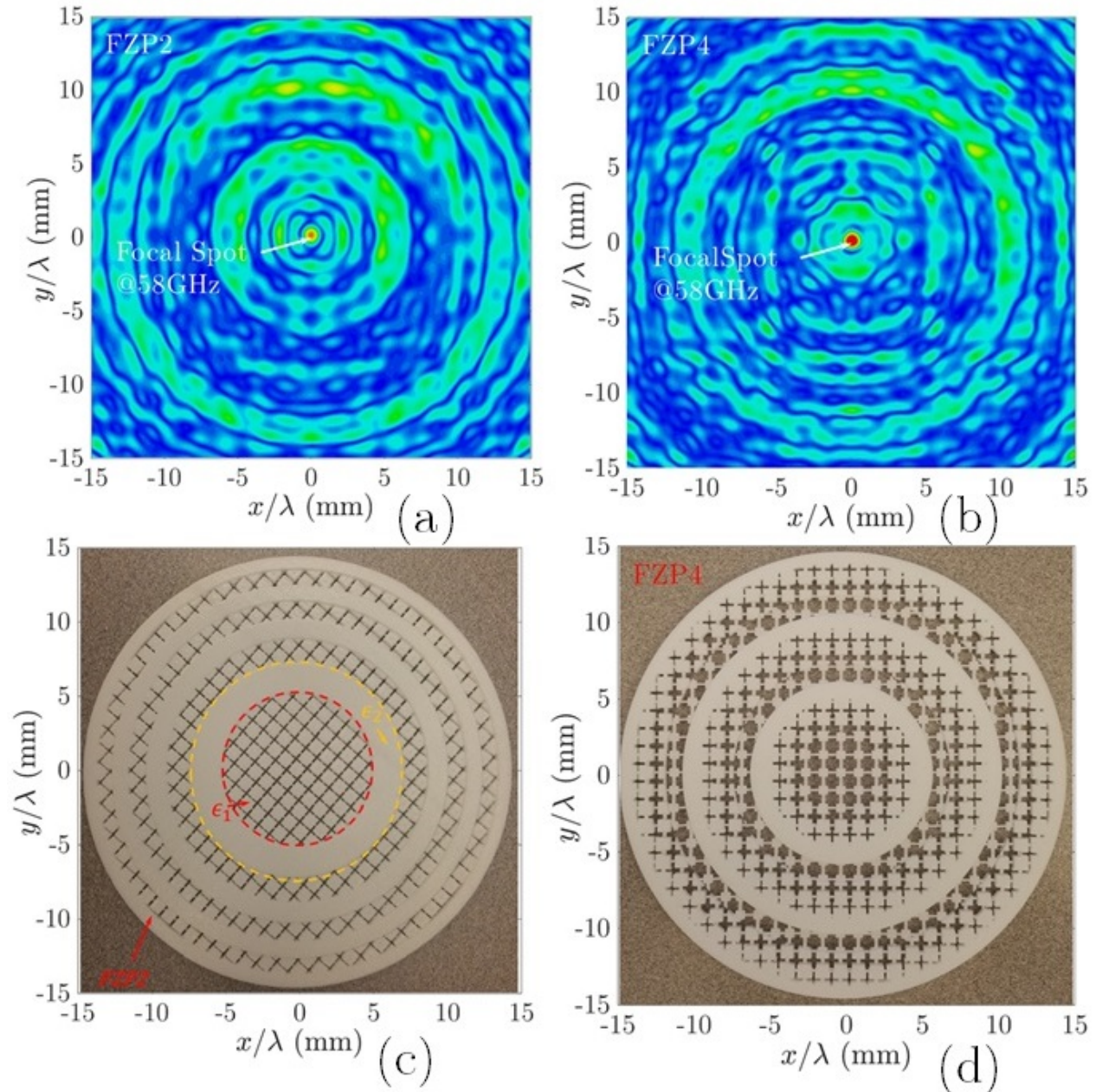
Figure 2.17 – **Example of the full dielectric zone plate lens antenna using cube-shaped framework for 60GHz applications is achieved. Transversal radiation output for the zone plates surfaces for perpendicular (⊥) illumination [11] at 58GHz. (a) half-wave, (b) quarter-wave; The fabricated zone plate lens structures: (a) half-wave, (b) quarter-wave; [11]**

arrangement of optical axes and presenting high stability for $|E|$−field orientation are highly desirable for constant virtual permittivity control. A vital challenge allowing the homogeneous platform GRIN medium is, therefore, the construction of virtual permittivity with constant properties in contribution various angle $|E|$−field orientations. The second substantially unexplored approach is creating free-form cell structure based on Euclidean and Fractal geometries that are based on

homogenous medium, which might demonstrate unbeaten in this interest. Also, new types of the additive manufacturing process including nanoscale printing, and high permittivity polymer jetting materials that can act as emerging research area are being developed because these inventions can often open new doors for optics and microwave engineers with the practical viability of the resultant porous GRIN devices.

An encouraging development is the compound of such 3D printed materials that can have a vast range of permittivity, permeability, and low loss properties. The construction of high-quality dielectric materials and metallic materials realizes a broad range of porous GRIN framework compounds, an extra challenge that is not novel but remains unsolved. Between the examples of 3D printed devices, the multi-scale manufacturing is highly desirable. However, proper devices can realize all compounds that include small electronic sensors or large scale mechanical parts have not yet been observed. Recently, the 3D printed microwave and THz devices were found to affect the microwave industry, solving some previous fabrication constraints. These 3D printed results, in combination with the use of new EM property materials, might provide a revolutionary distribution of EM properties and produce innovative devices. Printed metal homogeneous GRIN mediums might also get more attention in GRIN lens design applications. The development, characterization, and cell design formulation of homogeneous GRIN mediums with free forming designs look particularly hopeful. The current cube-shaped presentation is merely an encouraging example of improvements for Fresnel zone plates [11] that could start distinct device designs. Clearly, many challenges and objectives remained, but the speed of progress in 3D printed devices, which includes antennas, GRIN lenses, and circuits in all electromagnetic spectrums over the past decade, guarantees that the proposed research area will produce impressive advancements as a new spring for the third decade of the twenty-first century.

2.7   Conclusion

As a collective conclusion, regarding the extensive range of applications of permittivity control with porous structures, we can foresee the vast amount of exciting uses for the graded medium design in planar or 3D objects. Due to the extensive collection of utilization, this proposed concept uses 3D printing devices that can be employed (some of them have been experimentally confirmed in this thesis), and the presented project may motivate the development of an innovative form of lens de-

vices, more efficient lens devices as an antenna in the areas of mmWave communication. Advantages of these virtual permittivity design using full dielectric or full metal homogeneous approaches include **(i)** a notable simplification of the currently required graded setups based on material change approach to achieve the equivalent variety of functionalities; **(ii)** the possibility of realizing all-optical GRIN devices for lens antenna design applications, with development from millimeter (mm) to nanometer (nm) printing ranges to be achieved, so far, through additive manufacturing technology widely used nowadays; and **(iii)** the significant rest of previous GRIN medium design practical difficulties in the lens devices manufacturing processes is solved. All the suggested schemes appear as stable and dependable solutions for efficiently GRIN lens designs of practical applications, and they may also be entirely placed in the industry for short-term fabrication. Overall, we expect that the contributed investigation outcome of our porous design approach for the lens antenna design will have a markedly relevant scientific and economic effect in such diverse areas as mmWave communication and wave focus applications.

Chapter 3

mmWave Fresnel-Zone Plate Lens Antennas using Porous Plastics

This chapter has been taken partly from author published article [11].

3.1   Introduction

Control of permittivity is crucial to design of Gradient Refractive Index (GRIN) lenses such as Luneburg lens [77, 78, 79, 10], half-Maxwell Fisheye lens (HMFE)[77], and Fresnel zone plates [90, 91]. Related studies were principally focused on new material combination or material porosity and deforming to control permittivities [11]. Deforming rigid material structures such as air-holes, cube-shaped structures, or material pressing are an apparent material porosity methods to control intrinsic permittivity[80, 77, 23]. Among GRIN lenses, Fresnel Zone Plates (FZP), due to their planar merit, reduced weight, ease of fabrication, and cost-effectiveness are relatively more attractive structures to achieve high-gain focus in the millimeter and sub-millimeter wave spectrum [81, 90, 82, 92, 83]. Nevertheless, there are only a few studies on controlling the permittivities of phase correction zones with plastic porosity and experimental realization of the planar focus lens geometries. All investigations revealed hopeful ideas to achieve the following task: the material porosity was utilized to change the intrinsic material permittivity effects in a homogeneous medium, which was then used in controlling the intended permittivity distribution in the lens surface. A phase correction

is achieved by sub-zones in homogeneous or inhomogeneous medium to realize Fresnel-zones. Sub-zone phase correctors have been suggested by stepped zones thickness and air-holes in homogeneous zone plates [92, 83, 6], and distinct permittivity configuration is proposed with multi-dielectric concentric rings in inhomogeneous plates [83]. Cube-shaped material porosity urges the need of analysis to implement planar lens schemes. The cube-shaped plastic cells have been introduced and most recently realized by the additive manufacturing processes to control permittivity [38], which is inaccessible to achieve with conventional fabrication methods.

The subject of this work is the realization of Fresnel zone plate lenses based on material porosity control. We use multi-permittivity distribution with zone plate rules satisfaction to achieve focusing. Due to phase correction sub-zones with respect to the transmission direction, the objective is to find the zone-plates' geometry using the material porosity method. In order to realize the synthetic permittivity with plastic, the optimum value of cube size is determined through analysis. By employing a proper cube filling ratio, we identify possible geometries in each sub-zones for a focusing lens. Two half ($\lambda/2$) and quarter ($\lambda/4$) phase correction FZP lens geometries using Fused Deposition Modeling (FDM)[38] and Selective Laser Sintering (SLS)[38] manufacturing process are experimentally realized, which show a close agreement with the simulation results. The contribution of this work is as follows: **First**, implementation of low permittivity zones with low permittivity cube cells to reduce reflections. **Second**, homogeneous porous design ZPs. **Third**, the High efficiency, gain and low side lobe level compared to previous works. **Fourth**, the low fabrication costs with the fast manufacturing process.

3.2   Fresnel Zone Plate Lens Design

The topology of full dielectric Fresnel zone plate antenna is shown in Fig.3.1(a). The FZP lens structure is composed of dielectric rings for phase reversing of incidence waves instead of blocking as Soret type Zone Plates (ZP)[82]. D and F denote the aperture diameter of the zone plate and distance between the feed and the aperture of the plate, respectively. As shown in Fig.3.1(a), Fresnel zone plate is created to transform the incoming wave in transmission mode with a pencil beam in the z-axis direction. The Fresnel zone plate (FZP) boundary equation for a conventional planar
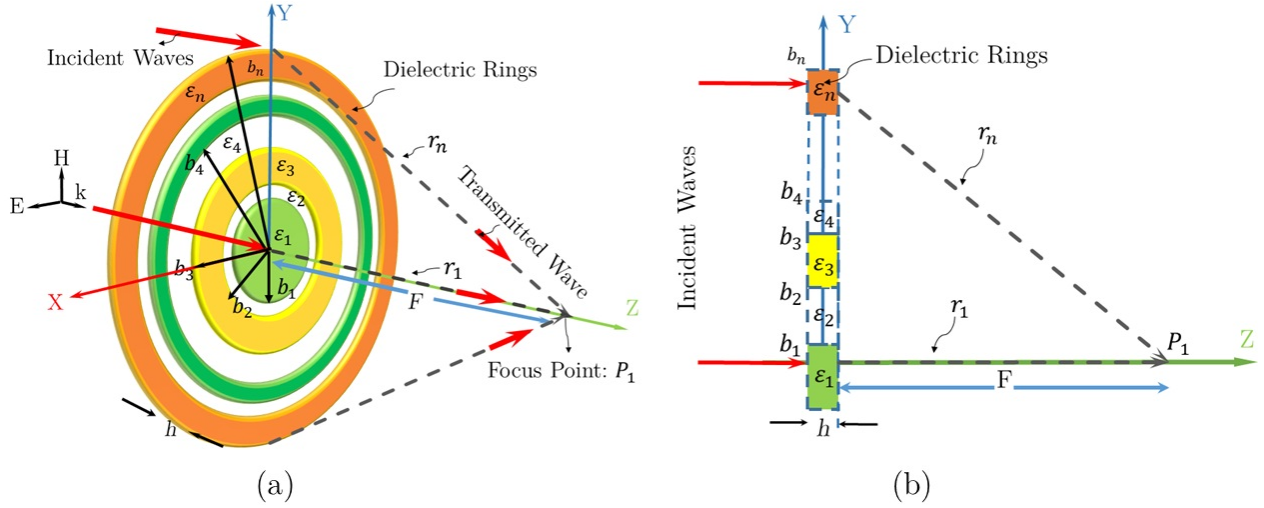
Figure 3.1 – Illustration of the dielectric Fresnel zone plate focusing at P_1 for (a) 3D topology and (b) half-portion multi-dielectric, phase correcting zone plate in xy-plane for perpendicular illumination.

zone lens with P full-wave circular zones is given by

$$b_p = \left(2pF\lambda + (p\lambda)^2\right)^{1/2}, \quad p = 1, 2, ..., P, \tag{3.1}$$

where b_p denotes the outer radius for the p-th sub-zone of the proposed lens, λ is the design wavelength at operating frequency, and F is the proposed lens focal length. Each full-wave zone in the zone plate (ZP) lens design is divided into an even number of sub-zones, i.e., q = 2, 4, ..., $2n$. In this ZP lens, the phase at each n-th sub-zone varies from the nearby sub-zone phase by $\pm\frac{2\pi}{q}$ radians [92, 83]. The external radius b_n of the n-th sub-zone is given by

$$b_n = \sqrt{\frac{2n\lambda F}{q} + \frac{n\lambda^2}{q}}, \; n = 1, 2, ..., S, \tag{3.2}$$

where S is equal to qP.

Therefore, with these equations, for the half-wave phase correction $q = 2$, the sub-zones are becoming to the half-wave Fresnel zones, and for $q = 4$, the ZP lens is equal to a quarter-wave phase correction lens [82, 83]. In the half-wave zone plate structure, the lens can be a amplitude (binary) or phase-reversal [82]. Therefore, we determine and classify the zone plates lens for $q = 6, 8, etc.$ with FZP_q subscriptions. The 3D focusing action of the zone plate lens is illustrated in Fig.3.1(a). This focusing action in upper half portion of the proposed lens is illustrated by a ray-tracing into

1-st, and n-th sub-zones in the first full-wave zone $(p = 1)$, where n is greater than one. The ray tracing equation for the r_n and $r_1 = F$ ray collisions at p_1 , as shown in Fig.3.1(b), is given by

$$(\beta\sqrt{(\epsilon_n)h} + \beta r_n) - (\beta\sqrt{(\epsilon_1)h} + \beta r_1) = 2\pi, \ n = 2, 3, ..., q, \tag{3.3}$$

where the free space-wave phase constant is $\beta = 2\pi/\lambda$, h is the concentric dielectric ring thickness, and ϵ_n and ϵ_1 are the permittivities of n-th order, and 1-st order dielectric rings phase shifters, respectively (see Fig.3.1). Similarly, with substituting $r_n = r_1 + (n-1)(\lambda/q)$ into (3), it becomes

$$\sqrt{\epsilon_n} = \sqrt{\epsilon_1} + (\frac{\lambda}{h})[\frac{1 - (n-1)}{q}], \tag{3.4}$$

As shown in Fig.3.1(b), for a perpendicular illumination the plane wave goes into the first zone without any reflection, if the proposed lens meets the standing wave condition as Eq.3.5. Since, the dielectric ring thickness h is measured by half-wavelength of the n-th standing dielectric, where n is the integer number, the λ_{ϵ_1} for the first sub-zone will be equal to λ.

$$h = \frac{n\lambda}{2\sqrt{\epsilon_1}} = \frac{n\lambda_{\epsilon_1}}{2}. \tag{3.5}$$

Finally, by replacing equation (3.4) into (3.5), the final dielectric zone plate mathematical equation is obtained as follows

$$\epsilon_n = \epsilon_1.[1 + \frac{2}{n}(1 - \frac{n-1}{q})]^2. \tag{3.6}$$

The thinnest designed lens thickness corresponds to $n = 1$, which is given by n and q. Accordingly, with increasing n, the proposed ZP lens thickness h will be proportional to n (i.e., $h \propto n$) and permittivity ratio ϵ_n/ϵ_1 will decrease. In the proposed design, we expand on previous multi-dielectric zone plates to provide the new result which is achievable with virtual permittivity for phase corrector design at the millimeter-wave spectrum. The design graphs for the zone plates are analyzed based on 3D printing[38] material porosity with the electromagnetic model and measurement. In order to show the designed lens focusing ability and geometrical properties with virtual permittivities. The additive manufacturing process is chosen to produce these models. A Cube-

shaped porosity model is described to provide necessary permittivity feature. For this reason, an optimum size of cubes is achieved through a full-wave analysis in combination with verifying results.

3.3   Permittivity Control with Material Porosity Method for ZP Zones

The cube-shaped material porosity techniques were utilized with additive manufacturing process to change the intrinsic material permittivity effects in a homogeneous medium, which is impossible with previous manufacturing processes. We expanded this porosity model to satisfy the expected relative permittivity to produce phase reversing of planar zones. The analyzed cube cells are used to realize entire zone plate volume with discrete and separate cells. Overall cube-shaped cells are constructed with two distinct polymer-based plastic, which is chosen from EOS additive manufacturing systems and materials [38]. Since the accurate permittivity of the proposed dielectric materials is crucial to simulate, design and fabricate millimeter-wave GRIN medium ranges efficiently. Therefore, both materials (ABS-M30, and Polyimide) waveguide fill samples with dimensions of $3.7 \times 1.8 \times 5$ mm^3 are built to fill WR-15 waveguide spacer. Then an Agilent E8361A PNA Network Analyzer is used to enable V-band measurements of the ABS-M30, and Polyimide dielectric samples.

The Kramers-Kronig (KK) relation is used to extract printed material characteristics (the relative permittivity and loss tangent) from the measured S_{11} and S_{21}-parameters. Fig.3.2 shows the extracted measurements of relative permittivity (ϵ_r) and loss tangent (tangδ) for the printed samples over the V-band. As shown in Fig.3.2, the relative permittivity ϵ_r measurements appear stable and fairly linear for frequencies up to above 70 GHz with a small downward slope as frequency increases. As expected, PA2200 nylon (Polyimide) SLS material exhibits a higher permittivity. The variation of the ϵ_r measurements for the Polyimide material are likely the result of dimensional variations for the waveguide fill samples due to the developing tuning of the processing conditions for this nylon. Currently, relative permittivity measurement variations of less than $\pm 3.2\%$ and $\pm 6\%$ are achieved for the ABS-M30 and Polyimide samples, respectively. Loss tangent (tanδ) measurements yield maximums of 0.059 and 0.068 for the ABS-M30 and Polyimide samples, respectively, demonstrating their suitability for millimeter-wave applications. The full size of these cell for both dielectric materials is $5 \times 5 \times 5$ mm^3, as shown in Fig.3.3(a), which η is the cube vertex size. These cells are connected with rectangular rods as a mechanical supporter to realize entire plates, as shown in
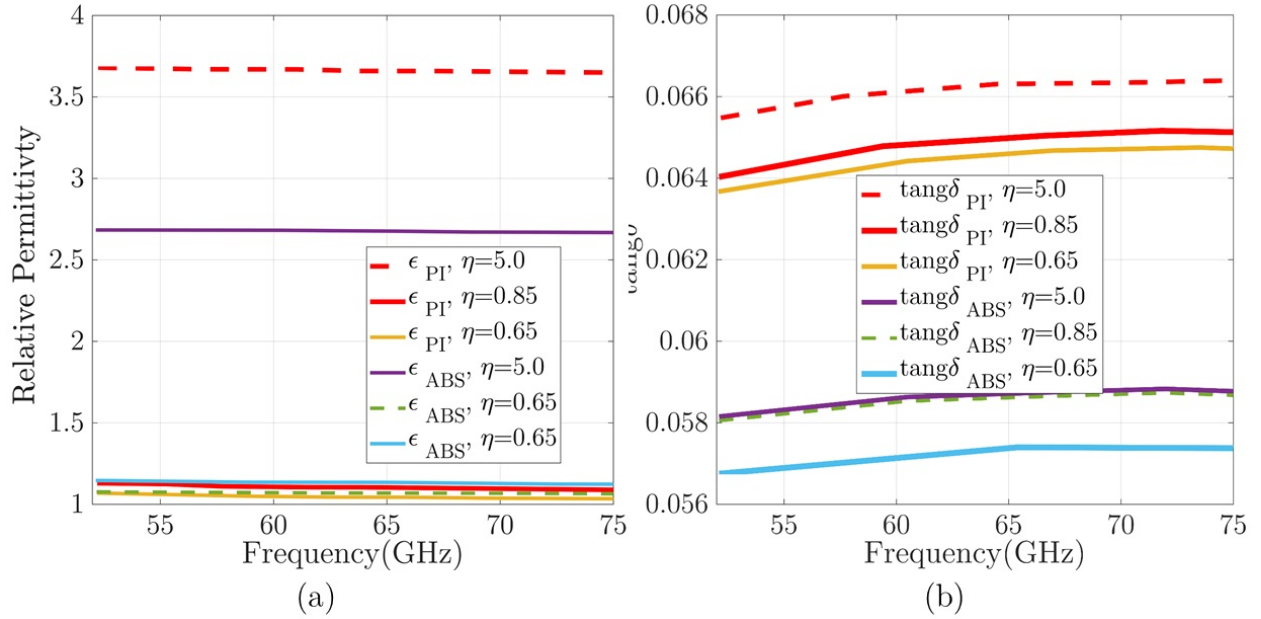
Figure 3.2 – Illustration of V-band characterization for ABS, and Polyimide 3D printed samples: (a) relative permittivity (ϵ_r) and (b) Loss tangent; for 3D printed materials extracted from the measured S_{11} and S_{21}-parameters with Kramers-Kronig relation.

Fig.3.3(a). The dimension of rod connector is fixed at 0.65mm diameter to have a little impact on the zone plates focusing ability. By tuning each cube vertex size η, the expected dielectric constant is produced.

As we expected in this material porosity model, by reducing the cube volume in control of the filling ratio (ζ), a lower effective permittivity compared to the full cube size is achievable. To achieve q zone geometry, the predetermined filling ratio (or cube sizes) are used to realize each zone based on the permittivity distribution given by (3.6).

Since the employed relative permittivity for ABS-M30 [38] and Polyimide[38] are 2.76 and 3.6, which is achieved with measurement, the desired permittivity realization within one up to those permittivities through filling ratio control is easy. The full cube size for this analysis is 5mm, which is equal to λ_0 at 60 GHz.

As shown in 3D volume reduction scheme in Fig.3.3(a), each cube is formed with air voids. In this scheme, by assuming effective permittivity and filling ratio as a set of data points such as ($x_0 = \epsilon_{Air}, y_0 = \zeta = 0$), ($x_1 = \epsilon_m, y_1 = \zeta = 1$), a new data points using linear interpolation is obtainable. Therefore, a cube-shaped cell effective permittivity with volume reduction is approximated with

linear interpolation given by

$$\epsilon_r = \epsilon_m . \zeta_m + \epsilon_{Air} . (1 - \zeta_m), \tag{3.7}$$

where ϵ_m is the material permittivity, which m is dedicated to ABS-M30 and Polyimide plastic materials, whereas ϵ_{Air} stands for the air permittivity.

Fig.3.3(b) shows the filling ratio ζ vs. effective permittivity results. As shown in Fig.3.3(b), the filling ratio versus effective permittivity analysis for $\epsilon_{rA} = 2.4$ and ABS-M30 even with close permittivities are so far. Moreover, raw material intrinsic permittivity is essential for a final cube size. For this reason, the distinct analysis should be considered for each particular substance individually. The extracted results for cube size vs. filling ratio shows that the cube size variation vs. effective permittivity is not linear. In order to obtain an acceptable design tolerance, we cannot confine just for this approximation to create the zone plate lenses. In a parallel study, an Ansys HFSS simulation setup is used to calculate the optimum value of cube size to reach this goal. Each ABS-M30 and polyimide plastic cube-shaped cells with rods are analyzed in the waveguide, with PMC and PEC boundaries for setting up the periodic environment. For this setup, the wave ports are located on the top and bottom of the cube cell, as shown in Fig.3.3(c). The effective permittivity of each cube-shaped cells is obtained from scattering parameters using the standard retrieval method. As shown in Fig.3.4(a), the extracted results of cube size vs. effective permittivity for filling ratio ζ and HFSS results are similar up to 2.2 mm. To solve these uncorrelated explanations, the exponential fitting method is applied to extracted cube sizes, as shown in Fig.3.4(a). By this fitting, the EF_m results matched well with $HFSS_m$ as HFSS setup outs, where m is the material types. To review, the realized lens cube sizes would be the HFSS and EF outs, as shown in Fig.3.4(b).

After parametric studies to extract optimum size using cube size versus effective permittivity analysis, the focusing ability of phase-correcting zones with cube-shaped cells was performed by commercial software CST Microwave Studio. The values of cube size were chosen based on typical ranges used for lens sub-zones given by (3.6) for millimeter-wave zone plate antenna implementation. The four primary geometrical parameters that determine our lens structure are cube size η, lens diameter D, focal length F, and the number of zones q, as shown in Fig.3.5(a). For zone plate design, D, F, and q are interrelated through (3.1). Therefore, we can choose just two sets of these parameters independently. Some interesting trends that are apparent based on (3.1) in our analysis which can highlight as guidelines for any design as follows. By increasing the zone plate diameter

$\eta = 0 \qquad \eta = 1.5 \qquad \eta = 2.6 \qquad \eta = 4.5 \qquad \eta = 5$

(a)

(b)

(c)
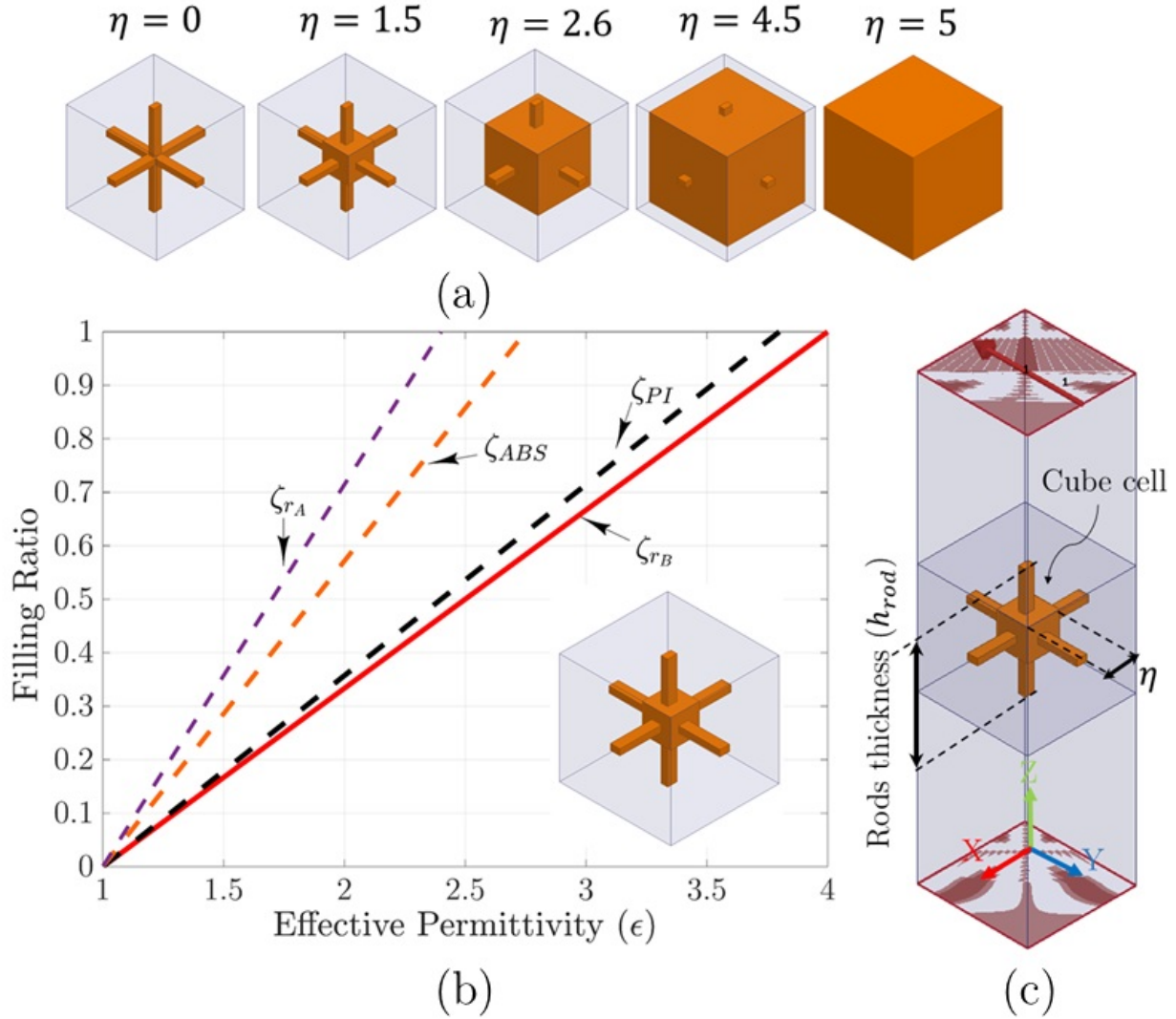
Figure 3.3 − **(a) Illustration of the filling ratio ζ vs. effective permittivity for ABS, Polyimide, and two materials with close permittivities $\epsilon_{r_A} = 2.4$, and $\epsilon_{r_B} = 4$ for the filling ratio ζ extracted from (1). (b) HFSS simulation setup for effective permittivity analysis, where $h_{rod} = 5mm$ is the thickness of rods, and η is the size of cube 0 to 5 mm;**

D and holding the focal point F constant, the lens focusing gain will be increased. This difference indicates that to have a more focus on incident energy with lens rules (3.1) satisfaction the higher number of zones should be enabled. However, this increase of the focusing gain is limited, which is prognosticated with geometrical optics.

In order to increase D, the outer zone widths relative to the operating frequency wavelength will be thinner, as shown in Fig.3.5(b), which makes the designed plates inaccurate. However, if we held the lens focal point and diameter variable, and number of zones constant with Equation (3.1), the lens focusing gain will improve like before, but this enhancement will not raise unbound

(a)   (b)
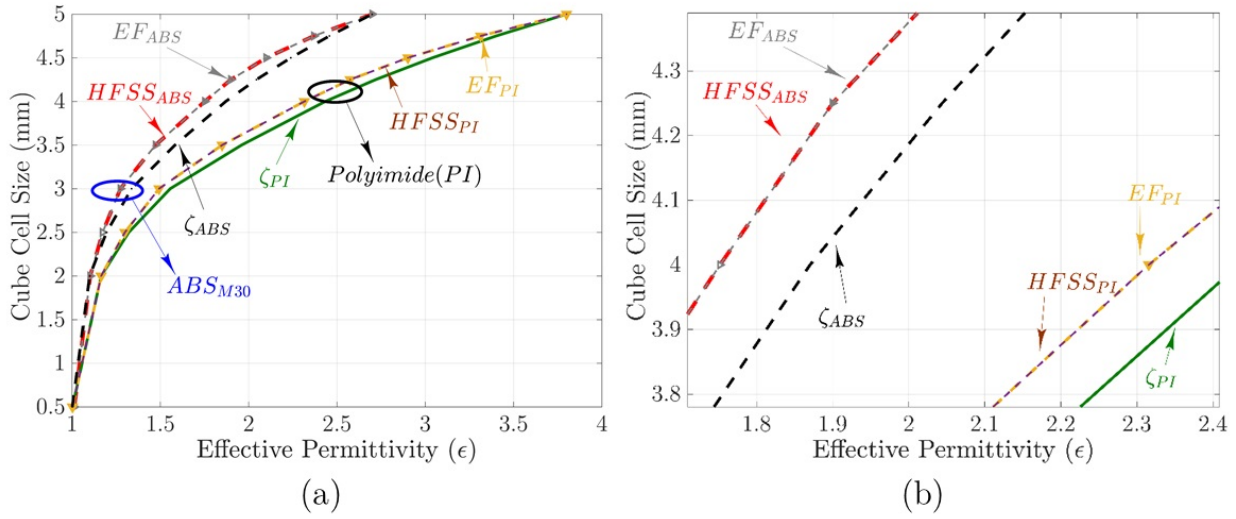
Figure 3.4 – **(a) Illustration of the Cube size vs. effective permittivity analysis for ABS-M30 and Polyimide plastics with filling ratio ζ, exponential fitting (EF), and Ansoft HFSS simulations. The EF_{ABS}, and EF_{PI} curves are the extracted data from exponential fitting function. The ABS polymer cube vertex size η for intended permittivity is obtained using exponential fitting (EF) equation, where $\eta = 5.545 - 58092 \times e^{-\epsilon_r/0.07564} - 9.5423 \times e^{-\epsilon_r/0.95527}$, ϵ_r is the intended permittivity, and η is the cube vertex size for ABS plastic cubes, (b) Zoomed for $1 \leq \epsilon \leq 2.4$;**

(a)   (b)
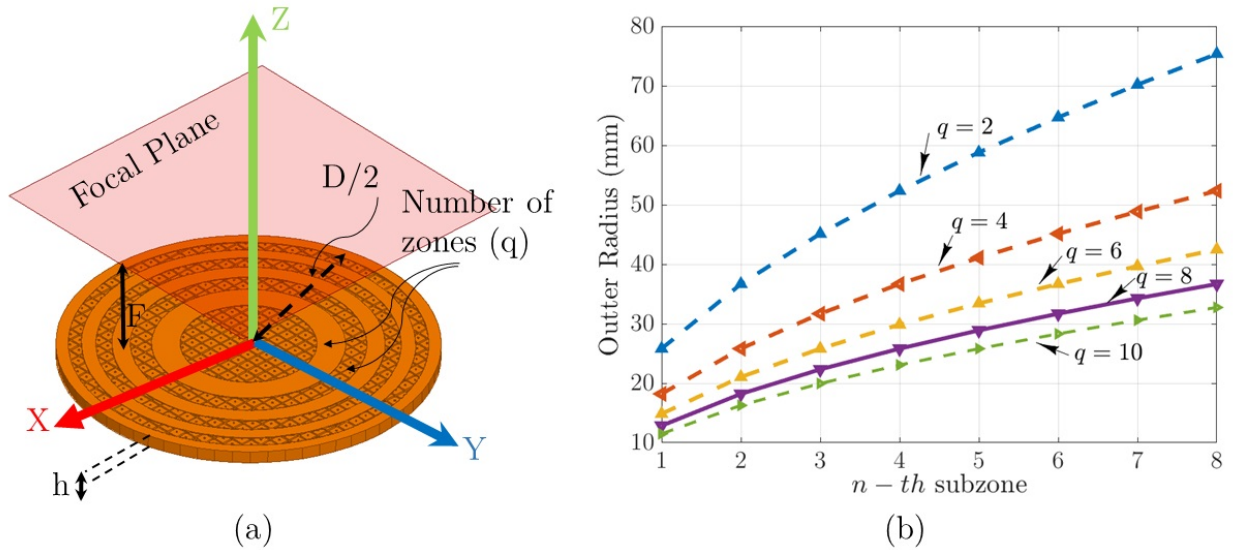
Figure 3.5 – **(a) The primary geometrical parameters that determine our lens structure are lens diameter D, focal length F, and the number of zones q (for this figure q is 2); (b) External radius of the Fresnel zone plate versus sub-zone for $2 \leq q \leq 10$ with $\lambda = 5mm$ given by (3.2);**

because of the multiple reflections by high permittivity zones. Therefore, to obtain a good focusing gain in our plates, all these trends are considered during the design.

In this study, the zone numbers q ranges from 1 to 10 but the lens focal length and diameter are fixed at $26\lambda_0$, and $35\lambda_0$, respectively. As mentioned before, with increasing of zone numbers, the lens surface is subdivided into thinner width zones, as shown in Fig.3.5(b) analysis given by (3.2). For this reason, the realization of high q lenses with 5 mm cells will be a critical design point with the implementation of the porosity cells. Therefore, only half and quarter wave phase correction is selected to evaluate the performance of zone plates with this porosity technique.

After choosing the zone number, the entire lens surface is subdivided into 5mm cells, which is divided plates surface to 900 unit cells. Then a predetermined cube size based on the parametric permittivity analysis, as shown in Figs.3.3(b) and 3.4(a), is chosen to fill these cells to realize the entire lenses. As mentioned before, the multiple reflections of the plate because of the high permittivity zones is conventional in the zone plate structures. To reduce these reflections in our plates, a thicker lens ($t = \lambda$) using smaller effective permittivity zones is designed to produce intended phase shift with lower attenuation. There are three reasons for the choice of this thickness. **First**, this increased thickness ($t = \lambda$) allows us to reduce the multiple reflections of high permittivity zones. **Second**, the implementation of low permittivity zones with low permittivity cube cells will be possible. **Third**, the designed lenses will achieve the required mechanical resistance due to the spatial state of construction. Therefore, the design of half and quarter-wave Fresnel zone plates using cube-shaped material porosity at 60 GHz will be possible. The proposed lens radiation system was simulated using the finite difference time domain method software CST.

Lens design criteria for the focusing devotions can be classified into two modes of illumination as follow: Transmission-mode and Reflection-modes. The essential devices of each focusing setup are assigned in two central part which can achieve them in all pieces of literature with specific names as follows: a lens device (focusing provider), and illuminator/feeder/wave-launcher. Generally, all classes of lens devices for wave focusing setup are independent of electromagnetic spectrums, and they had their treatment scenarios and producing of predetermined sub-zones permittivity techniques. However, the treatment of the proper illuminator and low error subzones permittivity implementation is the apparent goal in all focusing mechanisms which can be considered to guarantee the desired radiation effect in a predetermined setup with a defined focal point (F), lens diameter (D), and antenna gain parameters. As shown in 3.1 (a), Fresnel zone plate is a planar symmetric gradient index structure with z-axis at the center. Therefore, by providing axially symmetric illumination [98] for feeding lens aperture the zone plate out radiation patterns should be

symmetric with high gain and high efficiency in focusing point (P1). Therefore, we can verify that any asymmetrical zone plates' radiation is happened due to permittivity estimation error for the homogeneous design principles. To achieve this goal, an axially symmetric feed [91] or uniform feed [84, 24], based on [84, 24] feed analysis are considered.

In millimeter-wave band over 30GHz, the fabrication of illuminators that uniformly illuminates [84, 24] or axially symmetric illuminates [91] the lens surface to obtain an intended efficiency is difficult [24]. For this reason, amplitude tapering must be considered for illumination of lens feed to obtain the desired efficiency efficiency based on [84], and [24] feed analysis. To accomplish this goal, two crucial factors are considered based on [84] feed analysis, and approximations: the taper efficiency (η_{taper}) and the spill-over efficiency (η_{SP}) [84, 24]. In the classic design of Fresnel zone plates, horn antennas are employed as an illuminator to feed the zone plates, the radiation pattern of the lens feeder serves a $\cos^n$-like function [84, 98, 24]. Since the fabrication of this kind of feed at millimeter-wave band is complicated [24]. Therefore, a new type of illuminator or $\cos^n$-like radiation pattern horn with low SLL must be considered for illumination [24, 84, 98]. To reach this purpose, theoretical aperture efficiency versus $\cos^n$-like radiation pattern amplitude weighting is analyzed to obtain expected efficiency with n variations [24, 84]. The taper efficiency (η_{taper}) equation for the loss of non-uniform illumination of the aperture amplitude and the spill-over efficiency (η_{SP}) are given by (3.8) [[84], p905, Eq.22], [[85], Eq.6] and (3.9), individually [84, 85, 24]:

$$\eta_{taper} = \frac{1}{\pi . \tan^2(\frac{\theta_0}{2})} . \frac{[\int_0^{2\pi} \int_0^{\theta_0} |G(\theta, \phi)|^{0.5} . \tan(\frac{\theta}{2}) \, d\theta \, d\phi]^2}{\int_0^{2\pi} \int_0^{\theta_0} |G(\theta, \phi)| . \sin(\theta) d\theta d\phi}, \tag{3.8}$$

$$\eta_{SP} = \frac{\int_0^{2\pi} \int_0^{\theta_0} G(\theta, \phi). sin(\theta) d\theta \, d\phi}{\int_0^{2\pi} \int_0^{\theta_\pi} G(\theta, \phi). sin(\theta) d\theta \, d\phi}, \tag{3.9}$$

where G(θ, ϕ) is the radiation pattern, θ is dedicated to polar angle, and ϕ is the azimuthal angle[84, 85, 24].

$$G(\theta, n) = \{(2n + 1). cos^n(\theta), \; for \; 0 \le \theta \le \pi/2; \; 0, for \theta > \pi/2; \tag{3.10}$$
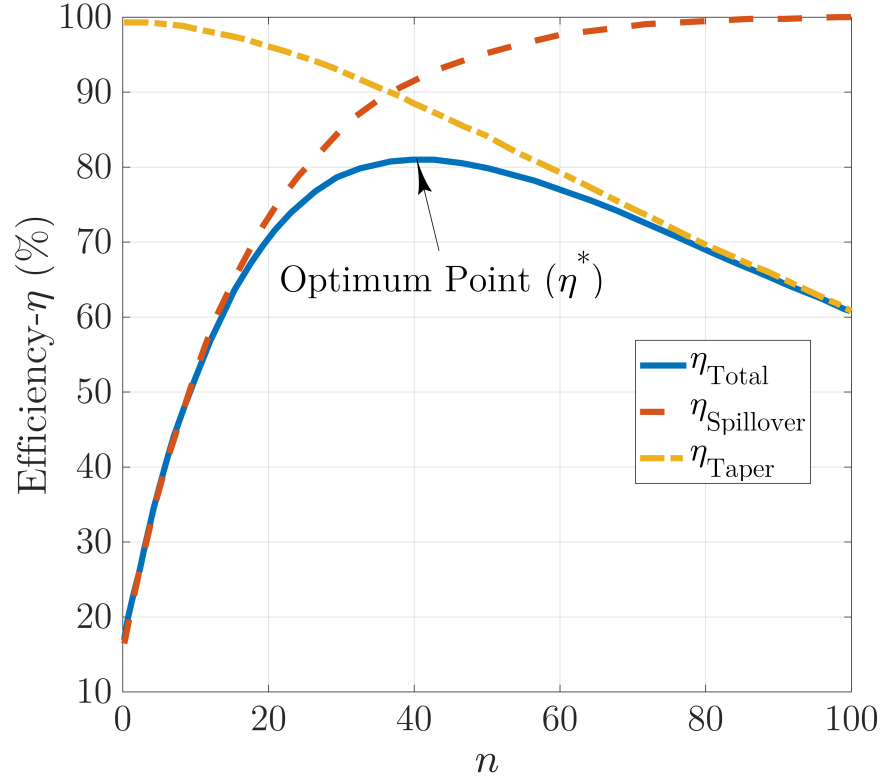
Figure 3.6 – **Graphical illustration of** η_{taper} **(Eq.3.8),** η_{SP} **(Eq.3.9), and** η_{total} **efficiency [24] over the amplitude weighting generated by cos ^{n}-like illumination [24, 98]**

.

Since the axially symmetric radiation pattern for illuminator is given by (3.10)[98], accordingly, with increasing n, the proposed feed will generate high spill-over efficiency (η_{SP}), and the taper efficiency (η_{taper}) will decrease[24]. Considering to the lens diameter and the lens focal length (F), a higher n for $\cos^n$-like radiation pattern to obtain a product of two efficiencies as total efficiency ($\eta_T = \eta_{SP}.\eta_{taper}$) is desirable [24, 84].

Illustration of this efficiency versus n value, as shown in Fig.3.6, shows that the optimum point (η^*) to obtain maximum total efficiency $\eta_T = 0.81$ is equal to $n = 40$ [24, 84]. As shown in Fig.3.6, to obtain the total efficiency between $0.31 \leq \eta_T \leq 0.71$, n must be chosen between $10 \leq n \leq 20$ ranges. Considering to provided information for total efficiency higher than $\eta_T = 0.71$, n must be chosen between 22 and 78. For this purpose, two types of feed as illuminators to study of the designed FZPs efficiency are considered: (a) a cos ^{10}-like radiation pattern feed, and (b) a cos ^{45}-like radiation pattern feed.

To achieve the first feed with cos ^{10}-like radiation pattern a microstrip dipole antenna is designed, and to obtain second feed with cos ^{40}-like radiation pattern a commercial horn antenna are considered to feed lens.

Concerning structural comparison with [24], the provided lenses do not have any structural similarities, and physical relationships and they are just determined in the classification of the Fresnel zone plate arrangements with different applications toward two distinct bodies: planar and corrugated form. In the case of feed types and illuminators design, all Fresnel lenses analysis with horn antenna illuminations is similar, which is illustrated in [98] for high-frequency treatments in detail. The presented study in [98] describes the high-efficiency lens treatments with focusing on the type of illuminations such as axially symmetric feeds Eq.3.9 and lens classes. Although based on [98] studies, the results of both hard and soft material lenses are foreseeable, but we and [24] designers tried to solve manufacturing zone plate difficulties with different soft and hard plastic materials.

In [24] Fresnel zone prototypes, the designers have decided to use high-efficiency luminosity in feeding section at the expense of manufacturing problems and maintenance costs in lens platform to achieve high efficiency. However, the general purpose of our structure is concentrated to produce of a cubic cell with the ability of intended permittivity control in a homogeneous environment, which is entirely dissimilar and innovative for Fresnel lens treatments. Based on two types of radiation feed applied to both lens surfaces, as described in next sections, lenses out radiation has an entirely symmetric form, high gain, and high efficiency. Expected results compared to previously reported devices with similar type feeds, as shown in Table.3.1, is indicates the accuracy of estimated permittivity method for phase corrector zones designed with hard plastic cube-shaped cells. Regarding the mentioned results with two distinct material, the proposed design scheme has already answered the earlier problems with low efficiencies in a hard plastic slab (See Table. 3.1). Also, it has responded to the issues of manufacturing and keeping in services for the similar Fresnel type lenses in [24] with soft foam materials.

In the first prototype, a microstrip dipole antenna because of the easy and cheap manufacturing process is used to illuminate phase plates surface. For this purpose, the dipole antenna is designed to illuminates plates on xy-plane with radiation at z-direction and antenna parameters were optimized to have cos ^{10}-like radiation patterns with optimized antenna parameter. The proposed dipole

antenna geometrical dimensions are plotted in Fig.3.7(a,b). The simulated and measured results show a good impedance bandwidth over the operating band, as shown in Fig.3.7(c). Measured radiation patterns for the dipole antenna in $\phi = 0°$ and $90°$ planes at 60 GHz are plotted in Fig.3.7(d). As shown in Fig.3.7(d), the measured E- and H- planes radiation patterns are matched with associated $\cos^n$- like radiation pattern with $n = 7$ and 10 at 60GHz. These results certify that the determined η_{taper} theoretically for antenna is valid.

In the second prototype, a Cemex Millimeter, Inc. commercial V-band horn antenna is used to illuminate phase plates surface on xy-plane, as shown in Fig.3.7(e). The proposed antenna is a conical horn that operates from 58 to 68 GHz with 41 mm length and aperture dimensions of 40 mm. The horn is fed by a WR-15 waveguide with UG-385/U flange. This horn provides a 20 dB nominal gain and a typical half-power beamwidth of $16°$ in the E (xz)-plane and $20°$ in the H(yz)-plane. The horn also offers a typical side lobe level of -20 dB on the E-plane and -28 dB on the H-plane, respectively, with x-polarization level lower than -23 dB. The measured voltage standing wave ratio (VSWR) is 1.15:1, over the frequency range. Fig.3.7(e) show the proposed conical horn antenna. Measured radiation patterns of the conical horn antenna in $\phi = 0°$ (xz-plane) and $90°$ (yz-plane) planes at 60GHz are plotted in Fig.3.7(f). As shown in Fig.3.7(f), the measured E- (xz-plane) and H-(yz-plane) planes radiation patterns are matched with associated $\cos^n$- like radiation pattern with $n = 61$ and 45 at 60GHz. These results certified that the determined η_{taper} theoretically for this horn antenna is valid with slightly high η_{SP} because of the side lobe level.

Sequential cross sections ($xz-$plane) for electric field distribution were analyzed in CST set up for a focal plane as shown in Fig.3.8(a,b). Using CST software, 3D view of electric field distribution on the focal plane and lens surface is prepared to have the transversal and longitudinal $|E|$-field distribution as shown in Fig.3.8(b). Observing longitudinal representations of the electric intensity, the FZP_2 lens focal spot is narrow. Regarding this result in Fig.3.8(b), the focal distance is located at 132mm for both feeder. The FZP_2 lens output radiation beams on focal plane are presented in Figs.3.9(a), 3.9(b), and 3.9(c) at 57, 60, and 61GHz, respectively. As shown in these figures, the successful conversion of waves in a focal spot at 57 GHz, 60 GHz, and 61 GHz is observed. In Figs.3.9(d), and 3.9(e), the transversal $|E|$-field distribution on FZP_2 top surface for $\phi = 0°$ and $\phi = 90°$ are depicted. In this case, it shows the influence of the number of zones with phase change on the top surface of FZP_2. The photograph of the dielectric FZP_2 model is shown in Fig.3.9(f), which is obtained by ABS-M30 polymer plastic with $\epsilon_r = 2.76$, and $tan\delta = 0.059$.
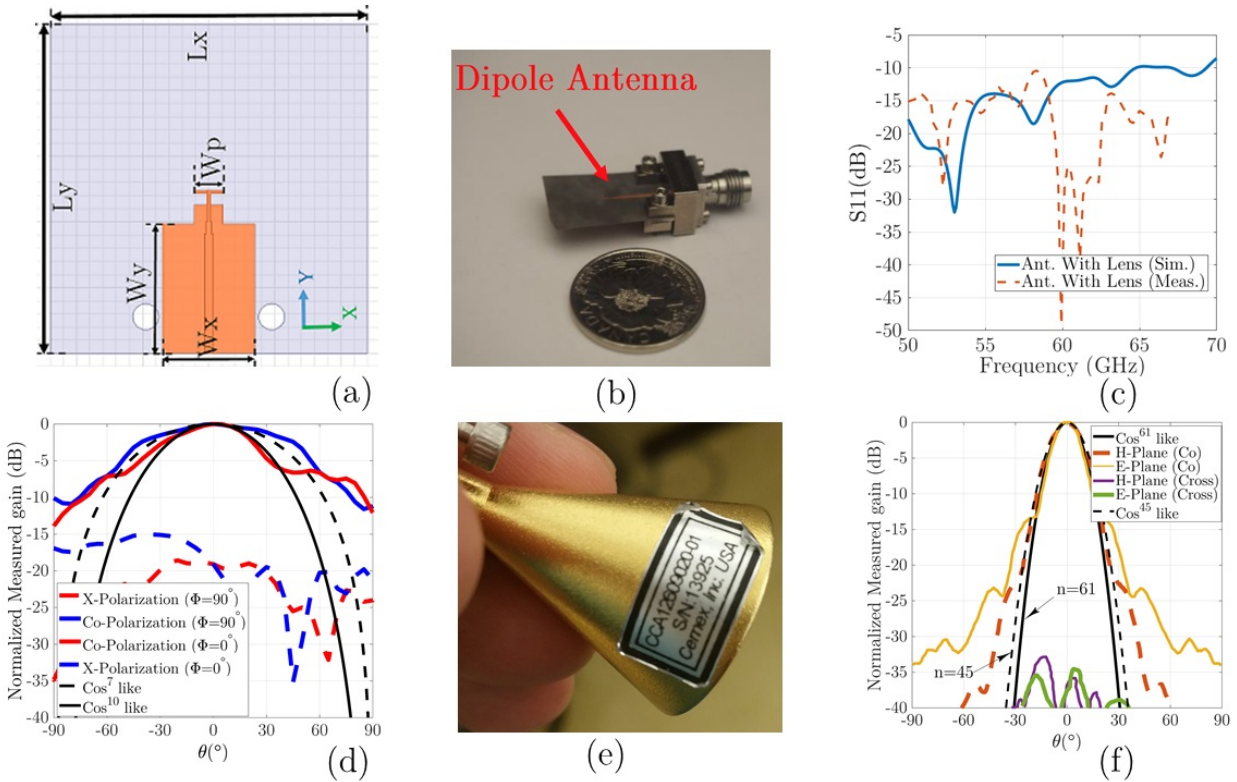
Figure 3.7 − **(a) Geometry of the proposed dipole antenna:** $L = 12$, $R = 6$, $L_x = 24$, $L_y = 24$, $W_x = 7$, $W_y = 9.8$, **and** $W_p = 2.2$ **(All in mm), (b) Fabricated dipole antenna; (c) The measured and simulated return loss for dipole antenna; (d) Measured radiation patterns for the dipole antenna and comparison with the associated** $\cos^n$ **like pattern at 60GHz; (e) A Commercial conical horn fed by WR-15 waveguide with UG-385/U flange; (f) Comparison of the conical horn antenna measured radiation pattern along** $\phi = 90°$ **(** yz**-plane) and** $\phi = 0°$ **(** xz**-plane) planes with the associated** $\cos^n$ **like pattern.**

In Figs.3.10(a-e), the simulated transversal profile for FZP_4 at the focal points are presented. The similar setup is used for the 3D view of the electric field distribution on the focal plane and lens surface. For FZP_2, the radiation beam has a 2.4° width, whereas for FZP_4 is 2°. This result shows the focusing of the wave is stronger for FZP_4 since the plate is composed more diffractive rings. In Figs.3.10(d), 3.10(e), the transversal $|E|$-field distribution on FZP_4 top surface shows the influence of the number of zones with phase change for $\phi = 0°$ and $\phi = 90°$, respectively. This $|E|$-field distribution for phase changes shows the effect of cube-shaped permittivity distribution of sub-zones. For the corresponding plots, all data are normalized with the maximum values. The analysis of the radiation beams of the $FZP_{2,4}$ phase plates follows a similar approach.

3.4   Half-wave and Quarter-wave zone plate Design Method

Two dielectric FZP lens antenna were fabricated using an additive manufacturing process including two different type plastic materials. To attain the best performance of the lens design, simulation analysis of dielectric FZP lens results by CST software was accomplished. Our review shows that the plastic lens structures with material porosity simplify the selection of the relative permittivity for lens fabrication in a homogeneous composition, yet with some design limitations. In some particular models, cube-shaped material porosity is examined to implement phase plates.

To conclude, the first lens design approach, the 3D printed planar FZP_2 plastic lens were built based on the FDM additive manufacturing process. In FDM printers, the lens model was created layer by layer by heating and extruding thermoplastic filament as follows. The photograph of the dielectric FZP_2 model is shown in Fig.3.9(f), which is obtained by ABS-M30 polymer plastic with ϵ_r =2.76, and $tan\delta$ =0.059. The intended plastic lens radiating aperture is composed of eight zones with a radius of 75 mm. The overall dimensions of the designed lens are $150 \times 150 \times 5mm^3$. Fig.3.9(f) shows the proposed lens sub-zones aperture with the plastic polymer cells. There are eight sub-zones for the plastic lens antenna to achieve $30\lambda_0$ diameter. The half-wave phase correction (with two relative permittivity (ϵ_r)) phase plate has a design frequency of $f_0 = 60$ GHz (wavelength $\lambda = 5$mm). The FZP_2 has a focal length $F \simeq 132$mm and lens aspect ratio of $F/D = 0.88$. These dielectric rings provide the half-wave phase correction over the entire aperture of the Fresnel-zone-plate. To solve multiple reflections issue, a lens with $h = \lambda$ thickness was designed with lower permittivity dielectric rings to obtain a better transmission performance and focus. This lens configuration has the advantage of flat shape on front and back surfaces. Dipole and horn antenna are used as a lens illuminator in yz-plane. Two dielectric relative permittivity used in the design of the FZP_2 zones typified as $\epsilon_r = 1.4, 2.76$ and $\tan\delta \simeq 0.05$. Both relative permittivities for dielectric sub-zones to satisfy the zone plate rules are designed with the optimized cube-shaped cells, with the help of (3.3) and (3.7), which are reviewed in Figs.3.3(b) and 3.4(a).

To conclude the second approach, the plastic FZP_4 was fabricated using the selective laser sintering method, by on-stock PA 2200 plastic, which is a non-filled powder based on PA-12. The PA 2200 is a nylon that is selected from EOS GmbH - Electro-Optical Systems (EOS) production list. The measured permittivity value for this plastic is ϵ_{PI} =3.6, which is a little bit higher than ABS-M30.
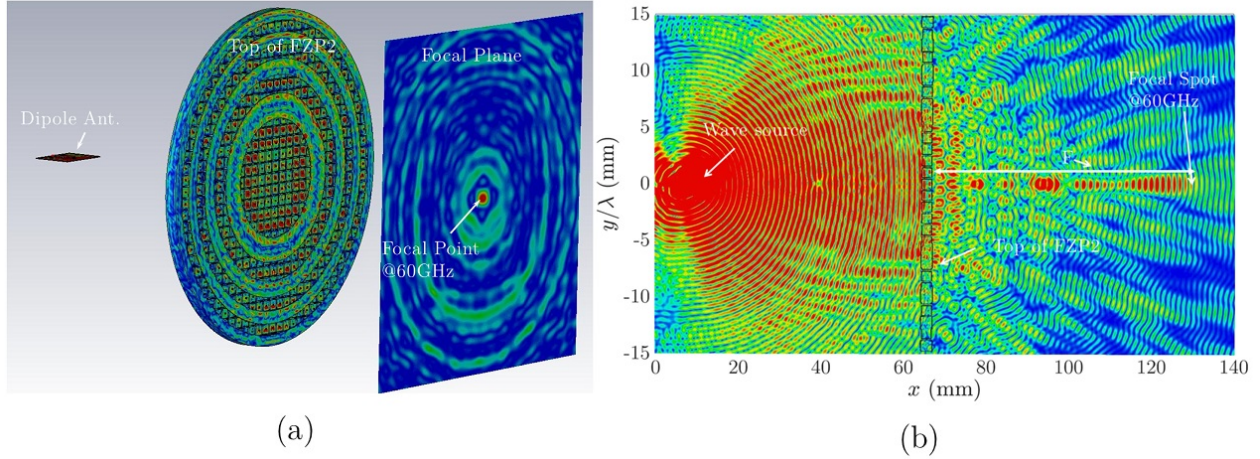
Figure 3.8 − **(a) Antenna setup for FZP antenna with E-field distribution on Lens surface and Focal plane; Longitudinal radiation output beam at the main focal point with dipole illuminator on** $yz-$**Plane;**
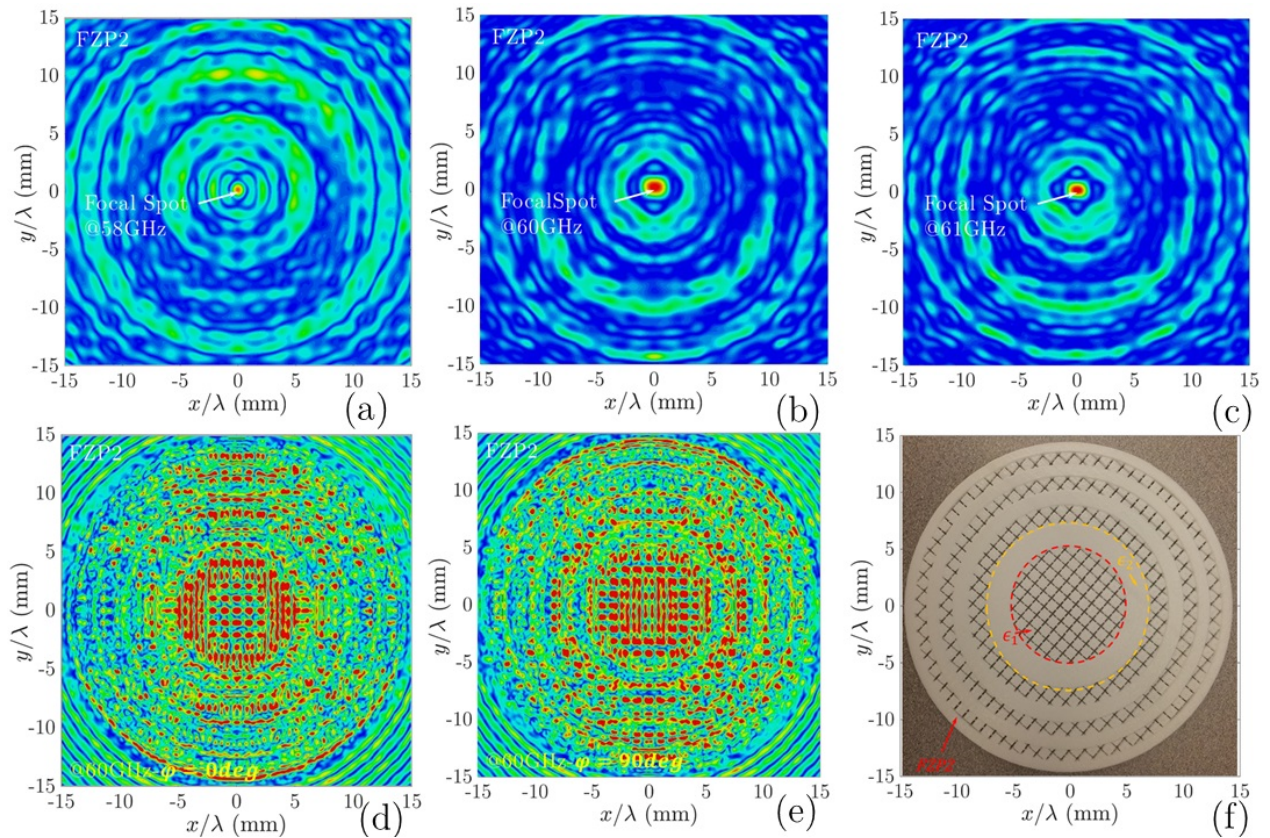
Figure 3.9 − **Transversal radiation output beam at the main focal point with dipole illuminator at: (a) 58 GHz; (b) 60 GHz (c) 61 GHz; Transversal** $|E|$**-field outputs for** FZP_2 **surface with dipole illuminator: (d)** $\phi = 0°$ **, (e)** $\phi = 90°$**; For the corresponding plots all data are normalized with maximum values. (f) The realized dielectric** FZP_2 **lens with ABS-M30 using FDM method;**

The four dielectric relative permittivity used in the design of the FZP_4 zones typified as $\epsilon_r = \{1.4, 2, 2.7, 3.6\}$ and $\tan\delta \simeq 0.06$. The dielectric ring radius of the FZP_4 is extracted with (3.3) to
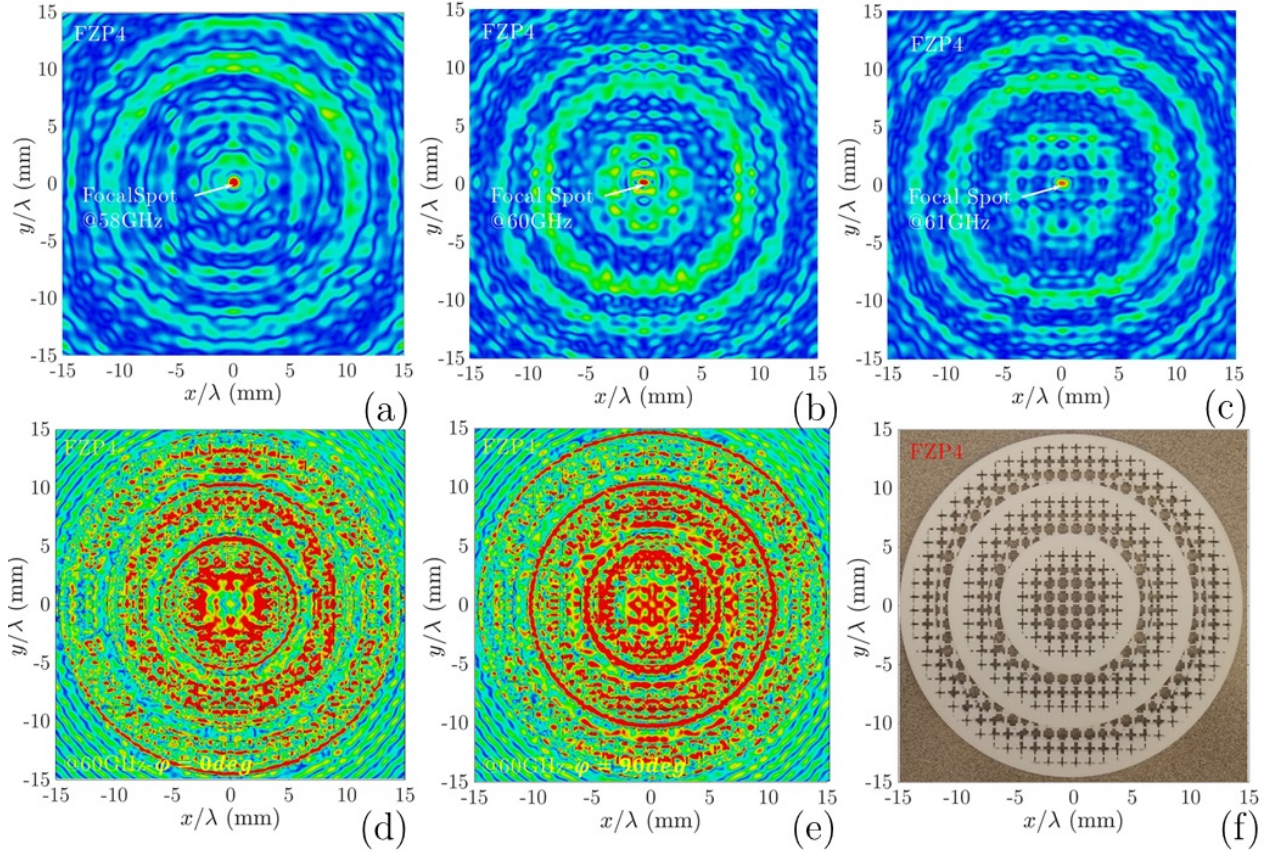
Figure 3.10 – **Transversal radiation output beam for the main focal point with dipole illuminator at: (a) 58 GHz; (b) 60 GHz (c) 61 GHz; Transversal $|E|$-field outputs for FZP_4 surface with dipole illuminator: (d)$\phi = 0°$, (e) $\phi = 90°$; For the corresponding plots all data are normalized with maximum values. (f) The manufactured whole dielectric FZP_4 lens with polyimide, using SLS method within twelve sub-zones, which is designed by material porosity reduction technique;**

achieve a quarter-wave phase correcting lens. The FZP_4 planar plastic lens aperture is composed of twelve zones with the whole radius of 75 mm. The quarter-wave phase correction (with four relative permittivity (ϵ_r)) FZP_4 lens, is shown in Fig. 3.10, has a design frequency of $f_0 = 60$GHz, and a focal length $F =$132mm. As shown in Fig.3.10, the realized lens is constituted by a solid ring, and three virtual permittivities created ring per full wave zone.

The simulation results show that the multi-relative permittivity zone plates hold on right permittivity tolerance which simplifies the lens design and manufacturing process. This permittivity tolerance for Polyimide (PI) that realized with cube-shaped cells is analyzed in Fig.3.3(b). The full design process of the draft FZP_4 lens is created with PI plastic.
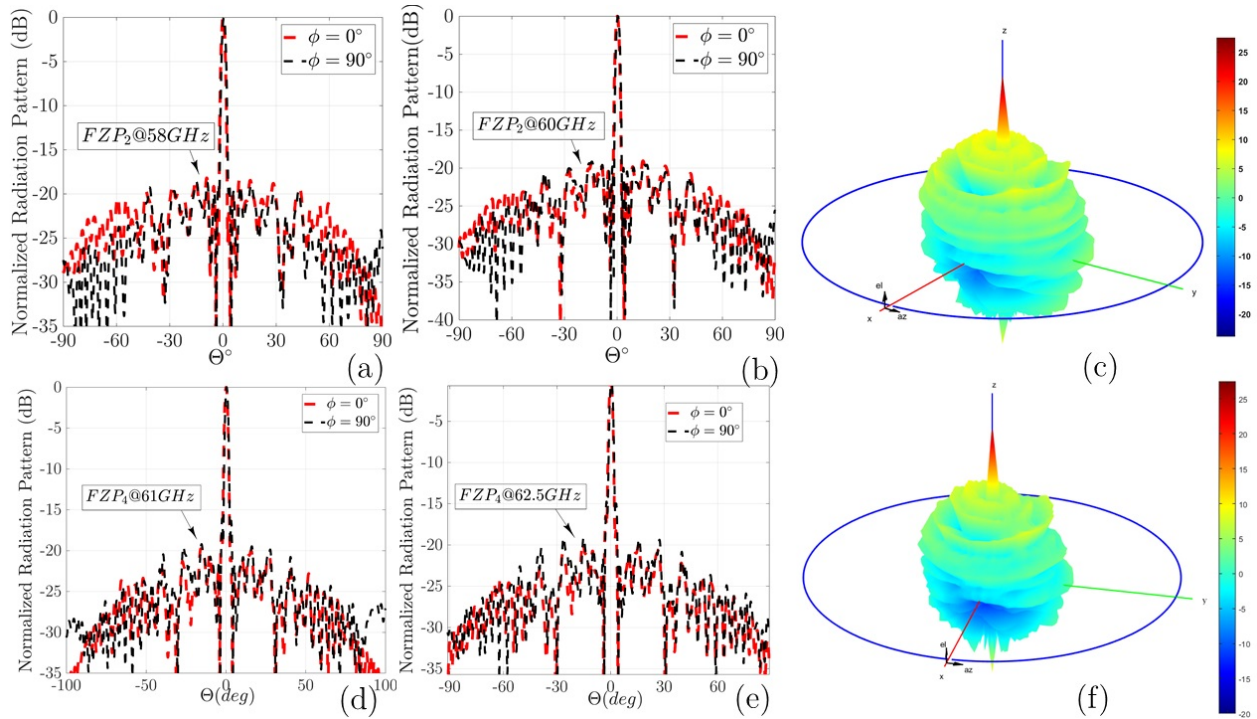
Figure 3.11 − **Measured radiation patterns in $\phi = 90°$, and $\phi = 0°$ for FZP_2: (a) 58 GHz. (b) 60 GHz. (c) 3D plots of far-field radiation patterns; Measured radiation patterns in $\phi = 90°$, and $\phi = 0°$ for FZP_4: (d) 61 GHz. (e) 62.5 GHz. (f) 3D.**

3.5   Experimental results and discussions

The measurement process for these antennas was performed in an anechoic chamber using the OML millimeter-wave standard modules with both illuminators. In this step, two customized FZP_2, and FZP_4 plastic lenses, Agilent E8361A PNA Network Analyzer, the OML millimeter-wave modules, a 60 GHz dipole antenna, and a V-band conical horn antenna are used as measurement components. Aligning the feeding aperture of the FZP lenses to the illuminator for measurements is a critical point at 60 GHz. Then, the plastic fixture is used to the fix the proposed lenses between the illuminator and reflector. The measured results for the radiation patterns for both ZPs are plotted in Figs.3.11. The impedance bandwidth of the proposed FZPL antennas for dipole illuminator is measured using the Agilent E8361A network analyzer, as shown in Fig.3.12, which covers the $55-65$ GHz operating bandwidth. For the first FZP_2 lens simulation, the maximum directivity is 27.6 dBi at 60 GHz, and the realized gain is higher than 25 dBi in $58-64$ GHz. The FZP_2 lens measurement results show that the maximum gain is 26.3 dBi at 60 GHz, and the measured gain is greater than 24 dBi in the $57-64$ GHz impedance bandwidth. The simulated and measured 2-D and 3-D radiation patterns over the operating band for both lenses are shown in Fig.3.11(a-
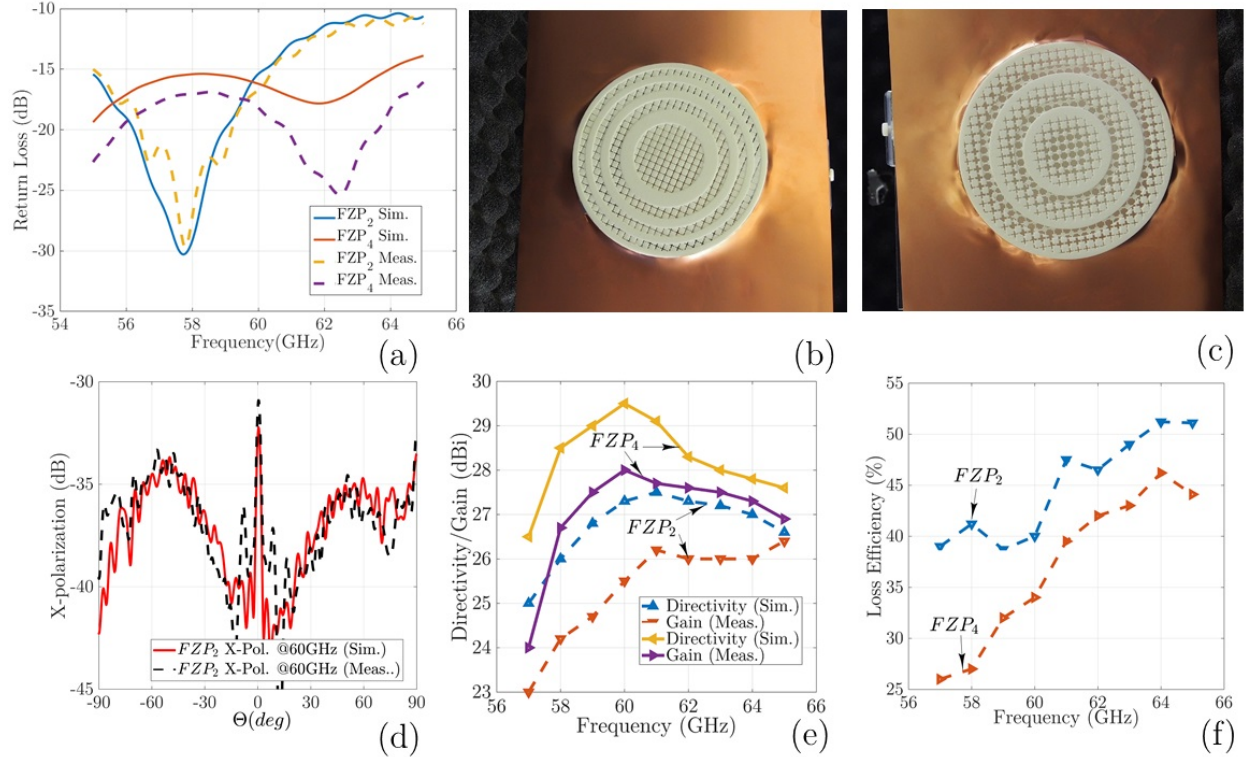
Figure 3.12 – (a) Simulated and measured return loss results for $FZP_{2,4}$ lens antennas;(b) Fabricated FZP_2 lens with metal sheet holder; (c) Fabricated FZP_4 lens with metal sheet holder; (d) Measured and simulated x-polarization level with foam and metal sheet holders; (e) Simulated directivity, and measured gain for $FZP_{2,4}$ lens antennas with dipole illuminators (f) The loss efficiency for $FZP_{2,4}$ lens antennas;

f) for $E(xz$-plane)- and $H(yz$-plane)- planes. The dipole antenna is optimized to have n=10 like radiation patterns to analyse proposed design spillover for similar diameter lens for both n=10 and n=61 radiation patterns. With constant diameters and analysis of the spillover and efficiency for different illuminators, the estimated n range for illuminators is approximated experimentally. The approximated n for $\cos^n$-like radiation patterns is equal to the average of n=10 and n=61, which is equivalent to 35. This number is very close to our analysis, as shown in Fig.3.6, to achieve optimum efficiency.

For both lens prototypes, the main radiating lobe keeps pointing as a pencil beam at the boresight direction over the operating band frequency. As shown in Fig.3.11, the half-power beam widths of the proposed FZP_2 and FZP_4 are 2.2° and 2°, and the side lobe levels are -20 dB, and -18 dB, respectively. The FZP_4 measured SLLs in the E-plane are below -18dB at 58 GHz, and 60 GHz, respectively. The E- and H-plane radiation patterns are symmetrical because of symmetrical structure of the lenses. Fig.3.11 shows the normalized measured radiation patterns at 58
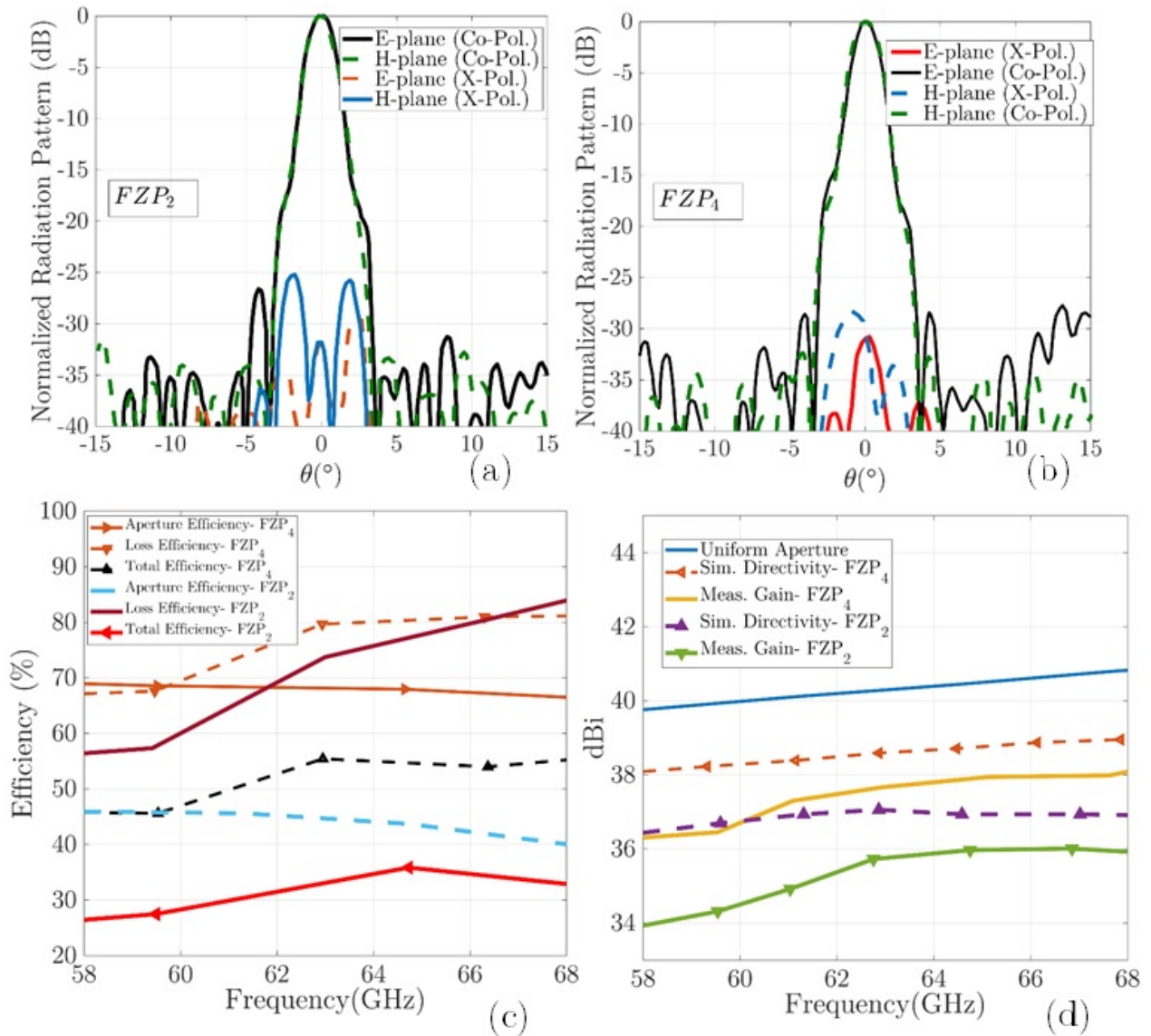
Figure 3.13 − **The normalized radiation patterns along E- and H- planes at 60 GHz performance with conical horn feed: (a) FZP_2, and (b) FZP_4 lenses; (c) Simulated and measured gain and directivity versus frequency; (d) illustration of the proposed lenses efficiency versus frequency;**

GHz and 60 GHz. The calculated 3D radiation patterns at 60 GHz, are shown in Figs.3.11(c), and 3.11(f) for FZP_2 and FZP_4, respectively. In the main lobe, the cross-polarization level in the E-plane are less than -24 dB, and -27 dB for FZP_2, and FZP_4, respectively. Figs.3.11(b),3.11(c), and measured results show good agreement, which is support our analysis and design. Simulated and measured return loss results for $FZP_{2,4}$ lens antennas for dipole illuminator are plotted in Fig.3.12(a). Fig.3.12(b-c) shows experimental measuring setup for Fresnel lenses which are surrounded by metal sheet screen. The cross-polarization for this structure is lower than -33 dB, as

shown in Fig.3.12(d). The simulation analysis shows a relatively good stability of the gain over the operating frequency with a gain difference of 2 dB. The results indicate, by inserting of additional phase correction zone $q > 2$ to optimizing of the radiation pattern, much higher gain for $q = 4$ lens is achieved. According to the obtained results for both lenses, the radiation pattern is very directive, i.e., a low SLL and a narrow beamwidth, which certify the design process. The cross-polarization for the FZP_2 structure is around -33 dB, which is low for all lens structures, as shown in Fig.3.12(d). The proposed antennas directivity, gain, and loss efficiency calculated as shown in Fig.3.12, small lobe at $\theta = 0°$ is observed.

During the measurement process, the intended dielectric lenses are surrounded by a metal sheet to reduce SLL for dipole feed with cos^{10}-like radiation patterns from an Omni-directional antenna. Our studies show that by using metal sheets for low n<20 value, low SLL is obtainable. However, because of spillover for Omni illuminators by utilizing the metal sheets, the reflected waves from metal sheets around the lens will be focused at one point, and the combination of reflected and incident waves will produce small lobe in x-polarization, which is -33dB lower than the primary beam.

Simulation results show that with decreasing the width of this surrounded metal sheet around λ_0 at operating frequency, both low SLL and low lobe effect in x-polarization are solvable. During the simulation, the metal sheet thickness attributed to the increase in mesh number is not considered. For this reason, the simulation and measurement results with the surrounded foam sheet are also added in a revised version, which certifies our analysis as regards the combined results of reflect and incident waves. This lobe is eliminated in foam measurements, and the cross-polarization level is under -37dB, as shown in Fig.3.12(d).

Fig.3.13 (a-d) shows a comparison between measured and simulated performances of the conical horn feed FZP_2, and FZP_4 lenses. Figs.3.13 (a,b) shows the normalized radiation patterns with cos^n-like feed conical horn at 60 GHz in E(xz)/H(yz) planes. As the obtained results, the E/H radiation patterns for conical horn feed are very directive, i.e., low SLLs and a narrow beamwidth. The cross-polarization for the FZP_4 with horn feed is around -29 dB, and for the FZP_2 is -25 dB. As shown in Fig.3.13, the half-power beamwidth of the proposed FZP_2, and FZP_4 is 2°, 1.8° , respectively, and the side lobe level is -25 dB, -26 dB, respectively. The FZP_4 measured SLL in the E-plane is below -26 dB at 60 GHz.

The E- and H-plane radiation patterns are symmetrical because of symmetrical structure of the lenses, and conical horn. During the measurement process for horn feed against dipole feed, a metal sheet is replaced with a Rohacell foam (ϵ_r=1.04) supports to consider foam base measurements also. In the main lobe, the cross-polarization level in the E-plane is less than -28 dB for both FZP_2, and FZP_4 zone plates, respectively.

The proposed antenna directivity, gain, and efficiency in Fig.3.13(b) and 3.15(c), and measured results show a good agreement, which validates the proposed design. As we expected, the measured gain and simulated directivity of the FZP_2 lens are lower than FZP_4. As shown in Fig.3.13(b) the FZP_4 maximum measured gain is 38 dBi at 65 GHz, whereas the FZP_2 maximum measured gain is 36 dBi at 64.2 GHz with variations of less than -2dB over operating band for both of them. Fig.3.13(b) shows the comparison gain and directivity of both lenses with uniform aperture (orange dash-line) directivity also. In Fig.3.13(c), three kinds of efficiency for conical horn feed FZP_2 and FZP_4 zone plates are presented as follows: aperture efficiency, loss efficiency, and total efficiency. In this study, aperture efficiency is the comparison of the maximum directivity of a uniform E-field (amplitude and phase) aperture of similar lens dimensions with the maximum simulated directivity of the lens using CST software. The measured loss efficiency is the comparison of the maximum simulated directivity with the maximum measured far-field gain of the antenna, and the total efficiency is the product of the aperture and loss. Fig.3.13(c) shows that the measured aperture efficiency for FZP_4 is 58%. By contrast, the measured aperture efficiency of FZP_2 just reaches 37%. The achieved directivity difference between the uniform aperture and FZPs indicates that a better overall efficiency for the proposed lenses with the low-SLL-optimized horn or another type of manufactural illuminator is possible. Table 3.1 shows the comparison of the proposed design performance to previously reported works with the homogenous medium platform.

According to [10] analysis, the rod size of cube-shaped cells was fixed near to $\epsilon_{air} = 1$ to connect provided cubes to realize sphere form, and the cube vertex size, as a filling ratio parameters, was used to achieve 1.1 up to 1.4 permittivities to satisfy lens rules. In this design scheme, the provided loss tangent deviations for layers were not close together, which cannot show the spherical lens's performance ideally, especially for millimeter wavelength applications. This issue shows itself as a 7dB gain drop over the operating band. However, the results and performance are very well at 10 GHz, and it can apply to the microwave industry as a new method to manufacture a large number of layers quickly and reduce total fabrication costs noticeably.

However, in previously reported work [12], both rods' thickness and cube sizes are analyzed together to solve this issue. This analysis is done based on the ceramic stereolithography material with a dispersion diagram analysis for rod size vs. cube size. In this scheme, a logical area for the cube cell is provided to control virtual permittivity based on permittivity and loss tangent, which helped the designer manufacture an extended 3D Lunenburg lens near the ideal lens with the 2dB gain drop. Based on this information, we presented two types of quarter-wave and half-wave zone plates' antennas with the above techniques. To our knowledge, our prototype design has not been analyzed and reported before.

In our model, the rod thickness is fixed near air permittivity at 60GHz. Based on our analyses for virtual permittivity implementations with HFSS and exponential approximations, the intended permittivity is given. The second approach is based on distinct rod thickness because the planar form of ZP plates was not possible as it can make our lens corrugated and result in difficulty of fabrication. For this reason, based on full dielectric zone plate rules, an FZP_2 and FZP_4 has been designed, manufactured, and measured. We presented a full dielectric zone plate with the cube-shaped cell. The ZP's permittivity deviations are not radial like those of the Lunenburg or half Maxwell fisheye lens, and the lens performance is directly relative to zone permittivity and thickness. All this information has been added to our design, and constant rod size method has been chosen for these reasons.

The multiple reflections of the plate because of the high permittivity zones and the thick zone plates are conventional in zone plate structures. To reduce these reflections in our plates, a thicker lens using smaller effective permittivity zones has been designed to produce the intended phase shift with lower attenuation. There are three reasons for the choice of this thickness with these cube cells: First, this increased thickness allows us to reduce the multiple reflections of high permittivity zones. Second, the implementation of low permittivity zones with low permittivity cube cells will be possible. Third, the designed lenses will achieve the required mechanical resistance due to the spatial state of construction. Therefore, the design of half and quarter-wave Fresnel zone plates using cube-shaped material porosity at 60 GHz will be possible.

The simulation and measurement results for these plastic zone plates certify them as an alternative prototype for conventional planar lenses. In addition, it is evident from results that additive manufacturing (ADM) process has significant potential with the combination of other technolo-

Table 3.1 – Summarized comparison with earlier reported works

Table.I. Summarized comparison with earlier reported works					
Antenna Type	η_{Total}	**Technology**	**Lens Type**	**SLL**(dB)	**Freq.** (GHz)
Metal Reflect-array [21]	30.2%	Full Metal	Homogeneous (Metal)	-22	75
Perforated $\lambda/4$ FZP[92]	33%	Full Plastic	Homogeneous (Plastic)	-22	30
Reflector-type $\lambda/4$ FZP [86]	43%	PCB	non-Homogeneous	-20	10
Our FZP_2	36%	3D-FDM	Homogeneous (Plastic)	-25	60
Our FZP_4	56%	3D-SLS	Homogeneous (Plastic)	-25	60

gies to contribute zone plate lens structures. It is also interesting to mention that according to our knowledge, the proposed lenses have been the first designed structures with this porosity controlling technique with cube-shaped cells, which is an alternative method to develop planar lens structures.

3.6   Conclusion

In this work, a new gradient refractive index FZP using dipole and horn antennas as lens illuminators have been presented. These FZP antennas in two and four phase correction sub-zones have been implemented with the homogeneous plastic material to realize inhomogeneous scheme. Two type of additive manufacturing process has been used to construct the proposed plastic lenses. The 60-GHz planar FZP lens antenna has been proposed for high-gain applications at millimeter-wave bands. The performance of the realized antennas has been measured in an anechoic chamber. Both analytical and measurement analysis show that the selection of the relative permittivity and lens fabrication with a homogenous material simplifies the realization of inhomogeneous lens schemes. The measured results have reasonably validated the proposed plastic based realization of multi-dielectric lens structures. Furthermore, it certifies the additive manufacturing (ADM) process as an alternative method to contribute zone plate lenses.
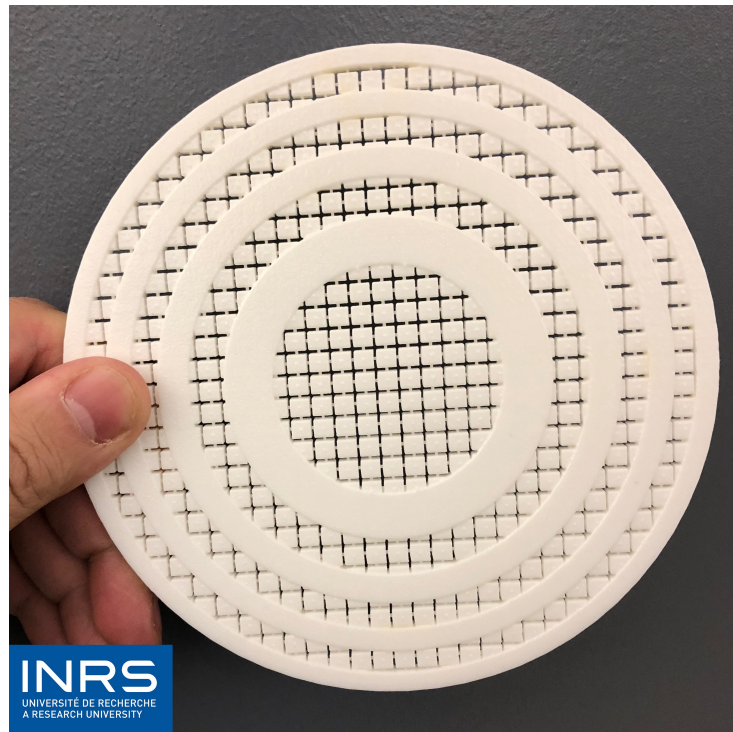
(a) Top view
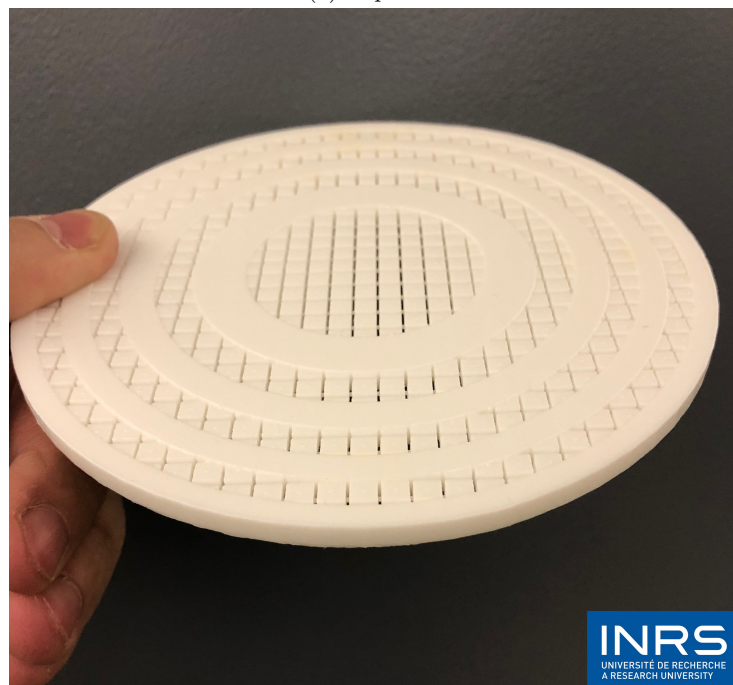
(b) Side view

Figure 3.14 − Photograph of the fabricated FZP_2 Lens (a) Top view, (b) Side view;
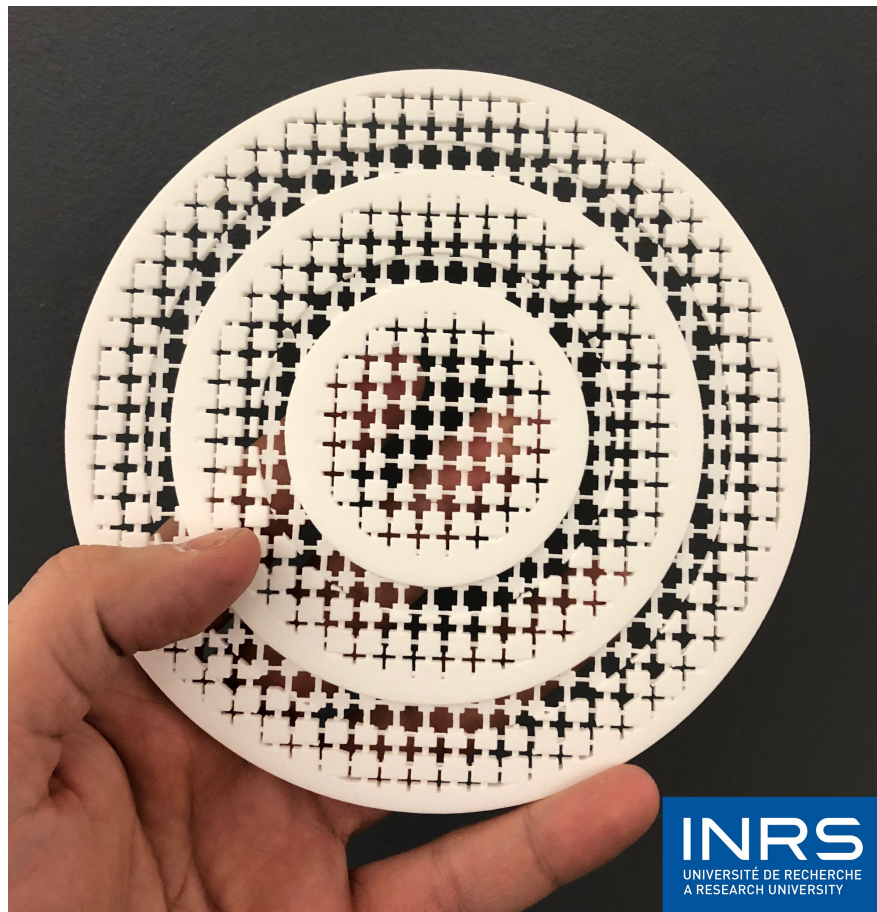
Figure 3.15 – Photograph of the fabricated FZP_4 Lens (a) Top view;

Chapter 4

Modification of plastic material to create mmWave tailored Lüneburg lens

This chapter has been taken partly from author submitted article with the similar title to IEEE TAP-CPMT.

This chapter present a 3D printed cylindrical full dielectric Luneburg lens antenna with physical porosity control to achieve intended permittivity of subzones in homogenous framework is presented for millimeter-wave applications. The microstrip dipole antenna with Cos^{10}-like radiation patterns is used as lens illuminator inside a parallel-plate waveguide operating in V-band. The intended gradient refractive indices are achieved using material porosity control in air-hole-based approach through the homogeneous medium to satisfy the required lens focusing rules. The air-hole radius is used to control the predetermined permittivity according to the presented lens focusing rules. To achieve this goal, the numerical analyses and approximations are performed to define the intended air-hole radius concerning the wave launcher illumination between parallel plates in TEM mode. The proposed porous lens with the air-hole approach is fabricated using polyimide 3D printing material with the whole thickness of $\lambda_0/2$ and $\epsilon_r = 3.4$. Selective laser sintering is the fabrication method utilized to manufacture this framework. The simulations and experiments verify the suggested designs method and results.

4.1 Introduction

Material porosity, due to its excellent capabilities to control effective permittivity widely used to achieve homogeneous framework gradient index (GRIN) media [1, 11, 93] to design new microwave devices. Up to now, with the development of additive manufacturing processes, a wide range of efforts to achieve GRIN distributions that are suitable for focusing lens design applications are ongoing. Material porosity control with host medium deforming has attractive electrical properties that can be applied to realize homogeneous and inhomogeneous lens devices [1, 94, 95]. GRIN lens implementation in a homogeneous medium using porous framework has been introduced as an alternative to traditional dielectric ones, where permittivity effects are controlled throughout the lens radius or volume rather than relying on a dielectric interface medium. Related studies on GRIN lens structures, such as Luneburg lens [7, 53, 1, 87, 35] and half-Maxwell Fisheye lens (HMFE)[93, 94, 95], are particularly focused on permittivity effects control with planar or 3D structures to satisfy lens focusing rules. The Luneburg and half-Maxwell fish eye (HMFE) GRIN devices are the most prominent examples of gradient-index optics that can be executed with material porosity at microwave and millimeter-wave frequencies for beam shaping and high gain antenna applications. The refractive index profile of both Luneburg and HMFE lenses decrease radially between $1 \leq n_r \leq \sqrt{2}$ [1]. As we now, the Eq. 4.1 gives this distribution as follows [10, 51, 52]:

$$n(r) = \sqrt{\epsilon_r \mu_r} = \sqrt{2 - (r/R_{Lun})^2}, (0 \leq n_r \leq R_{Lun}), \qquad (4.1)$$

where r is the radius of the sub-zones, ϵ_r is the host medium permittivity, μ_r is the permeability of host medium which is equal 1 and R_{Lun} is the lens radius. Based on the optics theory, The Luneburg lens is a spherically symmetric GRIN medium [51, 52]. Various classes of wave launchers, such as the horn antenna and coaxial-to-waveguide launchers, are applied as a primary source, to illuminate the proposed lens surface, which can increase the antenna size [87, 88]. In recent years, related studies have focused on a combination of wave launchers as a microstrip line, with the control being a microstrip line width in a metamaterial cell design [89], to achieve the intended permittivity of each subzone [93, 94, 95].

In the permittivity control approach that is based on porosity, the principle of the effective medium theory [5, 4] is used to design GRIN devices [1], and periodic porous unit cells, with the

dimension of about a one-tenth wavelength, are used [89]. Due to their small size, this cell analysis can be treated accurately with this theory, in the combination of experimental measurements, to produce the expected dielectric permittivity. In the predetermined GRIN devices, each subzone of unit cells can be introduced independently. In this design, a modified form of porous GRIN lens antenna, with polyimide nylon-based plastic in a parallel plate waveguide ($\parallel$), and a combination of a planar feeding platform for 60 GHz applications, is performed. The suggested plastic lenses have a cylindrical structure with a $13\lambda_0$ diameter fed with a $\cos^{10}$-like pattern dipole antenna as lens illuminator. This antenna is used to supply the surface of the lens as a point source in quasi-TEM mode. The dielectric lens antenna comprises three main blocks as follows: (i) 3D printed porous lenses, (ii) dipole antennas, and (iii) parallel plates waveguides.

The air-hole-based approach, in material permittivity control, is employed to control effective permittivity in a homogeneous medium in lens prototypes. After a detailed analytical analysis of lens parameters, the additive manufacturing technology (ADM)[35] is employed in the manufacturing process with the selective laser sintering (SLS) [35] method. The produced homogeneous lenses are realized using polyimide plastic, with a relative permittivity of $\epsilon_r = 3.57$ and loss tangent of $\tan\delta = 0.06$ at 60GHz (the recommended material 10GHz measured permittivity was 3.8). The air-holes optimum value radius is determined through analysis to realize the intended synthetic permittivity in a homogeneous medium. The planar dipole feed recommends an excellent matching to the symmetric geometrical position for perforated Luneburg lens focal points on its surface [94, 87]. Through a homogeneous design approach, the mismatching problem between subzones is solved, and excellent performance for both lens structures in radiating high-directivity beams for high-performance millimeter-wave lens antenna utilization is provided.

4.2   3D Printing Processes, and Materials

3D printing is a type of additive manufacturing process that can realize 3D objects created layer by layer printing from the bottom up with predefined materials [96, 35]. The term additive manufacturing (ADM) holds within such technologies as rapid prototyping (RP), layered manufacturing, direct digital manufacturing (DDM), and 3D printing [38, 35]. Between all of these processes there is no difference, and they are synonyms for the same process. This technology, because of a low fabrication cost, high scalability, ease of implementation, and combination of both metal and di-
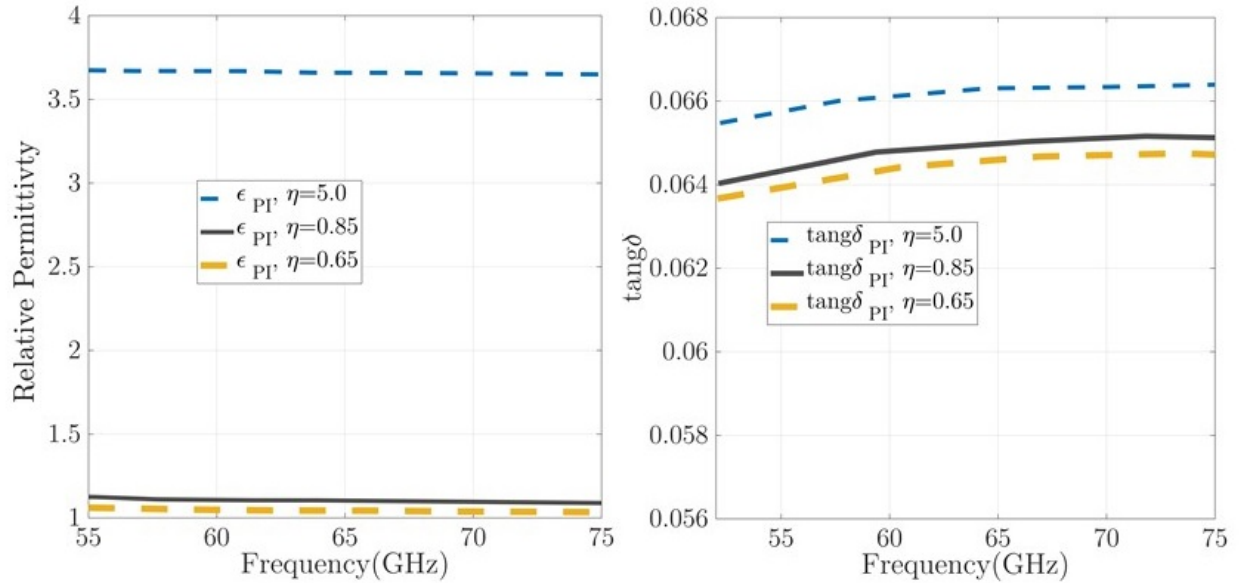
Figure 4.1 – **The extracted metarial characterization for Polyimide samples in V-band waveguide measurment set-up to obtain essential material properties:** (a) (ϵ_r) and (b) $\tan(\delta)$.

electric materials, has attracted great attention for production [35]. Moreover, this technology can be considered a green technology and an alternative to traditional laminating fabrication methods. This material jetting process can realize 3D-created objects by adding predefined materials layer by layer. Also, being able to shape the materials into both flexible and rigid forms, as needed with 3D printing technology, is another capability of this technology [35]. Accordingly, this design freedom can be applied to realize material porosity based devices which are impossible or difficult with conventional methods, especially GRIN device prototypes.

To realize printed compositions with material jetting technology with either metal or dielectric materials, the first step is the producing and slicing of the models in digital form. The patterning of this 3-D prototype model after designing it with 3-D software is sliced in digital form and transformed to the printer for prototyping. This software-using manufacturing device can prepare $100\mu m$ thick accurate layers for printing, but this accuracy varies from device to device, and from technology to technology. This dielectric-designed pattern can be achieved layer by layer, with a 3-D printer, called printing resolution. The prototyping resolution up to the printers is different from technology to technology, but the standard layer thickness is 100 - $150\mu m$ and the high definition layer thickness is around $60\mu m$.

$\eta = 0 \qquad \eta = 1.5 \qquad \eta = 2.6 \qquad \eta = 4.5 \qquad \eta = 5$
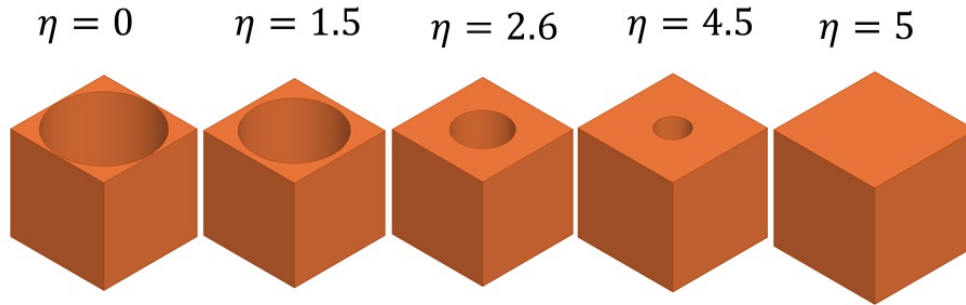
Figure 4.2 – The primary geometrical porous structures that determine our lens subzones;

However, the printing accuracy is $\pm$ 0.3% (with a limit of $\pm$ 0.3% tolerance) and realizing structures with element sizes lower than λ for V-band frequency is possible for antenna engineering. Also, because of the possibility of using different relative permittivity materials, such as PLA, polyimide, and ABS-M30, a wide range of refractive indices to actualize GRIN structures using porous frameworks are feasible. Since identifying the amount of the dielectric coefficient of the host environment for the desired frequency range was one of the cutting points in controlling and constructing of porous structures. For this reason, the intended $3.7 \times 1.8 \times 5$ mm^3 polyimide sample has been used to fill spacer of V-band waveguide measurement setup and extract expected material characteristics before design GRIN structure, as shown in Fig. 4.1. In the proposed design, the SLS manufacturing process is utilized for the manufacturing of cylindrical porous Luneburg lens. An SLS printer as a prototyping device is used in realizing the presented designs.

4.3 Virtual permittivity design based on air-hole porous approach

The 3D graded indices lenses are intended for additional full-wave numerical electromagnetic simulations at 60GHz. Based on effective medium theory, we can determine the permittivity of these subzones virtually based on the control of host medium porosity. Therefore, we suggest Lunenburg lens model with this technique. Both lens subzone profiles are divided into $3 \times 3 \times 3mm^3$ cells, each designed in plastic with cylindrical air holes. Each layer is formed of intended virtual permittivity arrangements of cubic cells, and as a result. The lenses as mentioned earlier are obtained from dielectric cells in the homogeneous platform to get a broad frequency operating range. The presented airhole porous approach [6, 26] was employed on polyimide concentric circular zone by selective laser sintering (SLS) [38]. We developed this modeling to satisfy Luneburg permittivity of layers by Eq.4.1 at 60GHz with porous cells as shown in Fig.4.2. The full-wave analyzed hole
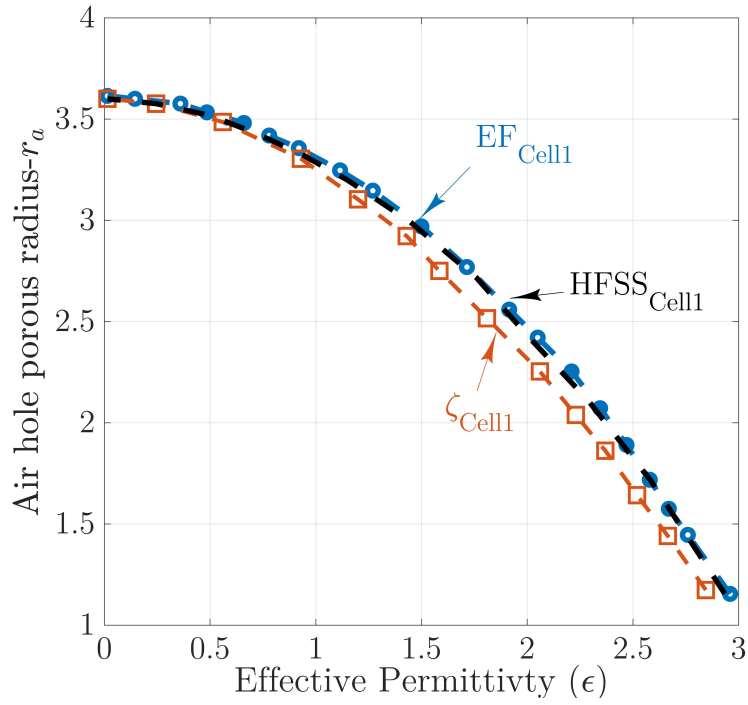
Figure 4.3 − Illustration of polyimide effective permittivity differences versus the Airhole porous cell radiuses-r_a defined as $Cell_1$;
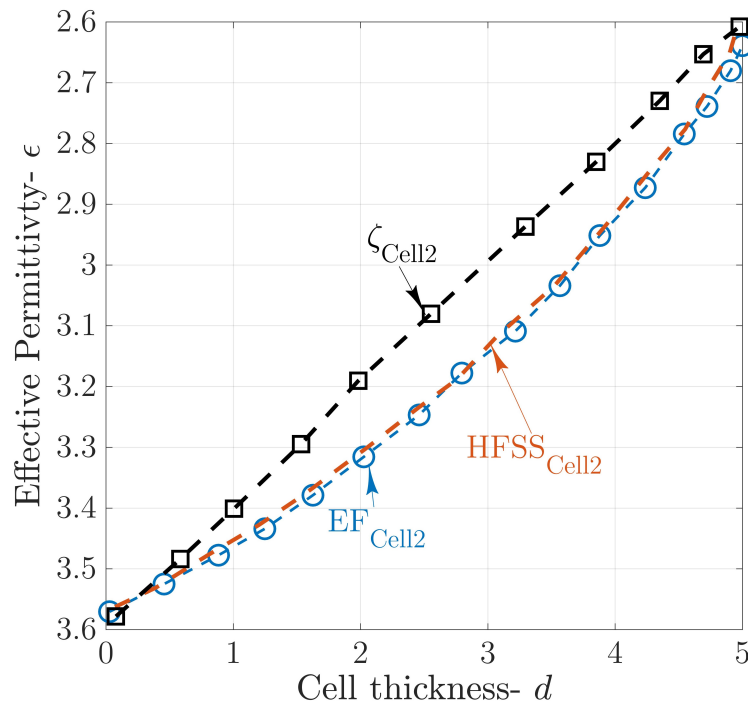
Figure 4.4 − Illustration of polyimide effective permittivity variations versus the Airhole porous cell thickness -d defined as $Cell_2$ for the constant hole radius at 2.5mm;

$\eta = 0 \qquad \eta = 1.5 \qquad \eta = 2.6 \qquad \eta = 4.5 \qquad \eta = 5$

(a) The primary geometrical porous structures that determine our lens subzones for distinct η filling ratio values;

(b)

(b)
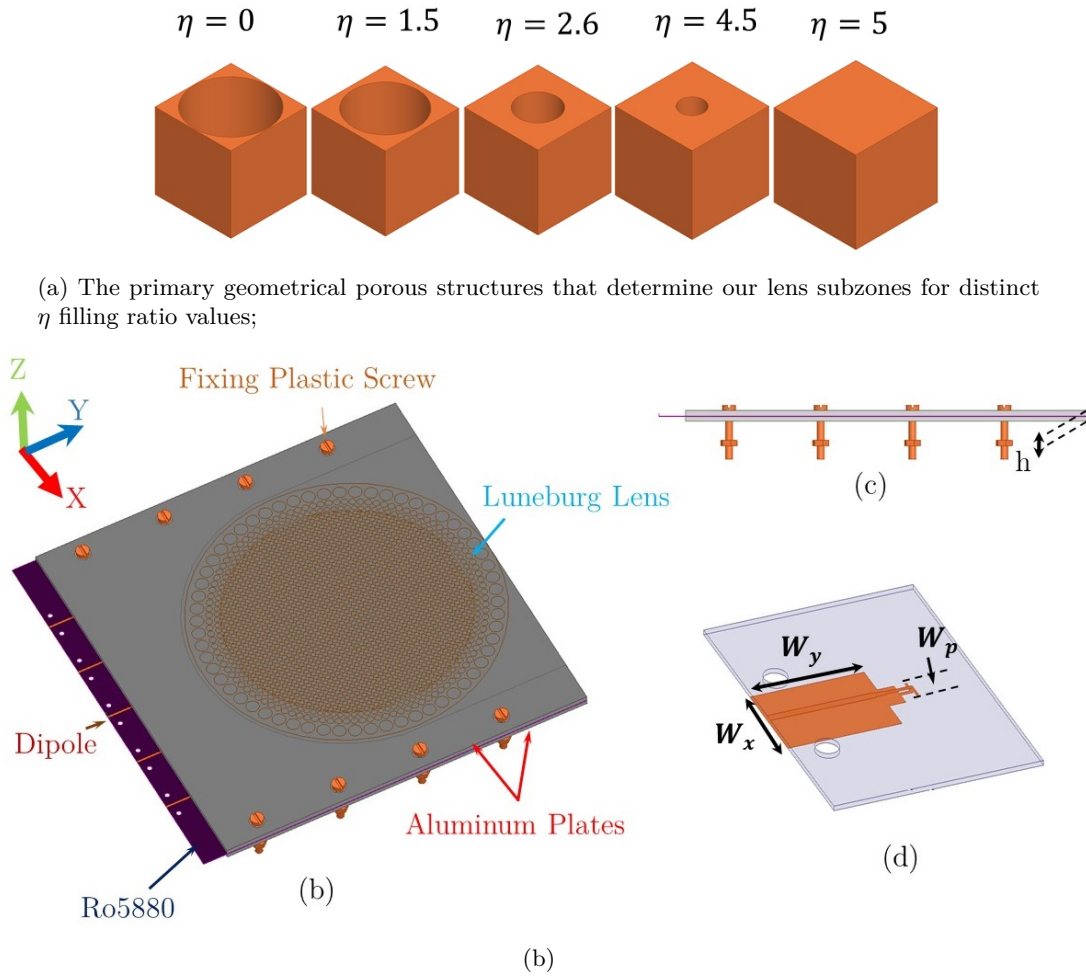
Figure 4.5 – **(a) The primary geometrical porous structures that determine our lens subzones; (b) Total antenna system, (c) side view, (d) Geometry of the proposed beam launcher:** $L_y = 24$, $W_x = 7$, $L_x = 24$, $h = 3$, $W_y = 9.8$, **and** $W_p = 2.2$ **(All in mm);**

radius in HFSS setup is used to complete intended zones scheme with perforated dielectric cells as shown in Fig.4.2. Overall air-hole radius is formed with polyimide [38, 26], which is preferred from EOS material list for click and print technologies [38],[11] to achieve expected refractive index (n_r) ranges. Two types of cells with thick and thin cells are used to control permittivity. The full radius of these holes for both dielectric materials is 5mm, as shown in Figs. 4.3 and 4.4, which r is the radius of the perforations, and d is cell thickness.

By tuning each air holes' radius r, the demanded virtual permittivity cell dimensions is provided. As we assumed in this perforated form, with increasing the radius of the perforations in charge of the filling-ratio, a lower permittivity compares to host medium properties near air permittivity (ϵ_{Air}) is attainable. To reach each lens' sub-zone geometry, the calculated air hole radius is utilized

to actualize each zone modeling given by Eq.4.1. The employed intrinsic relative permittivity for Polyimide plastic is ϵ_{PI}=3.6. The out of the desired cell changes is shown based on the radial (r_a) variations of the air holes and their thickness (d) to reach the range of possible permittivities, as shown in Figs. 4.2, 4.3.

As presented in the 3-D cells control scheme in Fig. 4.2, two types of cells can be formed with this approach to control material properties with distinct heights or radii. In mentioned steps, with considering permittivity variations and the perforated holes' radius as a group of known information, such as G1:($x_0 = \epsilon_{Air}, y_0 = \zeta = 0$), G2:($x_1 = \epsilon_m, y_1 = \zeta = 1$), a new holes' size is achievable using linear interpolation. Therefore, the air-hole cells' effective permittivities based on volume reduction are approximated using linear interpolation given by Eq.4.2 [11],

$$\epsilon_r = \epsilon_{PI}.\zeta_{PI} + \epsilon_{Air}.(1 - \zeta_{PI}), \tag{4.2}$$

where ϵ_{PI} is the host medium permittivity. Figs.4.2, and 4.3 shows the proposed air porous cells radius and height vs. effective permittivity results, respectively. Besides, new materials' intrinsic permittivity is a critical design feature for final cell radius. For this reason, a separate investigation should be conducted for particular dielectric substances. The obtained results reveal that the radius and thickness differences opposed to intended permittivity have non-linear variations. Therefore, an additional full wave simulation-based analysis is demanded to increase expected virtual permittivity truth [11]. In a related investigation, Ansys HFSS full simulations are used to evaluate the accurate estimation of cell values. All dielectric porous cell with discrete radius is considered in the HFSS simulated waveguide setup, with perfect-magnetic-conductor (PMC) and perfect electric conductor (PEC) boundaries to introducing up the periodic conditions. Concerning the defined settings for this cells, the right and left sides are assigned for wave-ports. The standard retrieval method with Kramer Kronig relations is used to obtain the effective permittivity of scattering parameters. As shown in Figs. 4.2, and 4.3, the obtained results of air-hole radius vs. permittivity for filling ratio and simulated setup effects are not comparable at all.

To determine this issue, the mathematical fitting approach is exercised to prepare more particular radiuses [11]. Through mentioned linear fitting, the estimated results agreed well with simulated full wave outputs. To estimate the last models, the obtained lens cell sizes would be the EF and

full wave simulation outputs, as shown in Figs. 4.2, and 4.3. After cell size comparisons to obtain the best size, the focusing ability of our prototypes was assessed by HFSS.

4.4   Dielectric lens designs

The dielectric Luneburg lens with radius R=30λ_0 was built for a millimeter-wave frequency band operation at 60GHz, as shown in Fig.4.5a. A cylindrical porous structure is employed as the primary unit cell to control the intrinsic permittivity of polyimide to satisfy perforated Luneburg lens subzones. In our experiments, the dielectric Luneburg lens in a homogeneous medium is embedded between two parallel aluminum plates in a quasi-TEM mode with 130×190 mm dimensions (at 60 GHz). As shown in Fig.4.6a, low permittivity Rohacell foam spacers $\epsilon= 1$ at 60 GHz, are used to fill up the free space between aluminum plates to suspend the proposed dipole antenna on air. In the perforated Luneburg lens design, the intended lens surface was separated into four concentric cylindrical zones, where each section is comprised of porous elements and related to a particular virtual refractive index. Therefore, the perforated lens n can vary from 1.01 to 1.4 to satisfy the lens rules.

4.5   Feed Design

A microstrip-fed dipole antenna, with cos^{10}-like radiation patterns, is embedded parallel aluminum plates containing the dielectric perforated Luneburg lens, to perform as a beam launcher, as shown in Fig.4.7. It is composed of a 0.5 mm-thick Rogers 5880 dielectric substrate. The microstrip dipole and ground is printed on the Roger substrate, as shown in Fig.4.7, and the antenna parameters are optimized to have a cos^{10}-like beam. The suggested beam launcher is installed between two pieces of Rohacell foam, in order to fix the antenna position perpendicular to the lens surface between the parallel metal plates. The presented beam launcher is a close estimate of a point source for the lens surface. In this design, it has been obtained from computational results that the phase center of perforated Lunenburg is located at a range of 2mm far from the intended lens boundary. Therefore, based on this analysis, a defocused type Luneburg lens is created. Based on this structure, the proposed lens gives rise to aperture phase errors. To determine this error, modified refractive index distribution based on the perforated Luneburg lens refraction function is analyzed to make design

feasible with the presented porous frameworks. Due to changing the perforated lens' refraction function [25], an effective point source (dipole antenna) outside of the given perforated lens would illuminate a planar wavefront on the reverse side of the perforated lens [25]. Therefore, based on the perforated lens' refraction function, we can reproduce it in exponential form $n = e^{\omega(nr,\zeta)}$, where ω is given by Eq.4.3[25]:

$$\omega(nr, \zeta) = \frac{1}{\pi} \int_{nr}^{1} \frac{\sin^{-1}(t/\zeta)}{\sqrt{t^2 - (nr)^2}} dt, \tag{4.3}$$

Where the ζ value is the normalized distance between the point and the lens' center [25]. For ideal lens excitation, the point source distance on the lens' surface is just $\zeta = 1$ [25]. By replacing $\zeta = 1$ in the intended equation Eq.4.3, the conventional refraction function is available as follows given by Eq.4.4 [25]:

$$\begin{aligned} \omega(nr, 1) &= \frac{1}{\pi} \int_{nr}^{1} \frac{\sin^{-1}(t)}{\sqrt{t^2 - (nr)^2}} dt \\ &= \frac{1}{2} \ln[1 + \sqrt{1 - (nr)^2}], \end{aligned} \tag{4.4}$$

By changing the point source position outside of the perforated Luneburg lens' surface, this distance can vary to $\zeta = 1 + \epsilon$, $\epsilon > 0$ [25]. By substituting the distinct distance function in the aforementioned equation, the new refraction function for perforated modified lens is given by Eq.4.5 [25]:

$$\begin{aligned} \omega(nr, 1) &= \frac{1}{\pi} \int_{nr}^{\zeta} \frac{\sin^{-1}(t/\zeta)}{\sqrt{t^2 - (nr)^2}} dt \\ &\quad - \frac{1}{\pi} \int_{1}^{\zeta} \frac{\sin^{-1}(t/\zeta)}{\sqrt{t^2 - (nr)^2}} dt \\ &= \frac{1}{2} \ln[1 + \sqrt{1 - (nr/\zeta)^2}] - \frac{1}{\pi} \int_{1}^{\zeta} \frac{\sin^{-1}(t/\zeta)}{\sqrt{t^2 - (nr)^2}}, \end{aligned} \tag{4.5}$$

By replacement of Eq.4.5 to the presented results in conventional exponential refraction function $n = e^{\omega(nr,\zeta)}$, the defocused perforated lens source refraction function with modified zones permittivty is obtainable by Eq.4.6 [25].

$$n = [1 + \sqrt{1 - (nr/\zeta)^2}]^{0.5} exp[-\frac{1}{\pi} \int_1^\zeta \frac{sin^{-1}(t/\zeta)}{\sqrt{(t^2 - (nr)^2)}}].$$ (4.6)

Based on this equation, the defocused refraction results are presented in Fig. 4.8. As shown in Fig.4.8, the subzones refraction values are lower than outside beam launchers for distinct ζ values [25]. Therefore, lower virtual permittivity based on this analysis is used to design this dielectric GRIN device[25].

4.6   Results and Discussions

A perfect qualitative compromise can be seen in simulations and measurement results for the proposed dielectric GRIN lens. As shown in E-fields distribution, fields near the wave launcher are not apparent because of the intensity of the beam launcher. Therefore, the E-field around the beam launcher is not surveyed. In this scheme, the incident waves, after transferring through the lens framework, are converted from cylindrical waves into quasi-plane waves on the reverse side of the dielectric lens periphery and reveal very directive illumination. In this scheme, the simulated and measured results for radiation patterns and S11 parameters match entirely for the perforated tailored lens expected results. From the mathematical analysis, and full wave simulations based on defocused perforated lens estimations, the proposed lens feed phase center confirming the point source (dipole antenna) is located 7mm from the perforated lens boundary. Secondly, it is crucial to prepare the air-gap properly with 1 mm-thick Rohacell foam. Therefore, using the wrong thickness can obviously change the intended effective medium parameters around the perforated lens. Nonetheless, the perforated lens beam focusing mechanisms are perceived at 60GHz, and 62GHz, as shown in Figs.4.9, and 4.10, respectively. The highly directive radiation patterns are seen at all measured frequencies. The measured results show that the sidelobes are below 18 dB, which is acceptable, based on the IEEE standards.

The sidelobes are symmetrical because of the dipole antenna and proportional lens prototype. In this scheme, the measured results for the lens contribute to making the transformed beams more directive and to having low sidelobe levels. The maximum directivity for the proposed design is 24.6dBi with 2.4dBi variations over operating bands between 57-67 GHz, as shown in Fig.4.12. The proposed lens total efficiency 58% with 4% variations over operating bands between 57-67 GHz.

4.7   Conclusion

In this work, the full dielectric perforated homogenous Luneburg lens antenna is performed, using the material porosity technique by click and print SLS technology. The perforated dielectric Luneburg lens is excited by a microstrip dipole source between parallel-plate waveguide at 60 GHz. The defocused analyses for perforated lens schemes are employed to design intended the zones with lower permittivity cells. The proposed lens results present a wideband performance for 55 to 65 GHz electromagnetic spectrum.
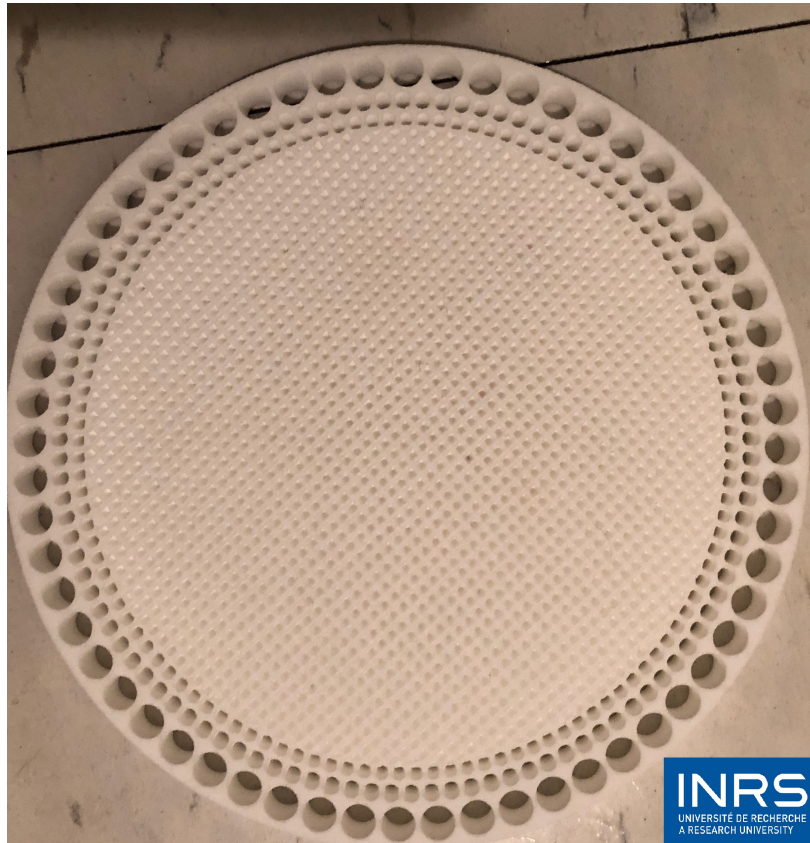
(a) Top view for the perforated Lens
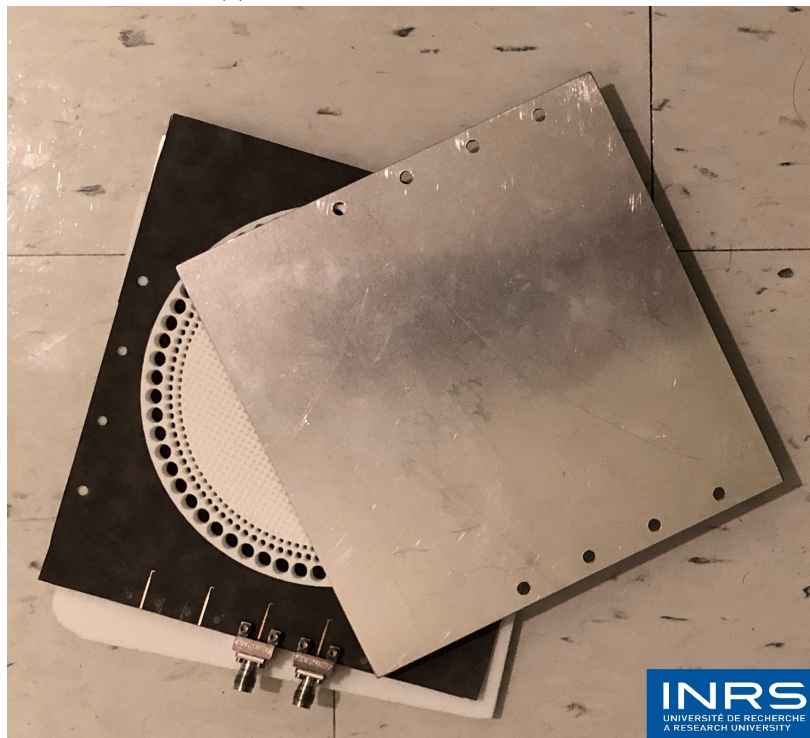
(b) Entire system view for the perforated lens

Figure 4.6 – Photograph of the fabricated full dielectric Luneburg Lens (a) Lens top view, (b) Total system view;

(a)   (b)   (c)
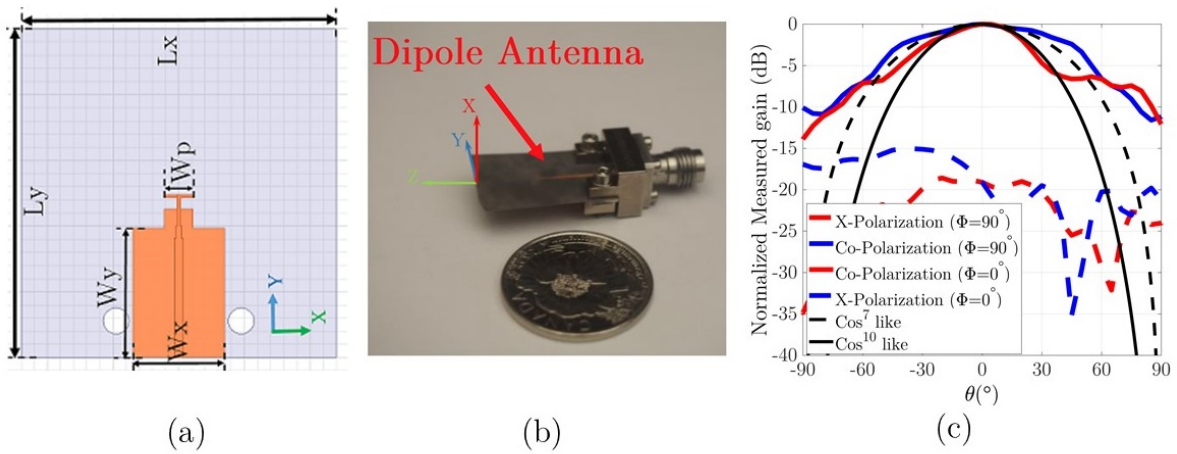
Figure 4.7 – (a) Geometry of the proposed beam launcher: $L = 12$, $R = 6$, $L_x = 24$, $L_y = 24$, $W_x = 7$, $W_y = 9.8$, **and** $W_p = 2.2$ **(All in mm), (b) photograph of the fabricated antenna on Roger 5880; (c) Measured radiation patterns for beam launcher without perforated lens, and parrallel plates; the proposed feed radiarion comparison with the associated** $\cos^{10}$ **like pattern at 60GHz [11];**
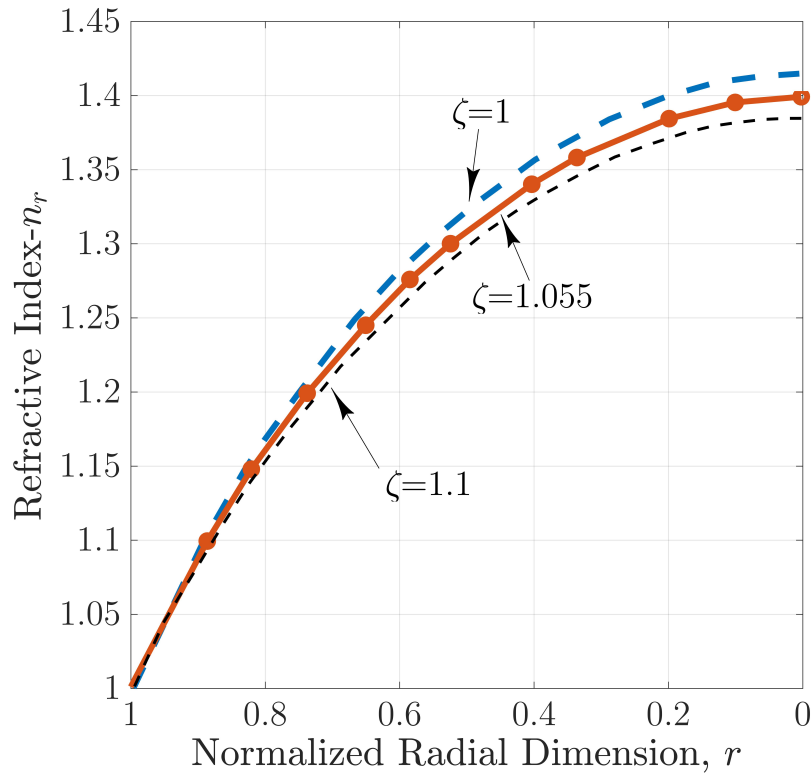
Figure 4.8 – Ilusstration of the refraction index for the defocused lens refraction results vs. normalized radial dimension for distinct $\zeta = 1, 1.05, 1.1$ **values [25];**
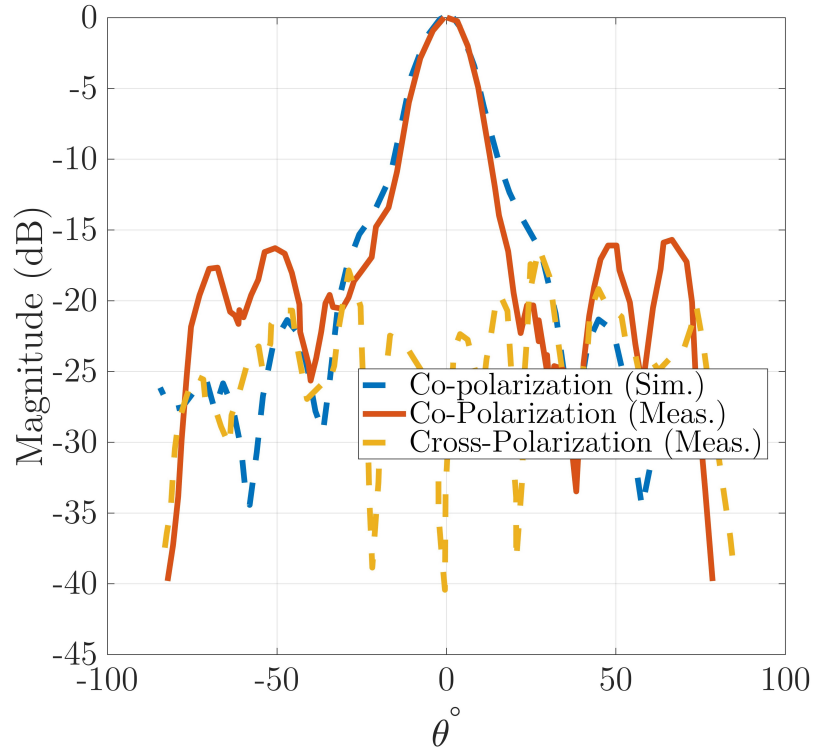
(a) $\phi = 0°$
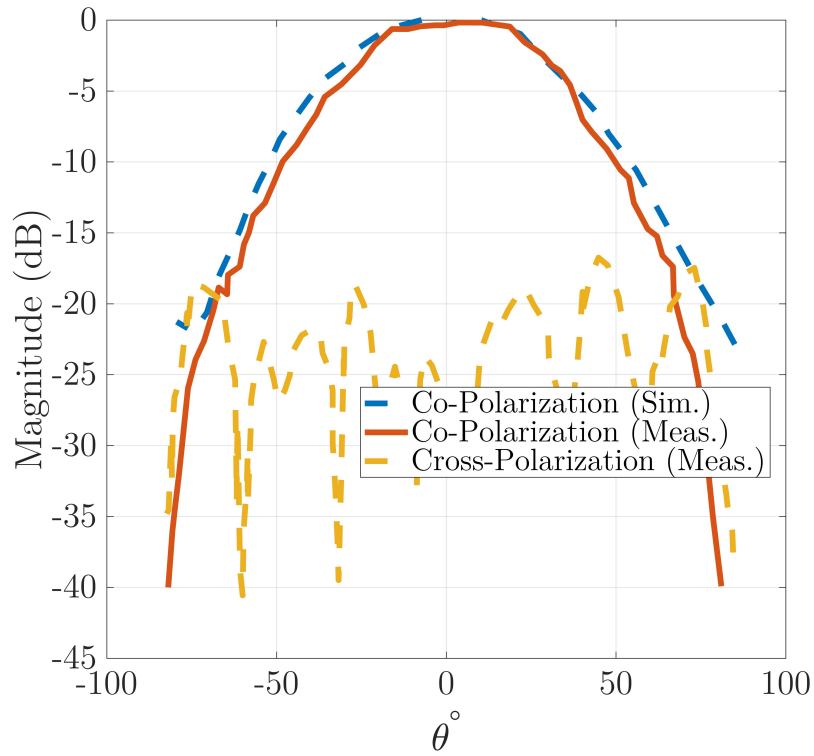
(b) $\phi = 90°$

Figure 4.9 – The simulated and measured results for the perforated lens: Co- and Cross- polarization both normalized E- and H-plane radiation patterns at 60GHz (a) $\phi = 0°$**, (b)** $\phi = 90°$**;**
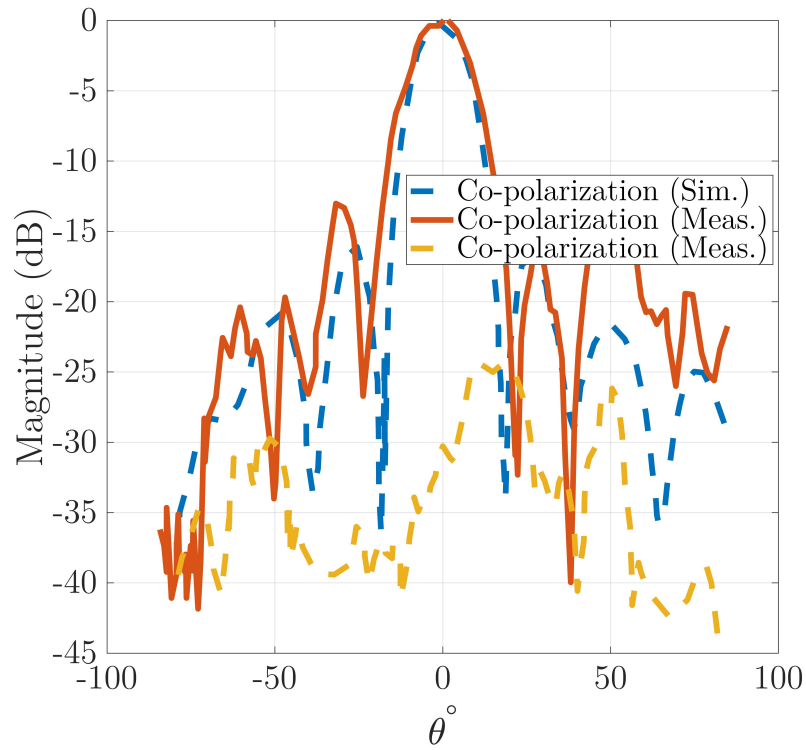
(a) $\phi = 0°$
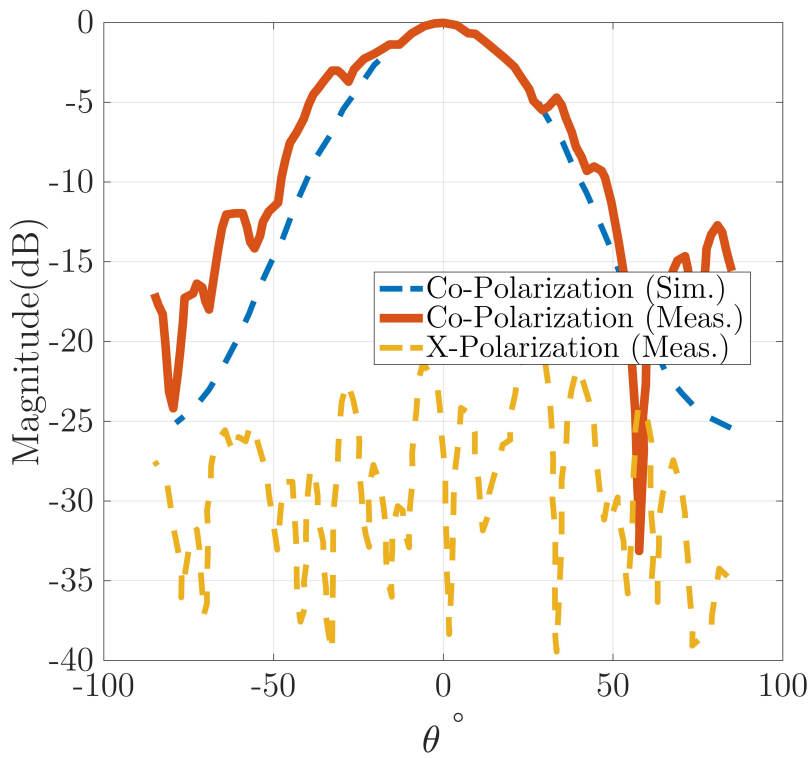
(b) $\phi = 90°$

Figure 4.10 – The simulated and measured Co- and Cross- polarization both normalized E- and H-plane radiation patterns at 62 GHz (a) $\phi = 0°$**, (b)** $\phi = 90°$**;**
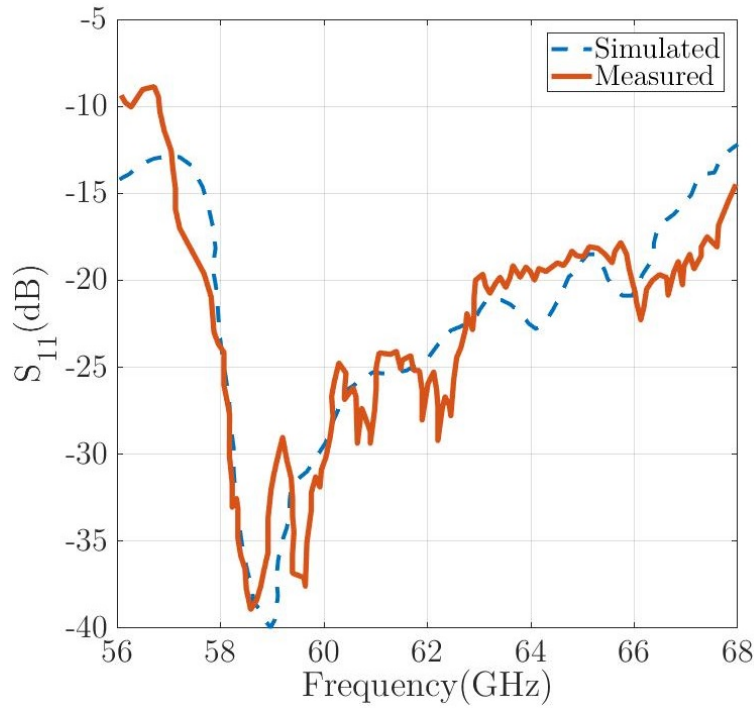
Figure 4.11 − **The simulated and measured S_{11} for the proposed dielectric GRIN lens antenna;**
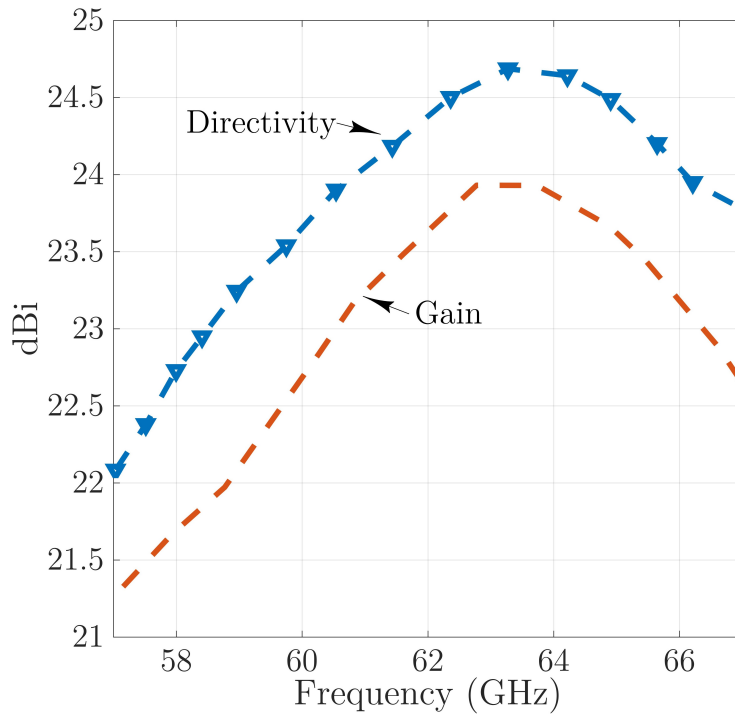
Figure 4.12 − **The simulated and measured realized gain and directivity for the proposed perforated Luneburg lens antenna;**

Chapter 5

Nonmagnetic FZPL antenna with analyzed porous cells for 30GHz

5.1   Introduction

Porous structures were among the first intrinsic permittivity control methods investigated for gradient refractive index medium design implementation [5], [4]. Using porous structures geometrical parameter control, intended virtual permittivity in desired $E-$field orientation be provided to fulfill homogeneously gradient refractive index (GRIN) medium over a broad range of frequencies, unlike conventional metamaterial GRIN frameworks with narrow bandwidths. Although porous based permittivity control is extensively applied in material engineering systems due to ease of permittivity reduction, and almost low cost to realize intended permittivity virtually in a similar medium, they are not analyzed well enough for GRIN lens antenna applications. Over the preceding decades, essential advancements have been performed in the additive manufacturing processes, which are simplified more complicated permittivity control achievement with free forming cells in high-gain GRIN lens devices for focusing applications (provided that a proper illuminator with the suitable Cos^n-like the pattern is applied). These porous structures are usually achieved using cylindrical and spherical array architectures. The tradeoffs existing within the conventional GRIN lens design cost, and subzones implementation employed in high-gain antenna platforms have limited these structures purpose in millimeter-wave communication systems above 30GHz. On the other hand,

traditional metamaterial-based GRIN medium suffers from excessive drawbacks such as narrow bandwidths, substantial dissipation, the difficulty and high cost of production. With the current growth in the additive manufacturing process, implementation of various innovative schemes of GRIN lens devices has been described as possible replacements of conventional GRIN device methods using all-dielectric periodic structures, and metamaterials with material porosity techniques. GRIN devices such as Luneburg, Half-Maxwell fisheye, and Fresnel zone plates have also gained more attention for numerous high-gain focusing applications with antenna design trade-off.

There has been an increasing consequence of Fresnel zone plate antenna purposes for some reasons in millimeter-wave and submillimeter-wave spectrums. First, ZPs offer high gain focusing like other GRIN lens structures, but they are a planar type, with decreased weight, ease of invention, and cost-effectiveness, which make them attractive. Additionally, a properly balanced illumination of lens aperture feeding reduces the defocus, and spill-over of lens taper that is an essential dilemma in the design of lens devices [28], [1]. Indeed, using proper Cos^n-like feeds to illuminate the zone plates surface to focus incidence waves through diffraction offers high-efficiency, high-gain, and low spillover values. Moreover, dielectric cells based on porosity procedures are used to control the phase shift gradient of subzones in a zone plate's surface/aperture for focusing. FZPs are composed of locally concentric subzones with multi-permittivity distributions that act as phase shifters. These subzones are regularly achieved with dielectric rings for the inhomogeneous framework or with porous structures such as cylindrical holes [5], [4] or deformed material for the homogeneous frame. Various prototypes of dielectric ZPs for designing all-dielectric formations have been reported in the past [29], [6].

The ZP prototypes in each subzone are composed of non-magnetic and non-metal materials for the homogeneous development and of single-resonant elements for the inhomogeneous composition. More recently, numerous efforts based on material theory have been made to produce intended subzone permittivity virtually via permeable drilled holes [6], either using cube-shaped cells fabricated on low permittivity dielectrics to design thinner lenses [11] or using full metal cells in the homogeneous medium [21]. However, such porous structures are highly dispersive for incidence wave illumination with sharp angles [4]. Therefore, they are not suitable for permittivity control of multiple feed illuminators and beamforming. Over the preceding years, four porous approaches, namely air-holes, dielectrically filled holes, full metal cells, and free-forming dielectric with subwavelength cell dimensions, were used to realize virtual permittivity in the homogeneous framework, which has

been considered for GRIN medium implementation. Unlike conventional FZPs that are formed with the fashion of periodic resonant elements, all-dielectric FZPs are fashioned with the array of porous cells having a highly miniaturized framework, ease of fabrication, and nonmagnetic structures. Unlike conventional FZPs that are formed with the fashion of periodic metal elements, all-dielectric FZPs are fashioned with the array of porous cells having a highly miniaturized framework, ease of fabrication, and nonmagnetic porous cells. Recently, specific porous approaches with a focus on 3D printing methods have been employed in composing wideband gradient refractive index lenses [6], [30], [97]. It was confirmed that applying full dielectric approach, low-profile lenses with wideband response could be designed. However, the homogeneous prototype structures both in metal and dielectric framework suffer from low efficiency that can be improved with total lens structure shaping or take illuminators thoughtfully.

In this work, we introduce novel porous cells in the homogeneous framework using high-dielectric Alumide plastic for designing low-profile, and wideband zone plate antennas. The proposed half-wave zone plate is constituted of the cube-shaped cells to provide intended permittivity of sub-zones for phase reversing. Each zone's cube size is analyzed based on full wave analysis with extracted S-parameters to offer a proper virtual permittivity cube size based on measured Alumide permittivity at 30GHz. Cube-shaped cells composed of high-dielectric powder-based Alumide were selected based on Electro-Optical Systems' (EOS) production list with rectangular rods to connect cells in a predetermined location to satisfy lens rules. Each dielectric cell is designed to provide a predetermined permittivity virtually within the in the desired electromagnetic spectrum. A prototype of the all-dielectric half-wave Fresnel zone plate with a Cos^{41}-like radiation beam conical horn located at its center is used to operate at 30 GHz. The realized dielectric ZPs overall thickness is 5mm, and the lateral physical dimensions of the printed lens aperture are $150 \times 150 mm^2$ (or equivalently $3\lambda_0 \times 3\lambda_0$). A model of the presented homogeneous zone plate composition is fabricated with the selective laser sintering (SLS) manufacturing process and experimentally identified in the antenna laboratory. The measurement results are conferred that the realized porous ZP provides a maximum gain of 34dB with a difference of lower than 4dB over the desired frequency band.

$\eta = 0$ $\eta = 1.5$ $\eta = 2.6$ $\eta = 4.5$ $\eta = 5$

(b)

(a)
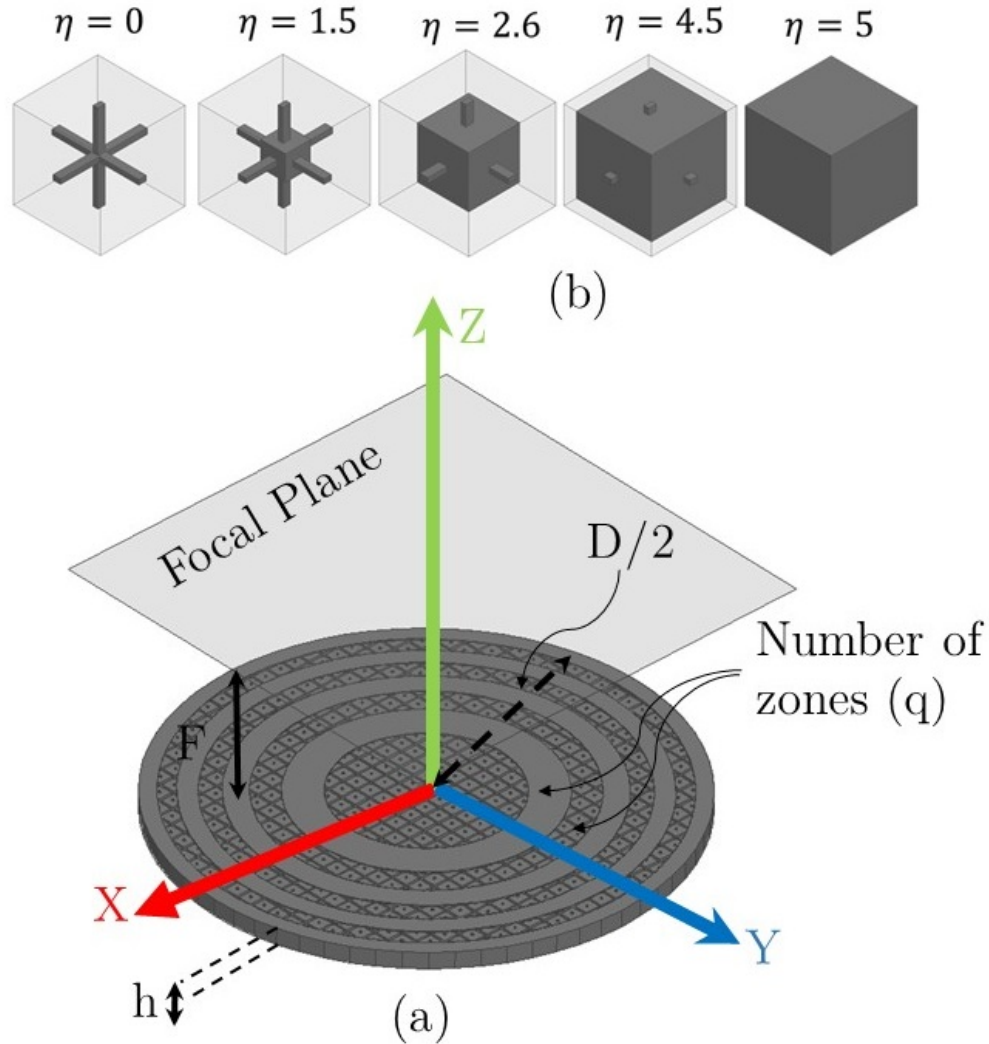
Figure 5.1 – (a) Illustration of the presented dielectric Fresnel zone plate (FZP) topology for Ka-band application with homogeneous framework; (b) Illustration of the graphical distinct filling ratio η for Alumide based porous structures to provide intended permittivity practically.

5.2   Lens Design

As we know, the entire lens design prototypes for the focusing applications can be classified into two modes of illumination as follow: Transmission-mode and Reflection-modes. The essential devices of each focusing setup with lens mechanism are assigned in two main part which can attain them in all pieces of literature with specific names as follow: a lens device (focusing provider), and illuminator/feeder/wave-launcher. Generally, all classes of lens devices for focusing setup are independent of electromagnetic spectrums; they had their own scenarios and providing of predetermined sub-zones permittivity techniques. But the standard point in all lens mechanism is a determination

(***a***) Original Foam shape   (***b***) Asymmetric deformation   (***c***) Symmetrical deformation
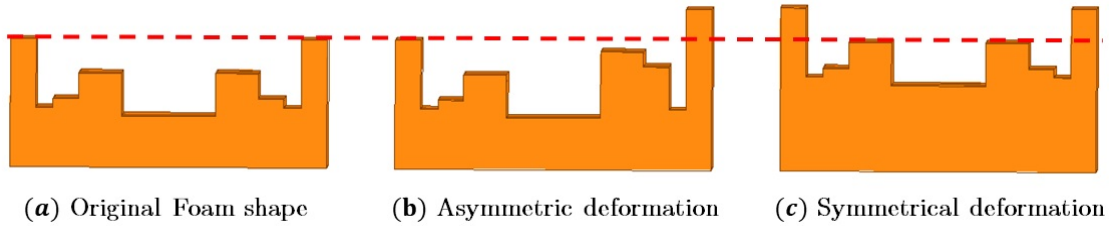
Figure 5.2 – Graphical illustration of the cross cut deformation for [24] built models over time and deformation scenarios that can affect 100% the manufactured device final performance.;

of proper illuminator, and low error subzones permittivity implementation, which can be considered to ensure the desired radiation effect in a predetermined setup with a defined focal point (F), lens diameter (D), and antenna gain parameters.

Upon to homogeneous framework configuration, we can classify porous cells to produce required virtual permittivity with higher or lower host medium permittivity in four approaches. A full metal approach [21], full dielectric framework with free-forming design approach [10], air-holes based porosity approach [80, 6], and multi-dielectric porosity approach to reach a wide range of permittivity control, which is not considered in antenna engineering because of production drawbacks. In [84], Kildal analyzed the classification of different illumination for Cassegrain and paraboloids antenna to accomplish high-efficiency feed goal as a first vital design factor. Using this analysis based on desired efficiency accuracy, and lens intrinsic parameters a related feed efficiency with four crucial factors [84]-Eq.28, are estimated as follows: spill-over efficiency [84]-Eq.23, polarization efficiency [84]-Eq.24, taper efficiency [84]-Eq.25, and phase error efficiency [84]-Eq.27. Using this review, a trusted efficiency area for all kind of illuminations are considered for proposed models in theoretical. Regard to this analysis to have high-efficiency feed for lens surface illumination, mechanism of the lens focusing should be analyzed to reduce back lobe level, and side level of transmitted or reflected waves. To achieve these goals, several scenarios based on homogeneous platforms are determined [80, 6]. In [6], perforated air-holes based ZPs with full air structure in first sub-zone (see 3.1), to reduce back lobe level because of utilizing high gain illuminator is presented. In [23], and [24], foam-based gradient refractive index homogeneous materials are employed to create low permittivity subzones for reflected waves issues with high permittivity materials.

Based on [23], and [24] built procedures, pressure devices are used to implement predetermined permittivity with reduction of captive air inside foam material. In mentioned designs, the elasticity of foam materials, which can be converted into its natural state at the time, has not been studied
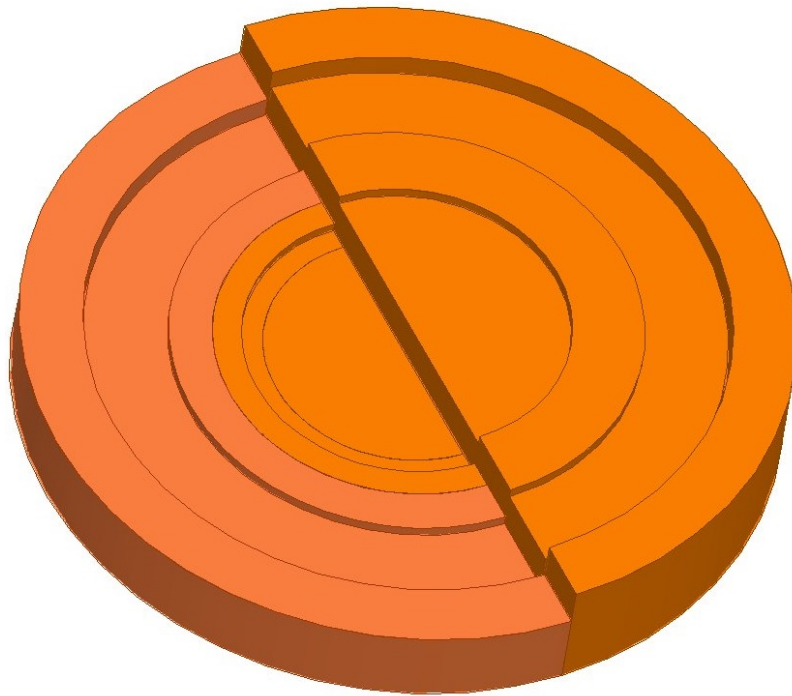
(a) Asymmetric deformation for half of the lens with 100% beam focusing reduction consequences
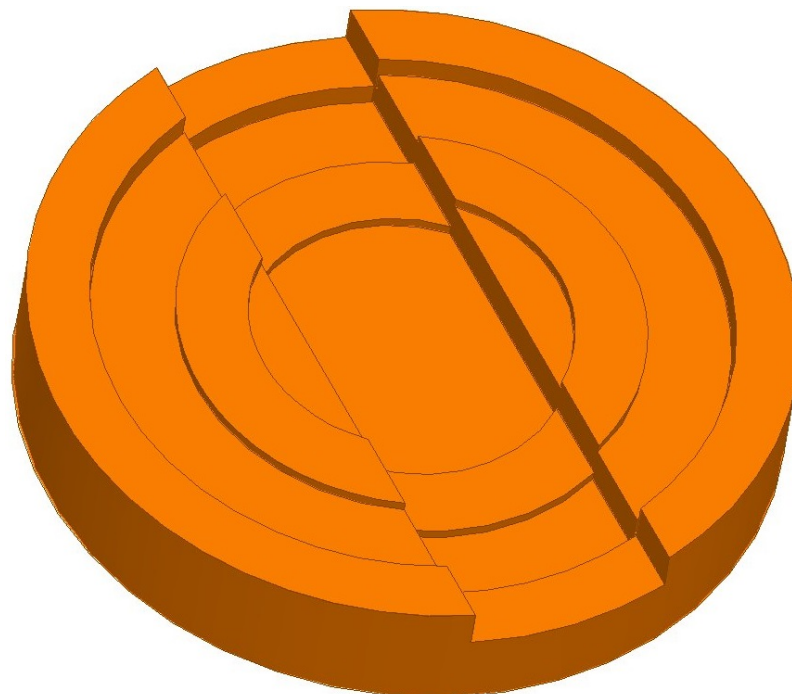
(b) Asymmetric deformation of the porous lens diaphragm with beam focusing reduction consequences

Figure 5.3 – The 3D graphical illustration of the deformation for [24] built models over time and deformation scenarios that can affect 100% **the manufactured device final performance.;**

and even its consequences on the total lens efficiency have not been investigated thoroughly with possible deformation scenarios Figs.5.2, and 5.3. Moreover, they decided to implement a metal circular frame to keep in the form of foam for lens shapes after using the lens device [23]-Fig.11, and [24]. Still, the proposed model is not becoming for long-term treatment, and there will have a significant manufacturing error for long time use with adding new difficulties for users. Accordingly, in a long time, a high-efficiency result even with designing highest efficiency feed with Kildal analysis to have an axially symmetric illumination on lens aperture at 75GHz will be ineffective [24]-Fig.5 and it is not a technical solution.

To solve this issue, a homogeneous based ZPs with material porosity techniques in a hard plastic host medium using low permittivity porous cells is presented. These configurations are used to reduce back lobe level which is provided with click and print technologies for 30 GHz, as shown in Fig.5.1. With considering all earlier ZPs design drawbacks and Kildal feed analysis, the cube-shaped cell porosity is estimated for our permittivity control modeling to solve the mentioned problems. In fact, we have tried to control the dielectric permittivity virtually with less than 5% error with consistent mechanical properties, as revealed in manufactured photographs, which is properly radiated even without using the high-efficiency feed with n=41 amplitude weighting. The proposed design support the best beam focusing mechanism factors mentioned above, to provide the competitive results in comparison with reported prototypes. Fig.5.1(a) reveals the topology of the presented dielectric zone plate. In this arrangement, the focusing setup is composed of a Cos^{41}-like pattern commercial horn antenna (conical) as an illuminator, and a dielectric zone plate as a lens device.

The proposed dielectric ZP has an overall aperture diameter of D and the focal length of F; focal length is the distance between the illuminator and lens aperture. The axially symmetric radiation conical horn illuminates the designed lens aperture, and it is produced to feed the lens aperture with Cos^{41}-like radiation pattern to have the maximum efficiency (as much as possible) with the theoretical analysis. The zone plate structure is composed of virtual multi-dielectric subzones to transform the incoming planar wavefront from the feed horn to a pencil beam in the opposite direction. The lens aperture is formed with whole dielectric $\lambda/2$ phase correction rings for incident waves instead of blocking waves like Soret type zones at 30GHz. These rings provide the desired phase correction with plastic porosity over the entire aperture within the considered focal length and operating band. In this work, each phase correction zone is composed of a cube-shaped plastic

unit cell with constant permittivity response versus frequency. Each porous cells is composed of the full dielectric structure with Alumide plastic and a rectangular rod in each vertex. The rod's size to vertex size ratio is analyzed based on quasi-static modeling to provide these ratio deviations for virtual permittivity and excellent mechanical strength for planar zone plate production. All the printed layers for the Alumide are attached by sintering a tray of powder, layer by layer. The detailed topology of cube-shaped cells configuration for distinct filling ratio and providing desired virtual permittivity for this unit cell are shown in Fig. 5.1(b). For this analysis, two type of approximation is performed for Alumide plastic cube cell array based on Brakora single cell Quasi-static modeling for 3D Luneburg [12], and full wave simulations comparison with mathematical fitting approximation [10, 11]. For the proposed estimation, Brakora analysis [12] for the ceramic material is applied equally to obtain the trusted area for Alumide based porous cells size to achieve zone plates framework at 30GHz.

5.3 Permittivity estimation for porous cell structures

Based on theoretical material permittivity analysis, when the graded variation occur on a much smaller scale that is considerably lower than a wavelength, an unauthorized environment with porous schemes can be defined as a homogeneous environment [12]. For this reason, the intrinsic dielectric constant of host medium can be controlled arbitrarily [12] with the 3D dimensions of the composite material or polymer based plastics such as 3D printing materials using the creation of porosity in the host medium environment. The effective control of dielectric constant through porosity with 3D printed approaches to realize innovative graded refractive index lenses for beam focusing applications is commonly used to reduce the intrinsic dielectric constant in a homogeneous environment, which requires single-cell full-wave analysis for more accuracy [11, 5, 12]. In this controlling approach, instead of applying stochastic porous structures, which is expected in the material engineering world to control the volume fraction of the host environment, the cell-based dielectric modifications [5] with 3D printing technologies [11] are used in a regular grid with polymeric materials composition. Through this m method, stable structural components can be used to create single dielectric or GRIN environments, which comparatively reveal little surface area [12]. Based on Brakora approximations [12], an effective dielectric tensor of a cub-shaped cellular structure can be defined precisely by controlling the size of linear and periodic dimensions as shown in Fig. 5.4. In this analysis instead
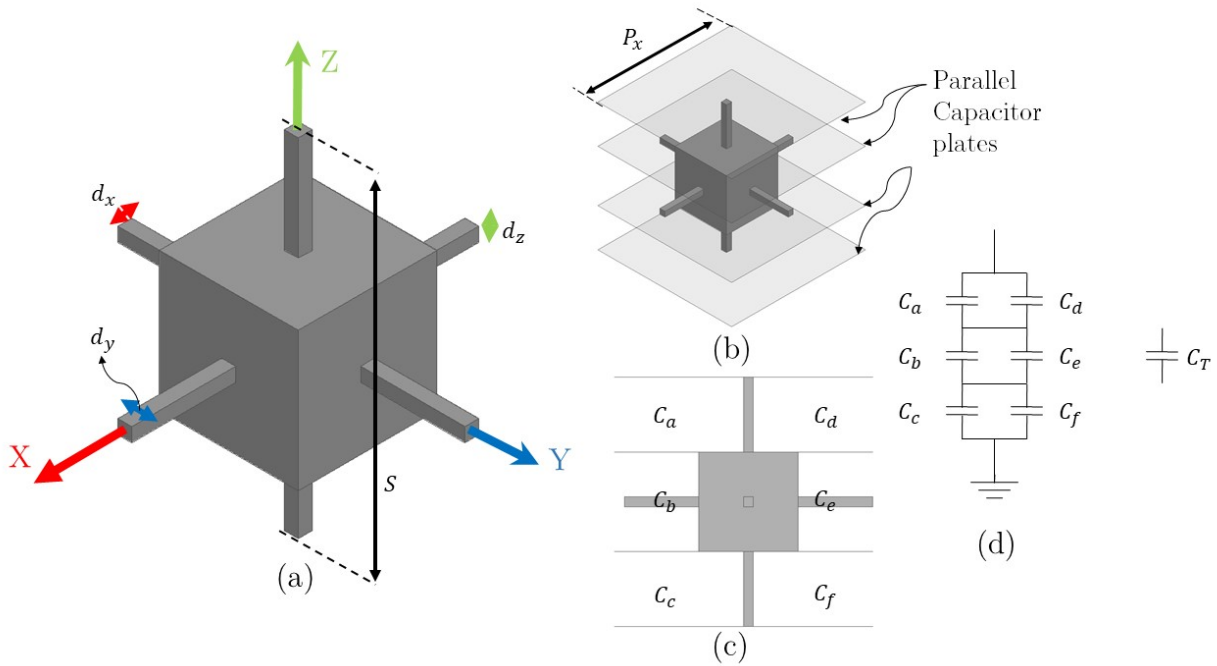
Figure 5.4 – **(a) The proposed Cube-cell dimensions; (b) 3D modeling for the Capacitive estimation of the ϵ_{eff} of the isotropic cubical lattice based on Brakora analysis [12].** S **is the area for the metal plate sizes of the parallel-plate capacitor,** h **is the cut length of these metal parallel plates, and** ϵ_r **is the relative permittivity of the dielectric-filled material. (c) vertical cut for equivalent capacitor model of cube cell; (d) Equivalent Circuit model based on series and parallel capacitance modeling rules;** $C_a = \frac{\epsilon_0 \epsilon_r d^2}{1/2(S-d)}$, $C_b = \frac{\epsilon_0 \epsilon_r (2Sd - d^2)}{d}$, $C_c = \frac{\epsilon_0 \epsilon_r d^2}{1/2(S-d)}$, $C_d = \frac{\epsilon_0 (S^2 - d^2)}{1/2(S-d)}$, $C_e = \frac{\epsilon_0 (S-d)^2}{d}$, $C_f = \frac{\epsilon_0 (S^2 - d^2)}{1/2(S-d)}$;

of full-wave simulations with HFSS and exponential fitting approximations, mathematical modeling is practiced to prove trusted area for cube size and rods sizes.

In this permittivity control approach, for cube-shaped porosity, the cube size produces precise levels of control over the effective anisotropy to achieve virtual permittivity creation.

As shown in Fig.5.4, this design scheme is considered to be the only cubical isotropic scheme with similar vertex size in which $d_x/S_x = d_y/S_y = d_z/S_z = d/S$ is supposed to achieve the perforated fresnel lens subzone's intended virtual permittivity. In periodic structures with diminishing intrinsic permittivity methods such as these, dielectric mixing with linear-based equations is open to the theory of materials, which provides the ineffective prognostication of dielectric properties virtually [5, 4, 12].

Up to this analysis [12], we use three evaluation methods, including full wave simulation, to produce the desired virtual permittivity of the cube size for the predetermined subzones. While the dimensions of a network of porous cells in a homogeneous medium are small compared to the wave-
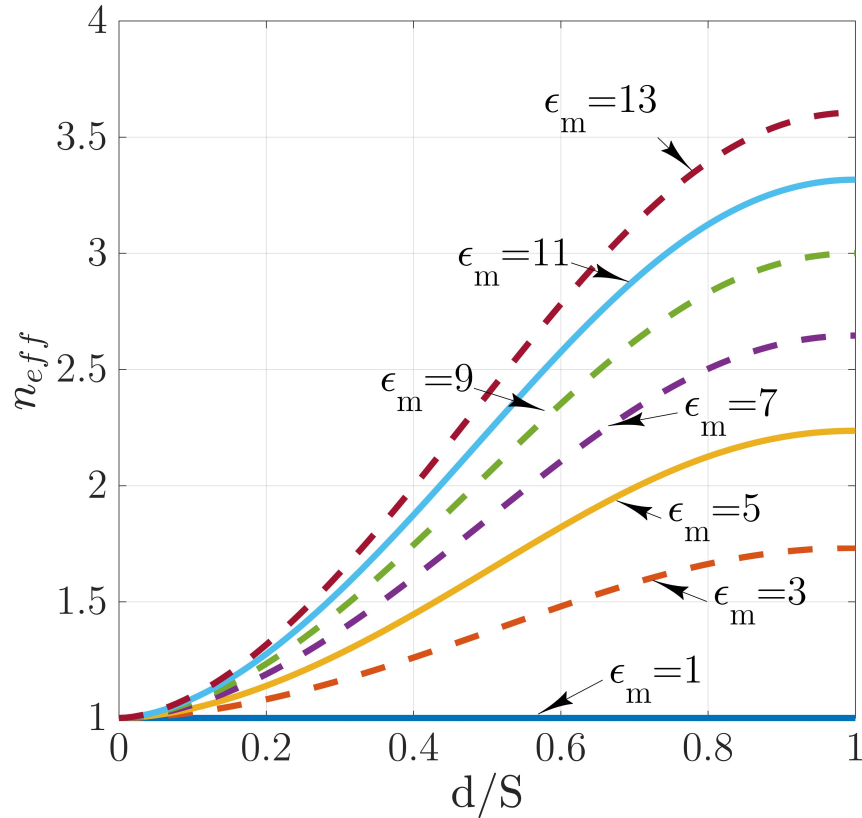
Figure 5.5 − **Illustration of the n_{eff} versus $\frac{d}{S}$ linewidth-to-periodicity ratio in the isotropic cub-shaped fashion array for distinct ϵ_m permittivity materials for capacitive approximation based on Eq. 5.1.**

length in the operating electromagnetic spectrum, the electrical behavior of the proposed medium can be described in a static capacitive sense with constant electrical field based on the prior investigations [99, 12]. Accordingly, with this static capacitive estimation, the total capacitance (C_T) with predetermined material as a host medium such as polyimide, Alumide, ABS-M30, ceramics for the proposed single porous cell between parallel plates is achievable with capacitance estimation. As shown in Fig.5.4, the estimated parallel and series capacitance for constant electrical field between parallel plates with equivalent capacitance are (C_T) attainable. In this way, the equivalent capacitance (C_T) effective dielectric constant (ϵ_d) is discovered by analysis of the ratio of the equivalent capacitance for capacitors, which contain the porous unit cell and empty capacitor (without any dielectric) corresponding dimensions based on static physics formula for the capacitor. This capac-

itance calculation of the static refractive index in the isotropic distribution of porous cells using Eq.5.1 is attainable for nonmagnetic medium [12, 99].

$$n_{eff} = \sqrt{\frac{(1 + 2\frac{d}{s}(\epsilon_m - 1) - (\frac{d}{s})^2(\epsilon_m - 1))(1 + (\frac{d}{s})^2(\epsilon_m - 1))}{(1 + 2\frac{d}{s}(\epsilon_m - 1) - 3(\frac{d}{s})^2(\epsilon_m - 1) + 2(\frac{d}{S})^3(\epsilon_m - 1)}}, \tag{5.1}$$

where ϵ_m is the intrinsic permittivity of the predetermined host medium plastic material to realize the homogeneous framework. Toward this virtual permittivity realization based on Eq.5.1's approximation, which comprises cube-shaped structures scheme with parallel and perpendicular surfaces, the estimation errors are around 5% for distinct 3D printing dielectric materials ranges as shown in Figs.5.5, and for Alumide bases cube cells, as shown in Fig.5.5.

With other porous compositions, such as cylindrical, triangles and spheres, the proposed capacitance modeling approach demonstrates a very poor estimation of virtual permittivity compare to Ward's [4] and Cokrum's analysis [5] for that classification or with fitting approximations [11, 57]. The significant error of the intended interpretation for sphere and cylindrical porosity cells is unbounded because of higher permittivities of host medium [99, 12], and this error performs the achievement of virtual permittivity in a more difficult and complicated way. What the estimator gives by the analysis mentioned above is to provide a precise analytical approximation of effective dielectric constants and refractive index for determining the virtual permittivity design of homogeneous environments.

Then, we can define some critical design limitations to provide realistic cube cells dimension with intended 3D printing material such as Alumide, ABS or polyimide. We should attempt to address our treatment concepts to the 3D printing manufacturing rules and produce our perforated zone plate lens prototypes. Upon to Brakora static analysis [12], we can classify four essential controls to design of the cube-shaped porous structures of lens subzones constructed from SLS manufacturing mathematically. The process of finding these four constraints and limitation with analytical equations based on Brakora method is reviewed here for Alumide Plastic[12]:

"The first limitation is regarding quasi-static conditions mentioned above for array of cubes to realize effective medium. Accordingly, the cube sizes should satisfy SLS fabrication tolerance and cube-shaped cell limitations given by Eq.5.2 [12].

$$d_{min} \leq d \leq S \leq \frac{0.33\lambda_0}{n_{eff}}, \tag{5.2}$$

Regarding the independence of random errors, which can be Selective laser sintering (SLS) manufacturing errors or other forms, the capacitive modeling approach analysis for cube-cells dimension in the anisotropic frameworks is crucial [12]. Since the cube vertex size in all coordinate planes x or y or z is assumed equally as $S = S_x = S_y = S_z$ based on Brakora estimates [12]. Then based on the capacitance circuit model estimation for single cube-cell model used in Fig.5.4, a biaxial refractive index tensor for the xx-directed component can be defined by Eq.5.3[12].

$$n_{eff}^{xx} = \sqrt{\frac{(1 + (\epsilon_m - 1)\frac{d_y d_z}{S^2})(1 + (\epsilon_m - 1)(\frac{d_z}{S} + \frac{d_y}{S} - \frac{d_y d_z}{S^2}))}{1 + (\epsilon_m - 1)(\frac{d_y}{S} + \frac{d_z}{S} - \frac{d_x d_y}{S^2} - \frac{d_x d_z}{S^2} - \frac{d_z d_y}{S^2} + 2\frac{d_x d_y d_z}{S^3})}}, \tag{5.3}$$

The biaxial refractive index tensor with Brakora estimations for other $yy-$ and $zz-$directed component can be defined with the presented equation also, with just transforming $x \to y$, $z \to x$, and $y \to z$. However, this modification is not required if refractive tensor for xx-element can expose all related derivatives in the homogeneous framework with considering this transformation and Eq.5.4 and Eq.5.5 [12].

$$\frac{dn_{eff}^{xx}(\bar{a})}{dn_x} = \frac{dn_{eff}^{yy}(\bar{a})}{da_y} = \frac{da_{eff}^{zz}(\bar{a})}{da_z}, \tag{5.4}$$

$$\begin{aligned} \frac{da_{eff}^{xx}(\bar{a})}{da_y} &= \frac{da_{eff}^{xx}(\bar{a})}{da_z} = \frac{da_{eff}^{yy}(\bar{a})}{da_x} \\ &= \frac{da_{eff}^{yy}(\bar{a})}{da_z} = \frac{da_{eff}^{zz}(\bar{a})}{da_x} = \frac{da_{eff}^{zz}(\bar{a})}{da_y}, \end{aligned} \tag{5.5}$$

$$\frac{S(\frac{d}{S})}{P_S n_{eff}(\frac{d}{S})} \leq S, and, \frac{U(\frac{d}{S})}{P_u n_{eff}(\frac{d}{S})} \leq S \tag{5.6}$$

where $\bar{a}=\bar{d}$ is the vector with a_x, a_y and a_z components, and these are second and third constraints for cube shaped porous cell size design mathematically.

Comprehending that these linear deviations for rod sizes are small quantities compare to periodicity and cube vertex size; therefore, the first order of virtual effective refractive index based on these Alumide cells composition is appropriately answered. By taking accounts of Eqs.5.4 and 5.5, the approximate error in the xx-directed effective refractive index with Alumide plastic can be calculated by Eq.5.7.

$$\Delta n_{eff}^{xx}(a) \approx \frac{\delta n_{eff}^{xx}(a)\Delta a_x}{\delta a_x} + \frac{\delta n_{eff}^{xx}(a)\Delta a_y}{\delta a_y} + \frac{\delta n_{eff}^{xx}(a)\Delta a_z}{\delta a_y}, \tag{5.7}$$

where Δa_y and Δa_y are zero-mean normally-distributed random variables with a standard deviation of σ, and Δa_z is uniformly-distributed random variable over one layer thickness of Selective laser sintering (SLS) printing resolution [38], $t_{printing}$ [12]. With the comparable approach, the errors in other directed components ($xx-$ and $zz-$components) of the refractive tensor are obtainable directly [99, 12, 100]. To help design purposes, W as a normalized average standard deviation in the effective refractive index is determined, which is normalized to Alumide based cube cell periodicity (S) with the arrangement of three biaxial constants produced by Eq.5.8 [12],

$$\begin{aligned} W(\frac{d}{S})^2 &= Var[\Delta n_{eff}(a)]S^2 \\ &= \frac{1}{36}[(\frac{\delta n_{eff}^{xx}}{\delta\frac{a_x}{S}})^2 + 2(\frac{\delta n_{eff}^{xx}}{\delta\frac{a_y}{S}})^2]t_{printing}^2 \\ &+ \frac{2}{3}[(\frac{\delta n_{eff}^{xx}}{\delta\frac{a_x}{S}})^2 + 2\frac{\delta n_{eff}^{xx}}{\delta\frac{a_x}{S}}\frac{\delta n_{eff}^{xx}}{\delta\frac{a_y}{S}}) + 3(\frac{\delta n_{eff}^{xx}}{\delta\frac{a_y}{S}})^2]\sigma^2. \end{aligned} \tag{5.8}$$

where Δn_{eff} is the average of the refractive tensor elements as defined in Eq. 5.6. However, because of the independence mentioned in above definitions for approximated errors from effective anisotropy, The normalized uniaxial error, U, should also be considered in treatments of much smaller values compare to W, which are given by Eq.5.9 [12]."

$$\begin{aligned} U(\frac{d}{S})^2 &= var[\Delta n_{eff}^{zz}(a) - \Delta n_{eff}^{xx}(a)]S^2 \\ &(\frac{\delta n_{eff}^{xx}}{\delta\frac{a_x}{S}} - \frac{\delta n_{eff}^{xx}}{\delta\frac{a_y}{S}})^2(\sigma^2 + \frac{1}{12}t_{printing}^2). \end{aligned} \tag{5.9}$$
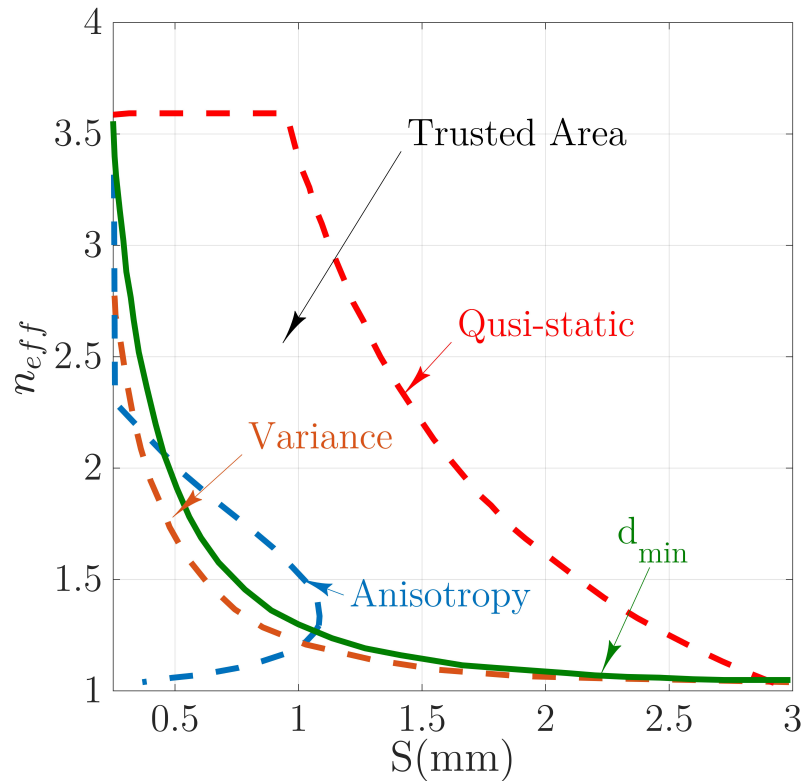
Figure 5.6 − **Range of trusted area for cube-shaped cell dimension with four constraints for Alumide based cells;**

Accordingly, we can classify proposed scheme thresholds based on these constraints to produce a trusted range of refractive indices for desired propagating frequency and host medium. These constraints can be plotted graphically to afford a trusted treatment area for porous cell size certainly. As shown in Fig. 5.6, the colored area will be our trusted area to produce any GRIN medium framework in the homogeneous structure.

To create the proposed Fresnel zone plate, type of lens and studied cells are demanded over the lens aperture in the homogeneous framework. Some parameters determine the phase corrector rings produced by four constraints. These values involve the number of phase corrector rings, the lens diameter D, the intended subzones permittivity depend on lens laws and the intrinsic permittivity of the host medium. The host medium dielectric and the trusted cube size are prepared principally from possible treatment considerations. Assuming these pair design options are arranged, the phase correction zones by dielectric compositions can be controlled by the lens laws, which can be a Luneburgh, Eaton, or ZPs.
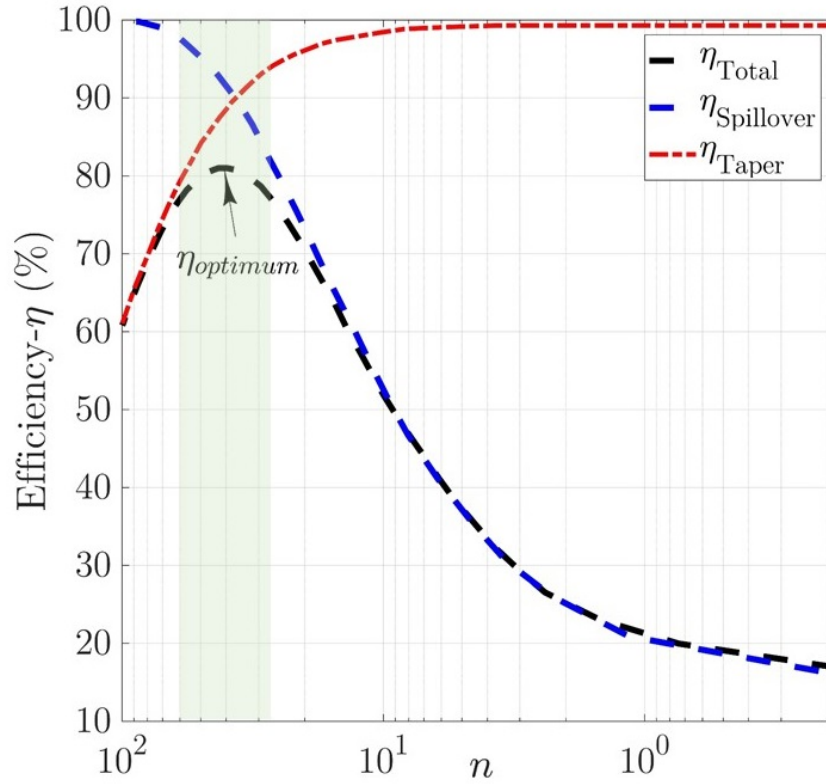
Figure 5.7 – **Illustration of logarithmic η_{taper}, η_{SP}, and η_{total} efficiency constraints for distinct amplitude weighting using symmetric cos ^{n}-like illumination to find trusted area for n to have maximum efficiency with optimised illuminators or commercial illuminators;**

5.4   ZP lens antenna treatment scheme

The design scheme of the intended lens antenna in the homogeneous framework consists of distinct levels. The beginning run is to determine the dielectric Fresnel zone plate equation, which is illustrated in detail before, and we will practice these commands given by Eqs. 5.10 and 5.11 [11, 83].

$$b_n = \sqrt{\frac{2n\lambda F}{q} + \frac{n\lambda^2}{q}}, \; n = 1, 2, ..., S, \tag{5.10}$$

where S is equal to qP.

$$\epsilon_n = \epsilon_1.[1 + \frac{2}{n}(1 - \frac{n-1}{q})]^2. \tag{5.11}$$

The second action is to determine the lens diameter, D, and the F/D ratio. To improve the designed millimeter-wave lens efficiency, spillover loss should be lessened by symmetrical, and well-formed radiation pattern within the $\cos^n$-like shape illuminators [11, 90]. Therefore, to achieve this treatment [84, 24, 11]the taper efficiency (η_{taper}) and the spill-over efficiency (η_{SP}) function described in Eq.5.11, and Eq.5.12 for $\cos^n$-like radiation pattern amplitude weighting is analyzed to attain trusted area for n values to obtain maximum efficiency [11]. In the result of axially symmetric illuminators given by Eq.5.13, η_{SP} can be increased by increasing n values while ensuring drop of η_{taper} antenna efficiency. Regarding the D, F, and n parameters, higher total efficiency as an outcome of two efficiencies, ($\eta_{Total} = \eta_{SP}.\eta_{taper}$) is desirable [24, 96, 11].

$$\eta_{taper} = \frac{1}{\pi.\tan^2(\frac{\theta_0}{2})}.\frac{[\int_0^{2\pi}\int_0^{\theta_0}|G(\theta,\phi)|^{0.5}.\tan(\frac{\theta}{2})\,d\theta\,d\phi]^2}{\int_0^{2\pi}\int_0^{\theta_0}|G(\theta,\phi)|.\sin(\theta)d\theta d\phi}, \tag{5.12}$$

$$\eta_{SP} = \frac{\int_0^{2\pi}\int_0^{\theta_0} G(\theta,\phi).sin(\theta)d\theta\,d\phi}{\int_0^{2\pi}\int_0^{\theta_\pi} G(\theta,\phi).sin(\theta)d\theta\,d\phi}, \tag{5.13}$$

where $G(\theta, \phi)$ is the radiation pattern, θ is dedicated to polar angle, and ϕ is the azimuthal angle[84, 85, 11].

$$G(\theta, n) = \{(2n+1).cos^n(\theta),\ for\ \ 0 \leq \theta \leq \pi/2;\ 0,\ \ for\ \ \theta > \pi/2; \tag{5.14}$$

These efficiencies can be plotted graphically to manage a trusted treatment area for $\cos^n$-like radiation pattern amplitude weighting. As shown in Fig. 5.7, the shaded zone will be our trusted area to obtain maximum $\eta_{optimum} = 0.81$ [84, 11, 24]. Up to these decisions, a new conical horn antenna with predetermined $n = 40$ values in radiation fields with low sidelobe levels (SLL) is developed to achieve this aim. The homogeneous lens aperture is then subdivided into concentric subzones q as shown in Fig.5.1, where q is a phase correcting number. The phase correcting zone number, q, is lens design configuration that can be preferred for half-wave ($q = 2$), quarter-wave ($q = 4$) or higher phase correction, which will be determined with ZPq subscriptions. To get the lens profile, after providing decided cells for each zones to complete lens propagation laws the aperture arranged for intended cell size.
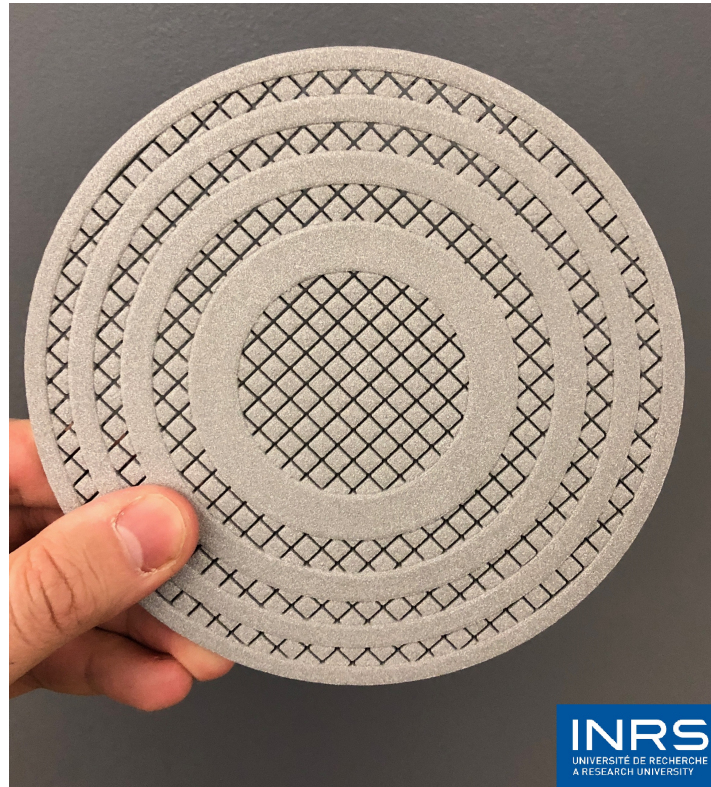
(a) Top view
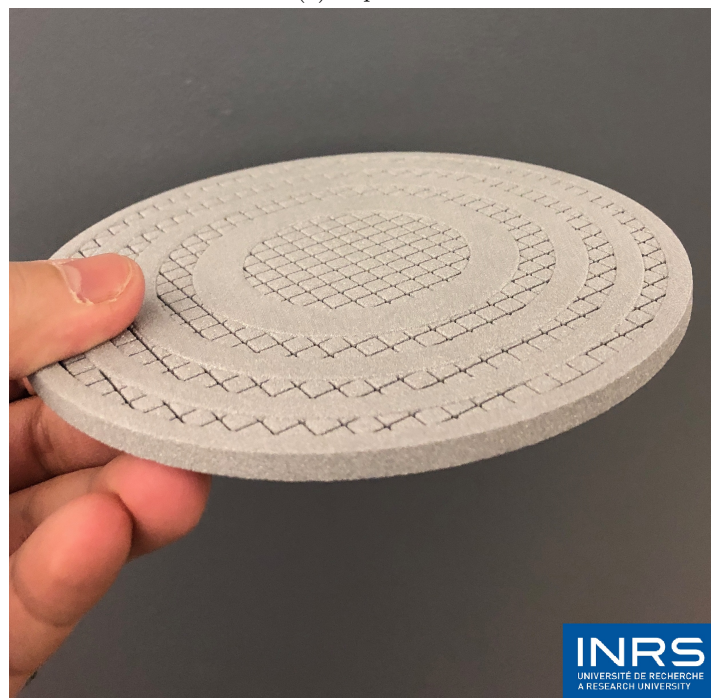
(b) Side view

Figure 5.8 – Photograph of the fabricated Alumide based $\lambda/2$-wave zone plate (a) Lens top view, (b) Side view;
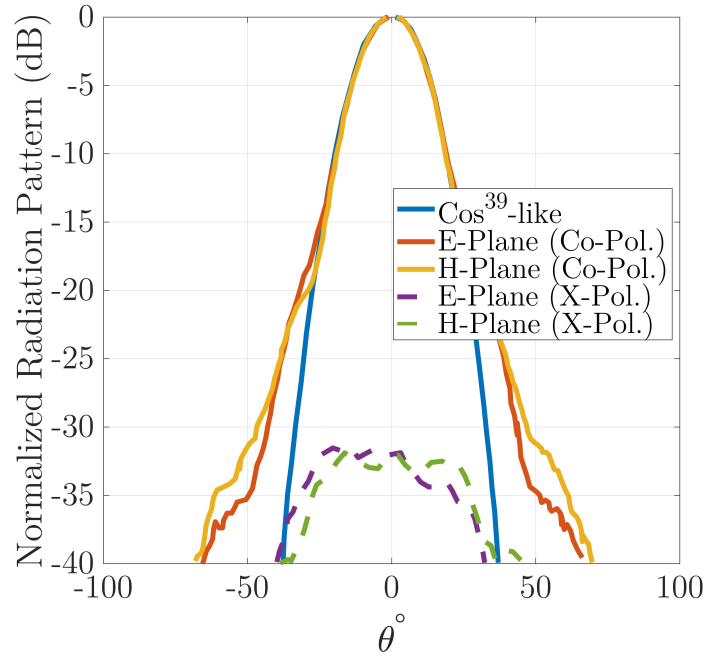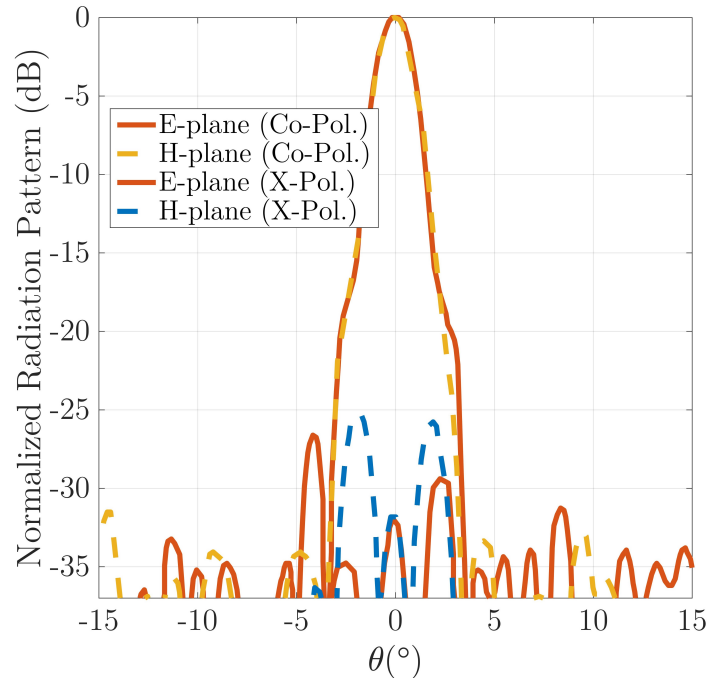
Figure 5.9 − The normalized radiation patterns along E- and H- planes at 30 GHz performance with axially symmetric conical horn feed: (a) $\cos^{39}$-like horn, and (b) FZP_2 radiation;

5.5   Design Example

The method manifested in Section II, and III was developed to compose a transmission-mode FZP_2 lens antenna with a material porosity technique in the homogeneous framework. The recommended Fresnel lens is produced to work on 28–40 GHz frequency bandwidth. As outlined in Section III, the $\cos^{41}$-like radiation pattern amplitude weighting is defined by the radiation pattern of the conical horn antenna. In this scheme, a commercial beam launcher is employed as an illuminator to feed dielectric ZP aperture which is a Ka-band conical horn antenna (A390-17). In the treatment method, a $\cos^{41}$-like illumination tapering is estimated to have a maximum tradeoff between the aperture and spillover efficiency. Since the dielectric constant of the material is frequency dependence, therefore, a waveguide-based dielectric measurement method is used to measure actual permittivity at operating band. For this reason, a printed Alumide sample with 7.1×3.5×2.99 dimensions is created to load WR-28 spacer for Ka-band measurements. In result, the dielectric host medium employed in the homogeneous design, which is a polymer base plastic, an obtained permittivity is about 10.8 at 30GHz. Because of the small elements of the introduced porous ZP lens antenna, full wave analyzing of whole structure demands good computational devices. For instance, the smallest parts of the lens will be our trial to simulate with commercial finite difference time domain (FDTD) technique software, which is needed smaller cell size for exploring. Therefore, simulation of the recommended lens antenna with 0.5 mm tiniest part and 900 cube cells composition is a prominent challenge and time-consuming. The proposed FZP_2 lens and $\cos^{39}$-like radiation patterns in the E-plane and the H-plane at 30GHz are plotted in Fig.5.9a.

5.6   Conclusion

In this chapter, a porous Fresnel zone plate lens composed of a homogeneous profile fed with a conical horn antenna was provided for millimeter-wave applications. The suggested ZP utilizes the cube-shaped unit cells, appropriately designed by providing analytical models to form homogeneous lens subzones' virtual permittivity and skeleton. A prototype of such half-wave FZP was built and experimentally identified in the lab. The fabricated FZP lens was intended to work at the center frequency of 30GHz. The experimental results confirmed that the lens antenna shows constant pencil beam radiation properties within the 25-40 GHz frequency spectrum. For the corresponding

lens aperture dimensions, homogeneous type lenses reported hereabouts are demanded to show higher gain and efficiencies than earlier reported prototypes with the Alumide base homogeneous frame. The lens illuminator performance of the presented Fresnel was also verified by spill over and taper efficiency equation analysis to find the best amplitude weighting for identifying symmetrical cos-like illuminators' character to achieve high efficiency.

Chapter 6

Conclusions and Future perspectives

6.1   Conclusions of the Thesis

In this thesis, we have introduced novel and optimized concepts in the frame of mmWave communications, namely nonmagnetic ($n = \sqrt{\epsilon\mu}, \mu = 1$) gradient refractive index lens antenna. The two ideas are intended for improving current manufacturing technologies for GRIN devices in the mmWave spectrum: the Luneburg lens and Fresnel zone plates (FZPs) in the homogeneous framework. On the one hand, material porosity can be useful to simplify virtual permittivity design, not only in the implementation and measurement steps but also to potentially enable new and broadband properties cells with simplified schemes for impairment compensation in the mmWave, and sub-mmWave spectrums. On the other hand, permittivity control techniques based on material porosity can also facilitate the development of new GRIN device design techniques for lens applications. In fact, the introduction of material theory based on material porosity processing is considered to be one of the most encouraging methods to control the intrinsic permittivity of the material.

The remarkable applicability of classical permittivity control with a volume reduction in a homogeneous medium within a full dielectric or full metal platform is due to its capacity to simultaneously control the amplitude and phase of GRIN medium subzones with an arbitrary material by use of porous cells or deformed structures. The ordered GRIN compositions based on permeable cells and reconstruction steps of these techniques and classifications have been reviewed in Chapter 2. Corkum's initial tries before 3D printing technologies have been introduced, highlighting the

principal problems of its virtual permittivity configuration, namely the fact that the virtual output permittivity for foam-based plastic with cylindrical air-holes directly related to the type of material, cell heights, and E-field orientations. To overcome the problem, an alternative spherical configuration has been reported by ward's, which was introduced by Corkum [5] a few years after his original proposal in Bell Laboratories. This spherical porous configuration was more independent of the incident wave orientation because of the symmetrical structure of the object compared to permeable cylinder cells. Thus, in the spherical porous structures, the different incident wave's angles can be used to control virtual permittivity of the medium.

In Chapter 3, we also reviewed the concept of deformed material based on cube-shaped plastic cells with rods connectors to realize Fresnel zone plates by additive manufacturing (ADM) processes. The additive manufacturing process consists of a technology solution to enable the implementation of complex shape porosity cells using a volume reduction similar to previous porosity techniques, employing polymer based plastics. For this purpose, the new porous cell with 3D-printing manufacturing ability consists of cube-shaped plastics analyzed to provide intended permittivity in a homogeneous medium. The concepts for the design and analysis methods reviewed in Chapter 2 constitute the core of the original porous GRIN ideas presented in this thesis. In particular, the free forming (FF) approach has been employed to generate deformed materials based on 3D printing technology to control the amplitude and phase profiles of the intended permittivity for required lens function subzones. Also, this free-forming and generation virtual permittivity method has been revised to implement simple planar half-wave and quarter-wave Fresnel zones, with a general multi-dielectric Fresnel zones technique for mmWave wavelength. The recommended design significantly simplifies previous multi-dielectric inhomogeneous approaches by (i) using single dielectric combined with material porosity and additive manufacturing processes, overcoming the manufacturing complexity with required permittivity implementation and the cost, and (ii) reducing multiple reflections of the plate because of the high permittivity zones by smaller effective permittivity zones to produce the intended phase shift with lower attenuation.

In Chapter 4, the concept of a parallel-plate, porous, dielectric Lüneburg lens is introduced with the tubular cells of a classical permittivity control approach in the TEM waveguide. The strong potential of this approach is in its capacity for simultaneously controlling the material filling ratio through cell thickness and radius with two degrees of freedom. The cost for achieving GRIN lenses using inhomogeneous metamaterial forms lies in fabrication problems, the challenge of broad-

range virtual permittivity control, and the narrowband properties which comprise at least half of the full dielectric structures' bandwidth. A possible configurations based on intended GRIN lens platforms and rules have been suggested, namely, an air hole approach. The proposed arrangement have been analytically confirmed by implementing interesting homogeneous GRIN lens designs with applications of mmWave communications.

In chapter 6, we briefly review various potential lines of future porous-base GRIN lens research considered to be of high relevance by the author.

As a collective conclusion, regarding the extensive range of applications of permittivity control with porous structures, we can foresee the vast amount of exciting uses for the graded medium design in planar or 3D objects. Due to the extensive collection of utilization, this proposed concept uses 3D printing devices that can be employed (some of them have been experimentally confirmed in this thesis), and the presented project may motivate the development of an innovative form of lens devices, more efficient lens devices as an antenna in the areas of mmWave communication. Advantages of these virtual permittivity design using full dielectric or full metal homogeneous approaches include (i) a notable simplification of the currently required graded setups based on material change approach to achieve the equivalent variety of functionalities; (ii) the possibility of realizing all-optical GRIN devices for lens antenna design applications, with development from mm to nm printing ranges to be achieved, so far, through additive manufacturing technology widely used nowadays; and (iii) the significant rest of previous GRIN medium design practical difficulties in the lens devices manufacturing processes is solved. All the suggested schemes appear as stable and dependable solutions for efficiently GRIN lens designs of practical applications, and they may also be entirely placed in the industry for short-term fabrication. Overall, we expect that the contributed investigation outcome of our porous design approach for the lens antenna design will have a markedly relevant scientific and economic effect in such diverse areas as mmWave communication and wave focus applications.

6.2 Future perspectives

Next, we briefly review various potential lines of future porous-base GRIN lens research considered to be of high relevance by the author:

1. In Chapter 2, we discussed the implementation of material porosity for the generation of composite porous structure cells of a GRIN mediums' framework in cell type and material arrangements, which is based on a materials theory and Corkum's studies. However, the previous inhomogeneous frame of GRIN structures' limitation in the operation bandwidth imposed by the employed narrow-band metamaterial cells and the dielectric metamaterial cells with porous design led to broadband output as a solution. In particular, the four porous-base permittivity control approaches were categorized to produce the expected graded medium rules. So, to have effective control of the intrinsic permittivity of a host medium corresponding to the realization of virtual permittivity, it was essential to attenuate part of the proposed host medium to decrease the intrinsic permittivity in classical theory. As explained in Chapter 2, there is an analogy between the offered configuration and the scheme of adding new material for permittivity increase more than host medium dielectric constant with material porosity technique. Accordingly, it should be feasible to use this approach in which the porous holes are filled by other kinds of materials-based configuration (as the one presented in [97]), in order to develop the production of the wide and high refractive index GRIN scheme in terms of lens design.

2. The design method revealed for the implementation of 3D GRIN optical devices such as Luneburg, Maxwell fish eye lens based on the homogeneous framework enabled the synthesis of 3D printed lenses and beam shaping devices in compact and modified formats for the antenna purposes. Among them, we can quote:

(a) 3D printed Luneburg lenses with free-forming approach [10, 15]: it is of great interest for the implementation of spherical multi-shell Luneburg lens [78], half Maxwell fish eye, or any desired non-resonant GRIN functions, e.g., Eaton lens beam-shaper [97]. In the last example, non-resonant woodpile construction in the metamaterial regime with a liquid compound medium allowed a wide refractive index range ($\Delta n = 1 \rightarrow 6.32$), which can be used for other types of GRIN lens antenna applications.

(b) Tubular porous cell: tubular permeable cells are widely manipulated to achieve lower refractive index. The ultra-flat Fresnel zone plate in plastic material for mmWave communication is one of these results by Petosa [6, 7]. They are also impressive as Luneburg lens, and Sieve lens design in THz.

(c) Free-forming material permittivity analysis due to the complexity of design is difficult: unique permittivity analysis based on Hausdorff dimension can be used for the implementation of tunable cells, permittivity control in complex geometric devices, and new optic transformation lenses, for other applications such as antenna engineering [10, 15, 11].

3. In Chapter 3, the introduced free-form design technique based on cube-shaped cells has been applied for the implementation of half- and quarter-wave Fresnel zone plates. However, that approach could be revised to achieve complex type refractive index distribution functionalities. Free-forming porous structures with 3D printing materials are of high interest for the compensation of virtual permittivity control and GRIN device design nowadays.

4. The common porous design approach presented in Chapter 4 for the realization of non-resonance dielectric Luneburg lens antenna based on defocus feeding approach with redesign permittivity distribution in TEM waveguide could be applied to a diversity of optical GRIN devices with similar radial refractive distribution. In particular, it would be of high-interest manufacturing of a non-resonant GRIN lens antenna, e.g., a Luneburg, and study high permittivity material with the addition of this approach and optic transformations would enable the achievement of thinner Luneburg lens antennas with a broader operation bandwidth than the one typically performed by resonant metamaterials.

5. In chapter 5, a porous Fresnel zone plate lens composed of a homogeneous profile fed with a conical horn antenna was provided for millimeter-wave applications. The suggested ZP utilizes the cube-shaped unit cells, appropriately designed by providing analytical models to form homogeneous lens subzones' virtual permittivity and skeleton. A prototype of such half-wave FZP was built and experimentally identified in the lab. The fabricated FZP lens was intended to work at the center frequency of 30GHz. The experimental results confirmed that the lens antenna shows constant pencil beam radiation properties within the 25-40 GHz frequency spectrum. For the corresponding lens aperture dimensions, homogeneous type lenses reported hereabouts are demanded to show higher gain and efficiencies than earlier reported prototypes with the Alumide base homogeneous frame. The lens illuminator performance of the presented Fresnel was also verified by spill over and taper efficiency equation analysis to find the best amplitude weighting for identifying symmetrical cos-like illuminators' character to achieve high efficiency.

Chapter 7

Résumé

7.1 Résumé

La structure de l'indice de réfraction de gradient (GRIN) est un résultat optique généré par une variation progressive de l'indice de réfraction d'un milieu hôte pour améliorer la conception de nouveaux dispositifs à micro-ondes 1. Ainsi, ces modifications du milieu hôte peuvent être utilisées pour produire des lentilles pour tous les spectres électromagnétiques à surfaces planes, ou volumes 3D ne présentant pas les aberrations des lentilles sphériques traditionnelles ou présentant un gradient de réfraction avec des variations sphériques, axiales ou radiales [1, 2]. Ce gradient de réfraction peut être réalisé dans un milieu homogène ou inhomogène en utilisant des méthodes soustractives ou additives comme technique de contrôle de la porosité du matériau. La porosité, ou fraction de vide, est une méthode technologique de contrôle de la permittivité permettant de mesurer le vide comme méthode soustractive en réduisant le milieu hôte ou en utilisant un ratio du remplissage de matériau comme méthode additive, qui peut avoir un pourcentage entre 0 % et 100 %, pour réaliser la plate-forme finale [3].

Les structures poreuses intégrées dans le cadre homogène ont des intérêts scientifiques et trouvent leur utilité dans la conception de lentilles GRIN en raison de leur capacité à atteindre la permittivité virtuelle voulue dans la masse du matériau. Sans surprise, le contrôle de la permittivité virtuelle traditionnelle avec des matériaux poreux impliquant des diélectriques en réduisant la densité (taux de remplissage) des trous sphériques ou cylindriques était déjà prouvée dans les années

1950 de même que toutes les techniques avec l'ordre de conception de haute liberté qui pourrait être produit avec un processus de fabrication additif [4]. Malheureusement, ces résultats n'ont pas reçu beaucoup d'attention aujourd'hui malgré l'analyse très intéressante et précise. Dans les années 1950, la première analyse visant à contrôler la permittivité virtuelle, en utilisant un tableau de cellules sphériques et cylindriques dans le Téflon et le polystyrène, a été étudiée et prouvée avec des expressions mathématiques [5, 4]. Sur la base des analyses de pores cylindriques, pour un rapport longueur-diamètre élevé, le contrôle de la permittivité est directement lié à l'orientation des champs électriques et des axes de pores cylindriques. En utilisant ces méthodes de porosité, le contrôle de la permittivité dans les plages comprises entre 1,1 et la permittivité du milieu hôte peut être obtenu. Pour élargir cette gamme, des matériaux liquides à cellules poreuses tels que le mélange acétonitrile/benzène peuvent être utilisés pour remplir et augmenter la permittivité relative du milieu hôte jusqu'à $\epsilon = 37$.

Dans cette thèse, nous avons introduit des concepts innovants et optimisés dans le cadre des communications mmWave, à savoir antennes optiques non magnétiques à gradient de réfraction. Les deux idées sont destinées à améliorer les technologies de fabrication actuelles pour les dispositifs GRIN dans le spectre mmWave: la lentille Lüneburg et les plaques zonales de Fresnel (FZP) dans le cadre homogène. D'une part, la porosité du matériau peut être utile pour simplifier la conception de permittivité virtuelle, non seulement dans les étapes de mise en œuvre et de mesure, mais aussi pour activer des cellules potentielles avec de nouvelles propriétés à large bande et des schémas simplifiés de compensation de perte dans les spectres mmWave et sub-mmWave. D'un autre côté, les techniques de contrôle de la permittivité basées sur la porosité du matériau peuvent également faciliter le développement de nouvelles techniques de conception de dispositifs GRIN pour les applications de lentilles. En fait, l'introduction de la théorie des matériaux basée sur le traitement de la porosité est l'une des méthodes les plus encourageantes pour contrôler la permittivité intrinsèque du matériau.

En conclusion, en ce qui concerne la vaste gamme d'applications du contrôle de la permittivité avec des structures poreuses, nous pouvons prévoir plusieurs cas d'utilisations passionnantes pour le design gradué du support dans les objets planaires ou 3D. En raison de la vaste collection d'utilisation, ce concept proposé utilise des dispositifs d'impression 3D (certains d'entre eux ont été confirmés expérimentalement dans cette thèse), et le projet présenté peut motiver le développement d'une forme innovante de dispositif de lentilles plus efficaces sous forme d'antenne dans les domaines de la communication mmWave. Les avantages de cette conception de la permittivité virtuelle en

utilisant des approches homogènes diélectriques ou métalliques complètes comprennent: (i) une simplification notable des configurations graduées actuellement requises et basées sur l'approche de changement de matériau pour obtenir la variété équivalente de fonctionnalités; (ii) la possibilité de réaliser des dispositifs GRIN tout optique pour des applications de conception d'antennes de lentilles, avec développement de plages d'impression de mm à nm à atteindre, jusqu'à présent, grâce à une technologie de fabrication additive largement utilisée de nos jours; et (iii) le reste significatif des difficultés pratiques antérieures de conception de milieu GRIN dans les procédés de fabrication des dispositifs de lentilles est résolu. Tous les schémas proposés apparaissent comme des solutions stables et fiables pour des conceptions de lentilles GRIN efficaces pour des applications pratiques, et ils peuvent également être entièrement intégrés dans l'industrie pour une fabrication à court terme. Dans l'ensemble, nous nous attendons à ce que le résultat de notre approche de conception poreuse pour la conception d'antennes à lentilles ait un effet scientifique et économique nettement pertinent dans des domaines aussi divers telque la communication mmWave et les applications de focalisation des ondes.

Mots-clés: Antenne, procédé de fabrication additif, plaque de Fresnel, indice de réfraction de gradient (GRIN), lentille, Luneburg, porosité du matériau, mmWave, perforation, stéréolithographie, frittage laser sélectif, impression en 3D.

7.2 Structures poreuses ordonnées pour les lentilles GRIN émergentes : une critique

La structure d'indice de réfraction de gradient (GRIN) est un résultat optique généré par une variation progressive de l'indice de réfraction d'un milieu hôte pour améliorer la conception de nouveaux dispositifs à micro-ondes [1]. Ces modifications du milieu hôte peuvent donc être utilisées pour produire des lentilles pour tous les spectres électromagnétiques à surfaces planes, ou volumes 3D ne présentant pas les aberrations des lentilles sphériques traditionnelles ou présentant un gradient de réfraction avec des variations sphériques, axiales ou radiales [1, 2]. Ce gradient de réfraction peut être réalisé dans un milieu homogène ou inhomogène en utilisant des méthodes soustractives ou additives comme technique de contrôle de la porosité du matériau.

La porosité, ou fraction de vide, est une méthode technologique de contrôle de la permittiv-
ité permettant de mesurer le vide comme méthode soustractive en réduisant le milieu hôte ou en
utilisant un ratio du remplissage de matériau comme méthode additive, qui peut avoir un pour-
centage entre 0 % et 100 %, pour réaliser la plate-forme finale [3]. Les structures poreuses intégrées
dans le cadre homogène ont des intérêts scientifiques et trouvent leur utilité dans la conception
de lentilles GRIN en raison de leur capacité à atteindre la permittivité virtuelle voulue dans la
masse du matériau. Sans surprise, le contrôle de la permittivité virtuelle traditionnelle avec des
matériaux poreux impliquant des diélectriques en réduisant la densité (taux de remplissage) des
trous sphériques ou cylindriques était déjà démontrée dans les années 1950 de même que toutes
les techniques avec l'ordre de conception de haute liberté qui pourrait être produit avec un proces-
sus de fabrication additif [4]. Malheureusement, ces résultats n'ont pas reçu beaucoup d'attention
aujourd'hui malgré l'analyse très intéressante et précise.

Dans les années 1950, la première analyse visant à contrôler la permittivité virtuelle en utilisant
un tableau de cellules sphériques et cylindriques dans le Téflon et le polystyrène a été étudiée et
prouvée avec des expressions mathématiques [5, 4]. Basé sur des analyses de pores cylindriques,
pour un rapport longueur-diamètre (L/D) élevé, le contrôle de la permittivité est directement lié à
l'orientation des champs E et des axes de pores cylindriques. En utilisant ces méthodes de porosité,
le contrôle de la permittivité est compris entre $\epsilon = 1,1$ ($\sim \epsilon_{Air} = 1$) jusqu'à la permittivité du
milieu hôte peut être obtenu. Pour élargir cette plage, des matériaux liquides poreux comme le
mélange acétonitrile / benzène peuvent être utilisés pour remplir et augmenter la permittivité rel-
ative du milieu hôte jusqu'à $\epsilon_r = 37$ [19, 14]. En outre, des échantillons à base de plastique avec
différentes tailles des formes de pores ont été discutés, et l'inclusion d'une analyse des caractéris-
tiques diélectriques telles que la permittivité et la perméabilité dans les matériaux hôtes poreux a
donné naissance à de nouveaux phénomènes et à concevoir des permittivités virtuelles.

Mais malgré ce rapport sur la réduction de la permittivité des matériaux et ses applications,
aucune de ces techniques n'a abouti à des succès pratiques dans la conception des lentilles GRIN
jusqu'à les inventions d'impression 3D en raison des limitations de fabrication et de mise en œuvre
[1, 26, 27, 34]. Le contrôle de la permittivité via les pores pour le milieu à indice gradué peut être
organisé en fonction de la taille, des formes et des volumes [5, 4]. Par conséquent, le contrôle de la
permittivité virtuelle à large spectre utilisant un milieu hôte diélectrique élevé [19, 14] est réalisable,
et ses applications sont intéressantes dans la conception de lentilles GRIN pour les spectres des

micro-ondes, les ondes millimétriques et optiques électromagnétiques. Pour la classification des tailles de pores, la gamme de pores classifie le type de porosité du matériau en fonction de la largeur des cellules de porosité par rapport aux diamètres ($\frac{w_{pores}}{D_{pores}} = \zeta_p$). On trouve les micropores ($\zeta_p \leq 2nm$), mésopores ($\zeta_p \leq 50nm$), et macropores avec des vides de taille supérieure à ($\zeta_p \geq 50nm$) [34]. Au cours des dernières décennies, la plupart des publications sur les structures de lentilles GRIN imprimées sont basées sur le contrôle de la porosité de type macropores qui est réalisé avec des méthodes de fabrication additive pour les applications d'ingénierie des antennes [28]. Classiquement, la plupart des lentilles optiques ont été fabriquées par des techniques soustractives, telles que les rainures de coupe [29], les trous d'air de coupe [6, 7] et les lentilles d'usinage.

7.3   Processus d'impression 3D et matériaux

L'impression 3D est un processus additif de fabrication [32, 33, 35] qui peut réaliser des objets créés en 3D en ajoutant une couche à la fois de bas en haut avec un matériau prédéfini. Le terme fabrication additive (ADM) est présenté dans des technologies telles que le prototypage rapide (RP), la fabrication en couches, la fabrication numérique directe (DDM) et l'impression 3D [32, 35]. Par conséquent, il n'y a pas de différence entre tous ces processus, et ils sont synonymes pour le même processus. Au cours des dernières années, cette technologie a attiré plus d'attention pour la fabrication en raison de son faible coût de fabrication, de sa grande évolutivité, de sa facilité de mise en œuvre et de la combinaison de matériaux métalliques et diélectriques. De plus, cette technologie peut être considérée comme une technologie verte, qui est une alternative aux méthodes de fabrication de stratification conventionnelles.

Dans les travaux rapportés, les procédés de fabrication SLS, SLA et FDM sont utilisés pour la fabrication de prototypes micro-ondes et GRIN, et les résultats sont comparés avec les composants fabriqués de façon conventionnelle [32, 21, 36]. Pendant SLS, de petites particules à base de matériaux en poudre tels que le plastique, le verre ou la céramique sont combinées par la chaleur laser pour former une structure 3D rigide [32, 33]. Ce processus a été inventé dans les années 1980 par Deckard et Beaman à l'Université du Texas (UT) [32, 36]. Comparable à d'autres dispositifs d'impression 3D, le mécanisme du dispositif SLS commence par un fichier de conception assistée par ordinateur (CAO) [33, 36]. Les fichiers CAO sont transformés en format numérique .STL avec un logiciel d'interface, qui joue un rôle crucial dans la transformation des couches souhaitées entre

le matériel et les ordinateurs [33, 35, 36]. En se basant sur les rapports de [36], dans cette méthode de machine d'impression, les objets imprimés sont créés avec des matériaux de base de poudre tels que PA12, qui est enduit sur la fine couche imprimée sur la plaque de travail de la machine SLS. Un laser commandé par un ordinateur, outre que la tâche d'impression de l'objet, effectue également la tâche de détection des coins de l'objet réalisé sur les particules de poudre [36]. Ensuite, le processus de frittage et de fusion par faisceau laser continue encore et encore pour imprimer tout l'objet [36]. Lorsque toutes les couches d'impression de l'objet sont complètement développées, il doit être laissé dans le dispositif SLS pour le refroidissement de l'objet entier [36].

Contrairement aux autres méthodes d'impression 3D, le SLS utilise un petit outil supplémentaire après la sortie d'un objet, ce qui signifie que, régulièrement, à la sortie du dispositif SLS, les objets ne doivent pas être rincés autrement ou correctement changés [36]. SLS n'a pas besoin d'utiliser de support supplémentaire pour garder un objet à l'intérieur pendant qu'il est encore en train de l'imprimer comparer aux méthodes SLA ou FDM [33, 36]. Ce traitement de fabrication additif comprend des matériaux distincts tels que le nylon ou le polystyrène, des métaux tels que l'acier, le titane et des mélanges composites, et du sable vert [36, 37]. La capacité de l'impression à base de poudre SLS à créer une géométrie hautement sophistiquée rapidement et directement contribue aux données CAO numériques par rapport à d'autres techniques [33, 35, 36]. SLS est de plus en plus utilisé dans l'industrie avec des composants de faible quantité nécessitant des composants de haute qualité tels que l'industrie aérospatiale, l'ingénierie des voitures de sport et l'ingénierie micro-ondes [33, 35, 36].

7.4 La permittivité artificielle utilisant l'utilisation de la déformation poreuse

Le contrôle de la permittivité virtuelle pour réaliser la fonction désirée, telle que radiale dans les structures de lentilles de Lunenburg [49, 50, 51, 52, 53] ou d'autres applications particulières, est directement lié à la taille, les formes, et les volumes de porosité, qui sont appelées des cellules, comme représenté sur la Fig. 7.1. En raison des progrès dans les procédés de fabrication additive et les matériaux, la nécessité de créer des structures de lentilles GRIN a régulièrement augmenté au cours des dernières années, ce qui peut mener à la fabrication de structures supérieures et complexes bon marché et rapidement. Fig. 7.1 à Fig. 7.2 montrent des structures conventionnelles de cellules
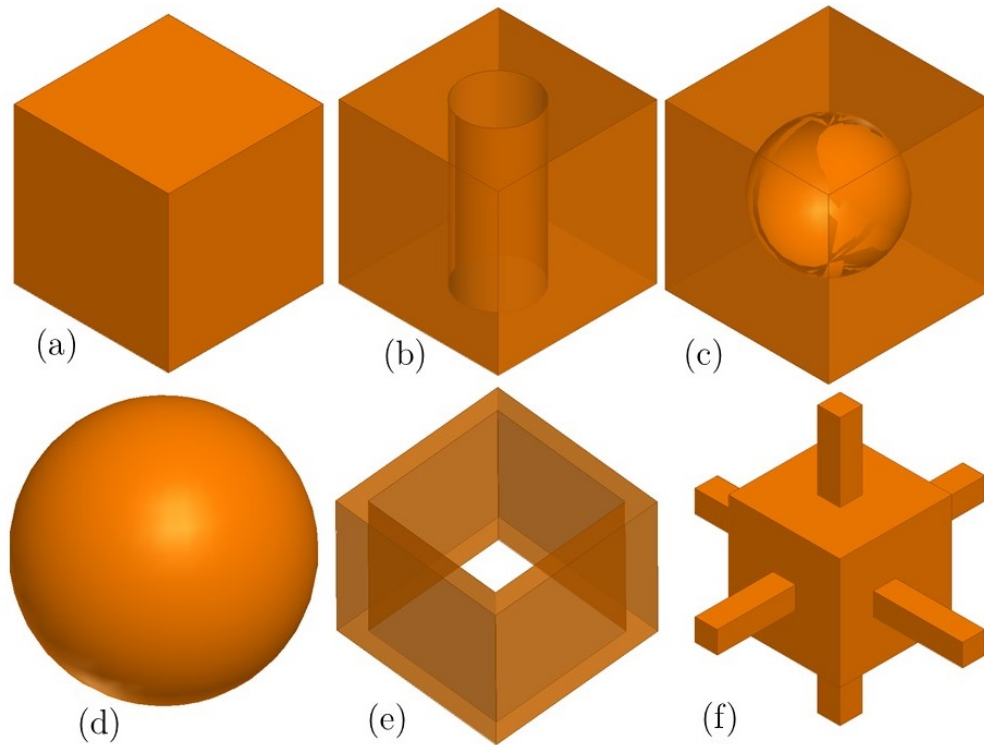
Figure 7.1 – Structures poreuses unicellulaires diélectriques ou métalliques pour le contrôle fonctionnel de la permittivité diélectrique (ϵ_{eff}), de l'indice de réfraction (n_r) et des milieux GRIN avec une permittivité prédéterminée. (a) une structure de cube typique pour contrôler la permittivité diélectrique en changeant l'épaisseur du cube ; C'est approprié pour les orientations verticales du champ E. (b) Une structure perforée avec une porosité de forme cylindrique pour contrôler la permittivité. Elle a deux degrés de liberté comme étant le rayon et la hauteur du cylindre. (c) un cube perforé avec une porosité sphérique. (d) une cellule sphérique. (e) un cube perforé. (f) une cellule de porosité en forme de cube avec des tiges de connexion qui est appropriée pour produire des milieux GRIN sphériques;

poreuses uniques pour façonner des porosités de réseau à la permittivité de contrôle fonctionnel virtuel et atteindre des milieux gradués. Dans ce processus, une réduction de la taille des pores ou du taux de remplissage réduirait la permittivité du milieu hôte et la capacité de contrôle de la permittivité avec des échelles différentes. La croissance continue des technologies de fabrication additive, en particulier dans les types de matériaux avec différentes permittivités, rend les expansions et les applications des structures de lentilles GRIN raisonnables.

126
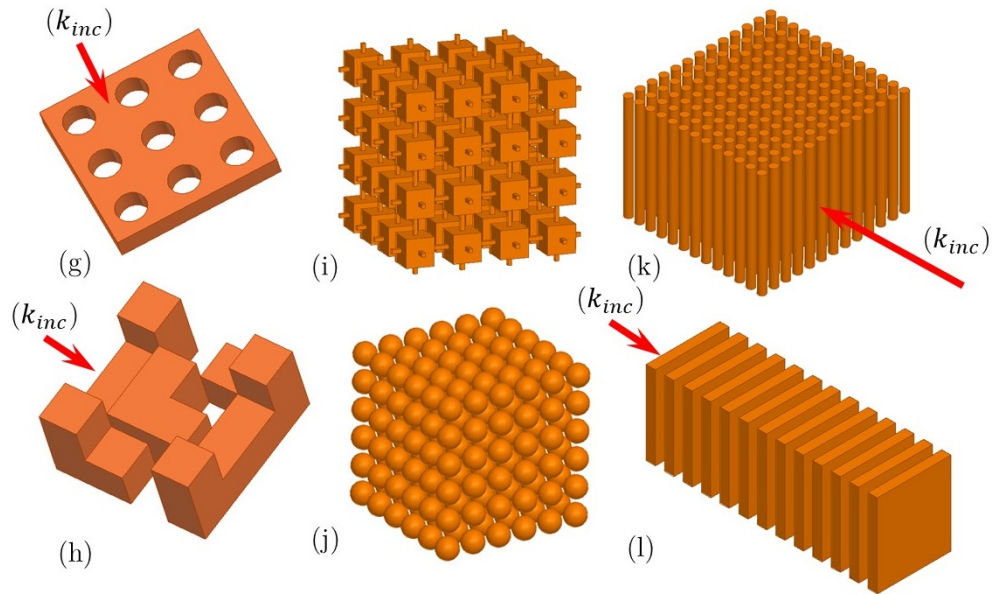
Figure 7.2 – Modes conventionnels de tableaux pour contrôler la permittivité virtuelle avec les frameworks homogènes. Milieu spatialement homogène pour réaliser une permittivité prédéterminée ou peut être utilisé avec des cellules poreuses distinctes pour atteindre un milieu GRIN [6, 7, 8]. (g) Fournir un contrôle de permittivité par épaisseur de cube et réaliser un milieu GRIN pour le façonnage du faisceau sur le front d'onde du champ E ($\perp$ incidence) [9]. (h) Dans les diélectriques déformées, le champ E a une composante de propagation le long de la direction de l'onde d'incidence, un treillis en forme de cube [10, 11, 12]. (i), treillis sphérique [5, 4]. (j), Les paramètres de structure proposés typiques incluent un réseau 3D pour la conception de milieu GRIN [13] (k), ou peuvent être réalisés dans une géométrie de guide d'ondes [13], [14, 15] (l);
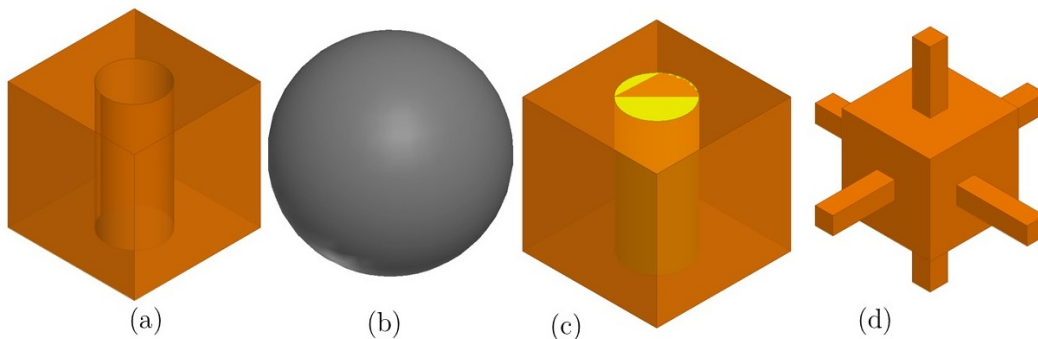
Figure 7.3 – Les Catégories de techniques de porosité pour la conception de la permitabilité virtuelle: **(a)** Porosité à base de trou d'air. **(b)** Entièrement métal. **(c)** Des porosités de matériaux remplis de permittivité, et **(d)** des structures poreuses de type formation libre.

7.5 Catégories de techniques de porosité pour la conception de Permittivité Virtuelle

Il y a quatre cellules poreuses communes appliquées dans la conception de la permittivité virtuelle, qui sont résumées sur les Fig. 7.3 (a-d). Ici, nous définissons les méthodes de porosité utilisées

pour concevoir la permittivité prévue basée sur le schéma homogène ; la majorité des conceptions de permittivité virtuelle dans cette catégorie manipulent le rapport de matériau en réduisant ou en déformant le milieu hôte qui compose les cellules. Une des nombreuses approches possibles est représentée sur la figure 7.3 (a), par laquelle une cavité de trou d'air sous des formes cylindriques est integré dans le milieu hôte différent. La deuxième approche est l'option entièrement métallique qui est montrée dans Fig. 7.3 (b), en vertu de laquelle des cellules métalliques sphériques avec la permittivité spécifique sont incorporées dans le milieu hôte différent. Par conséquent, si un indice de réfraction gradué est désiré, un volume sphérique variant peut être uni dans le milieu hôte pour rendre cette approche réalisable [4]. Il est également possible d'augmenter la permittivité voulue en utilisant des matériaux à constante diélectrique plus élevée à partir du milieu hôte sous forme de liquide ou de poudre pour augmenter la gamme de milieux gradué désiré. Ce schéma est présenté dans la Fig. 7.3 (c) [19]. Ainsi, pour contrôler la permittivité virtuelle sous forme dynamique, cette méthode peut potentiellement être utilisée dans la partie des différents matériaux de l'élément à fabriquer avec des matériaux de fabrication additive, aboutissant à la conception innovante de la lentille GRIN, comme le montre la Fig. 7.3(d). Enfin, pour les ondes avec une polarisation circulaire, la combinaison des éléments diélectriques et métalliques résultantes avec des technologies d'impression 3D peuvent être considérées pour produire les déphasages requis dans les sous-zones de lentilles GRIN, comme le montre la Fig. 7.3(c) en raison de la facilité de fabrication.

7.6 Permittivité virtuelle conçue en fonction de la porosité du trou d'air

Alors que les milieux à indice de réfraction non homogène modifient les diélectriques des sous-zones pour changer leur indice de réfraction, le milieu homogène réalise ceci en utilisant des cellules remplies d'air [5, 4, 6, 7]. La porosité du trou d'air qui contrôle l'indice de réfraction des sous-zones virtuelles est connue depuis longtemps. Par exemple, grâce à l'utilisation de trous forés dans la mousse et Plexiglas [4], la première permittivité virtuelle contrôlée était basée sur un design homogène [6]. Cependant, il est essentiel de contrôler avec précision le choix de la permittivité prévue à la taille des sphères et des cylindres afin d'atteindre les larges plages diélectriques réalisables avec les éléments remplis d'air et cette conception précoce basée sur les plastiques en mousse n'atteint qu'entre 1,1 et 2,6 de la plage ($\Delta n = 1, 5$) [5]. Une plus grande gamme de permittivité a été obtenue

à partir de ce concept en considérant divers schémas géométriques de chargement pour les trous remplis d'air basés sur des orientations E classées [5, 4, 7] et en incorporant les trous au milieu hôte diélectrique en taille appropriée [7, 30, 31].

7.7   Conception de permittivité virtuelle basée sur différentes porosités matérielles de type "Permittivity-filled"

Plutôt que de contrôler la permittivité virtuelle avec une porosité remplie d'air telle que présentée jusqu'ici [5, 4], il est également possible d'améliorer les propriétés diélectriques et ferroélectriques par une approche poreuse remplie de diélectrique. Dans ce cas, les nanofibres avec un rapport d'aspect élevé sont utilisées comme charges diélectriques dans les polymères pour améliorer la permittivité du milieu hôte. Le pourcentage de nanofibres est ensuite contrôlé dans une fraction à faible volume, ce qui donne la valeur de permittivité voulue. Cette méthode a d'abord été appliquée à des composites à base de polymères, puis étendue à des charges de nanocarbone conductrices en appliquant des longueurs et des rayons de phase contrôlables qui peuvent également être utilisés pour concevoir des guides d'ondes intégrés. L'approche remplie de diélectrique pour la conception d'un milieu GRIN présente à la fois des avantages et des inconvénients par rapport à la technique de porosité remplie d'air.

Premièrement, les cellules poreuses remplies d'air de la première méthode sont plus accessibles au développement, à l'optimisation et à la fabrication. En effet, alors que la modélisation est assez similaire pour les deux approches, le fait que les propriétés diélectriques et ferroélectriques peuvent être optimisées indépendamment dans l'approche remplie de diélectrique conduit à un contrôle élevé de la permittivité [69]. Par exemple, dans les simulations d'échantillons de conception, il est assez simple d'obtenir un haut niveau de contrôle de la permittivité virtuelle et d'ajouter des propriétés ferroélectriques, alors que le faire en laboratoire et l'ajout de fibres chargées dans des polymères ou dans un milieu hôte prévu peut nécessiter des procédés de fabrication additive compliqués ou des dispositifs encore à l'étude [68, 69, 61].

Une seconde amélioration de cette méthode est qu'un comportement de la constante diélectrique plus élevé est atteint car un indice de réfraction plus élevé peut être conçu pour produire une capacité de réfraction élevée pour les lentilles GRIN remodelées avec des couches d'adaptation

d'impédance [31]. Plusieurs études ont été développées basées sur la seconde approche du contrôle de la permittivité virtuelle, centrée sur le contrôle de la permittivité des mileux métasurfaces GRIN [70] et de la surface sélective en fréquence (FSS) [71, 72] comme conception de structures périodiques. La conception des lentilles utilisant la seconde approche dans le milieu homogène permet un réglage de la permittivité avec une densité nanométrique dans une forme de revêtement spécifiée, incluant un anneau circulaire, une grille planaire ou d'autres formes sur le support hôte souhaité dans la fréquence désirée [70].

7.8 Conception de la permittivité virtuelle basée sur des porosités entièrement métalliques

Un choix judicieux pour les méthodes de contrôle de la permittivité virtuelle ci-dessus, bien que limité aux matériaux conducteurs, est celui du milieu homogène uniquement métallique [21, 20, 67]. Ce principe de conception et d'analyse a été initialement appliqué aux lentilles de retard en métal en 1948 par W. Kock [67], et le système de développement associé et les équations basées sur le réseau de sphères métalliques sont bien connus [4]. Ici, nous passons en revue une formulation primaire pour la constante diélectrique d'un milieu de sphère métallique à base de tableau [5, 4]. Considérons une cellule métallique sphérique telle que la cellule soit noyée dans le métal ou en suspension dans l'air, comme le montre la figure Fig. 7.3. Sur la base de la théorie mentionnée ci-dessus, en arrangeant des sphères de conducteur électrique parfait (PEC) dans le réseau cubique et en plaçant ces réseaux dans un champ E statique uniforme ou un champ alternatif E, la charge libre de la sphère métallique sera supprimée par le champ appliqué [5]. Ce mouvement se produira lorsque le diamètre des sphères est beaucoup plus petit que la longueur d'onde dans le milieu diélectrique résultant [5]. Un choix judicieux pour les méthodes de contrôle de la permittivité virtuelle ci-dessus [5], bien que limité aux matériaux conducteurs, tels que le cuivre, l'aluminium, le titane et le carboneMide, avec conductivité électrique accrue, est celui du milieu homogène uniquement métallique. Ce mouvement se produira lorsque le diamètre des sphères est beaucoup plus petit que le λ dans le diélectrique hôte résultant [5].

7.9 Conception de la permittivité virtuelle basée sur la formation de structures poreuses libres qui ne peuvent être construites qu'avec une imprimante 3D

L'étude sur les cellules de contrôle de la permittivité virtuelle avec des matériaux diélectriques formateurs libres s'est d'abord concentrée sur le contrôle de deux paramètres : le taux de remplissage et la fabrication des cellules. Sur la base ci-dessus, cette analyse a vérifié que l'approche par gradient de réfraction est une solution favorable en gain élevé avec une lentille de focalisation, et exhorte à étudier des capacités plus avancées en matière de fabrication avec des coûts et une fréquence de fonctionnement raisonnables. Notamment, l'idée des cellules diélectriques de conception de formage libre basées sur des procédés et matériaux de fabrication additive est de supporter un contrôle de réfraction local dynamique pour la mise en forme du faisceau basé sur des milieux GRIN tout en réalisant simultanément des dispositifs bidimensionnels et tridimensionnels en plate-forme diélectrique complète. De tels modes de performance vers l'avant favoriseraient l'intérêt pour les lentilles planoconcave diélectrique, reflectarray, Lunenburg, Fresnel, polariseur et « sieve », offrant par exemple une ouverture commune pour les applications bi-fonctionnelles qui est l'une de ces approches et qui est aussi demandées dans des applications en ondes millimétriques (MMwave) et submillimétriques [74]. De plus, la plage élevée d'indice de réfraction avec des diélectriques à permittivité élevée peut être mise en œuvre pour réduire les tailles de lentilles sur la base de transformations optiques vers des objectifs de focalisation MMwave et sous-MMwave.

7.10 Défis futurs

Des structures poreuses sphériques contenant un arrangement symétrique d'axes optiques et présentant une grande stabilité pour une orientation de champ de $| E |$ sont hautement souhaitables pour un contrôle constant de la permittivité virtuelle. Un défi vital permettant la plate-forme homogène du milieu GRIN est, par conséquent, la construction de la permittivité virtuelle avec des propriétés constantes dans la contribution de diverses orientations de champ d'angle $| E |$. La deuxième approche essentiellement inexplorée consiste à créer une structure cellulaire de forme libre basée sur des géométries euclidienne et fractale qui sont basées sur un milieu homogène, ce qui pourrait s'avérer invaincu dans cet intérêt. En outre, de nouveaux types de processus de fabrication additive,

y compris l'impression à l'échelle nanométrique, et des matériaux de jets de polymères à haute permittivité qui peuvent faire l'objet d'un domaine de recherche émergent sont en cours d'élaboration car ces inventions peuvent souvent ouvrir de nouvelles portes pour les ingénieurs en optique et en micro-ondes avec la viabilité pratique des dispositifs GRIN poreux qui en résultent.

Un développement encourageant est le composé de ces matériaux imprimés en 3D qui peuvent avoir une vaste gamme de propriétés de permittivité, de perméabilité et de faible perte. La construction de matériaux diélectriques et métalliques de haute qualité permet de réaliser une large gamme de composés poreux GRIN, un défi supplémentaire qui n'est pas nouveau mais reste non résolu. Entre les exemples de dispositifs imprimés en 3D, la fabrication multi-échelle est hautement souhaitable. Cependant, les dispositifs appropriés peuvent réaliser tous les composés qui incluent de petits capteurs électroniques ou des pièces mécaniques à grande échelle n'ont pas encore été observées. Récemment, on a découvert que les dispositifs micro-ondes et THz imprimés en 3D affectaient l'industrie des micro-ondes, ce qui permettait de résoudre certaines contraintes de fabrication antérieures. Ces résultats imprimés en 3D, combinés à l'utilisation des materiaux avec de nouvelles propriétés EM, pourraient fournir une distribution révolutionnaire des propriétés EM et produire des dispositifs innovants. Les supports GRIN homogènes en métal imprimé pourraient également bénéficier d'une plus grande attention dans les applications de conception de lentilles GRIN. Le développement, la caractérisation et la formulation de la conception de cellules de milieux GRIN homogènes avec des conceptions de formage libres semblent particulièrement prometteurs. La présentation actuelle en forme de cube est simplement un exemple encourageant d'améliorations pour les plaques de zone de Fresnel [11] qui pourrait démarrer des conceptions de dispositifs distinctes. Bien sûr, de nombreux défis et objectifs demeurent, mais la vitesse de progression des appareils imprimés 3D, qui comprend des antennes, des lentilles GRIN et des circuits dans tous les spectres électromagnétiques de la dernière décennie, garantit que le domaine de recherche proposé produira des progrès impressionnants pour la troisième décennie du XXIe siècle.

7.11 Antennes de lentille mmWave à plaque de zone de Fresnel utilisant des plastiques poreux

Le contrôle de la permittivité est crucial pour la conception des lentilles GRIN (Gradient Refractive Index) telles que les lentilles Luneburg [77, 78, 79, 10], les lentilles demi-Maxwell Fisheye (HMFE)

[77] et les plaques zone de Fresnel [90, 91]. Les études connexes étaient principalement axées sur la nouvelle combinaison de matériaux ou sur la porosité du matériau et la déformation pour contrôler les permittivités. Déformer des structures de matériaux rigides telles que des trous d'air, des structures en forme de cube ou des matériaux de pressage sont des méthodes de porosité de matière apparente pour contrôler la permittivité intrinsèque [80, 77, 23]. Parmi les lentilles GRIN, les plaques zone de Fresnel (FZP), en raison de leur mérite planaire, de leur poids réduit, de leur facilité de fabrication et de leur rentabilité, sont des structures relativement plus attrayantes pour obtenir une focalisation à gain élevé dans le spectre des ondes millimétriques et submillimétriques [81, 90, 82, 92, 83]. Néanmoins, il n'existe que peu d'études sur le contrôle des permittivités des zones de correction de phase avec porosité en plastique et sur la réalisation expérimentale des géométries de lentille de mise au point planaire. Toutes les recherches ont révélé des idées prometteuses pour réaliser la tâche suivante : la porosité du matériau a été utilisée pour modifier les effets de la permittivité intrinsèque du matériau dans un milieu homogène, qui a été utilisé ensuite pour contrôler la distribution de la permittivité dans la surface de la lentille. Une correction de phase est réalisée par des sous-zones en milieu homogène ou inhomogène pour réaliser des zones de Fresnel. Les correcteurs de phase de sous-zone ont été suggérés par l'épaisseur des zones étagées et des trous d'air dans des plaques de zone homogènes [92, 83, 6], et une configuration de permittivité distincte est proposée avec des anneaux concentriques multi-diélectriques dans des plaques inhomogènes [83]. La porosité du matériau en forme de cube fait appel au besoin d'analyse pour mettre en œuvre des schémas de lentilles planaires. Les cellules en plastique en forme de cube ont été introduites et plus récemment réalisées par les procédés de fabrication additive pour contrôler la permittivity [38], ce qui est inaccessible avec les méthodes de fabrication conventionnelles.

Le sujet de ce travail est la réalisation de lentilles à plaques de zone de Fresnel basées sur le contrôle de la porosité du matériau. Nous utilisons la distribution multi-permittivité avec la satisfaction des règles de la plaque de zone pour atteindre la focalisation. En raison des sous-zones de correction de phase par rapport à la direction de transmission, l'objectif est de trouver la géométrie des zones de plaques en utilisant la méthode de la porosité du matériau. Afin de réaliser la permittivité synthétique avec du plastique, la valeur optimale de la taille des cubes est déterminée par analyse. En employant un taux de remplissage de cube approprié, nous identifions des géométries possibles dans chaque sous-zone pour une lentille de focalisation. Deux géométries de lentilles FZP à correction de phase demi ($\lambda/2$) et quart ($\lambda/4$) utilisant la modélisation par dépôt en fusion (FDM)
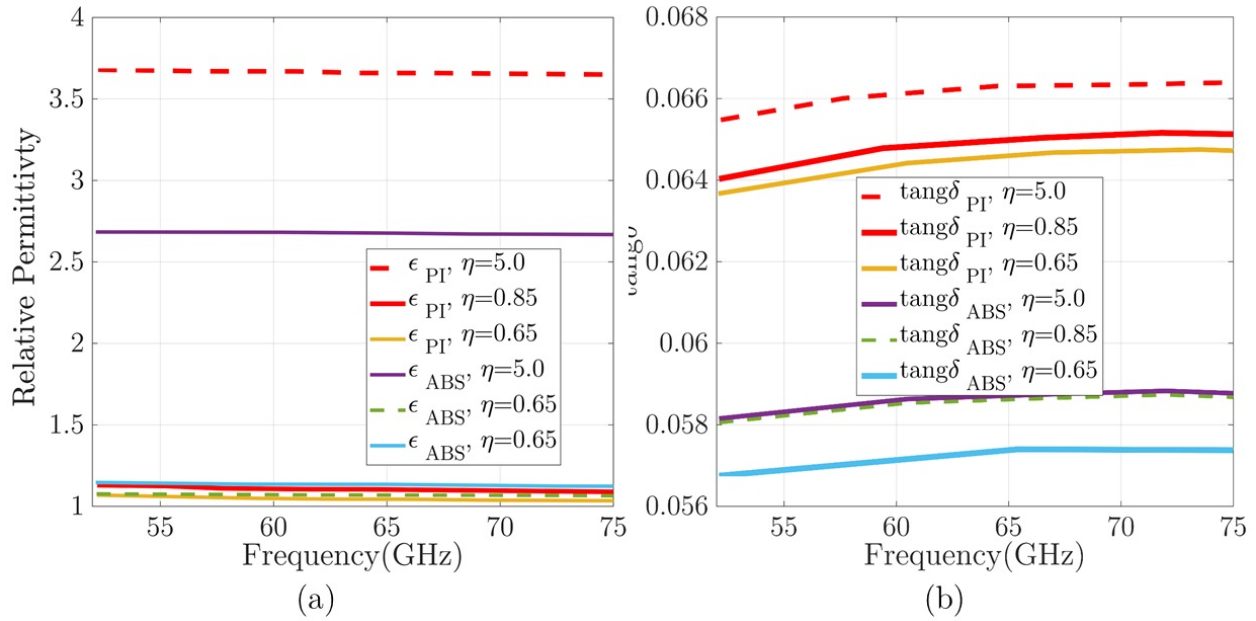
Figure 7.4 – **Illustration de la caractérisation de la bande V pour les échantillons imprimés en ABS et en polyimide 3D: (a) permittivité relative (ϵ_r) et (b) tangente de perte; pour les matériaux imprimés en 3D extraits des paramètres S $_{11}$ et S $_{21}$ mesurés avec la relation de Kramers-Kronig.**

[38] et le frittage sélectif laser (SLS) [38] comme processus de fabrication, sont expérimentalement réalisés, ce qui montrent un accord étroit avec les résultats de la simulation. La contribution de ce travail est la suivante : tout d'abord, la mise en place de zones à faible permittivité avec des cellules cubiques à faible permittivité pour réduire les réflexions. Deuxièmement, la conception de ZP poreuse homogène. Troisièmement, le rendement élevé, le gain et le faible niveau de lobe latéral par rapport aux travaux précédents. Quatrièmement, les faibles coûts de fabrication avec le processus de fabrication rapide.

7.12 Contrôle de la permitabilité avec méthode de la porosité du matériau pour les zones ZP

Les techniques de porosité du matériau en forme de cube ont été utilisées avec un procédé de fabrication additif pour modifier les effets de la permittivité intrinsèque du matériau dans un milieu homogène, ce qui est impossible avec les procédés de fabrication précédents. Nous avons étendu ce modèle de porosité pour satisfaire la permittivité relative attendue pour produire l'inversion de phase des zones planaires. Les cellules cubiques analysées sont utilisées pour réaliser le volume

entier de la zone de plaque avec des cellules discrètes et séparées. Les cellules globales en forme de cube sont construites avec deux plastiques distincts à base de polymères, qui sont choisis parmi les systèmes et les matériaux de fabrication additive EOS [38].

Puisque la permittivité exacte des matériaux diélectriques proposés est cruciale pour une simulation, une conception et une fabrication efficace des GRIN d'onde millimétrique de gammes moyennes. Par conséquent, les deux matériaux (ABS-M30 et Polyimide) échantillons de remplissage de guide d'ondes de dimensions de $3.7 \times 1.8 \times 5$ mm^3 sont conçuent pour remplir l'espaceur de guide d'onde WR-15. Ensuite, un analyseur de réseau PNA Agilent E8361A est utilisé pour permettre les mesures en bande V de l'ABS-M30 et des échantillons diélectriques en polyimide. La relation Kramers-Kronig (KK) est utilisée pour extraire les caractéristiques des matériaux imprimés (la permittivité relative et la tangente de perte) à partir des paramètres S$_{11}$ et S$_{21}$ mesurés. Fig. 7.4 montre les mesures extraites de la permittivité relative (ϵ_r) et de la tangente de perte (tang δ) pour les échantillons imprimés sur la bande V. Comme le montre la figure 7.4, les mesures de permittivité relative ϵ_r semblent stables et assez linéaires pour les fréquences supérieures à 70 GHz avec une légère pente descendante à mesure que la fréquence augmente. Comme prévu, le matériau en nylon PA2200 (polyimide) SLS présente une permittivité supérieure. La variation des mesures ϵ_r pour le matériau Polyimide est probablement le résultat de variations dimensionnelles pour les échantillons de remplissage du guide d'ondes en raison du développement des conditions de traitement pour ce nylon.

Actuellement, des variations de mesure de la permittivité relative inférieures à $\pm 3.2\%$ et $\pm 6\%$ sont obtenues pour les échantillons ABS-M30 et Polyimide, respectivement. Les mesures de tangente de perte (tan δ) donnent des valeurs maximales de 0,059 et 0,068 pour les échantillons ABS-M30 et Polyimide, respectivement, démontrant leur aptitude à des applications à ondes millimétriques. La taille totale de ces cellules pour les deux matériaux diélectriques est $5 \times 5 \times 5$ mm^3, comme le montre la figure 7.5 (a), où η est la taille du sommet du cube. Ces cellules sont reliées à des tiges rectangulaires en tant que support mécanique pour réaliser des plaques entières, comme le montre la figure 7.5 (a). La dimension du connecteur de la tige est fixée à 0,65 mm de diamètre pour avoir un petit impact sur la capacité de mise au point des plaques. En ajustant chaque taille de sommet de cube η, la constante diélectrique attendue est produite.
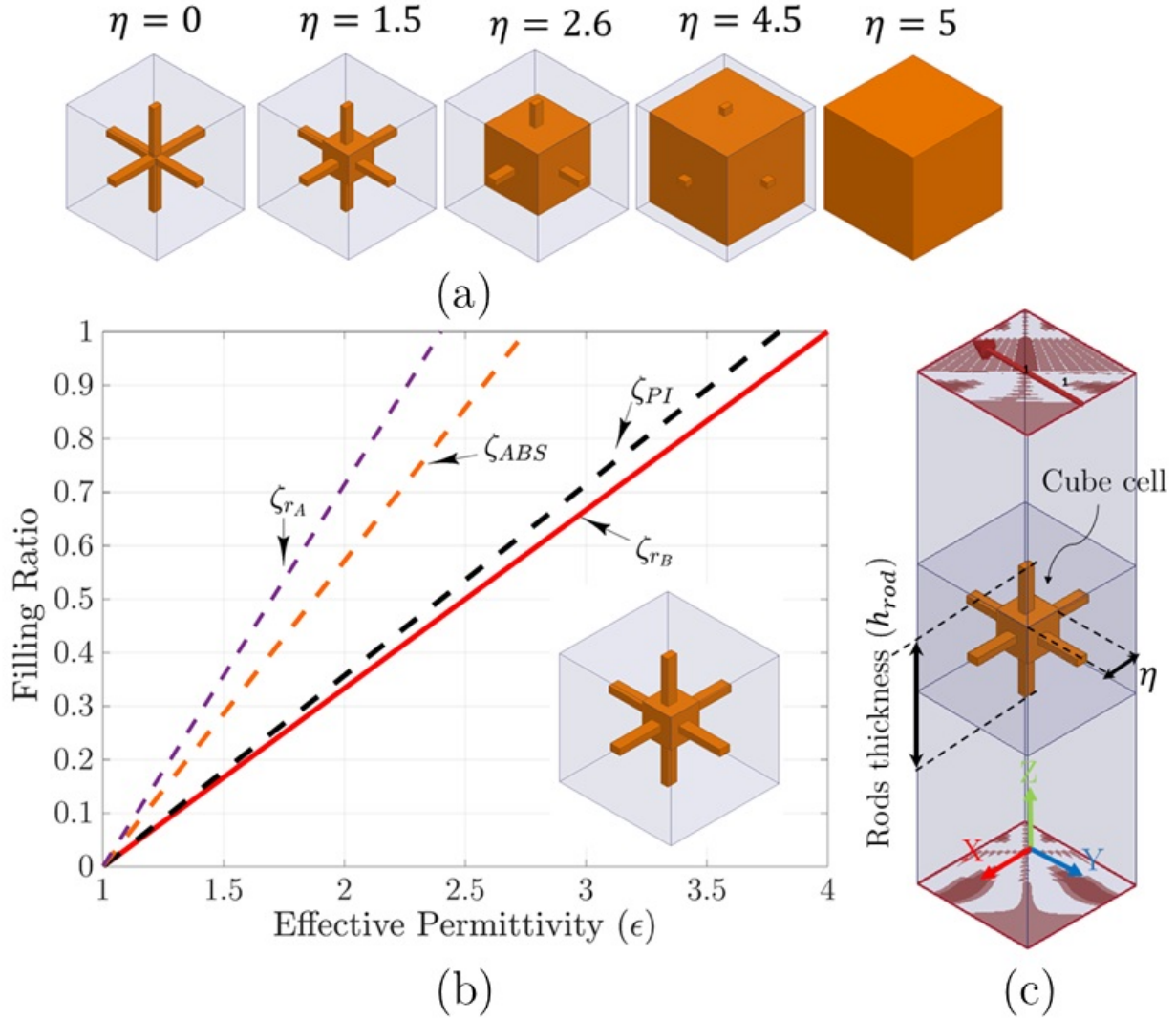
Figure 7.5 – **(a) Illustration du taux de remplissage ζ par rapport à la permittivité effective pour l'ABS, le polyimide et deux matériaux ayant des permittivités proches $\epsilon_{r_A} = 2, 4$, et $\epsilon_{r_B} = 4$ pour le taux de remplissage ζ extrait de (1). (b) Configuration de simulation HFSS pour une analyse de permittivité efficace, où $h_{tige} = 5mm$ est l'épaisseur des tiges, et η est la taille du cube de 0 à 5 mm;**

Comme nous l'avions prévu dans ce modèle de porosité du matériau, en réduisant le volume du cube dans le contrôle du taux de remplissage (ζ), une permittivité effective inférieure à la taille totale du cube est réalisable. Pour obtenir une géométrie de zone q, le taux de remplissage prédéterminé (ou tailles de cube) est utilisé pour réaliser chaque zone basée sur la distribution de permittivité donnée par Éq.(7.1). Comme la permittivité relative employée pour ABS-M30 [38] et Polyimide [38] est de 2,76 et 3,6, ce qui est réalisé avec une mesure, la réalisation de permittivité désirée dans
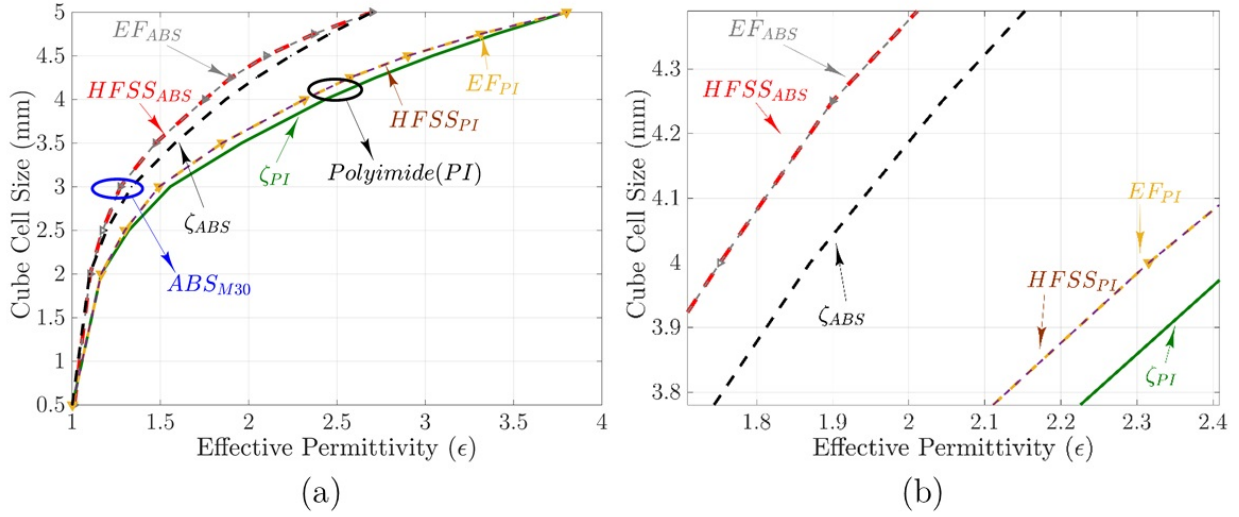
Figure 7.6 – **(a) Illustration de la taille du cube par rapport à l'analyse de la permittivité effective pour les plastiques ABS-M30 et Polyimide avec un taux de remplissage ζ, un ajustement exponentiel (EF) et des simulations Ansoft HFSS. Les courbes EF_{ABS} et EF_{PI} sont les données extraites de la fonction d'ajustement exponentiel. La taille du vertex cubique du polymère ABS η pour la permittivité prévue est obtenue en utilisant l'équation d'ajustement exponentiel (EF), où $\eta = 5.545 - 58092\ times\ e^{-\epsilon_r/0.07564} - 9.5423 \times e^{-\epsilon_r/0.95527}$, ϵ_r est la permittivité prévue, et η est la taille du cube pour les cubes en plastique ABS, (b) Un Zoom pour $1 \le \epsilon \le 2,4$;**

l'une jusqu'à ces permittivités par le contrôle du taux de remplissage est facile. La taille totale du cube pour cette analyse est de 5 mm, ce qui est égal à λ_0 à 60 GHz.

$$\epsilon_n = \epsilon_1.[1 + \frac{2}{n}(1 - \frac{n-1}{q})]^2. \tag{7.1}$$

Comme indiqué dans le schéma de réduction de volume 3D de la Fig. 7.5 (a), chaque cube est formé avec des vides d'air. Dans ce schéma, en supposant une permittivité effective et un taux de remplissage comme un ensemble de points de données tels que $(x_0 = \epsilon_{Air}, y_0 = \zeta = 0)$, $(x_1 = \epsilon_m, y_1 = \zeta = 1)$, un nouveau point de donnée utilisant l'interpolation linéaire est disponible. Par conséquent, une permittivité effective d'une cellule en forme de cube avec une réduction de volume est approximée avec une interpolation linéaire donnée par Éq.(7.2),

$$\epsilon_r = \epsilon_m.\zeta_m + \epsilon_{Air}.(1 - \zeta_m), \tag{7.2}$$

où ϵ_m est la permittivité matérielle et le paramètre m est dédiée aux matériaux plastiques ABS-M30 et Polyimide, alors que ϵ_{Air} représente la permittivité de l'air.
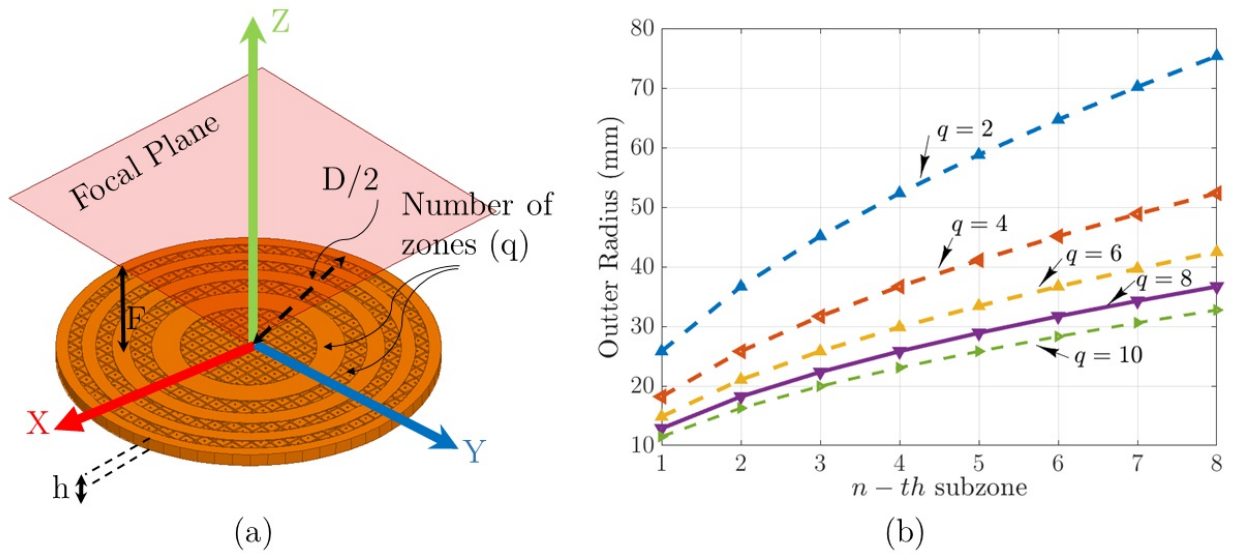
Figure 7.7 – (a) Les paramètres géométriques primaires qui déterminent la structure de notre lentille sont le diamètre de la lentille D, la distance focale F et le nombre de zones q (pour cette figure q est 2); (b) Rayon externe de la plaque de la zone de Fresnel par rapport à la sous-zone pour $2 \leq q \leq 10$ avec $\lambda = 5mm$ donné par **(7.2);**

Fig. 7.5 (b) montre le taux de remplissage ζ par rapport aux résultats de la permittivité effective. Comme le montre la figure 7.5(b), le rapport de remplissage par rapport à l'analyse de permittivité effective pour $\epsilon_{rA} = 2,4$ et ABS-M30 même avec des permittivités proches sont differents. De plus, la permittivité intrinsèque de la matière première est essentielle pour la taille finale d'un cube. Pour cette raison, l'analyse distincte devrait être considérée pour chaque substance particulière individuellement. Les résultats extraits pour la taille des cubes par rapport au taux de remplissage montrent que la variation de la taille des cubes par rapport à la permittivité effective n'est pas linéaire. Afin d'obtenir une tolérance de conception acceptable, nous ne pouvons pas nous contenter de cette approximation pour créer les lentilles de la plaque de zone. Dans une étude parallèle, une configuration de simulation HFS Ansys est utilisée pour calculer la valeur optimale de la taille du cube pour atteindre cet objectif. Chaque cellule ABS-M30 et plastique polyimide en forme de cube avec des tiges sont analysées dans le guide d'ondes, avec des limites PMC et PEC pour la mise en place de l'environnement périodique. Pour cette configuration, les ports d'onde sont situés sur le haut et le bas de la cellule de cube, comme indiqué sur la figure 7.5 (c). La permittivité effective de chaque cellule en forme de cube est obtenue à partir des paramètres de diffusion en utilisant la méthode de récupération standard. Comme le montre la figure 7.6 (a), les résultats extraits de la taille des cubes par rapport à la permittivité effective pour le rapport de remplissage
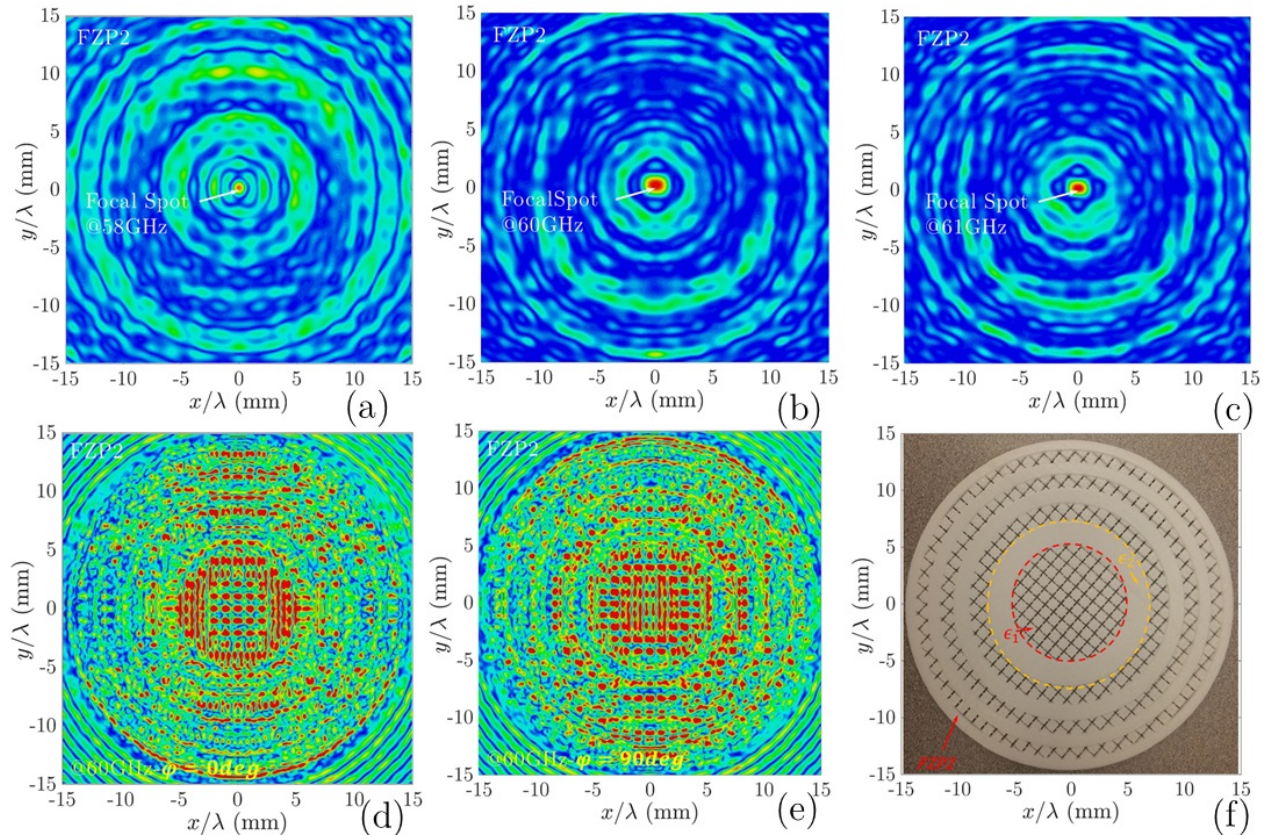
Figure 7.8 – Faisceau de sortie de rayonnement transversal au point focal principal avec un illuminateur dipôle à: a) 58 GHz; (b) 60 GHz (c) 61 GHz; Les sorties Transversales du champ $|E|$ pour la surface FZP_2 avec illuminateur dipolaire: (d) $\phi = 0°$, (e) $\phi = 90°$; Pour les graphiques correspondants, toutes les données sont normalisées avec des valeurs maximales. (f) La lentille diélectrique FZP_2 réalisé avec l'ABS-M30 en utilisant la méthode FDM;

ζ et les résultats HFSS sont similaires jusqu'à 2,2 mm. Pour résoudre ces explications non corrélées, la méthode d'ajustement exponentiel est appliquée aux tailles de cube extraites, comme le montre la figure 7.6 (a). Par cet ajustement, les résultats EF_m correspondaient bien avec $HFSS_m$ comme paramètres de sortie HFSS, où m est le type de materiau. Pour passer en revue, les tailles de cubes de lentilles réalisées seraient les sorties HFSS et EF, comme indiqué sur la Fig. 7.6 (b).

7.13 Méthode de conception de zone de plaque demi-onde et quart d'onde

Deux antennes de lentille diélectrique FZP ont été fabriquées en utilisant un procédé de fabrication additif comprenant deux types de matériaux plastiques différents. Pour atteindre la meilleure
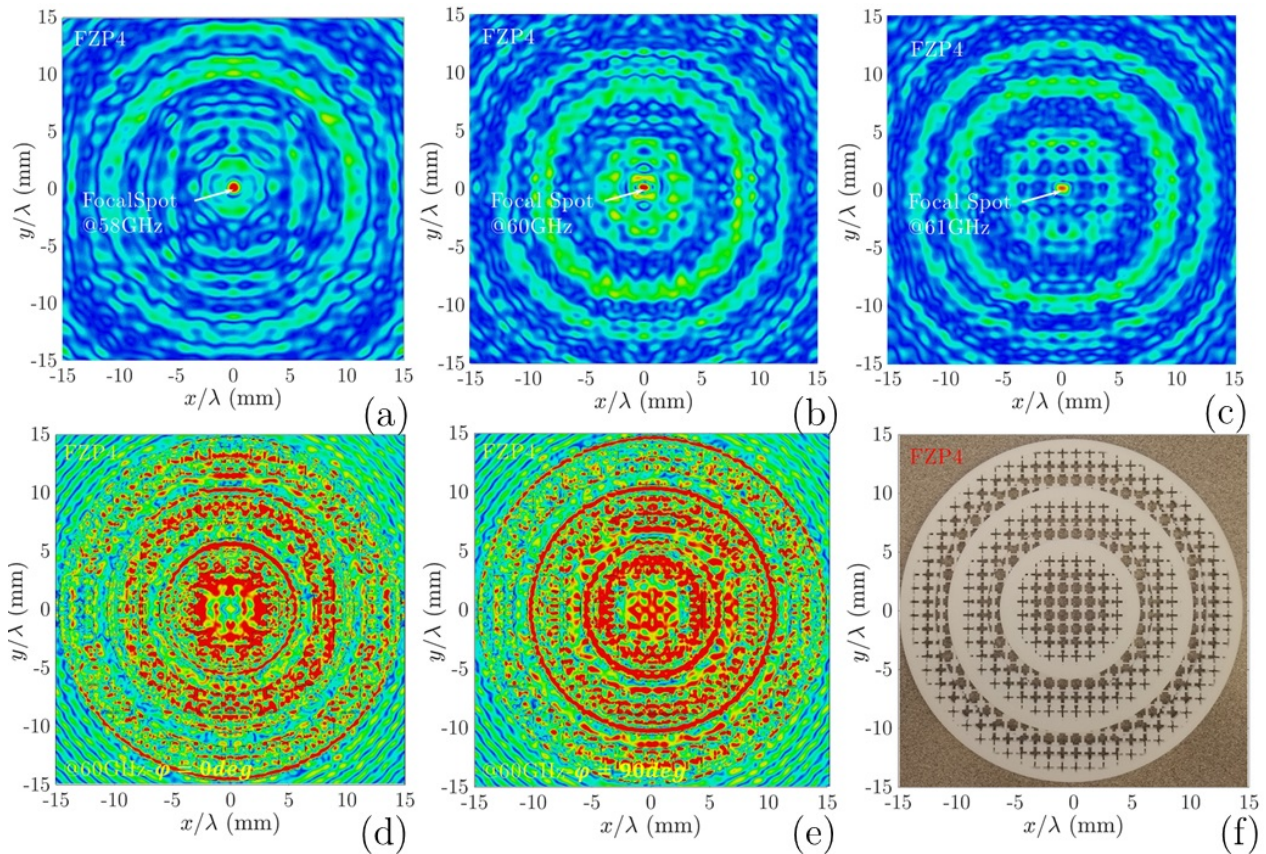
Figure 7.9 – **Faisceau de sortie de rayonnement transversal pour le point focal principal avec illuminateur dipôle à: (a) 58 GHz; (b) 60 GHz (c) 61 GHz; Les sorties Transversales du champ $|E|$ pour la surface FZP_4 avec illuminateur dipolaire: (d) $\phi = 0°$, (e) $\phi = 90°$; Pour les graphiques correspondants, toutes les données sont normalisées avec des valeurs maximales. (f) La lentille diélectrique entièrement fabriquée FZP_4 avec du polyimide, en utilisant la méthode SLS dans douze sous-zones, qui est conçue par la technique de réduction de la porosité du matériau;**

performance de la conception de l'objectif, une analyse de simulation des résultats de lentilles diélectriques FZP par le logiciel CST a été réalisée. Notre revue montre que les structures de lentilles en matière plastique avec une porosité de matériau simplifient la sélection de la permittivité relative pour la fabrication de lentilles dans une composition homogène, mais avec certaines limitations de conception. Dans certains modèles particuliers, la porosité du matériau en forme de cube est examinée pour mettre en œuvre des plaques de phase.

En conclusion, la première approche de conception de lentilles, la lentille plastique planaire imprimée en 3D FZP_2 a été construite sur la base du processus de fabrication additive FDM. Dans les imprimantes FDM, le modèle de lentille a été créé couche par couche en chauffant et en extrudant le filament thermoplastique comme suit. La photographie du modèle diélectrique FZP_2 est montrée sur la figure 7.8 (f), qui est obtenue par le plastique polymère ABS-M30 avec $\epsilon_r = 2.76$,

et $tan\delta = 0,059$. L'ouverture de rayonnement de lentille en plastique prévue est composée de huit zones d'un rayon de 75 mm. Les dimensions globales de la lentille conçue sont $150 \times 150 \times 5mm^3$. Fig. 7.8 (f) montre l'ouverture des sous-zones de lentilles proposée avec les cellules polymères en plastique.

Il y a huit sous-zones pour que l'antenne de lentille en plastique atteigne un diamètre de 30 λ_0. La correction de phase demi-onde (avec deux permittivités relatives (ϵ_r)) sur le diaphragme de la lentille a une fréquence de conception de $f_0 = 60$ GHz (longueur d'onde $\lambda = 5$ mm). Le FZP_2 a une longueur focale $F \simeq 132$ mm et un rapport d'aspect de lentille de $F/D = 0.88$. Ces anneaux diélectriques fournissent la correction de la phase demi-onde sur toute l'ouverture de la plaque de la zone de Fresnel. Pour résoudre le problème des réflexions multiples, une lentille d'épaisseur $h = \lambda$ a été conçue avec des anneaux diélectriques à permittivité plus faible pour obtenir une meilleure performance de transmission et une meilleure mise au point. Cette configuration de lentilles présente l'avantage d'une forme plate sur les surfaces frontale et en arrière. Des Antennes dipôle et en corne sont utilisés comme un illuminateur de lentille dans le plan yz. Deux permittivités relatives diélectriques sont utilisées dans la conception des zones FZP_2, typifiées comme $\epsilon_r = \{1.4, 2.76\}$ et $\tan \delta \simeq 0.05$.

Les deux permittivités relatives des sous-zones diélectriques pour satisfaire aux règles de la plaque de zone sont conçues avec les cellules en forme de cube optimisées, à l'aide de Éqs.(7.1) et (7.2), qui sont examinées sur les figures 7.6 (b) et 7.7 (a).

Pour conclure la deuxième approche, le plastique FZP_4 a été fabriquée en utilisant la méthode de frittage sélectif au laser, par du plastique PA 2200 en stock, qui est une poudre non chargée à base de PA-12. Le PA 2200 est un nylon sélectionné dans la liste de production EOS GmbH - Electro-Optical Systems (EOS). La valeur de permittivité mesurée pour ce plastique est $\epsilon_{PI} = 3.6$, ce qui est un peu plus élevé que l'ABS-M30. Les quatre permittivités relatives diélectriques utilisées dans la conception des zones FZP_4 représentées par $\epsilon_r = \{1.4, 2, 2.7, 3.6\}$ et $\tan \delta \simeq 0.06$. Le rayon de l'anneau diélectrique du FZP_4 est extrait avec Éq.(7.1) pour obtenir une lentille de correction de phase quart d'onde. L'ouverture de la lentille en plastique planaire FZP_4 est composée de douze zones avec le rayon entier de 75 mm. La correction de phase quart d'onde (avec quatre lentilles de permittivité relative (ϵ_r)) FZP_4, est représentée sur la figure. 7.9, a une fréquence de conception de $f_0 = 60$-GHz et une distance focale $F = 132$ mm. Comme représenté sur la figure 7.9, la lentille
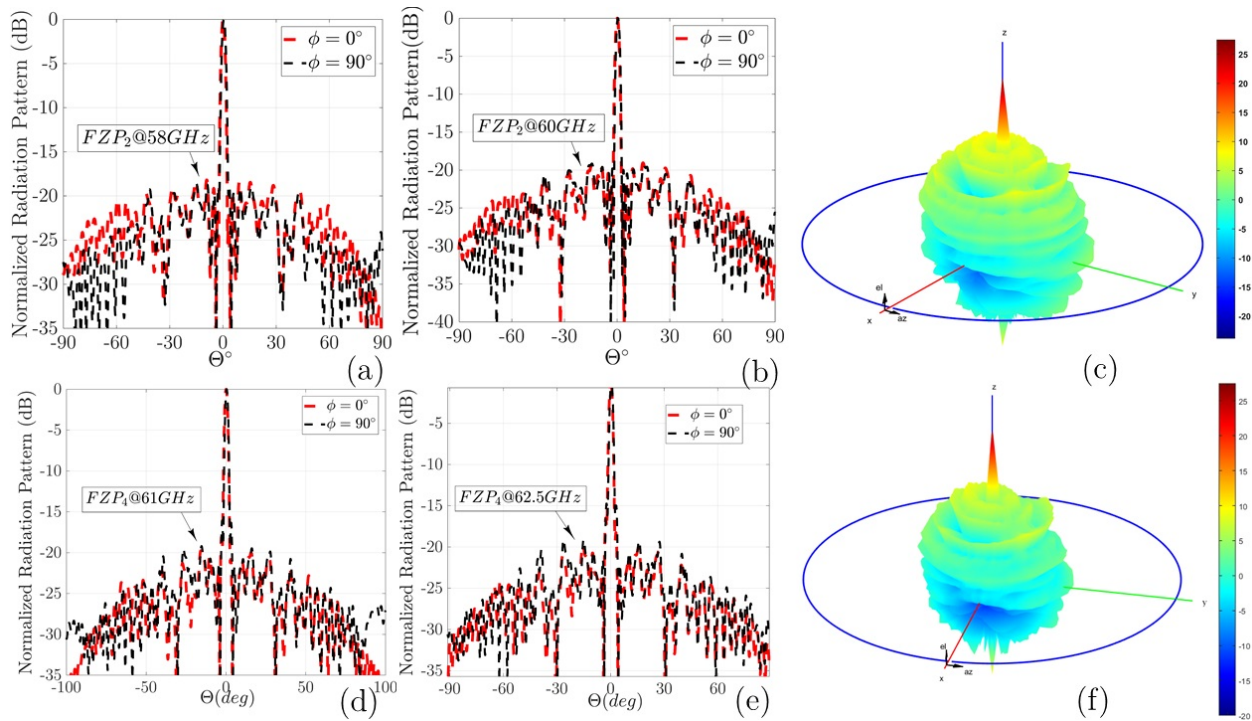
Figure 7.10 – **Les diagrammes de rayonnement mesurés dans $\phi = 90°$, et $\phi = 0°$ pour FZP_2: (a) 58 GHz. (b) 60 GHz. (c) les tracés 3D des diagrammes de rayonnement à champ lointain; Les diagrammes de rayonnement mesurés dans $\phi = 90°$, et $\phi = 0°$ pour FZP_4: (d) 61 GHz. (e) 62,5 GHz. (f) 3D.**

réalisée est constituée d'un anneau solide, et de trois zones avec une permittivité virtuelle créée par zone de pleine onde. Les résultats de la simulation montrent que les plaques de zone de permittivité multi-relative conservent une tolérance de permittivité correcte, ce qui simplifie la conception de la lentille et le processus de fabrication. Cette tolérance de permittivité pour Polyimide (PI), qui est réalisée avec des cellules en forme de cube, est analysée dans la Fig. 7.5 (b). Le processus de conception complet de l'objectif FZP_4 est créé avec du plastique PI. Pour les deux prototypes de lentille, le lobe rayonnant principal continue de pointer comme un faisceau de crayon à la direction de l'axe de visée sur bande de fréquence de fonctionnement. Comme le montre la figure 7.10, les largeurs de faisceau à demi-puissance des FZP_2 et FZP_4 proposés sont de 2,2 ° et 2 °, et les niveaux des lobes latéraux sont respectivement de -20 dB et -18 dB. Les SLLs mesurées du FZP_4 dans le plan E sont inférieures à -18 dB à 58 GHz et 60 GHz, respectivement. Les plans E et H des diagrammes de rayonnement sont symétriques en raison de la structure symétrique des lentilles. Fig. 7.10 montre les diagrammes de rayonnement normalisés, mesurés à 58 GHz et 60 GHz. Les diagrammes de rayonnement 3D calculés à 60 GHz sont représentés sur les figures 7.10 (c) et 7.10 (f) pour FZP_2 et FZP_4 , respectivement. Dans le lobe principal, le niveau de polarisation croisée dans le plan E est inférieur à -24 dB et -27 dB pour FZP_2 et FZP_4, respectivement.
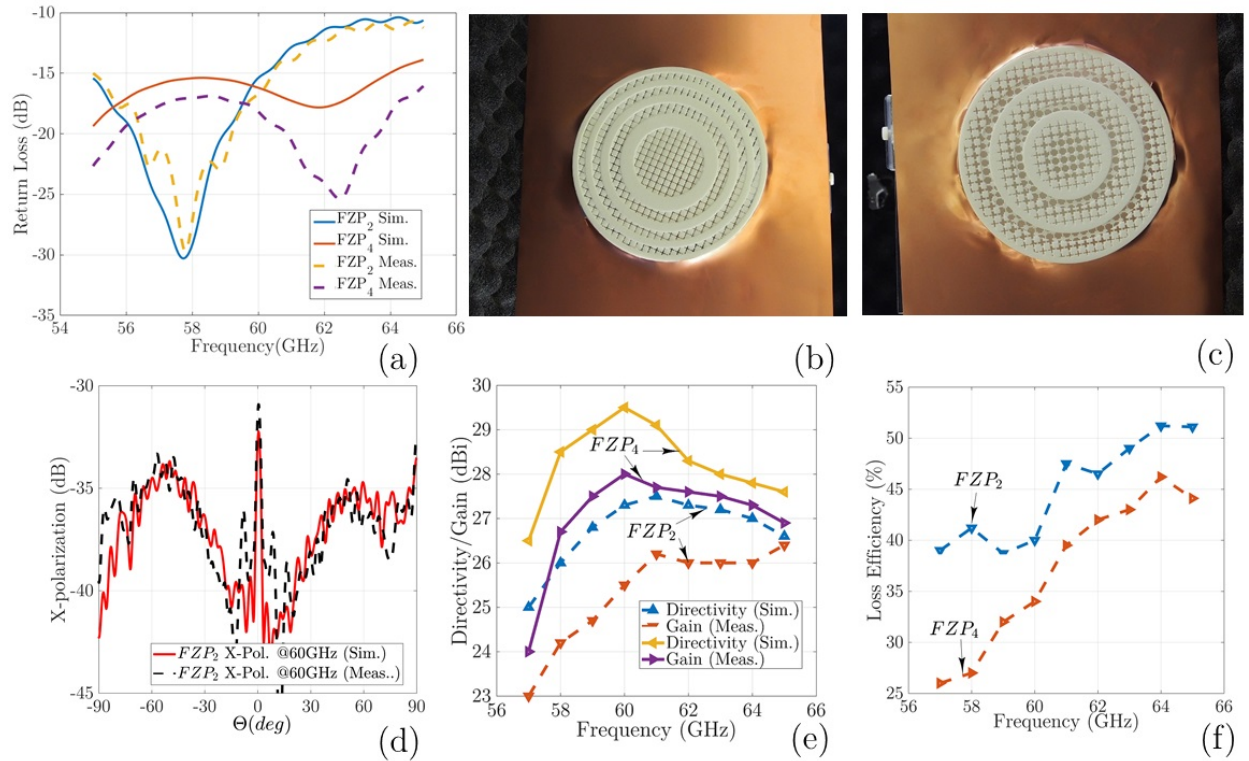
Figure 7.11 – **(a) Résultats des pertes de retour simulées et mesurées pour les antennes à lentilles** $FZP_{2,4}$ **(b) Lentilles** FZP_2 **fabriquées avec un support en tôle; (c) Lentille fabriquée** FZP_4 **avec support de tôle; d) niveau de polarisation x mesuré et simulé avec des supports de mousse et de tôle; (e) Directivité simulée et gain mesuré pour les antennes à lentilles** $FZP_{2,4}$ **avec illuminateurs dipolaires (f) Efficacité des pertes pour les antennes à lentilles** $FZP_{2,4}$**;**

Les figures 7.10 (b), 7.10 (c), et les résultats mesurés montrent un bon accord, ce qui supporte notre analyse et notre conception. Les résultats des pertes de retour simulées et mesurées pour les antennes à lentilles $FZP_{2,4}$ pour l'illuminateur dipolaire sont représentés sur la figure 7.11 (a). Fig. 7.11 (b-c) montre une configuration de mesure expérimentale pour des lentilles de Fresnel qui sont entourées d'un écran en tôle. La polarisation croisée pour cette structure est inférieure à -33 dB, comme le montre la Fig. 7.11 (d). L'analyse de simulation montre une stabilité relativement bonne du gain sur la fréquence de fonctionnement avec une différence de gain de 2 dB. Les résultats indiquent, en insérant une zone de correction de phase supplémentaire $q > 2$ à l'optimisation du diagramme de rayonnement, qu'un gain beaucoup plus élevé pour la lentille $q = 4$ est atteint. Selon les résultats obtenus pour les deux lentilles, le diagramme de rayonnement est très directif, c'est-à-dire un SLL bas et une largeur de faisceau étroite, qui certifient le processus de conception. La polarisation croisée pour la structure FZP_2 est d'environ -33 dB, ce qui est faible pour toutes les structures de lentilles, comme le montre la figure 7.11 (d). La directivité des antennes proposées, le
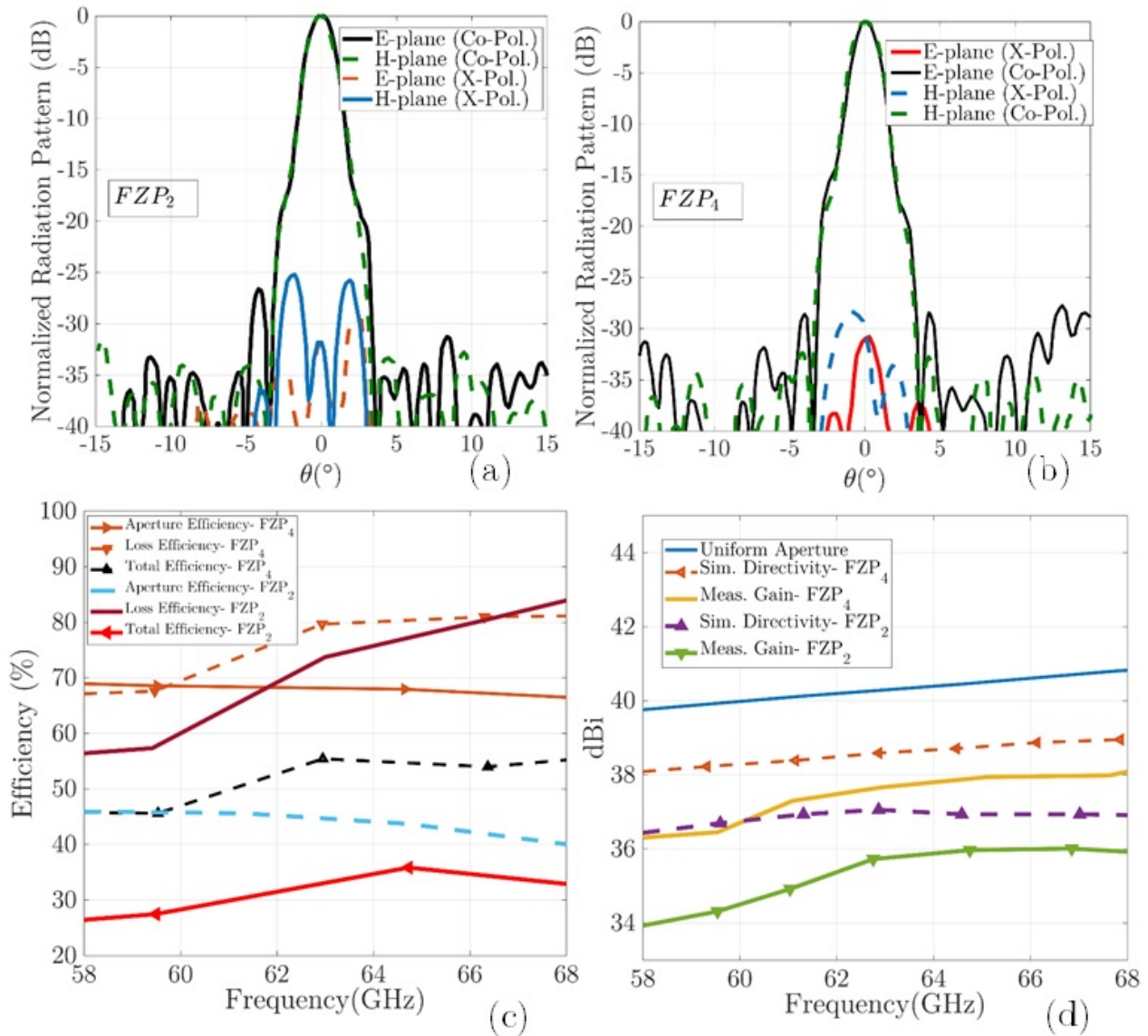
Figure 7.12 – **Les diagrammes de rayonnement normalisés le long des plans E et H à une fréquence de 60 GHz avec alimentation corne conique: a) lentilles** FZP_2 **et (b)** FZP_4**; (c) gain et directivité simulés et mesurés en fonction de la fréquence; (d) illustration de l'efficacité des lentilles proposées en fonction de la fréquence;**

gain et l'efficacité de la perte calculés sont affichéés dans la figure 7.11, où on observe un petit lobe à $\theta = 0°$.

Au cours du processus de mesure, les lentilles diélectriques prévues sont entourées d'une feuille de métal pour réduire le SLL pour l'alimentation dipolaire avec des diagrammes de rayonnement de la forme d'un $\cos^{10}$ provenant d'une antenne omnidirectionnelle. Nos études montrent qu'en utilisant des feuilles de métal pour une faible valeur de n< 20, il est possible d'obtenir une faible

SLL. Cependant, en raison du débordement pour les projecteurs Omni en utilisant les feuilles de métal, les ondes réfléchies par les feuilles de métal autour de la lentille seront focalisées en un point, et la combinaison des ondes réfléchies et incidentes produira un petit lobe en polarisation x, qui est - 33 dB plus bas que le faisceau primaire. Les résultats de la simulation montrent qu'en diminuant la largeur de cette feuille de métal entourée autour de λ_0 à la fréquence de fonctionnement, tous les deux, l'effets SLL faible et l'effet de faible lobe en polarisation x, peuvent être résolus.

Pendant la simulation, l'épaisseur de tôle attribuée à l'augmentation du nombre de mailles n'est pas prise en compte. Pour cette raison, les résultats de simulation et de mesure avec la feuille de mousse entourée sont également ajoutés dans une version révisée, qui certifie notre analyse en ce qui concerne les résultats combinés des ondes réfléchissantes et incidentes. Ce lobe est éliminé dans les mesures de mousse, et le niveau de polarisation croisée est inférieur à -37dB, la figure 7.11 (d). Fig. 7.12 (a-d) montrent une comparaison entre les performances mesurées et simulées de la corne conique d'alimentation pour les lentilles FZP_2 et FZP_4. Les figures 7.12 (a, b) montrent les diagrammes de rayonnement normalisés avec une corne conique d'alimentation de type cos^n à 60 GHz dans les plans E (xz) / H (yz). En tant que résultats obtenus, les diagrammes de rayonnement E / H pour une alimentation en cornet conique sont très directifs, c'est-à-dire, des SLLs faibles et une largeur de faisceau étroite. La polarisation croisée pour le canal FZP_4 avec une corne d'alimentation est d'environ -29 dB, et pour le FZP_2 est de -25 dB. Comme le montre la Fig. 7.12, l'ouverture de faisceau à demi-puissance des FZP_2 et FZP_4 proposés est de 2 °, 1,8 °, respectivement, et le niveau du lobe latéral est de -25 dB, -26 dB, respectivement. La SLL mesurée du FZP_4 dans le plan E est inférieure à -26 dB à 60 GHz. Les diagrammes de rayonnement des plans E et H sont symétriques en raison de la structure symétrique des lentilles et de la corne conique. Pendant le processus de mesure pour l'alimentation de corne contre l'alimentation de dipôle, une feuille de métal est remplacée par une mousse de Rohacell ($\epsilon_r = 1,04$) est considérée pour examiner les mesures à base de mousse aussi. Dans le lobe principal, le niveau de polarisation croisée dans le plan E est inférieur à -28 dB pour les plaques de zone FZP_2 et FZP_4, respectivement.

7.14 Modification de la matière plastique pour créer des lentilles Lüneburg sur mesure pour mmWave

Une antenne de lentilles Luneburg à diélectrique entièrement cylindrique imprimée en 3D avec contrôle de la porosité physique pour atteindre la permittivité voulue des sous-zones dans un cadre homogène est présentée pour des applications à ondes millimétriques. L'antenne dipôle à microruban avec des diagrammes de rayonnement de type Cos^{10} est utilisée comme illuminateur de lentille à l 'intérieur d'un guide d'ondes à plaques parallèles fonctionnant en bande V. Les indices de réfraction de gradient prévus sont obtenus en utilisant un contrôle de la porosité du matériau dans une approche à base de trous d'air à travers le milieu homogène pour satisfaire les règles de focalisation de lentille requises. Le rayon du trou d'air est utilisé pour contrôler la permittivité prédéterminée selon les règles de focalisation de lentille présentées. Pour atteindre cet objectif, les analyses numériques et les approximations sont effectuées pour définir le rayon d'air prévu pour l'illumination du lanceur d'ondes entre les plaques parallèles en mode TEM. La lentille poreuse proposée avec l'approche air-trou est fabriquée en utilisant un matériau d'impression 3D en polyimide avec l'épaisseur totale de $\lambda_0/2$ et $\epsilon_r = 3,4$. Le frittage sélectif au laser est la méthode de fabrication utilisée pour fabriquer ce cadre. Les simulations et les expériences vérifient la méthode de conception suggérée et les résultats.

7.15 Conception de la permittivité virtuelle basée sur l'approche poreuse du trou d'air

Les lentilles à indice gradué 3D sont destinées à des simulations électromagnétiques numériques supplémentaires pour ondes complètes à 60 GHz. Basé sur la théorie du milieu efficace, nous pouvons déterminer la permittivité de ces sous-zones en se basant virtuellement sur le contrôle de la porosité du milieu hôte. Par conséquent, nous suggérons le modèle de lentille de Lunenburg avec cette technique. Les deux profils de sous-zones de lentilles sont divisés en cellules de $3 \times 3 \times 3mm^3$, chacune étant conçue en plastique avec des trous d'air cylindriques. Les lentilles mentionnées ci-dessus sont obtenues à partir de cellules diélectriques dans la plate-forme homogène pour obtenir une plage de fonctionnement à large fréquence. L'approche poreuse de trous d'air présentée [6, 26] a été utilisée sur une zone circulaire concentrique en polyimide par frittage sélectif au laser (SLS) [38]. Nous avons développé cette modélisation pour satisfaire la permittivité des couches de Luneburg

$\eta = 0$ $\eta = 1.5$ $\eta = 2.6$ $\eta = 4.5$ $\eta = 5$

(a) Les structures poreuses géométriques primaires qui déterminent les sous-zones de nos lentilles ;

(b)

(b)
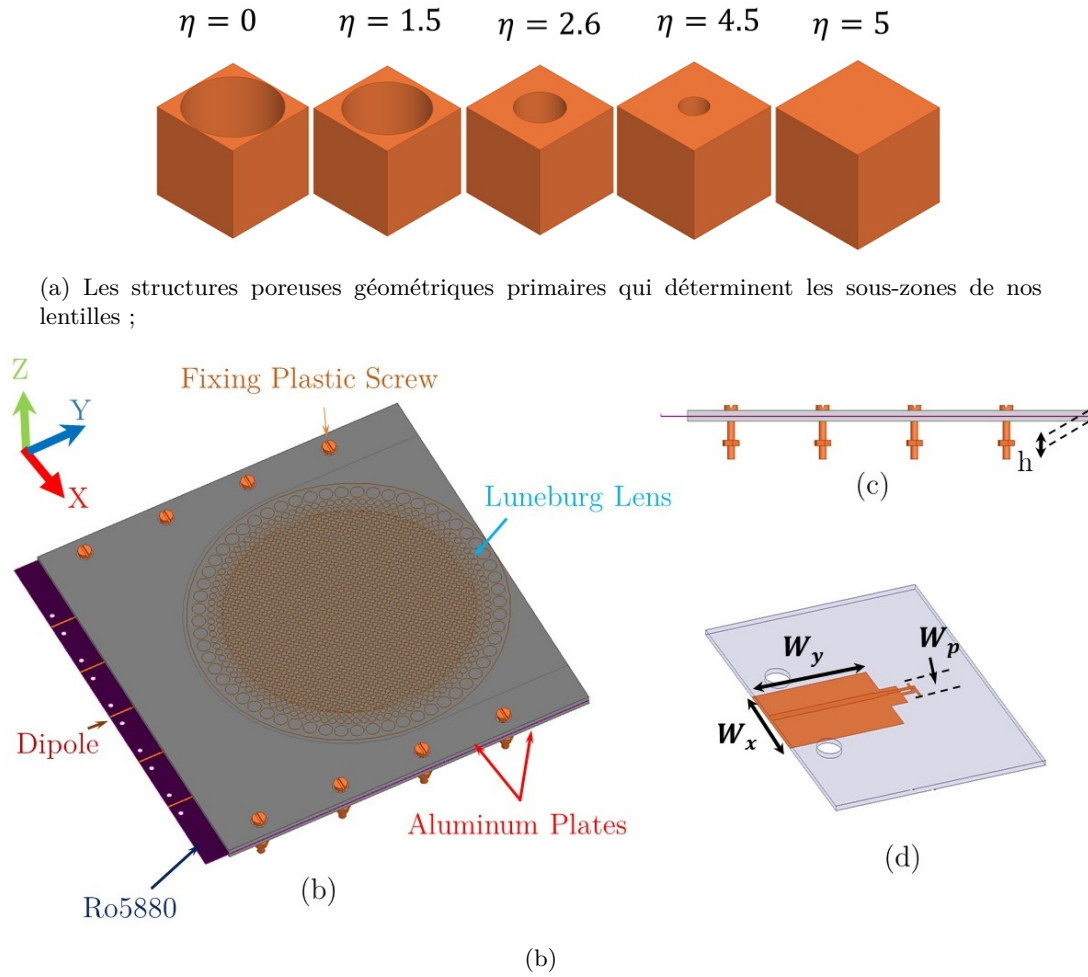
Figure 7.13 – a) Les structures poreuses géométriques primaires qui déterminent les sous-zones de nos lentilles ; (b) Système d'antenne total, (c) vue de côté, (d) Géométrie du lanceur de faisceaux proposé: $L_y = 24$, $W_x = 7$, $L_x = 24$, $h = 3$, $W_y = 9,8$ et $W_p = 2,2$ (tous en mm);

par Éq.7.3 à 60GHz. Le rayon de trou analysé à pleine onde dans la configuration HFSS est utilisé pour compléter le schéma de zones prévues avec des cellules diélectriques perforées comme indiqué dans la figure 7.13a. Le rayon global du trou d'air est formé avec du polyimide [38, 26], ce qui est préférable à partir de la liste de matériaux EOS pour les technologies click et imprimer [38], [11] pour atteindre l'indice de réfraction attendu (n_r). Deux types de cellules avec des cellules épaisses et fines sont utilisés pour contrôler la permittivité. Le rayon total de ces trous pour les deux matériaux diélectriques est de 5 mm, comme le montre la figure 7.13a, où r est le rayon des perforations, et d est l'épaisseur de la cellule.

$$n(r) = \sqrt{\epsilon_r \mu_r} = \sqrt{2 - (r/R_{Lun})^2}, (0 \leq n_r \leq R_{Lun}), \tag{7.3}$$
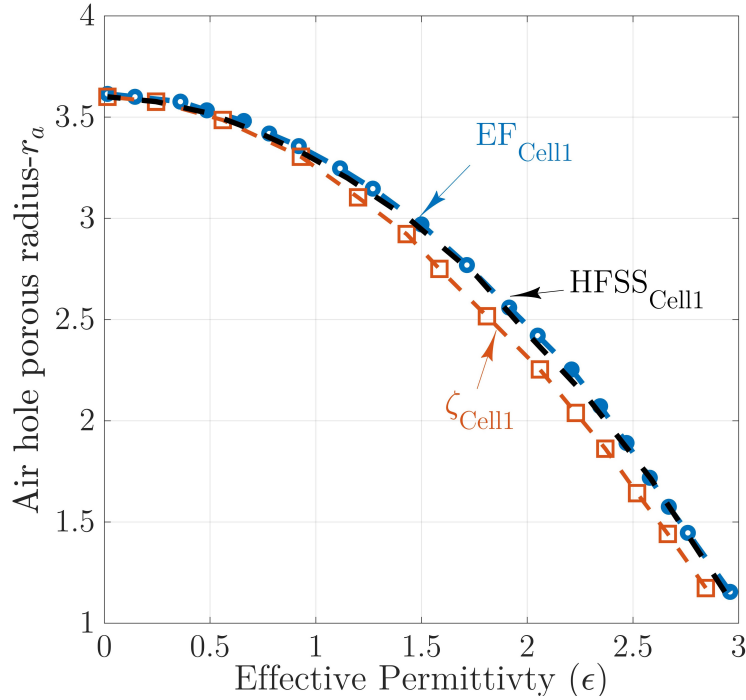
Figure 7.14 – **Illustration des différences de permittivité effective du polyimide par rapport aux rayons-r_a de la cellule poreuse à trou d'air défini comme $Cell_1$;**

En ajustant le rayon de chaque trou d'air r, les dimensions de cellule de permittivité virtuelle demandées sont fournies. Comme nous l'avons supposé sous cette forme perforée, en augmentant le rayon des perforations en charge du taux de remplissage, une permittivité inférieure à celle des propriétés du milieu hôte proche de la permittivité de l'air (ϵ_{Air}) est atteignable. Pour atteindre la géométrie de sous-zone de chaque lentille, le rayon de trou d'air calculé est utilisé pour actualiser chaque modélisation de zone donnée par Éq.7.3. La permittivité relative intrinsèque utilisée pour le plastique polyimide est $\epsilon_{PI} = 3{,}6$. Le resulat des changements de cellules souhaités sont montrés sur la base des variations radiales (r_a) des trous d'air et de leur épaisseur (d) pour atteindre la gamme de permittivités possibles, comme montré dans les Figs. 7.13a, 7.14, 7.15.

Comme présenté dans le schéma de contrôle des cellules en 3D dans Fig. 7.13a, deux types de cellules peuvent être formées avec cette approche pour contrôler les propriétés du matériau avec des hauteurs ou des rayons distincts. Dans les étapes mentionnées, en considérant les variations de permittivité et le rayon des trous perforés comme un groupe d'informations connues, telles que G1: $(x_0 = \epsilon_{Air}, y_0 = \zeta = 0)$, G2: $(x_1 = \epsilon_m, y_1 = \zeta = 1)$, une nouvelle taille de trous est réalisable en utilisant l'interpolation linéaire. Par conséquent, les permittivités effectives des cellules d'air-trou basées sur la réduction de volume sont approximées en utilisant l'interpolation linéaire et sont
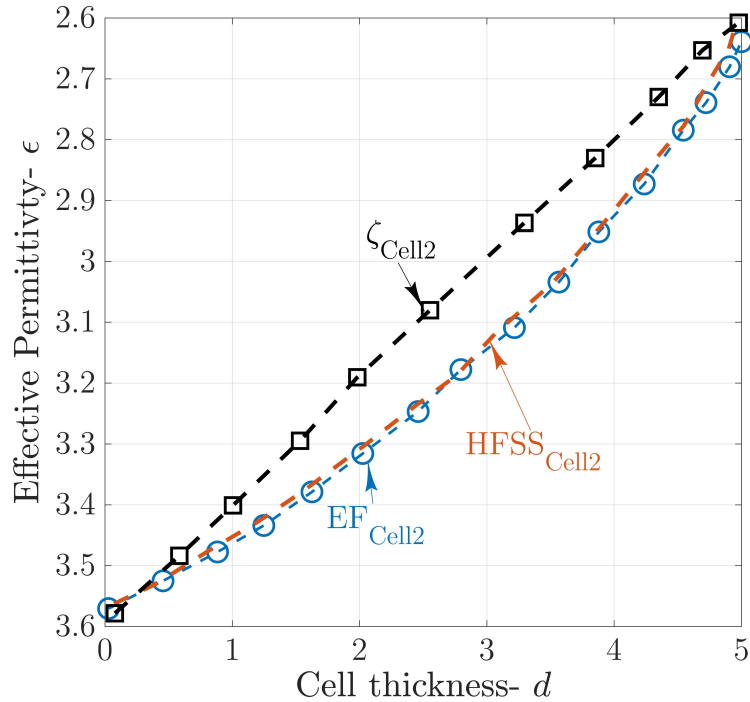
Figure 7.15 – Illustration des variations de la permittivité effective du polyimide par rapport à l'épaisseur - d de la cellule poreuse à trou d'air définie comme $Cell_2$ pour le rayon du trou constant à 2,5 mm;

données par Éq. 7.4 [11],

$$\epsilon_r = \epsilon_{PI}.\zeta_{PI} + \epsilon_{Air}.(1 - \zeta_{PI}). \tag{7.4}$$

En outre, la permittivité intrinsèque des nouveaux matériaux est une caractéristique de conception critique pour le rayon final de la cellule. Pour cette raison, une enquête distincte doit être menée pour des substances diélectriques particulières. Les résultats obtenus révèlent que les différences de rayon et d'épaisseur opposées à la permittivité voulue ont des variations non linéaires. Par conséquent, une analyse supplémentaire basée sur une simulation d'onde complète est requise pour augmenter la vérité de la permittivité virtuelle attendue [11]. Dans une enquête connexe, les simulations complètes d'Ansys HFSS sont utilisées pour évaluer l'estimation précise des valeurs de cellules. Toute cellule diélectrique poreuse avec un rayon discret est considérée dans la configuration de guide d'onde HFSS simulée, avec des limites de conducteur magnétique parfait (PMC) et de conducteur électrique parfait (PEC) pour l'introduction des conditions périodiques. Concernant les paramètres définis pour ces cellules, les côtés droit et gauche sont affectés aux ports d'ondes. La méthode de récupération standard avec les relations de Kramer Kronig est utilisée pour obtenir la permittivité effective des paramètres de diffusion. Comme montré dans les Figs. 7.13a, et 7.14,7.15,

les résultats obtenus du rayon du trou d'air par rapport à la permittivité pour le taux de remplissage et les effets simulés ne sont pas du tout comparables.

Pour déterminer ce problème, l'approche d'ajustement mathématique est utilisée pour préparer des rayons plus particuliers [11]. Grâce à l'ajustement linéaire mentionné, les résultats estimés concordaient bien avec les sorties d'onde pleine simulées. Pour estimer les derniers modèles, les tailles de cellules de lentilles obtenues seraient les sorties de simulation EF et pleine onde, comme montré dans les Figs. 7.13a, et 7.14. Après des comparaisons de taille de cellule pour obtenir la meilleure taille, la capacité de mise au point de nos prototypes a été évaluée par HFSS.

7.16   Conceptions de lentilles diélectriques

L'objectif diélectrique de Luneburg avec un rayon R = $30\lambda_0$ a été construit pour un fonctionnement en bande de fréquence à ondes millimétriques à 60GHz. Une structure poreuse cylindrique est utilisée comme cellule unitaire primaire pour contrôler la permittivité intrinsèque du polyimide pour satisfaire les sous-zones de lentilles de Luneburg perforées. Dans nos expériences, la lentille diélectrique de Luneburg dans un milieu homogène est encastrée entre deux plaques d'aluminium parallèles dans un mode quasi-TEM avec des dimensions de 130 ×190 mm (à 60 GHz). Comme le montre la Fig.7.16a, des espaceurs en mousse Rohacell de faible permittivité $\epsilon = 1$ à 60 GHz sont utilisés pour remplir l'espace libre entre les plaques d'aluminium pour suspendre l'antenne dipôle proposée sur l'air. Dans la conception de lentille de Luneburg perforée, la surface de lentille prévue a été séparée en quatre zones cylindriques concentriques, chaque section étant composée d'éléments poreux et associée à un indice de réfraction virtuel particulier. Par conséquent, la lentille perforée n peut varier de 1,01 à 1,4 pour satisfaire aux règles de la lentille.

7.17   Conception de lentilles de Luneburg : Résultats et discussions

Un compromis qualitatif parfait peut être vu dans les les résultats simulations et de mesures pour la lentille GRIN diélectrique proposée. Comme indiqué dans la distribution des champs E, les champs proches du lanceur de vagues ne sont pas apparents en raison de l'intensité du lanceur de faisceau.

150

Par conséquent, le champ E autour du lanceur de faisceau n'est pas examiné. Dans ce schéma, les ondes incidentes, après transfert à travers le cadre de la lentille, sont converties à partir d'ondes cylindriques en ondes quasi-planes sur le verso de la périphérie de la lentille diélectrique et révèlent un éclairage très directif. Dans ce schéma, les résultats simulés et mesurés pour les diagrammes de rayonnement et les paramètres S11 correspondent entièrement aux résultats attendus des lentilles perforées sur mesure. A partir de l'analyse mathématique et des simulations d'ondes complètes basées sur des estimations de lentilles perforées défocalisées, le centre de phase d'alimentation de lentilles proposé confirmant la source ponctuelle (antenne dipôle) est situé à 7 mm de la limite de la lentille perforée. Deuxièmement, il est crucial de préparer correctement le trou d'air avec de la mousse Rohacell de 1 mm d'épaisseur. Par conséquent, l'utilisation d'une mauvaise épaisseur peut évidemment modifier les paramètres du fluide efficace voulu autour de la lentille perforée. Néanmoins, les mécanismes de focalisation du faisceau de la lentille perforée sont perçus à 60 GHz et à 62 GHz, comme le montrent Figs. 7.17, et 7.18, respectivement. Les diagrammes de rayonnement hautement directifs sont visibles à toutes les fréquences mesurées. Les résultats mesurés montrent que les lobes latéraux sont inférieurs à 18 dB, ce qui est acceptable, sur la base des normes IEEE.

Les lobes latéraux sont symétriques grâce à l'antenne dipôle et au prototype de lentille proportionnelle. Dans ce schéma, les résultats mesurés pour la lentille contribuent à rendre les faisceaux transformés plus directifs et à avoir de faibles niveaux de lobes latéraux. La directivité maximale de la conception proposée est de 24,6 dBi avec des variations de 2,4 dBi par rapport aux fréquences de fonctionnement comprises entre 57 et 67 GHz, comme indiqué dans la Fig. 7.19. La lentille proposée offre un rendement total de 58 % avec des variations de 4 % par rapport aux bandes d'exploitation comprises entre 57 et 67 GHz.

7.18   Antenne FZPL non magnétique avec cellules poreuses analysées pour 30 GHz

Les structures poreuses ont été parmi les premières méthodes de contrôle de la permittivité intrinsèque étudiées pour l'implémentation du design du milieu à indice de réfraction en gradient [5], [4]. En utilisant un contrôle des paramètres géométriques des structures poreuses, la permittivité virtuelle voulue dans l'orientation de champ E désirée est fournie pour obtenir un milieu de gradient de réfraction homogène (GRIN) sur une large gamme de fréquences, contrairement aux structures

GRIN métamatériaux conventionnelles à bande passante étroite. Bien que le contrôle de la permittivité poreux soit largement appliqué dans les systèmes d'ingénierie des matériaux en raison de la facilité de réduction de la permittivité et du coût faible pour réaliser la permittivité prévue dans un milieu similaire, ils ne sont pas suffisamment analysés pour les applications d'antennes de lentilles GRIN. Au cours des décennies précédentes, des progrès essentiels ont été accomplis dans les procédés de fabrication additive, simplifiant la réalisation de contrôles de permittivité plus complexes avec des cellules de formage libres dans des lentilles GRIN à gain élevé pour des applications de focalisation (à condition qu'un illuminateur approprié avec le motif approprié de la forme Cos ^{n} soit appliqué). Ces structures poreuses sont généralement réalisées en utilisant des architectures de réseaux cylindriques et sphériques. Les compromis existants dans le coût de conception des lentilles GRIN conventionnelles, et la mise en œuvre des sous-zones utilisées dans les plates-formes d'antennes à gain élevé ont limité l'utilité de ces structures dans les systèmes de communication à ondes millimétriques au-dessus de 30GHz. D'autre part, le médium GRIN à base de métamatériaux traditionnels souffre d'inconvénients excessifs tels que des bandes passantes étroites, une dissipation importante, une production difficile et à coût élevé. Avec la croissance actuelle dans le processus de fabrication additive, la mise en œuvre de divers systèmes innovants de lentilles GRIN a été décrite comme des remplacements possibles des méthodes GRIN conventionnelles utilisant des structures périodiques entièrement diélectriques, et des métamatériaux avec des techniques de porosité matérielle. Les dispositifs GRIN tels que les plaques Luneburg, Half-Maxwell fisheye et zone de Fresnel ont également attiré l'attention pour de nombreuses applications de focalisation à gain élevé avec compromis de conception d'antennes.

Il y a eu une conséquence croissante de l'utilisation de l'antenne à plaques de zone Fresnel dans les spectres d'ondes millimétriques et submillimétriques et ceci a été pour des raisons bien determinées. Tout d'abord, les ZP offrent une focalisation de gain élevée comme les autres structures de lentilles GRIN, mais ils sont de type planaire, avec un poids réduit, une facilité d'invention et un rapport coût-efficacité ce qui les rendent attrayants. De plus, un éclairage correctement équilibré de l'alimentation de l'ouverture de la lentille réduit la défocalisation et le débordement de l'effilement des lentilles qui est un dilemme essentiel dans la conception des dispositifs de lentille [28], [1]. En effet, en utilisant des alimentations similaires à Cos ^{n} pour éclairer la surface des plaques de zone afin de focaliser les ondes d'incidence par diffraction, on obtient des valeurs de débordement faibles, un haut rendement et un gain élevé.

De plus, des cellules diélectriques basées sur des procédures de porosité sont utilisées pour contrôler le gradient de déphasage des sous-zones dans la surface/ouverture de la plaque de zone pour la focalisation. Les FZP sont composés de sous-zones localement concentriques avec des distributions de multi-permittivité qui agissent comme des déphaseurs. Ces sous-zones sont régulièrement réalisées avec des anneaux diélectriques pour la structure inhomogène ou avec des structures poreuses telles que des trous cylindriques [5], [4] ou des matériaux déformés pour la structure homogène. Différents prototypes de ZP diélectriques pour la conception de formations entièrement diélectriques ont été rapportés dans le passé [29], [6].

Les prototypes ZP dans chaque sous-zone sont composés de matériaux non magnétiques et non métalliques pour le développement homogène et d'éléments à simple résonance pour la composition inhomogène. Plus récemment, de nombreux efforts basés sur la théorie des matériaux ont été réalisés pour produire une permittivité de sous-zone virtuelle via des trous percés perméables [6], soit en utilisant des cellules cubiques fabriquées sur des diélectriques à faible permittivité pour concevoir des lentilles plus minces [11] ou en utlisant des cellules entièrement métalliques dans le milieu homogène [21]. Cependant, de telles structures poreuses sont très dispersives pour l'illumination d'onde d'incidence avec des angles aigus [4]. Par conséquent, ils ne sont pas adaptés au contrôle de la permittivité de multiples illuminateurs d'alimentation et à la formation de faisceau. Au cours des années précédentes, quatre approches poreuses, à savoir trous d'air, trous remplis de diélectrique, cellules métalliques pleines et diélectrique de formage libre avec des dimensions de cellule sublongueur d'onde, ont été utilisés pour réaliser la permittivité virtuelle dans le cadre homogène qui a été considéré pour la mise en œuvre d'un milieu GRIN. Contrairement aux FZP classiques qui sont formées à la manière d'éléments résonants périodiques, les FZP entièrement diélectriques sont façonnées avec l'ensemble de cellules poreuses ayant un cadre hautement miniaturisé, une facilité de fabrication et des structures non magnétiques. Contrairement aux FZP classiques qui sont formées à la manière d'éléments métalliques périodiques, les FZP entièrement diélectriques sont façonnées avec l'ensemble de cellules poreuses ayant un cadre hautement miniaturisé, une facilité de fabrication et des cellules poreuses non magnétiques. Récemment, des approches poreuses spécifiques mettant l'accent sur les méthodes d'impression 3D ont été employées dans la composition des lentilles à gradient d'indice de réfraction large bande [6], [30], [97]. Il a été confirmé que l'application d'une approche entièrement diélectrique, les lentilles à profil bas avec une réponse large bande pourrait être conçu.

Cependant, les prototypes des structures homogènes, à la fois dans le cadre métallique et diélectrique, souffrent d'une faible efficacité qui peut être améliorée avec la mise en forme totale de la structure de la lentille ou prendre des illuminateurs de façon réfléchie.

Dans ce travail, nous présentons de nouvelles cellules poreuses dans le cadre homogène en utilisant un plastique à haute densité diélectrique en Alumide pour la conception de d'antennes à plaques de zone qui sont à profil bas et à large bande. La plaque de zone demi-onde proposée est constituée des cellules en forme de cube pour fournir la permittivité prévue des sous-zones pour l'inversion de phase. La taille des cubes de chaque zone est analysée sur la base d'une analyse de pleine onde avec des paramètres S extraits pour offrir une taille de cube de permittivité virtuelle appropriée basée sur la permittivité d'Alumide mesurée à 30 GHz. Des cellules en forme de cube composées d'Alumide à base de poudre diélectrique élevée ont été sélectionnées sur la base de la liste de production EOS (Electro-Optical Systems) avec des tiges rectangulaires pour connecter les cellules dans un emplacement prédéterminé pour satisfaire les règles de lentilles. Chaque cellule diélectrique est conçue pour fournir une permittivité prédéterminée dans le spectre électromagnétique désiré. Un prototype de la plaque de zone de Fresnel à demi-onde entièrement diélectrique avec une corne conique à faisceau de rayonnement de type Cos [41] situé en son centre est utilisé pour fonctionner à 30 GHz. L'épaisseur totale des ZP diélectriques réalisés est de 5 mm et les dimensions physiques latérales de l'ouverture de la lentille imprimée sont $150 \times 150 mm^2$ (ou équivalents $3\lambda_0 \times 3\lambda_0$). Un modèle de la composition de plaque de zone homogène présentée est fabriqué avec le procédé de fabrication par frittage laser sélectif (SLS) et identifié expérimentalement dans le laboratoire d'antenne. Les résultats de mesure sont conférés que le ZP poreux réalisé fournit un gain maximum de 36 dB avec une différence inférieure à 4 dB sur la bande de fréquence désirée.

7.19 Résultats de FZP à base d'Alumide non magnétique

La méthode décrite dans les sections II et III a été élaborée pour composer une antenne à lentille FZP_2 en mode de transmission avec une technique de porosité du matériau dans le cadre homogène. La lentille de Fresnel recommandée est produite pour fonctionner sur la bande passante 28-40 GHz. Comme indiqué dans la section III, la pondération de l'amplitude du diagramme de rayonnement de type cos [41] est définie par le diagramme de rayonnement de l'antenne de type corne conique. Dans ce schéma, un lanceur de faisceau commercial est utilisé comme illuminateur pour alimenter

une ouverture ZP diélectrique qui est une antenne conique à cornet conique (A390-17) operant dans la bande « Ka ». Dans la méthode de traitement, une réduction de l'éclairage de type cos [41] est estimée à avoir un compromis maximal entre l'ouverture et l'efficacité du débordement. Puisque la constante diélectrique du matériau dépend de la fréquence, une méthode de mesure diélectrique à base de guide d'ondes est utilisée pour mesurer la permittivité réelle à la bande de fonctionnement. Pour cette raison, un échantillon d'Alumide imprimé avec des dimensions de 7.1×3.5×2.99 est créé pour charger l'espaceur WR-28 pour les mesures en bande « Ka ». En résultat, pour le milieu hôte diélectrique employé dans la conception homogène, qui est une matière plastique à base de polymère, une permittivité d'environ 10,8 à 30 GHz est obtenue. En raison des petits éléments de l'antenne de lentille ZP poreuse introduite, l'analyse en pleine onde de toute la structure exige de bons dispositifs de calcul. Par exemple, les plus petites parties de la lentille seront notre essai à simuler avec un logiciel commercial utlisant la technique de domaine temporel à différence finie (FDTD), ce qui nécessite une plus petite taille de cellule pour l'exploration. Par conséquent, la simulation de l'antenne de lentille recommandée avec la partie la plus minuscule de 0,5 mm et la composition de 900 cellules cubiques est un défi important et prend du temps. les lentilles FZP_2 proposés et les diagrammes de rayonnement de type cos [39], dans le plan E et le plan H, à 30 GHz sont représentés dans la figure 7.20b.

7.20   Perspectives

Ensuite, nous passons brièvement en revue différentes lignes potentielles de la future recherche sur les lentilles GRIN à base poreuse, considérées comme très pertinentes par l'auteur :

1. Dans le chapitre 2, nous avons discuté de la mise en œuvre de la porosité des matériaux pour la génération de structures de cellules composites poreuses de milieux GRIN dans des arrangement de type cellulaire et materiels, qui est basé sur une théorie des matériaux et des études de Corkum. Cependant, le cadre inhomogène précédent de la limitation des structures GRIN dans la bande passante de fonctionnement imposée par les cellules de métamatériaux à bande étroite employées et les cellules de métamatériaux diélectriques avec une conception poreuse a conduit à une sortie à large bande en tant que solution.

En particulier, les quatre approches de contrôle de la permittivité à base poreuse ont été catégorisées pour produire les règles de milieu gradué attendues. Ainsi, pour avoir un contrôle efficace de la permittivité intrinsèque d'un milieu hôte correspondant à la réalisation de la permittivité virtuelle, il était essentiel d'atténuer une partie du milieu hôte proposé pour diminuer la permittivité intrinsèque en théorie classique. Comme expliqué dans le chapitre 2, il y a une analogie entre la configuration offerte et le schéma d'ajout de nouveau matériau pour l'augmentation de la permittivité plus que la constante diélectrique du milieu hôte avec la technique de la porosité du matériau.

En conséquence, il devrait être possible d'utiliser cette approche dans laquelle les trous poreux sont remplis par d'autres types de configuration basée sur les matériaux (comme celui présenté dans [97]), afin de développer la production du schéma GRIN à indice de réfraction large et élevé en termes de conception de lentilles.

2. La méthode de conception révélée pour la mise en œuvre de dispositifs optiques 3D GRIN tels que Luneburg et la lentille oeil de poisson de Maxwell, basé sur le cadre homogène a permis la synthèse de lentilles imprimées 3D et des dispositifs de mise en forme de faisceau dans des formats compacts et modifiés pour les antennes. Parmi eux, nous pouvons citer :

(a) Lentilles de Luneburg imprimées en 3D avec approche de formation libre [10, 15] : il est d'un grand intérêt pour la mise en œuvre de lentilles sphériques multishell Luneburg [78], de demi œil de poisson de Maxwell ou de toutes fonctions GRIN non résonnantes souhaitées, par exemple, le « Eaton lens beam-shaper » [97]. Dans le dernier exemple, la construction non résonnante « woodpile » dans le régime métamatériel avec un milieu composé liquide a permis une large plage d'indice de réfraction ($\Delta n = 1 \rightarrow 6,32$), qui peut être utilisée pour d'autres types d'applications des d'antennes de lentilles GRIN.

(b) Cellule poreuse tubulaire : les cellules perméables tubulaires sont largement manipulées pour atteindre un indice de réfraction plus faible. La plaque de Fresnel ultra-plate en matière plastique pour la communication mmWave est l'un de ces résultats proposé par Petosa [6, 7]. Ils sont également impressionnants en tant que lentille de Luneburg, et conception de lentilles Sieve en THz.

c) L'analyse de permittivité des matériaux de formage libre vu que la complexité de conception est difficile : l'analyse de permittivité unique basée sur la dimension de Hausdorff peut être utilisée pour la mise en œuvre de cellules accordables, le contrôle de permittivité dans des dispositifs géométriques complexes, et de nouvelles lentilles de transformation optique, pour d'autres applications telles que l'ingénierie des antennes [10, 15, 11].

3. Dans le chapitre 3, la technique de conception à forme libre introduite basée sur des cellules en forme de cube a été appliquée pour la mise en œuvre de plaques de Fresnel à demi et quart d'onde. Cependant, cette approche pourrait être révisée pour obtenir des fonctionnalités de distribution d'indice de réfraction de type complexe. Les structures poreuses à formation libre avec des matériaux d'impression 3D sont d'un grand intérêt pour la compensation du contrôle de la permittivité virtuelle et la conception des dispositifs GRIN de nos jours.

4. L'approche de conception poreuse commune présentée dans le chapitre 4 pour la réalisation de l'antenne de lentille de Luneburg diélectrique sans résonance basée sur l'approche d'alimentation en défocalisation avec redistribution de la permittivité dans le guide TEM peut être appliqué à une diversité de dispositifs GRIN optiques avec une distribution réfractive radiale similaire. En particulier, il serait intéressant de fabriquer une antenne à lentille GRIN non résonnante, par exemple un Luneburg, et d'étudier des matériaux à forte permittivité avec l'ajout de cette approche et des transformations optiques permettraient d'obtenir des antennes lentilles Luneburg plus minces avec une bande passante plus large que celle généralement effectuée par les métamatériaux résonants.

5. Dans le chapitre 5, une lentille poreuse à zone de Fresnel composée d'un profil homogène alimenté par une antenne cornet conique a été fournie pour des applications millimétriques. La ZP suggérée utilise les cellules unitaires en forme de cube, convenablement conçues en fournissant des modèles analytiques pour former la permittivité et le squelette virtuels des sous-zones de lentilles homogènes. Un prototype d'un tel FZP à demi-onde a été construit et identifié expérimentalement dans le laboratoire. La lentille FZP fabriquée était destinée à fonctionner à la fréquence centrale de 30 GHz. Les résultats expérimentaux ont confirmé que l'antenne de lentille présente des propriétés de rayonnement de faisceau de crayon constant dans le spectre de fréquences 25-40 GHz. Pour les dimensions d'ouverture de la lentille correspondante, les lentilles de type homogène doivent montrer des gains et des efficacités plus élevés que les prototypes précédemment rapportés avec le cadre homogène à base d'Alumide.

La performance de l'illuminateur de lentille du Fresnel présenté a également été vérifiée par analyse des équations d'efficacité de « spill over and taper » pour trouver la meilleure pondération d'amplitude pour identifier le caractère symétrique des illuminateurs de type cos pour obtenir un rendement élevé.

7.21   Conclusions de la thèse

Dans cette thèse, nous avons introduit des concepts nouveaux et optimisés dans le cadre des communications mmWave, à savoir l'antenne à gradient d'indice de réfraction non magnétique ($n = \sqrt{\epsilon\mu}, \mu = 1$). Les deux idées sont destinées à améliorer les technologies de fabrication actuelles pour les dispositifs GRIN dans le spectre mmWave : la lentille de Luneburg et les plaques de zone de Fresnel (FZP) dans le cadre homogène. D'une part, la porosité du matériau peut être utile pour simplifier la conception de permittivité virtuelle, non seulement dans les étapes de mise en œuvre et de mesure, mais aussi pour activer des cellules potentielles avec de nouvelles propriétés à large bande et des schémas simplifiés de compensation de perte dans les spectres mmWave et sub-mmWave. D'un autre côté, les techniques de contrôle de la permittivité basées sur la porosité du matériau peuvent également faciliter le développement de nouvelles techniques de conception de dispositifs GRIN pour les applications de lentilles. En fait, l'introduction de la théorie des matériaux basée sur le traitement de la porosité est l'une des méthodes les plus encourageantes pour contrôler la permittivité intrinsèque du matériau.

(a) Vue supérieure de la lentille
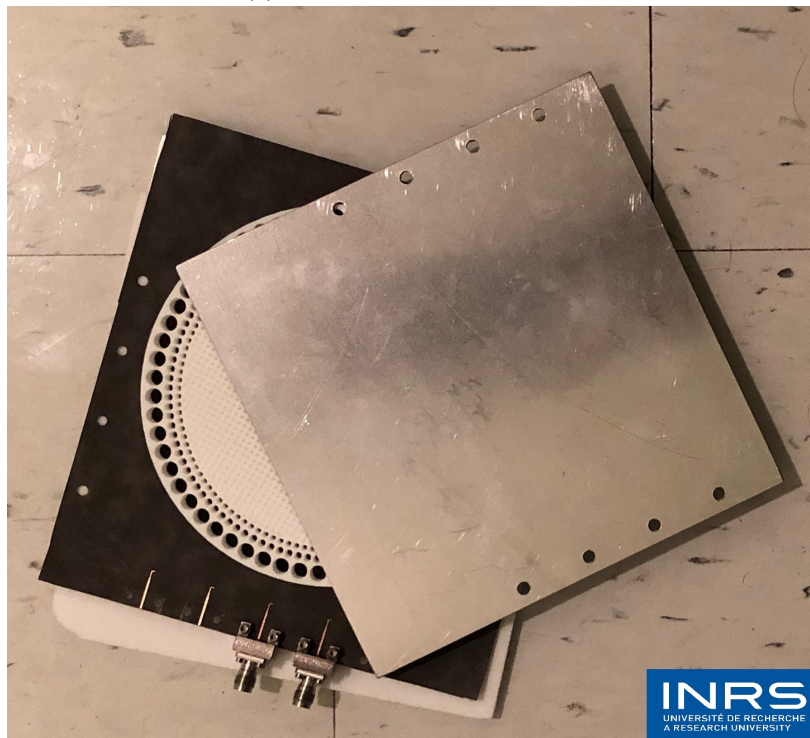
(b) Vue globale du système

Figure 7.16 – (a) Vue de dessus pour la lentille perforée (b) Photographie de la lentille de Luneburg entièrement diélectrique fabriquée (a) Vue de dessus de la lentille, (b) Vue globale du système;
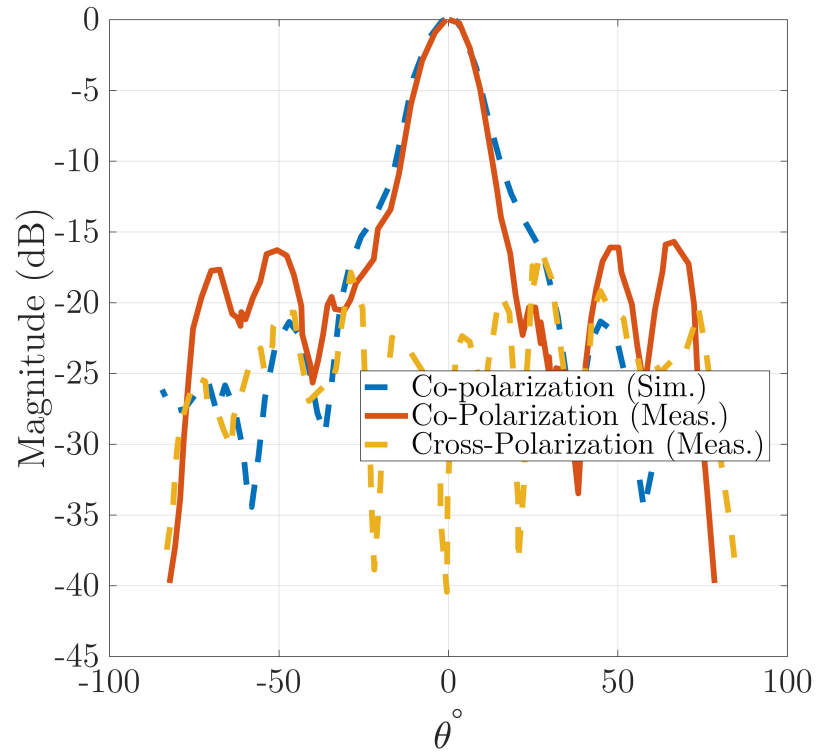
(a) $\phi = 0°$
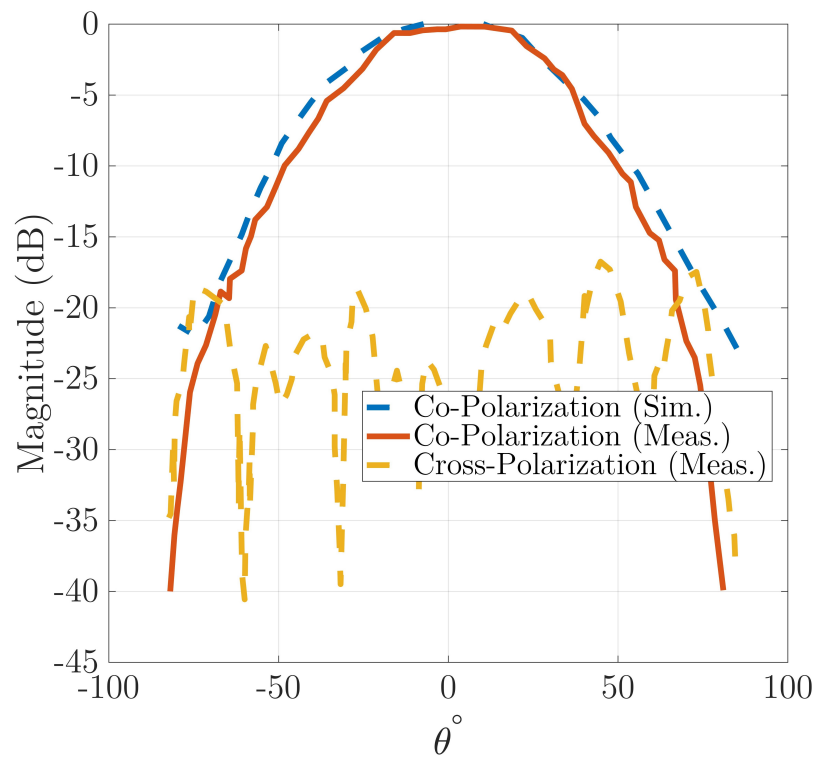
(b) $\phi = 90°$

Figure 7.17 – Les résultats simulés et mesurés pour la lentille perforée : copolarisation et polarisation croisée à la fois les diagrammes de rayonnement normalisés sur les plans E et H à 60 GHz (a) $\phi = 0°$, (b) $\phi = 90°$;
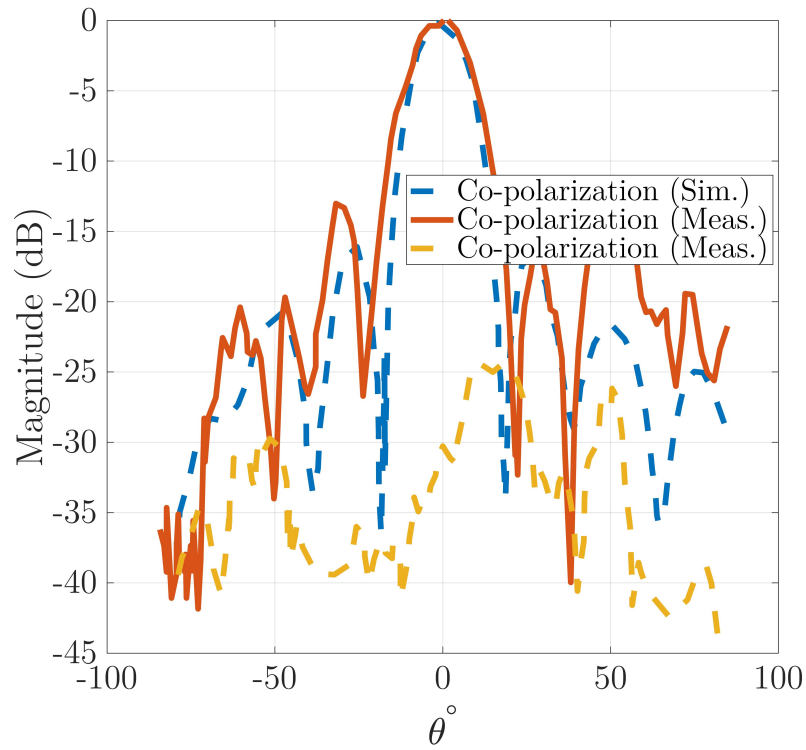
(a) $\phi = 0°$
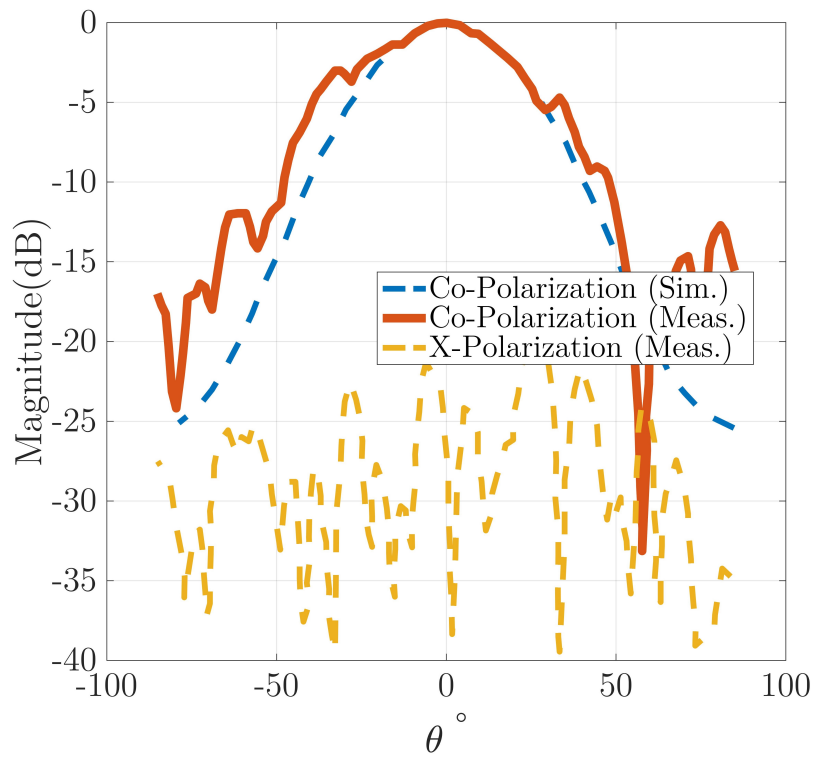
(b) $\phi = 90°$

Figure 7.18 – La copolarisation et polarisation croisée à la fois les diagrammes de rayonnement normalisés sur les plans E et H à 62 GHz (a) $\phi = 0°$, (b) $\phi = 90^{circ}$;
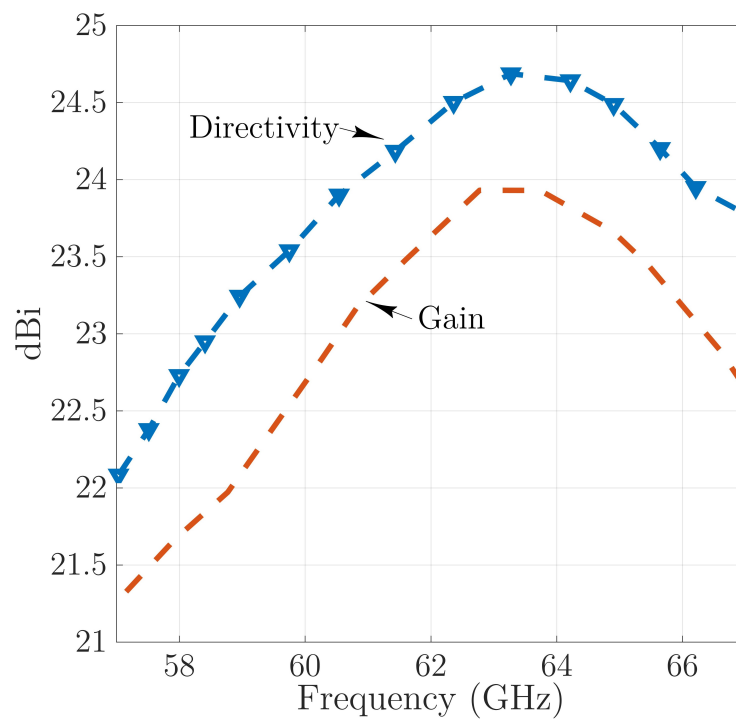
Figure 7.19 – Le gain et la directivité mesurés simulés et mesurés pour l'antenne à lentille de Luneburg perforée proposée;

162
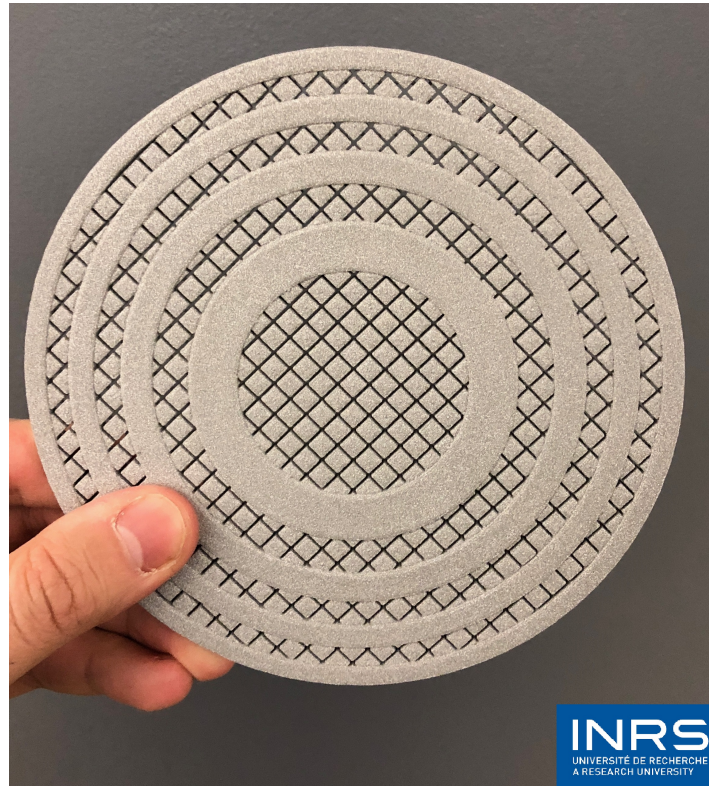
(a) Top view
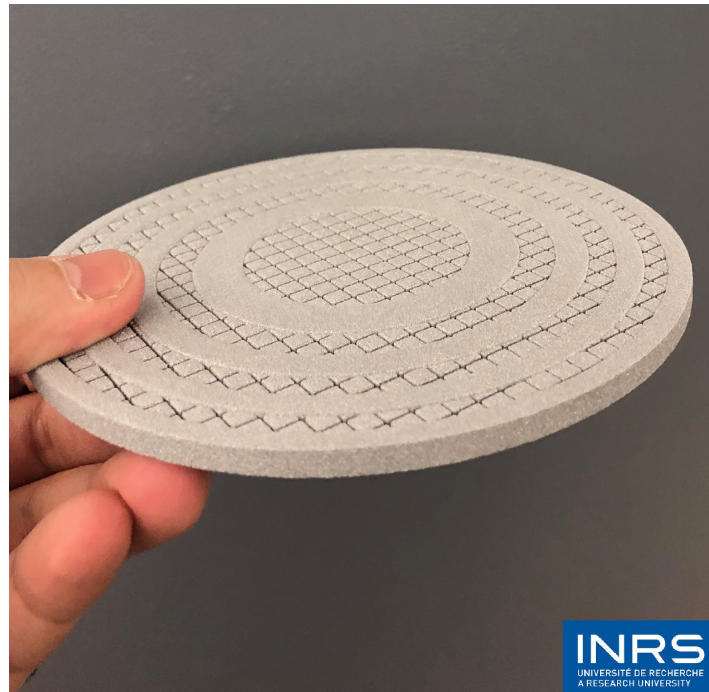
(b) Side view

Figure 7.20 – Photographie de la plaque de zone $\lambda/2$ produite par Alumide (a) Vue supérieure de la lentille, (b) Vue latérale;

Références

[1] E. W. Marchand. *VII Gradient index lenses*, volume 2943. Elsevier, 1973.

[2] Maksymilian Pluta. *Gradient Index Optics in Science and Engineering*, volume 2943. Proceedings of SPIE, The International Society for Optical Engineering, 1996.

[3] Y. He and G. V. Eleftheriades. A highly-efficient flat graded-index dielectric lens for millimeter-wave application. *2017 IEEE Antennas and Propagation Society International Symposium, Proceedings*, 2017-January:2655–2656, 2017.

[4] H. T. Ward, W. O. Puro, and D. M. Bowie. Artificial dielectrics utilizing cylindrical and spherical voids. *Proceedings of the IRE*, 1956.

[5] R. W. Corkum. Isotropic artificial dielectric. *Proceedings of the IRE*, 1952.

[6] A. Petosa, A. Ittipiboon, and S. Thirakoune. Investigation on arrays of perforated dielectric fresnel lenses. *IEE Proceedings: Microwaves, Antennas and Propagation*, 153(3):270–276, 2006. Cited By :14.

[7] K. Sato and H. Ujiie. A plate luneberg lens with the permittivity distribution controlled by hole density. *Electronics and Communications in Japan, Part I: Communications (English translation of Denshi Tsushin Gakkai Ronbunshi)*, 85(9):1–12, 2002. Cited By :38.

[8] S. H. Zainud-Deen, S. M. Gaber, A. M. Abd-Elhady, K. H. Awadalla, and A. A. Kishk. Wide-band perforated rectangular dielectric resonator antenna reflectarray. In *IEEE Antennas and Propagation Society, AP-S International Symposium (Digest)*, pages 113–116, 2011. Cited By :11.

[9] P. Nayeri, M. Liang, R. A. Sabory-Garcia, M. Tuo, F. Yang, M. Gehm, H. Xin, and A. Z. Elsherbeni. 3d printed dielectric reflectarrays: Low-cost high-gain antennas at sub-millimeter waves. *IEEE Transactions on Antennas and Propagation*, 62(4):2000–2008, 2014. Cited By :77.

[10] M. Liang, W. R. Ng, K. Chang, K. Gbele, M. E. Gehm, and H. Xin. A 3-d luneburg lens antenna fabricated by polymer jetting rapid prototyping. *IEEE Transactions on Antennas and Propagation*, 2014.

[11] J. Pourahmadazar and A. T. Denidni. Towards millimeter-wavelength: Transmission-mode fresnel-zone plate lens antennas using plastic material porosity control in homogeneous medium. *Scientific Reports*, 8, 2018.

[12] K. F. Brakora, J. Halloran, and K. Sarabandi. Design of 3-d monolithic mmw antennas using ceramic stereolithography. *IEEE Transactions on Antennas and Propagation*, 55(3 II):790–797, 2007. Cited By :39.

[13] I. Staude and J. Schilling. Metamaterial-inspired silicon nanophotonics. *Nature Photonics*, 11(5):274–284, 2017. Cited By :51.

[14] D. Isakov, C. J. Stevens, F. Castles, and P. S. Grant. 3d-printed high dielectric contrast gradient index flat lens for a directive antenna with reduced dimensions. *Advanced Materials Technologies*, 1(6), 2016. Cited By :4.

[15] A. Sayanskiy, S. Glybovski, V. P. Akimov, D. Filonov, P. Belov, and I. Meshkovskiy. Broadband 3-d luneburg lenses based on metamaterials of radially diverging dielectric rods. *IEEE Antennas and Wireless Propagation Letters*, 16:1520–1523, 2017.

[16] S. . Park, K. Lee, D. Han, J. Ahn, and K. . Jeong. Subwavelength silicon through-hole arrays as an all-dielectric broadband terahertz gradient index metamaterial. *Applied Physics Letters*, 105(9), 2014. Cited By :11.

[17] J. Yi, G. . Piau, A. De Lustrac, and S. N. Burokur. Electromagnetic field tapering using all-dielectric gradient index materials. *Scientific Reports*, 6, 2016. Cited By :4.

[18] Z. L. Mei, J. Bai, and T. J. Cui. Gradient index metamaterials realized by drilling hole arrays. *Journal of Physics D: Applied Physics*, 43(5), 2010. Cited By :45.

[19] M. Yin, X. Yong Tian, L. Ling Wu, and D. Chen Li. All-dielectric three-dimensional broadband eaton lens with large refractive index range. *Applied Physics Letters*, 104(9), 2014. Cited By :12.

[20] M. Hao. Xin liang. Metal 3d printed luneberg rf lense. *University of Arizona*, 2016.

[21] Y. H. Cho, W. J. Byun, and M. S. Song. High gain metal-only reflectarray antenna composed of multiple rectangular grooves. *IEEE Transactions on Antennas and Propagation*, 59(12):4559–4568, Dec 2011.

[22] R. Deng, S. Xu, F. Yang, and M. Li. Design of a low-cost single-layer x/ku dual-band metal-only reflectarray antenna. *IEEE Antennas and Wireless Propagation Letters*, 16:2106–2109, 2017.

[23] A. Jouade, J. Bor, O. Lafond, and M. Himdi. Millimeter-wave fresnel zone plate lens based on foam gradient index technological process. In *2016 10th European Conference on Antennas and Propagation (EuCAP)*, 2016.

[24] A. Jouade, M. Himdi, and O. Lafond. Fresnel lens at millimeter-wave: Enhancement of efficiency and radiation frequency bandwidth. *IEEE Transactions on Antennas and Propagation*, 65(11):5776–5786, 2017.

[25] D. K. Cheng. Modified luneberg lens for defocused source. *IRE Transactions on Antennas and Propagation*, 8(1):110–111, 1960. Cited By :14.

[26] M. Liang and H. Xin. Three-dimensionally printed/additive manufactured antennas. *Handbook of Antenna Technologies*, 1:661–697, 2016.

[27] E. Macdonald, R. Salas, D. Espalin, M. Perez, E. Aguilera, D. Muse, and R. B. Wicker. 3d printing for the rapid prototyping of structural electronics. *IEEE Access*, 2:234–242, Dec 2014.

[28] S. Ilyas and M. Gal. Single and multi-array grin lenses from porous silicon. *Conference on Optoelectronic and Microelectronic Materials and Devices, Proceedings, COMMAD*, pages 245–248, 2006. Cited By :1.

[29] J. M. Rodríguez, H. D. Hristov, and W. Grote. Fresnel zone plate and ordinary lens antennas: Comparative study at microwave and terahertz frequencies. *European Microwave Week 2011: "Wave to the Future", EuMW 2011, Conference Proceedings - 41st European Microwave Conference, EuMC 2011*, pages 894–897, 2011. Cited By :6.

[30] T. DIng, J. Yi, H. Li, H. Zhang, and S. N. Burokur. 3d field-shaping lens using all-dielectric gradient refractive index materials. *Scientific Reports*, 7(1), 2017.

[31] H. Frid, F. Töpfer, S. Bhowmik, S. Dudorov, and J. Oberhammer. Optimization of micromachined millimeter-wave planar silicon lens antennas with concentric and shifted matching regions. *Progress In Electromagnetics Research C*, 79:17–29, 2017.

[32] G. Thrivikraman, C. M. França, A. Athirasala, A. Tahayeri, and L. E. Bertassoni. 3d printing: Prospects and challenges: Nanomaterials in 3d bioprinting: Current approaches and future possibilities. *Nanotechnologies in Preventive and Regenerative Medicine: An Emerging Big Picture*, pages 349–379, 2017.

[33] J. P. Martins, M. P. A. Ferreira, N. Z. Ezazi, J. T. Hirvonen, and H. A. Santos. 3d printing: Prospects and challenges: Smart 3d printing and nanomaterials for tissue regeneration. *Nanotechnologies in Preventive and Regenerative Medicine: An Emerging Big Picture*, pages 299–349, 2017.

[34] M. E. Davis. Ordered porous materials for emerging applications. *Nature*, 417(6891):813–821, 2002. Cited By :3490.

[35] H. Xin and M. Liang. 3-d-printed microwave and thz devices using polymer jetting techniques. *Proceedings of the IEEE*, 105(4):737–755, April 2017.

[36] Elizabeth Palermo. What is selective laser sintering? *Report*, 2013.

[37] F. Kühner, R. A. Lugmaier, S. Mihatsch, and H. E. Gaub. Print your atomic force microscope. *Review of Scientific Instruments*, 78(7), 2007. Cited By :8.

[38] I. Gibson, D. Rosen, and B. Stucker. Additive manufacturing technologies: 3d printing, rapid prototyping, and direct digital manufacturing, second edition. *Additive Manufacturing Technologies: 3D Printing, Rapid Prototyping, and Direct Digital Manufacturing, Second Edition*, pages 1–498, 2015. Cited By :169.

[39] X. Lu, Y. Lee, S. Yang, Y. Hao, R. Ubic, J. R. G. Evans, and C. G. Parini. Fabrication of electromagnetic crystals by extrusion freeforming. *Metamaterials*, 2(1):36–44, 2008. Cited By :27.

[40] P. I. Deffenbaugh, T. M. Weller, and K. H. Church. Fabrication and microwave characterization of 3-d printed transmission lines. *IEEE Microwave and Wireless Components Letters*, 25(12):823–825, Dec 2015.

166

[41] Y. Lee, X. Lu, Y. Hao, S. Yang, R. Ubic, J. R. G. Evans, and C. G. Parini. Rapid prototyping of ceramic millimeterwave metamaterials: Simulations and experiments. *Microwave and Optical Technology Letters*, 2007.

[42] M. Vaezi, H. Seitz, and S. Yang. A review on 3d micro-additive manufacturing technologies. *International Journal of Advanced Manufacturing Technology*, 67(5-8):1721–1754, 2013. Cited By :253.

[43] David A Roper, Brandon L Good, Raymond McCauley, Shridhar Yarlagadda, Jared Smith, Austin Good, Peter Pa, and Mark S Mirotznik. Additive manufacturing of graded dielectrics. *Smart Materials and Structures*, 2014.

[44] P. I. Deffenbaugh, R. C. Rumpf, and K. H. Church. Broadband microwave frequency characterization of 3-d printed materials. *IEEE Transactions on Components, Packaging and Manufacturing Technology*, 3(12):2147–2155, 2013. Cited By :53.

[45] J. Baker-Jarvis, M. D. Janezic, and D. C. Degroot. High-frequency dielectric measurements. *IEEE Instrumentation Measurement Magazine*, 13(2):24–31, April 2010.

[46] *Keysight Technologies Basics of Measuring the Dielectric Properties of Materials [Online]. Available:http://literature.cdn.keysight.com/litweb/pdf/5989-2589EN.pdf.*

[47] *Agilent Technologies. (2009). Agilent Technologies Impedance Measurement Handbook, 4th ed., Santa Clara, CA, USA [Online]. Available: http://cp.literature.agilent.com/litweb/pdf/5950-3000.pdf.*

[48] *Agilent Technologies. (2013). Agilent E4980A Precision LCR Meter 20 Hz to 2 MHz Data Sheet, Santa Clara, CA, USA [Online]. Available:http://cp.literature.agilent.com/litweb/pdf/5989-4435EN.pdf.*

[49] M. Liang, W. Ng, K. Chang, M. Gehm, and H. Xin. An x-band luneburg lens antenna fabricated by rapid prototyping technology. *2011 IEEE MTT-S International Microwave Symposium*, pages 1–1, June 2011.

[50] H. F. Ma, B. G. Cai, T. X. Zhang, Y. Yang, W. X. Jiang, and T. J. Cui. Three-dimensional gradient-index materials and their applications in microwave lens antennas. *IEEE Transactions on Antennas and Propagation*, 61(5):2561–2569, 2013. Cited By :32.

[51] K. Gbele, M. Liang, W. . Ng, M. E. Gehm, and H. Xin. Millimeter wave luneburg lens antenna fabricated by polymer jetting rapid prototyping. *International Conference on Infrared, Millimeter, and Terahertz Waves, IRMMW-THz*, 2014.

[52] M. Liang and H. Xin. Design of additive manufactured luneburg lens working at w-band. In *2015 USNC-URSI Radio Science Meeting (Joint with AP-S Symposium), USNC-URSI 2015 - Proceedings*, page 354, 2015.

[53] Min Liang, Xiaoju Yu, R. Sabory-García, Wei-Ren Ng, M. E. Gehm, and Hao Xin. Direction of arrival estimation using luneburg lens. In *2012 IEEE/MTT-S International Microwave Symposium Digest*, pages 1–3, June 2012.

[54] T. Zentgraf, Y. Liu, M. H. Mikkelsen, J. Valentine, and X. Zhang. Plasmonic luneburg and eaton lenses. *Nature Nanotechnology*, 6(3):151–155, 2011. Cited By :160.

[55] Q. Wu, X. Feng, R. Chen, C. Gu, S. Li, H. Li, Y. Xu, Y. Lai, B. Hou, H. Chen, and Y. Li. An inside-out eaton lens made of h-fractal metamaterials. *Applied Physics Letters*, 101(3), 2012. Cited By :9.

[56] A. J. Danner and U. Leonhardt. Lossless design of an eaton lens and invisible sphere by transformation optics with no bandwidth limitation. In *2009 Conference on Lasers and Electro-Optics and 2009 Conference on Quantum electronics and Laser Science Conference*, pages 1–2, June 2009.

[57] Y. He and G. V. Eleftheriades. Matched, low-loss, and wideband graded-index flat lenses for millimeter-wave applications. *IEEE Transactions on Antennas and Propagation*, 2018.

[58] N. T. Nguyen, R. Sauleau, and C. J. M. Pérez. Very broadband extended hemispherical lenses: Role of matching layers for bandwidth enlargement. *IEEE Transactions on Antennas and Propagation*, 57(7):1907–1913, 2009. Cited By :31.

[59] C. A. Fernandes, E. B. Lima, and J. R. Costa. Broadband integrated lens for illuminating reflector antenna with constant aperture efficiency. *IEEE Transactions on Antennas and Propagation*, 58(12):3805–3813, 2010. Cited By :19.

[60] H. Frid. Closed-form relation between the scan angle and feed position for extended hemispherical lenses based on ray tracing. *IEEE Antennas and Wireless Propagation Letters*, 15:1963–1966, 2016. Cited By :2.

[61] B. Liu, X. Gong, and W. J. Chappell. Applications of layer-by-layer polymer stereolithography for three-dimensional high-frequency components. *IEEE Transactions on Microwave Theory and Techniques*, 52(11):2567–2575, 2004. Cited By :47.

[62] Z. Wu, J. Kinast, M. E. Gehm, and H. Xin. Rapid and inexpensive fabrication of terahertz electromagnetic bandgap structures. *Optics Express*, 16(21):16442–16451, 2008. Cited By :48.

[63] J. J. Adams, E. B. Duoss, T. F. Malkowski, M. J. Motala, B. Y. Ahn, R. G. Nuzzo, J. T. Bernhard, and J. A. Lewis. Conformal printing of electrically small antennas on three-dimensional surfaces. *Advanced Materials*, 23(11):1335–1340, 2011. Cited By :202.

[64] D. F. Filipovic, S. S. Gearhart, and G. M. Rebeiz. Double-slot antennas on extended hemispherical and elliptical silicon dielectric lenses. *IEEE Transactions on Microwave Theory and Techniques*, 41(10):1738–1749, 1993. Cited By :500.

[65] L. Xue and V. F. Fusco. 24 ghz automotive radar planar luneburg lens. *IET Microwaves, Antennas Propagation*, 1:624–628, June 2007.

[66] C. Pfeiffer and A. Grbic. A 2d broadband, printed luneburg lens antenna. *2009 IEEE Antennas and Propagation Society International Symposium*, pages 1–4, June 2009.

[67] W. E. Kock. Metallic delay lenses. *The Bell System Technical Journal*, 27(1):58–82, Jan 1948.

[68] G. Sui, B. Li, G. Bratzel, L. Baker, W. . Zhong, and X. . Yang. Carbon nanofiber/polyetherimide composite membranes with special dielectric properties. *Soft Matter*, 5(19):3593–3598, 2009. Cited By :17.

[69] Y. Song, Y. Shen, H. Liu, Y. Lin, M. Li, and C. . Nan. Enhanced dielectric and ferroelectric properties induced by dopamine-modified batio 3 nanofibers in flexible poly(vinylidene fluoride-trifluoroethylene) nanocomposites. *Journal of Materials Chemistry*, 22(16):8063–8068, 2012. Cited By :138.

[70] D. Lin, P. Fan, E. Hasman, and M. L. Brongersma. Dielectric gradient metasurface optical elements. *Science*, 345(6194):298–302, 2014. Cited By :524.

[71] J. H. Barton, C. R. Garcia, E. A. Berry, R. Salas, and R. C. Rumpf. 3-d printed all-dielectric frequency selective surface with large bandwidth and field of view. *IEEE Transactions on Antennas and Propagation*, 63(3):1032–1039, 2015. Cited By :23.

[72] L. Li, J. Wang, J. Wang, H. Ma, H. Du, J. Zhang, S. Qu, and Z. Xu. Reconfigurable all-dielectric metamaterial frequency selective surface based on high-permittivity ceramics. *Scientific Reports*, 6, 2016. Cited By :7.

[73] J. Gómez, A. Tayebi, J. de Lucas, and F. Cátedra. Metal-only fresnel zone plate antenna for millimetrewave frequency bands. *IET Microwaves, Antennas and Propagation*, 8(6):445–450, 2014. Cited By :4.

[74] X. Wan, X. Shen, Y. Luo, and T. J. Cui. Planar bifunctional luneburg-fisheye lens made of an anisotropic metasurface. *Laser and Photonics Reviews*, 8(5):757–765, 2014. Cited By :29.

[75] R. C. Rumpf, J. Pazos, C. R. Garcia, L. Ochoa, and R. Wicker. 3d printed lattices with spatially variant self-collimation. *Progress in Electromagnetics Research*, 139, 2013.

[76] Georgios Zouganelis and Djuradj Budimir. Effective dielectric constant and design of sliced luneberg lens. *Microwave and Optical Technology Letters*, 2007.

[77] B. Fuchs, O. Lafond, S. Palud, L. Le Coq, and M. Himd et. al. Comparative design and analysis of luneburg and half maxwell fish-eye lens antennas. *IEEE Transactions on Antennas and Propagation*, 2008.

[78] B. Fuchs, L. Le Coq, O. Lafond, S. Rondineau, and M. Himdi. Design optimization of multishell luneburg lenses. *IEEE Transactions on Antennas and Propagation*, 2007.

[79] H. Mosallaei and Y. Rahmat-Samii. Nonuniform luneburg and two-shell lens antennas: radiation characteristics and design optimization. *IEEE Transactions on Antennas and Propagation*, 2001.

[80] S. Zhang. Design and fabrication of 3d-printed planar fresnel zone plate lens. *Electronics Letters*, 2016.

[81] H. D. Hristov, J.M. Rodriguez, and W. Grote. The grooved-dielectric fresnel zone plate: An effective terahertz lens and antenna. *Microwave and Optical Technology Letters*, 2012.

[82] Hristo D. Hristov. *Fresnal Zones in Wireless Links, Zone Plate Lenses and Antennas*. Artech House, Inc., 2000.

[83] H. D. Hristov and J. M. Rodriguez. Design equation for multidielectric fresnel zone plate lens. *IEEE Microwave and Wireless Components Letters*, 2012.

[84] P. S. Kildal. Factorization of the feed efficiency of paraboloids and cassegrain antennas. *IEEE Transactions on Antennas and Propagation*, 1985.

[85] R. Collin. Aperture efficiency for paraboloidal reflectors. *IEEE Transactions on Antennas and Propagation*, 1984.

[86] Y. J. Guo and S. K. Barton. Phase correcting zonal reflector incorporating rings. *IEEE Transactions on Antennas and Propagation*, 1995.

[87] A. Dhouibi, S. N. Burokur, A. De Lustrac, and A. Priou. Compact metamaterial-based substrate-integrated luneburg lens antenna. *IEEE Antennas and Wireless Propagation Letters*, 11:1504–1507, 2012. Cited By :17.

[88] G. D. M. Peeler and D. H. Archer. A two-dimensional microwave luneberg lens. *Transactions of the IRE Professional Group on Antennas and Propagation*, 1(1):12–23, 1953. Cited By :30.

[89] C. Pfeiffer and A. Grbic. A printed, broadband luneburg lens antenna. *IEEE Transactions on Antennas and Propagation*, 58(9):3055–3059, 2010. Cited By :77.

[90] D. N. Black and J. C. Wiltse. Millimeter-wave characteristics of phase-correcting fresnel zone plates. *IEEE Transactions on Microwave Theory and Techniques*, 1987.

[91] H. D. Hristov and M. H. A. J. Herben. Millimeter-wave fresnel-zone plate lens and antenna. *IEEE Transactions on Microwave Theory and Techniques*, 1995.

[92] A. Petosa and A. Ittipiboon. Design and performance of a perforated dielectric fresnel lens. *IEE Proceedings - Microwaves, Antennas and Propagation*, 1994.

[93] A. Dhouibi, S. N. Burokur, A. De Lustrac, and A. Priou. Low-profile substrate-integrated lens antenna using metamaterials. *IEEE Antennas and Wireless Propagation Letters*, 12:43–46, 2013. Cited By :21.

[94] A. Dhouibi, S. N. Burokur, A. De Lustrac, and A. Priou. Broadband metamaterial-based half maxwell fish-eye lens antenna. *IEEE Antennas and Propagation Society, AP-S International Symposium (Digest)*, pages 1294–1295, 2013.

[95] A. Dhouibi, S. Nawaz Burokur, A. De Lustrac, and A. Priou. Metamaterial-based half maxwell fish-eye lens for broadband directive emissions. *Applied Physics Letters*, 102(2), 2013. Cited By :17.

[96] S. Zhang, R. K. Arya, S. Pandey, Y. Vardaxoglou, W. Whittow, and R. Mittra. 3d-printed planar graded index lenses. *IET Microwaves, Antennas and Propagation*, 10(13):1411–1419, 2016. Cited By :6.

[97] M. Yin, X. Yong Tian, L. Ling Wu, and D. Chen Li. All-dielectric three-dimensional broadband eaton lens with large refractive index range. *Applied Physics Letters*, 104(9), 2014. Cited By :12.

[98] Hristov,H. D. and Rodriguez,J. M. and Grote,W. The grooved-dielectric Fresnel zone plate: An effective terahertz lens and antenna. *Microwave and Optical Technology Letters*, 54(6), 2012.

[99] S. Datta, C. T. Chan, K. M. Ho, and C. M. Soukoulis Effective dielectric constant of periodic composite structures. *Phys. Rev. B, vol.*, 48, pp. 14936–43, 1993.

[100] Katsumoto,Y. and Hayashi,Y. and Oshige,I. and Omori,S. and Kishii,N. and Yasuda,A. and Asami,K. Dielectric cytometry with three-dimensional cellular modeling. *Biophysical journal*, 95, pp. 3043-3047, 2008.

Appendix A

Associated publications

A.1   Journal Articles

1. Pourahmadazar, J., Denidni, T. A. 2018, " Towards Millimeter-wavelength: Transmission-Mode Fresnel-Zone Plate Lens Antennas using Plastic Material Porosity Control in Homogeneous Medium", *Nature Scientific Reports*, vol. 8, (Accepted)

2. Pourahmadazar, J., Denidni, T. A., " Ordered porous structures for emerging Gradient refractive index Lens design: A Review", IEEE TAP-CPMT (Submitted)

3. Pourahmadazar, J., Denidni, T. A., " mmWave Luneburg lens antenns with material porosity permittivty control", Applied Physics, IEEE TAP-CPMT (Submitted)

4. Pourahmadazar, J., Denidni, T. A., "millimeter-wave planar antenna on flexible polyethylene terephthalate substrate with water base silver nanoparticles conductive ink," *MOTL Wiley* DOI:10.1002/mop.31079 (published)

5. Pourahmadazar, J., Denidni, T. A., "A Millimeter-Wave Dipole Antenna on an Extended Hemispherical 3D Printed Plastic Lens" *IEEE Transactions on Components, packaging, and Manufacturing Technology.*(2nd Round)

6. Pourahmadazar, J., Denidni, T. A., "60 GHz antenna array for millimeter-wave wireless sensor devices using silver nanoparticles inkjet printing technologies mounted on a flexible polymer substrate", *MOTL Wiley* DOI:10.1002/mop.30834.(published)

7. M. Farahani, Pourahmadazar, J, Denidni, T. A., et. al "Mutual Coupling Reduction in mm -Wave MIMO Antenna Array Using Metamaterial Polarization Rotator Wall," *IEEE Antennas and Wireless Propagation Letters.*(published)

A.2   Conference papers

1. Pourahmadazar, J., TA Denidni, "V-band Printed Ridge Gap Waveguide Phased Array Antenna with ±40° Scanning Angular Sector and ETSI Class II Radiation Patterns," IEEE Antem, 2018, University of Waterloo (accepted)

2. Pourahmadazar, J., Farahani, M., TA Denidni, "Printed Ridge Gap Waveguide Rotman Lens for Millimetre-wave Applications," IEEE Antem, 2018, University of Waterloo (accepted)

3. Pourahmadazar, J., M. Dashti, S. Tatu, TA Denidni, "V-band Dipole Phased Array Antennas on Extended Hemispherical Dielectric Lenses," IEEE URSI. 2017. (published)

4. Pourahmadazar, J., TA Denidni, "Extended Hemispherical Integrated Lens Antenna for V-band Application," IEEE URSI. 2017. (published)

5. R. Amiri, B. Zarghooni, J. Pourahmadazar and T. A. Denidni, "The fabrication and test of paraffin-based dielectric lenses for metamaterial characterization using the free-space method for 10–18 GHz," 2017 (EUCAP), Paris, France, 2017. (published)

6. R. Amiri, B. Zarghooni, A. Dadgarpour, Pourahmadazar, J., TA Denidni, "Reconfigurable Metamaterial Unit-cell with Controllable Refractive Index," ANTEM, 2016. (published)

7. R. Amiri, B. Zarghooni, A. Dadgarpour, Pourahmadazar, J., TA Denidni, "Anisotropic Meta-material Unit-cell for Millimeter-Wave Applications," ANTEM, 2016. (published)

8. M. Farahani, J. Zaid, Pourahmadazar, J., TA Denidni, M. Nedil "Miniaturized Two-Dimensional Circular Polarized Magneto-Dielectric Substrate Antenna," ANTEM, 2016. (published)

9. Pourahmadazar, J., R. Karimian, M. Farahani, TA Denidni, "10-GHz Microwave Lens based Beam-forming Phased Antenna Array System Using SIW Fed Bowtie Antenna", ANTEM, 2016.(published)

10. Pourahmadazar, J., R. Karimian, TA Denidni, "8–12-GHz Beam-Shaping/Steering Phased Antenna Array System Using SIW Fed Nonplanar Director Yagi-Uda antenna", APS, USNC/URSI, 2016.(published)

11. R. Karimian, Pourahmadazar, J., TA Denidni, "Free space Mutual Coupling Reduction between two SIW antennas at a millimeter-wave frequency," APS, USNC/URSI, 2016. Doi: 10.1109/APS.2016.7696798 (published)

12. Pourahmadazar, J., R. Karimian, TA Denidni, "A Steerable Yagi-Uda Array Antenna Using a Substrate Integrated Waveguide Rotman Lens," APS, USNC/URSI, 2016. (published)

13. Pourahmadazar, J., R. Karimian, TA Denidni, "A High Data-Rate Kiosk Application Circularly Polarized Fractal Antenna for Millimeter Wave Band Radio with 0.18u CMOS Tech.", (EuCap), 2016. Doi: 10.1109/EuCAP.2016.7481317, (published)

14. R. Karimian, Pourahmadazar, J., TA Denidni, "On the Design of Low SAR CPW Antenna with Magneto-Dielectric AMC Based Ground Plane," (EuCap), 2016.doi: 10.1109/EuCAP.2016.7481411

15. Pourahmadazar, J., TA Denidni, "High Gain Substrate Integrated Waveguide Resonant Slot Antenna Array for mm-Wave Band Radio," Ubiquitous Wire.(ICUWB), 2015 IEEE Int. Confer, 2015. (published)

16. Pourahmadazar, J., TA Denidni, "Multi-beam tapered slot antenna array using substrate integrated waveguide Rotman lens," Radar Conference (EuRAD), 2015 European, 425-428, 2015. doi: 10.1109/EuRAD.2015.7346328

17. Pourahmadazar, J., TA Denidni, "X-band substrate integrated Rotman Lens with ±24° scanning capability", APS, USNC/URSI National Radio Science Meeting, 2015. (published)

18. Pourahmadazar, J., TA Denidni, "X-band substrate integrated waveguide Rotman Lens," APS, USNC/URSI National Radio Science Meeting, 2015. (published)

19. B. Zarghooni, A Dadgarpour, Pourahmadazar, J., TA Denidni, "Supershape metamaterial unit cells using the gielis formula," APS, USNC/URSI National Radio Science Meeting, 2015. (published)